DOCTOR OF PHILOSOPHY

The impact of large-scale sea-level changes on tides in the past, present and future

Wilmes, Sophie-Berenice

Award date:
2016

Awarding institution:
Bangor University

PRIFYSGOL
BANGOR
UNIVERSITY

The impact of large-scale sea-level changes on tides in the past, present and future

PhD Thesis

presented by

Sophie-Berenice Wilmes

March 2016

Supervisors:

Dr. Mattias Green

Prof. James Scourse

School of Ocean Sciences

Bangor University

Menai Bridge, UK

"En outre, j'ai surpris ces courants de haut en bas et de bas en haut, qui forment la vraie respiration de l'Océan"

Jules Verne, Vingt mille lieues sous les mers

Abstract

Tides propagate through the oceans as shallow water waves and are therefore sensitive to changes in water depth and areal extent of the ocean. In this thesis the impacts of climatologically driven sea-level changes and the resulting changes in ocean extent on the global tidal dynamics are investigated. The large global sea-level adjustments between the Last Glacial Maximum (LGM, 18,000-21,000 years BP) and the present are considered; the present day tidal changes are analysed and the impact of future collapses of the West Antarctic and Greenland Ice Sheets on the tides are investigated using a global tidal model. The 130 m glacio-eustatic sea-level drop during the LGM had a profound impact on the principal semi-diurnal tide, doubling global dissipation rates and resulting in 'megatides' in the North Atlantic region. It is shown that the magnitude of the Atlantic tides is sensitive to the grounding line location of the Antarctic Ice Sheet. Next, the impacts of the altered dissipation for LGM ocean mixing and the meridional overturning circulation (MOC) in the glacial ocean are explored using an intermediate complexity climate model. The importance of tidal mixing for the global ocean circulation is highlighted. Strong LGM tidal mixing could have provided a mechanism for sustaining a vigorous LGM MOC. During the deglacial period glacio-eustatic sea-level rose rapidly and large adjustments of the global tides occurred into the early Holocene. In the late Holocene sea-level adjustments were small and tidal dynamics remained fairly constant over this period. Tide-gauge records covering the past decades show global changes in tidal amplitudes occurring in parallel with large-scale sea-level changes which have been attributed to global warming. Using simulations forced with observed sea-level trends an attempt is made to reproduce the large-scale change patterns. For M_2 the patterns agree well, but for K_1 the model is unable to reproduce the trends, possibly due to the small magnitude of the K_1 trends. A number of recent studies have highlighted an accelerated ice loss from the ice streams draining the West Antarctic and Greenland Ice Sheet together with widespread grounding line retreats in West Antarctica. It has been suggested that both ice sheets could undergo collapses under certain climate warming scenarios leading to increases in global mean sea-level of 5 m and 7 m, respectively. It is shown that the collapse of a polar ice sheet would lead to large changes in tidal dynamics and thus changes in sea-level variability. These changes have further reaching consequences for shelf-sea dynamics, ecosystems, and open ocean tidal mixing.

Key words: Tides, Sea Level, Last Glacial Maximum, Tidal Mixing, Meridional Overturning Circulation, Grounding Line, Tide gauges, Ice Sheet Collapse, Mixing Fronts, Climate Change

Acknowledgements

It would have not been possible to put this thesis together without the help of some very kind people around me, some of which I would mention here.

First and foremost, I would like to thank my principle supervisor Dr. Mattias Green for the guidance and advice he gave me throughout the PhD, without which this work would not have been possible. His encouragement and patience helped me see this work through to the end. Prof. James Scourse provided helpful advice and motivation on the way and was key in initiating the project in the first place.

HPC Wales and Fujitsu provided the funding for this study in form of a studentship and the access to high performance computing technology. Ade Fewings from HPC Wales provided invaluable technical assistance on the HPC Wales computer system and went the extra mile to make programs run smoothly.

The collaboration with Dr. Andreas Schmittner provided a very interesting insight into large-scale ocean processes. Dr. Natalya Gomez and Harriet Lau calculated the sea-level fingerprints for Chapter 7 and, together with Prof. Tom Rippeth, contributed very valuable discussion points to this chapter. Dr. Robert Mawdsley and Dr. Ivan Haigh very kindly provided the tide gauge data for Chapter 6. Jess Madge helped me proofread this work and guided me through the perils of English grammar and sentence structure.

A big thank you goes to Tash, Alice and all the PhD students from my office for the fun times and distractions we had, and all the help, support and backing they gave me.

My parents, Rachel and Herbert, and my siblings, Berend, Lars and Leonie, have been a constant source of inspiration, support and encouragement throughout my PhD. Without their guidance, perspective and values I would never have been in the place to consider starting and carrying through a project like this one. Special thanks go to my dad for reading and commenting on my thesis.

Last but not least, I would thank my partner Adam for being by my side during last couple of years, encouraging and supporting me, discussing my thesis with me, and for the amazing adventures we had outside work.

Preface

This work has been prepared following a standard thesis structure with an introduction to the subject matter, a chapter with background information on tidal dynamics, and a chapter on the details of tidal modelling. This includes a detailed description of the tidal model and its setup, and the analysis methods applied. The three results chapters are prepared in paper format, i.e., they each have their own introduction, methods, results and discussion section. This format was chosen as the work has either been published or is being prepared for publication. The results chapters are drawn together in an overall discussion and conclusion section.

Chapter 4 has been published in a similar version (see appendix) under following bibliographic references:

Wilmes, S.-B. and J. A. M. Green (2014), The evolution of tides and tidal dissipation over the past 21,000 years. *Journal of Geophyiscal Reseach*, *119*(17), 4083–4100.

Schmittner, A., J. A. M. Green, and S.-B. Wilmes (2015), Glacial ocean overturning intensified by tidal mixing in a global circulation model, *Geophysical Research Letters*, *42*(10), 4014–4022.

Chapter 6 is being prepared for publication under following bibliographic reference:

Wilmes, S.-B., J. A. M. Green, N. Gomez, T. P. Rippeth and H. Lau (2015), Global marine impacts of large-scale ice sheet collapses, *in preparation*.

Author Contributions

Wilmes and Green (2014) was based on an idea by J. A. M. Green. S.-B. Wilmes carried out the simulations and the analysis and wrote the core of the text with contributions and comments from J. A. M. Green.

A. Schmittner carried out the climate model simulations and the analysis, and wrote the core of the text in *Schmittner et al.* (2015). S.-B. Wilmes provided the tidal simulations and carried out the analysis of the latter, and commented on the manuscript, and J. A. M. Green calculated the stratification fields for the tide model simulations, wrote the tide model description, and gave comments and feedback on text.

Chapter 7 is based on an idea by S.-B. Wilmes who carried out the simulations and subsequent analysis with input from J. A. M. Green and T. P. Rippeth. S. B. Wilmes wrote the core of the manuscript with feedbacks and comments from all authors. N. Gomez and H. Lau provided the files with the sea-level fingerprints for the different ice sheet collapse scenarios.

Contents

List of Figures

List of Tables

Chapter 1

Introduction

1.1 Global mean sea level changes

Global mean sea-level has been rising at a rate of 1.7 mm yr^{-1} over the past century, which increases to 3.2 mm yr^{-1} when data between 1993 and 2000 is considered (*Church and White*, 2011; *Jevrejeva et al.*, 2014). The sea-level changes are primarily driven by the thermal expansion of the ocean due to warming and the transfer of water stored on land in the form of glaciers or ice caps into the ocean (e.g., *Nerem et al.*, 2006; *Church et al.*, 2013). These processes have been attributed to the warming of the Earth due to increased greenhouse gas emissions throughout the industrial era (e.g., *Church et al.*, 2013). It has been estimated that global mean sea-level rise by the end of this century will most likely lie between 0.63 and 0.98 m, depending on the emissions scenario applied (*Church et al.*, 2013), with an upper limit estimated at 1.8 m (*Jevrejeva et al.*, 2014). Over 1 billion people currently live in coastal regions, with over 200 million in areas that lie lower than 5 m above sea-level (*Bollmann et al.*, 2015). Over $1/5^{th}$ of the population's livelihoods is tied to the oceans. These sea-level changes are therefore expected to be one of the most destructive aspects of the current climate change bringing large social, economic and ecological impacts (e.g., *Nicholls and Cazenave*, 2010).

However, over the recent geological past much larger sea-level changes have occurred. During the last glacial maximum (here 21,000 – 18,000 yr BP, LGM) for example, sea-level was between 120 and 130 m lower than at present due to large amounts of fresh water locked up in land-based ice masses (e.g., *Clark and Mix*, 2002; *Clark et al.*, 2009). In the transition period from the LGM to early Holocene sea-level increased to near-present day values (e.g., *Carlson and Clark*, 2012).

Recent investigations of the Antarctic ice streams have shown rapid and wide-spread grounding line retreats in the West Antarctic sector (*Rignot et al.*, 2014; *Joughin et al.*, 2014) together with strongly enhanced ice loss (*Pritchard and Vaughan*, 2007; *Shepherd*, 2012; *Mouginot et al.*, 2014). Large areas of the West Antarctic Ice Sheet (WAIS) are grounded below sea-level and therefore inherently unstable (*Clark and Lingle*, 1977; *Oppenheimer*, 1998; *Bamber et al.*, 2009; *Gomez et al.*, 2010; *Joughin et al.*, 2014). This implies that a marine ice sheet instability may be underway resulting in a possible future collapse of the West Antarctic Ice Sheet (WAIS) (*Joughin et al.*, 2014; *Mouginot et al.*, 2014). The Greenland Ice Sheet (GIS) has exhibited a strongly negative mass balance over the past decades (*Velicogna*, 2009; *Velicogna et al.*, 2014) and it has been suggested that in a strongly warming world the GIS could fully melt (*Gregory et al.*, 2004; *Robinson*

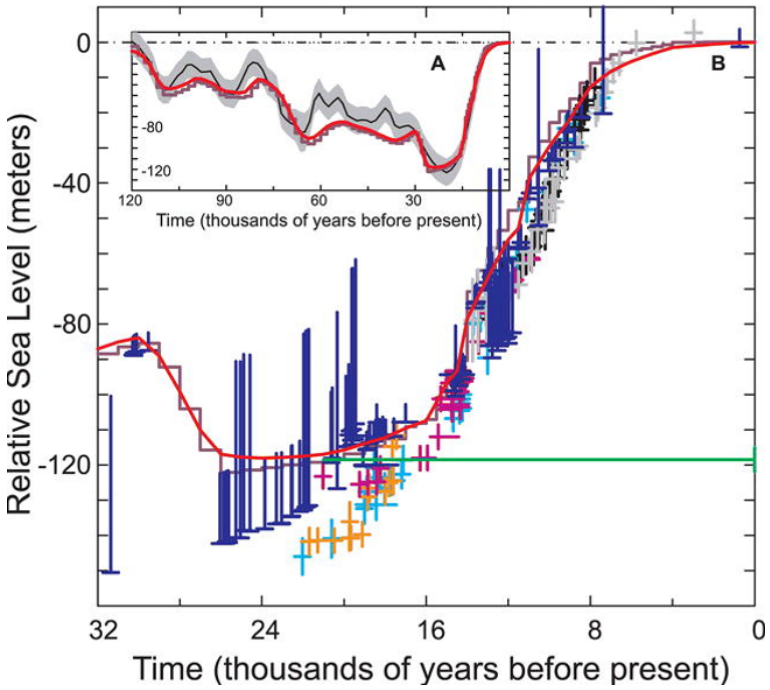

Figure 1.1: (A) Deep-sea sea oxygen isotope-derived global eustatic sea-level curve (black) and relative sea-level history at Barbados derived from the ICE-5G model (red line). (B) Extended Barbados record for the last glacial and Holocene (blue line and crosses) and modelled sea-level records for the same location (red line). The other crosses represent record from further locations in the Pacific. Figure from *Peltier* (2007).

et al., 2012). Collapses of the WAIS and the GIS would lead to global mean sea-level increases of 5 m and 7 m (e.g., *Gomez et al.*, 2010; *Gregory et al.*, 2004).

However, it is not only long-term changes in mean sea-level that are important, but also its variability on much shorter time scales. On intra-annnual to inter-annual time scales sea-level variability is driven by the tides, storm surges generated by tropical or extratropical cyclones (e.g., *Pugh and Woodworth*, 2014), seasonal variability (e.g., *Pugh and Woodworth*, 2014), local Ekman pumping (e.g., *Timmermann*, 2010), large-scale interannual climatic patterns such as the El Niño Southern Osciallation (ENSO) (*Nerem et al.*, 1999; *Landerer*, 2008) or the NAO (*Wakelin et al.*, 2003), or variations in ocean currents inducing sea surface height changes (e.g., *Stammer et al.*, 2013).

1.2 Importance of tides

Ocean tides are the main source of day-to-day large-scale sea-level variability, making them an important consideration in the planning of coastal defence structures due to the

considerable sea-level changes they cause. Furthermore, it has been shown that the phase of the tide modifies the propagation of storm surges and consequently their impacts on coastlines (*Horsburgh and Wilson*, 2007). The navigation of ships in coastal seas, shallow water ports and estuaries requires knowledge of the phase of the tide and the associated tidal currents. Tidal currents also play an important role in sediment transport and thus influence (near-)coastal morphology in shallow seas (*Perillo*, 1995).

In temperate and polar seasonally stratified shelf seas, tides influence the locations of tidal mixing fronts (the interfaces between seasonally stratified and fully mixed waters). Their position is determined by a balance between buoyancy fluxes by solar heating and mixing by the tide and winds (*Simpson and Hunter*, 1974). Mixing fronts are highly productive as they are transition zones between calmer but nutrient-depleted stratified waters and nutrient-rich but turbid waters, thus supporting large amounts of primary and secondary productivity (*Pingree et al.*, 1978; *Holligan et al.*, 1984). Tides are therefore also important for fisheries. Furthermore, the distribution of fully mixed versus seasonally stratified waters also determines the export of dissolved inorganic carbon into the deep ocean and therefore influences atmospheric CO_2 concentrations (*Tsunogai et al.*, 1999; *Thomas et al.*, 2004; *Rippeth et al.*, 2008).

Tides are however not only important in coastal areas. Approximately half of the 2 TW of the energy driving the mixing deemed necessary to sustain the meridional overturning circulation (MOC) is supplied by the tide (e.g., *Munk*, 1966; *Munk and Wunsch*, 1998; *Wunsch and Ferrari*, 2004). At rough topography in the deep ocean energy from the barotropic tide is transferrred to internal waves which subsequently break and cause bursts of mixing (e.g., *Egbert and Ray*, 2000; *Ledwell et al.*, 2000). This turbulent mixing by the internal tide together with wind-driven upwelling and mixing by turbulent eddies (e.g., *Wunsch and Ferrari*, 2004) balances the formation of very cold deep waters at high latitudes by creating a pathway for the deep waters to return to the surface ocean and heat to be transferred into the deep ocean (e.g., *Stommel*, 1961; *Munk*, 1966). The MOC is a major oceanic pathway for transporting heat, momentum, freshwater and nutrients across the globe. It is therefore an important determinant of global climate patterns (e.g., *Rahmstorf*, 2002).

It has been shown that tides interact with ice sheets via the floating part of an ice sheet, the ice shelf, by inducing flexing and hinging along the grounding line. This leads to pronounced modulations of flow speeds in ice streams at tidal frequencies (e.g.,

Gudmundsson, 2011; *Rosier et al.*, 2014a,b). It has also been hypothesised that megatides during the last glacial may have contributed to the break-up of large ice sheets (*Arbic et al.*, 2004; *Griffiths and Peltier*, 2008).

Recently, tides have been considered as a more reliable renewable energy source than the sun or the wind. Tidal power can be extracted by two methods: (1) from tidal streams with help of turbines making use of the kinetic energy of the tide; (2) the potential energy can be harnessed with help of tidal lagoons or barrages (e.g., *Nicholls-Lee and Turnock*, 2008).

At present the tides dissipate about 3.8 TW of energy throughout the ocean. This energy loss creates torque on the Earth-Moon system which transfers energy to the Moon's orbit and results in an acceleration of the Moon and an increase in its distance from the Earth. The recession rate of the Moon is therefore tied directly to the amount of tidal dissipation in the Earth's oceans (e.g., *Brosche and Sündermann*, 1978).

1.3 Changes in the tides

Tidal dynamics can change for a variety of reasons. Different driving mechanisms are of importance over different time scales:

1. Changes in the tidal potential occur over long, geological time scales, when the Earth-Moon distance differs significantly from its present-day state (*Brosche and Sündermann*, 1978), but are small during the more recent geological past (tens of million years) and near future (e.g., *Green and Huber*, 2013).

2. As tides essentially behave like shallow water waves (e.g., *Pugh and Woodworth*, 2014), they are strongly affected by water depth and basin geometry changes. These bathymetry changes can occur for a number of different reasons. Global mean sea-level changes occur in response to water density changes caused by climatic changes and alterations in ice mass on land (see e.g., *Church et al.*, 2013). Vertical land movement in response to the loading and unloading of the Earth's crust from the melting or formation of large ice masses, glacio-isostatic adjustment processes (GIA), cause large-scale relative sea-level changes on decadal to centennial time-scales (*Peltier*, 2004). Elastic responses of the Earth's crust to changes in loading of the crust, in contrast to the viscous processes in the case of GIA, occur on much shorter time scales (*Mitrovica et al.*, 2009; *Gomez et al.*, 2010).

Changes in ocean depth and shape are also caused by tectonic processes, which are of importance on geological time scales (e.g., *Green and Huber*, 2013). Local changes in water depth can also be induced by changes in coastal morphology, e.g., sediment transport patterns, land reclamation, harbour dredging, or changes in river outflow (e.g., *Pelling et al.*, 2013b).

3. Changes in the internal tide through e.g., stratification changes, alter the amount of energy transferred from the barotropic to the baroclinic tide and can therefore lead to changes in the surface tide (e.g., *Colosi and Munk*, 2006).

It has been suggested that the 130 m global mean sea-level decrease during the LGM significantly impacted global tidal dynamics, resulting in strong enhancements in M_2 tidal amplitudes in the North Atlantic region and an increase in global tidal dissipation by over 50% (e.g., *Egbert et al.*, 2004; *Arbic et al.*, 2004; *Uehara et al.*, 2006; *Griffiths and Peltier*, 2008, 2009). A number of studies have highlighted uncertainties in the LGM grounding line locations of the Antarctic ice sheet (*Anderson et al.*, 2002; *Hillenbrand et al.*, 2012; *Bentley et al.*, 2014) with considerable variations in the Antarctic bathymetries for the different cases. It has been shown that these bathymetry variations lead to considerable changes in the regional tidal dynamics, however, so far the impact of the Antarctic grounding line variations on the global tides remains to be investigated.

A number of studies have hypothesised that the enhanced tidal energy dissipation could have altered the strength and structure of the MOC during the last glacial (*Munk and Wunsch*, 1998; *Montenegro et al.*, 2007; *Green et al.*, 2009, e.g.,), however previous investigations into the impacts of the tidal changes on the MOC have been carried out with coarse resolution tide model input for global intermediate complexity climate models (*Montenegro et al.*, 2007; *Green et al.*, 2009) and a simplified tidal mixing parameterisation (*Green et al.*, 2009).

Most studies investigating the impacts of sea level variations during the last glacial period have generally focussed on the LGM and concentrated on changes in the M_2 tide, however, large sea level increases occurred over a relatively short time period during the transition from the glacial to the Holocene (e.g., *Carlson and Clark*, 2012). Tidal studies addressing the impacts of theses changes have generally been carried out at either low temporal resolution (*Egbert et al.*, 2004), low spatial resolution (*Uehara et al.*, 2006) or have had a regional focus (*Hill et al.*, 2011; *Hall et al.*, 2012).

Recent studies using both global and regional tide-gauge data show that significant

changes in tidal ranges, amplitudes and phases have occurred at many locations across the globe over the 20^{th} century and continuing into the 21^{st} century (e.g., *Woodworth*, 2010; *Mawdsley et al.*, 2015). A number mechanisms have been proposed as the driving mechanisms (see e.g., *Woodworth*, 2010, and the list above) but regional and global mean sea level changes stand out as a likely forcing mechanism of the global tidal changes over this time period. However, to date global tidal models forced with neither the GIA-driven sea level changes over the past century or the observed global sea-level trends have not been able to reproduce the observed changes (e.g., *Müller et al.*, 2011), in the latter case possibly due to the low resolution of the model used for the study.

To date most studies investigating the impacts of future sea-level changes have had a regional focus (e.g., *Ward et al.*, 2012; *Pickering et al.*, 2012; *Pelling et al.*, 2013a; *Pelling and Green*, 2013; *Pelling et al.*, 2013b; *Luz Clara et al.*, 2015) and have assumed regional sea level changes following the global mean. A number of recent studies have suggested that the WAIS and the GIS could be unstable in a future warmer climate resulting in possible collapses of these ice sheets (e.g., *Gregory et al.*, 2004; *Robinson et al.*, 2012; *Joughin et al.*, 2014; *Mouginot et al.*, 2014). For the WAIS a full collapse of the marine parts of this ice sheet would result in a global mean increase in sea-level by 5m. It has however been shown that the sea-level changes across the globe are highly non-uniform due to unloading of the Earth's crust, changes in gravitational attraction and Earth rotation (*Gomez et al.*, 2010). To date the impact of large-scale ice sheet collapses on global tides has not been examined.

1.4 Aims and Objectives

This work investigates the impact of climatically driven large-scale sea-level changes on the tides in the past, present and future using the global tidal model OTIS (*Egbert et al.*, 1994; *Egbert and Erofeeva*, 2002). The emphasis lies on time scales over which sea-level changes are primarily driven by the amount of water stored in land-based ice masses, but tectonics and changes in the tidal potential are not important. We focus on the time period ranging from the last glacial maximum to the present and explore future scenarios. More specifically, the impacts of global sea-level changes on M_2 and K_1 tidal amplitudes and tidal dissipation are examined. There are a number of aspects motivating this work:

1. Considerable sea-level changes are occurring at present and larger ones are expected

in the future due to global increases in temperature. In this respect the large-sea level adjustments at the end of the last glacial can be used as an analogy for possible future changes and some of the past mechanisms of change could be applicable for future changes. Even though the present-day sea level changes are small in comparison to the changes that occurred over the deglacial period it is likely that they are contributing to the tidal changes that are being observed at present, and that the mechanisms driving the amplitude changes are the same as during the deglacial period. Similarly, the ice sheet collapses of the past can contribute to our understanding of the impacts of possible future losses of for example the WAIS or the GIS.

2. It is not only mean sea-level changes that are important for societies inhabiting low-lying coastal regions and coastal ecosystems but also crucially their variability. Tides are a very important aspect of this variability. Understanding the impacts of sea-level changes on tidal dynamics help us predict the changes in the variability of sea-level.

3. Tides also influence a number of different aspects of the climate system: they determine the structure of coastal and shelf-sea ecosystems, and they provide part of the energy sustaining the large-scale ocean circulation. Changes in the tides are therefore expected to have further reaching consequences than mere changes in sea-level variability.

In order to enhance the understanding of tides in the past part 1 of this thesis revisits the tidal dynamics of the last glacial maximum. Using a global tide model the impacts of the Antarctic grounding line locations on global tidal dynamics are investigated. In a next step the impact of altered LGM tidal dissipation on the global ocean circulation is highlighted where tide model simulations are used to force an intermediate complexity climate model (*Schmittner et al.*, 2015). Furthermore, the model is forced with the reconstructed sea-level changes occurring over the deglacial period and the Holocene and an overview of the evolution of tides and tidal dissipation between the LGM and the present is given. Following questions are addressed in this part:

1. Were global K_1 tidal dynamics altered during the LGM?

2. How does the grounding line extent of the Antarctic ice sheets during the LGM impact global tidal dynamics?

3. How did the tidal dynamics of the principle semi-diurnal and diurnal tidal constituents M_2 and K_1 evolve between the LGM and the present when the large Northern Hemisphere ice sheets melted and sea-level rose rapidly over the deglacial period and the transition to the Holocene?

4. How did the changes in tidal dissipation during the LGM impact the large-scale overturing circulation during the last glacial?

Part 2 of this work investigates whether the currently observed global mean sea-level changes could be the cause of tidal amplitude changes over the past decades observed over most of the globe (e.g., *Ray*, 2006, 2009; *Jay*, 2009; *Woodworth*, 2010; *Devlin et al.*, 2014; *Zaron and Jay*, 2014). In order to test this hypothesis a global dataset of sea-level and tidal amplitude trends is used (*Mawdsley et al.*, 2015) the observed trends are compared to tide model simulations forced with the observed sea-level changes. In particular following objectives are met:

1. Present a global picture of significant trends in sea level and tidal dynamics for the M_2 and the K_1

2. Rexamine the link between global sea-level trends and changes in the tides by comparing the observed trends to global tide model simulations forced with both uniform and non-uniform sea-level rise scenarios: are the observed sea level trends the driver of the secular tide trends?

The last part of this work examines the impacts of possible future large-scale ice sheet collapses of the WAIS and GIS and investigates the implications of the changes in tidal processes for shelf sea and open ocean dynamics. Following questions shall be addressed:

1. How do the non-uniform sea-level changes induced by collapses of the WAIS and the GIS impact tidal amplitudes and dissipation?

2. How do the tidal responses to uniform and nonuniform sea-forcing differ?

3. What further implications do the tidal changes have for shelf-sea biogeochemisty and the global climate system?

1.5 Thesis structure

Chapter 2 gives background information on tides and tidal dynamics. The first part of this chapter gives an overview of the equlibirum tidal theory, the second part discusses

global tidal dynamics and explores how sea-level changes can alter tides. Chapter 3 gives an overview of global tidal modelling and introduces the tidal model used in this work. Chapter 4 investigates aspects of LGM tidal dynamics and the evolution of tides and tidal dissipation from the LGM to the present. In particular, the impacts of Antarctic grounding line position on the tides, and the implications of altered tidal dissipation on the LGM MOC are explored here. Chapter 5 examines the link between observed secular changes in the tides over the past century and the observed sea level changes. Chapter 6 investigates at the impacts of large-scale ice sheet collapses and highlights the implication for both coastal biogeochemistry and open-ocean dynamics. Chapter 7 draws the results from the previous chapters together and puts them into a wider context, and an outlook of future work is given.

The results chapters are presented in paper format as a number of them are published or are being prepared for publication. Therefore each results chapter has its separate introduction, a methodology which explains how the model set up differs from the standard setup and the analysis carried out, a results section and its own discussion.

Chapter 2

Tide Theory

This chapter elaborates on the theory of tides. In the first part the theory leading to astronomic tide generating potential is developed, and the concept of the equilibrium tide, i.e. the structure of the tide in an idealised ocean with uniform water depth and no landmasses, is explored. The second part looks at tides in the real world and aspects which influence tidal dynamics such as continent configuration, dissipation and conversion of energy to internal waves, and self-attraction and loading effects. The chapter finishes with a description of how sea level changes lead to changes in tidal dynamics.

2.1 Equilibrium Tidal Theory

Correlations between the phase of the ocean tide and position of the moon were recognised by the societies of ancient Greece, but the basis of oceanic tide theory was not established until the late 17^{th} century with *Newton* (1687)'s *Principa*. The key elements of Newton's tidal theory are the following:

1. The effect of one gravitating body on another combined with their rotation around a common centre of gravity is to produce diametrically opposed equal bulges under head of the attracting body.

2. The Moon and the Sun cause these bulges in the ocean with the strength of the latter being approximately half of the former.

3. The bulges generated by the Moon and the Sun move independently across the Earth, driven by the orbital motions of the Moon around the Earth and the Earth around the Sun. They are affected by friction.

From Newton's principles the astronomic tide generating force can be derived. In a coordinate system, in which the rotation of the Earth around its own axis is neglected and which concentrates on the joint revolution of the Earth and the Moon (Sun) around a common centre of gravity, the lunar (solar) astronomic tide generating force at a given point on the Earth's surface is given by the difference in the solar (lunar) gravitational attraction at that given point and the centre of the Earth.

2.1.1 Tidal Potential

In this chapter the astronomic tide generating potential, a concept established by *Laplace* (1799), will be discussed as for ocean dynamic applications it is a more useful concept.

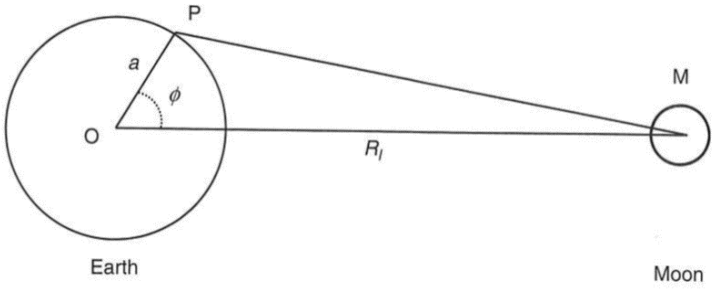

Figure 2.1: The location of the point P on the Earth's surface and its relation to the Moon. Figure from *Pugh and Woodworth* (2014).

The tide generating potential based on tidal harmonics was first introduced by *Doodson* (1922) and resulted in the Doodson numbers which are still used today. The tide generating force of Newton's tidal theory represents the spatial gradient of the harmonically decomposed tide generating potential. The following development of the tidal potential is based on *Pugh* (1996), *Pugh and Woodworth* (2014), and *Stewart* (2009).

The gravitational potential of a body quantifies the work necessary to remove a particle from the body, against the gravitational force of attraction, to an infinitive distance from the body. For the Earth-Moon system the gravitational potential at point P on the Earth's surface (see Figure 2.1), Ω_P, is given by

$$\Omega_P = -\frac{gm_l}{p} = -\frac{gm_l}{R_l}(1 - 2\frac{a}{R_l}\cos\phi + \frac{a^2}{R_l^2})^{-\frac{1}{2}} \tag{2.1}$$

where g is the universal gravitational constant, R_l is the distance between the centre of the Earth, O, and the centre of the Moon, M (see Figure 2.1). m_l is the mass of the Moon, and p the distance between point P and M. a denotes the distance between M and P, and ϕ is the angle between the axis OM and OP, also known as the lunar angle. p can be rewritten as

$$p^2 = 1 - 2\frac{a}{R_l}\cos\phi + \frac{a^2}{R_l^2}. \tag{2.2}$$

The square-root term in Ω_P can now be expanded into a series of Legendre-polynomials:

$$\Omega_P = -\frac{gm_l}{R_l}(1 + (\frac{a}{R_l})\cos\phi + (\frac{a}{R_l})^2\frac{1}{2}(3\cos^2\phi - 1) + \ldots). \tag{2.3}$$

The spatial gradients of the terms in the polynomials represent the tidal forces. $\nabla 1$ is zero and will thus produce no force. The second term produces a constant force parallel to R_l which is the force keeping the Earth in orbit around the common centre of mass

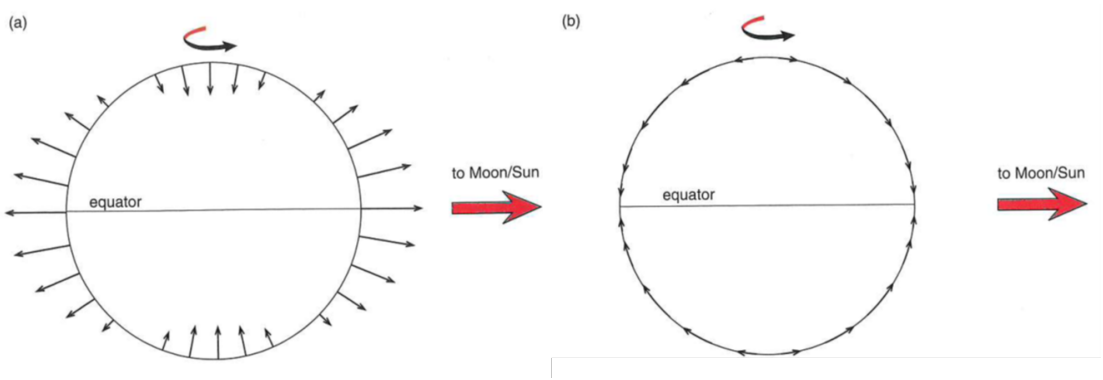

Figure 2.2: The distribution of the (a) vertical and (b) horizontal tractive forces across the Earth's surface. Figure from *Pugh and Woodworth* (2014).

with the Moon. The third expression is the effective tide producing term. The fourth and further higher terms are normally neglected as the term $(\frac{a}{R_l})^n \approx (\frac{1}{60})^n$ becomes very small as n increases. The tide producing potential is thus given by

$$\Omega_P = -\frac{1}{2} g m_l \frac{a^2}{R_l^3}(3\cos^2\phi - 1). \tag{2.4}$$

The forces at point P can be resolved into a horizontal and a vertical component. The vertical forces produce small variations in weight which are balanced by the pressure at the sea bed and are therefore negligible. The horizontal component is given by

$$-\frac{\partial \Omega_P}{a\partial\phi} = \frac{2G}{a}\sin 2\phi, \tag{2.5}$$

$$\text{where } G = \frac{3}{4} g m_l (\frac{a^2}{R_l^3}). \tag{2.6}$$

These horizontal forces, despite being very small in comparison to the gravitational attraction of the Earth, give rise to the tidal acceleration required to induce water movements. Taken together across the surface of the Earth the horizontal forces are also known as tractive forces (see Figure 2.2).

The tractive forces vary across the surface of the Earth as the Earth rotates and the position of the Moon alters through its orbit. The alteration of the lunar angle ϕ can also be regarded as rotary periodic tilting of the horizontal axis.

The lunar angle ϕ is dependent on the northward latitude of the point P, ϕ_P, the northward declination of the Moon against the Earth's equator, d_l, and the hour angle of P, C_P, which is the difference in longitude between the meridian of P and the meridian of the sub lunar point V (the point at which the Moon is directly overhead) (see Figure 2.3).

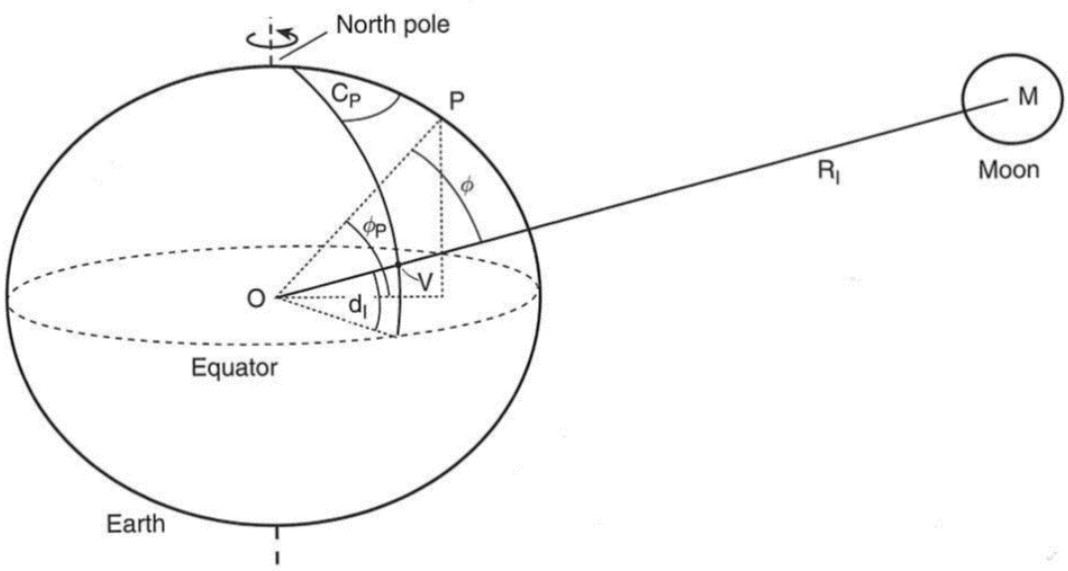

Figure 2.3: Schematic showing the three-dimensional location of the point P on the Earth's surface relative to the Moon. ϕ is the angle between the point P, O and V. V is on the Earth's surface on the axis O to M. Figure from *Pugh and Woodworth* (2014).

$\cos\phi$ is related to all other angles by

$$\cos\phi = \sin\phi_P \sin d_l + \cos\phi_P \cos d_l \cos C_P \tag{2.7}$$

so that the tidal potential can be written as

$$-\Omega_P = \frac{3}{2} ag \frac{m_l}{me} \left(\frac{a}{Rl}\right)^3 \left\{ \begin{array}{l} \frac{3}{2}(\sin^2 d_l - \frac{1}{3})(\sin^2 \phi_P - \frac{1}{3}) \\ +\frac{1}{2} \sin 2d_l \sin 2\phi_P \cos C_P \\ +\frac{1}{2} \cos^2 d_l \cos^2 \phi_P \cos 2C_P \end{array} \right\} \tag{2.8}$$

2.1.2 The Equilibrium Tide

Commonly, from Equation 2.8 an expression for the Equilibrium Tide is derived. The Equilibrium Tide is defined as the sea-surface elevation that would be in balance with the tidal force, were the Earth covered completely with water deep enough to result in an instantaneous response to the tidal forces. The Equilibrium Tide shows no resemblance to the real tides but is nevertheless a very useful concept: it is used as a reference framework to which the observed amplitudes and phases of the harmonic tidal constituents can be compared, especially when preparing tidal model input.

In the concept of the Equilibrium Tide, the free surface is a level surface under the

combined action of the tide generating force $-\frac{\partial \Omega_P}{\partial x}$ and the gravitational attraction of the Earth g. The tractive forces cause an apparent deflection from the vertical (Figure 2.4). x marks a direction at right angles to the undisturbed force of gravity.

We therefore have

$$\tan\alpha = -(\frac{\partial \Omega_P}{\partial x})/g \tag{2.9}$$

and

$$\tan\alpha = \frac{\bar{\zeta}}{\partial x}. \tag{2.10}$$

Combining Equations 2.9 and 2.10 we get

$$g\frac{\bar{\zeta}}{\partial x} + \frac{\partial \Omega_P}{\partial x} = \frac{\partial}{\partial x}(g\bar{\zeta} + \Omega_P) = 0 \tag{2.11}$$

and

$$\frac{\partial}{\partial y}(g\bar{\zeta} + \Omega_P) = 0 \tag{2.12}$$

If the latter two equations are integrated horizontally over the surface of the ocean yields

$$g\bar{\zeta} + \Omega_P = 0 \tag{2.13}$$

Equation 2.13 can now be applied to Equation 2.8 so that the Equilibrium Tide becomes

$$\bar{\zeta} = a(\frac{m_l}{m_e})[C_0(t)(\frac{3}{2}\sin^2\phi_P - \frac{1}{2}) + C_1(t)2\sin 2\phi_P + C_2(t)\cos^2\phi_P] \tag{2.14}$$

where the time-dependent coefficients are

$$\begin{aligned} C_0(t) &= (\frac{a}{R_l})^3(\frac{3}{2}\sin^2 d_l - 12) \\ C_1(t) &= (\frac{a}{R_l})^3(\frac{3}{4}\sin^2 2d_l \cos C_P) \\ C_2(t) &= (\frac{a}{R_l})^3(\frac{3}{4}\cos^2 2d_l \cos 2C_P) \end{aligned} \tag{2.15}$$

These three coefficient characterise the main types of tides: the long-period tidal constituents, the diurnal tides ($\cos C_P$) and the semi-diurnal tides ($\cos 2C_P$). The magnitude of each term is modified by a common term which is proportional to the inverse of the cube of the distance to the Moon R_l.

The long-period constituents are also a result of monthly variations in the declination of the Moon d_l. Their amplitudes are maximum at the poles and minimum at 35° 16′ N and S.

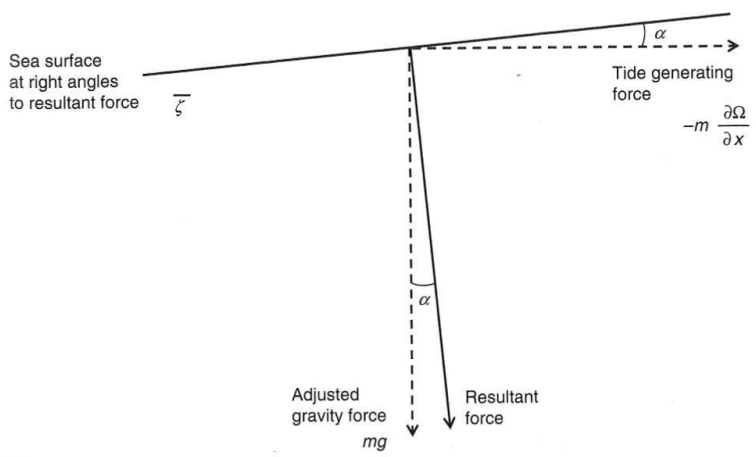

Figure 2.4: The interaction between the Equilibrium water surface, the tide-generating force, and the normal Earth's gravity force. Figure from *Pugh and Woodworth* (2014).

Both the diurnal and the semidiurnal species are modulated at twice the lunar declination (Term $2d_l$ in Equation 2.15). The diurnal components have their maximum amplitudes at 45° latitude N and S and an amplitude of zero at the poles and the equator. The semi-diurnal constituents have their maximum amplitudes at the equator and are zero at the poles.

The amplitudes of the Equilibrium Tide are small. For example, at the equator the semi-diurnal tide has an amplitude of 0.27 m. The observed tides have their energy frequencies on the same bands as the Equilibrium Tides. However, the observed tides are generally much greater due to the dynamic response of the ocean to the tidal forcing.

The Equilibrium Tide due to the Sun can be expressed in the same way as for the Moon by simply replacing d_l, m_l and R_l by d_s, m_s and R_s. The solar tidal amplitudes are smaller than the lunar tides by a factor of 0.46 but their energy frequencies are on similar bands as the lunar tides.

2.2 The Moon-Earth-Sun system

In order to define the total Equilibrium Tide as a reference system it is necessary to understand the moments of the Moon and the Sun over time in relation to the Earth. The complete motions are very complex and beyond the scope of this work but here some of the basic concepts need to be explored.

There are two reference systems against which the movements of the Sun and the Moon

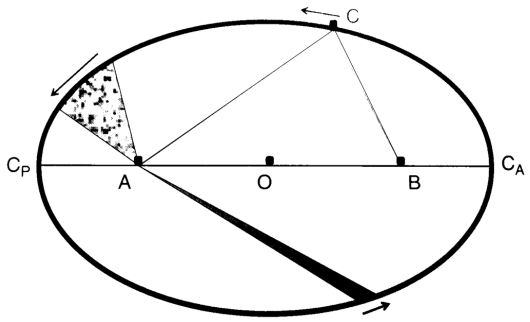

Figure 2.5: Properties describing an ellipse and an elliptical orbit. Figure from *Pugh and Woodworth* (2014).

can be evaluated. The first is the equatorial system which is a plane which intersects horizontally with the Earth's equator. Declinations are given as angles North and South of this plane. Angular distances are evaluated against the vernal equinox, the point on the Earth's equator at which the Sun's orbit intersects the plane from South to North. The vernal equinox is not fixed in time but gradually migrates over time completing one revolution in 26,000 years.

The second reference system, the ecliptic, is the celestial extension of the plane traced out by the motion of the Earth around the Sun. Again, the point reference zero-point is the vernal equinox. The location of celestial objects is defined according to their ecliptic latitude and longitude. The angle between the equatorial plane and the ecliptic is the obliquity of the ecliptic.

In the previous section, for simplicity, the orbital motions of the Sun and the Moon were considered to be circular. However both Newton and Keppler showed that two objects, moving under the sole influence of their mutual gravitational attraction, orbit around the common centre in form of ellipses, with the focus of the ellipse given by the centre of mass of the bodies.

Figure 2.5 shows an ellipse with a mass at C travelling around a mass at A with foci at A and B. In order to describe the elliptic orbit of a mass at least three parameters are necessary. The shape of the ellipse is defined by $AC + CB = constant$. The distance between C and A is minimum when C is at C_P and maximum when C is at C_A. C_P and C_A are also known as perigee and apogee of the orbit. The eccentricity of the ellipse, e, is given by ratio between OA/OC_A and the distance between OC_A and OC_P is called the semi-major axis. The object orbiting around A has its fastest angular speed at the

perigee and the slowest at the apogee (e.g., *Hilbert and Cohn-Vossen*, 1999).

In order to calculate the Equilibrium Tide in Equation 2.14, three parameters are needed: distance, declination and hour angle of the tide generating body. For the Sun these are R_S, d_S, and C_S. The Earth-Sun case is simpler than for the Earth-Moon as the declination against the ecliptic is always zero. The orbit of the Earth around the Sun has an eccentricity of 0.0168. The distance of the sun from the Earth, R_S, can now by approximated by

$$\frac{\bar{R}_S}{R_S} = 1 + \cos(h - p') \tag{2.16}$$

with $\bar{R}_S$ as the mean solar distance, h being the Sun's mean ecliptic longitude and p' is the longitude of the solar perigee, the perihelion, which completes a full cycle every 21,000 years.

As shown previously the ecliptic longitude of the Sun does not increase at a regular rate. The actual longitude λ_s in radians is given by

$$\lambda_S = h + 2e\sin(h - p'). \tag{2.17}$$

where e denotes the eccentricity of the ellipse.

The motions of the Moon are more complicated to describe. This is because the Earth-Moon plane is inclined against the ecliptic with a mean angle of $5°9'$ and gradually rotates over a time period of 18.61 years. The ascending node, the point at which the Moon crosses the ecliptic from South to North, displays a backward rotation of $0.053°$ per solar day, thus completing a full rotation every 18.61 years. The maximum lunar declination of $28°\ 36'$ with respect to the equator occurs when the ascending node corresponds to the Vernal Equinox. Conversely the minimum declination of $18°\ 18'$ when the descending node is at the Vernal Equinox. This process gives rise to a distinct modulation of the lunar tides over a 18.6 year cycle (see e.g., *Woodworth*, 2010; *Haigh et al.*, 2011).

The eccentricity of the lunar orbit, having a mean value of 0.0549, is more than three times larger than that of the solar orbit. Due to the gravitational attraction of the Sun both the lunar eccentricity and the obliquity of the Moon vary. The lunar distance R_l to a first order is given by

$$\frac{\bar{R}_l}{R_l} = 1 + e\cos(s - p) + \text{solar perturbations} \tag{2.18}$$

where $\bar{R}_l$ is the mean lunar distance, s denotes the Moon's geocentric mean ecliptic longitude which increases by $0.059°$ per mean solar hour and p is the longitude of the

Table 2.1: Basic astronomic frequencies

Symbol	Frequency °/hour	Astronomic Period			Source
ω_0	15	1.000	mean solar days	Mean solar day	Local mean solar time
ω_1	14.49205211	1.035	mean solar days	Mean lunar day	Local mean lunar time
ω_2	0.54901663	27.322	mean solar days	Sidereal month	Moon's mean longitude
ω_3	0.04106864	365.242	mean solar days	Tropical year	Sun's mean longitude
ω_4	0.00464184	8.85	Julian years	Moon's perigee	Longitude of Moon's Perigee
ω_5	-0.00220641	16.61	Julian years	Regression of Moon's nodes	Longitude of Moon's ascending node
ω_6	0.00000196	20,942	Julian years	Perihelion	Longitude of Sun's perigee

lunar perigee rotating with an 8.85 year period.

The lunar ecliptic longitude also varies at a slightly irregular rate through its orbit which is approximated by

$$\lambda_l = s + 2e\sin(s-p) + \text{solar perturbations} \tag{2.19}$$

The right ascension of the Moon can be derived from its ecliptic latitude longitude as

$$A_l = \lambda_l - \tan^2(\frac{\epsilon_l}{2})\sin 2\lambda_l \tag{2.20}$$

In relation to the ecliptic the lunar latitude can be calculated as

$$\sin(\text{ecliptic latitude}) = sin(\lambda_l - N)\sin(5°9' \,) \tag{2.21}$$

where N is the mean longitude of the ascending node.

The declination and the right ascension of the Moon and Sun can be represented as a series of harmonics each with different angular speeds and amplitudes. These can then be entered into the equation describing the Equilibrium Tide (Equation 2.14).

2.2.1 Tidal Harmonics

The effect of the variations in declination and distances of the tide-generating bodies discussed above are to modify the parameters in Equation 2.14. These variations can be decomposed into harmonic constituents using Fourier-Transformation and result in modulations of the three basic tidal components (long-period, diurnal and semi-diurnal tides). The tidal potential as a function of the geographical longitude and latitude of P on the Earth's surface λ and θ can now be written as a combination of these three constituents

$$\Omega(\lambda,\theta) = \Omega_0(\lambda,\theta) + \Omega_1(\lambda,\theta) + \Omega_2(\lambda,\theta) \tag{2.22}$$

Table 2.2: The most important tidal harmonics.

Tide Species	**Name**	**Frequency**	**Period**	**Doodson Number**	**Relative amplitude** ($M_2 = 1$)
Semi-diurnal					
Principal lunar	M_2	$2\omega_1$	12.421	255555	1.000
Principal solar	S_2	$2\omega_1 + 2\omega_2 - 2\omega_3$	12.000	273555	0.465
Lunar elliptic	N_2	$2\omega_1 - \omega_2 + \omega_4$	12.658	245655	0.192
Lunisolar	K_2	$2\omega_1 + 2\omega_2$	11.967	275555	0.087
Diurnal					
Lunisolar	K_1	$\omega_1 + \omega_2$	23.934	165555	0.399
Principal lunar	O_1	$\omega_1 - \omega_2$	25.819	145555	0.4151
Principal solar	P_1	$\omega_1 + \omega_2 - 2\omega_3$	24.066	163555	0.193
Elliptic lunar	Q_1	$\omega_1 - 2\omega_2 + \omega_4$	26.868	135655	0.079
Long-period					
Fortnightly	M_f	$2\omega_2$	327.85	075555	0.172
Monthly	M_m	$\omega_2 - \omega_4$	661.31	065455	0.091
Semi-annual	M_{sa}	$2\omega_3$	4383.05	057555	0.082

where $s = 0, 1, 2$ stands for the long-period, diurnal and semi-diurnal tidal constituents, respectively.

The tidal potential for each tidal constituent is given by

$$\Omega_s(\lambda, \theta) = DG_s \sum_j C_j \cos(\sigma_j t + s\lambda + \theta_j) \tag{2.23}$$

with $G_0 = \frac{1}{2}(1 - 3\sin^2\theta)$, $G_1 = \sin\theta$, $G_2 = \cos^2\theta$. Here, D is the Doodson constant (see further explanation below), C_j is the amplitude of the constituent and σ_j denotes the harmonic frequency of the constituent.

Doodson (1922) transformed Equations 2.23 and 2.14 in a way that the frequency of each harmonic constituent could be represented by the sum of a series of basic astronomic frequencies. There are six basic frequencies (ω_{1-6}) (see Table 2.2) expressed with respect the mean solar day ω_0. Generally, ω_6 is omitted as the variations induced by the solar perigee are very small.

The frequency of any tidal constituent ω_{tc} can be described as a positive and/or negative linear combination of the basic astronomic frequencies in Table 2.2:

$$\omega_{tc} = n_1\omega_1 + n_2\omega_2 + n_3\omega_3 + n_4\omega_4 + n_5\omega_5 \tag{2.24}$$

where the factors n_{1-5} can take values between -5 and 5.

For convenience, the angular frequency of the given tidal constituent ω_{tc} can also be

written as the Doodson number where

$$\text{Doodson number} = n_1 n_2 n_3 n_4 n_5 + 055555 \tag{2.25}$$

where the addition of 055555 leads to the Doodson numbers becoming positive.
The resulting tidal constituents with the largest amplitudes are listed in Table 2.2.1.
In addition to the harmonics in the three basic frequency bands, higher harmonic species appear. These originate from shallow-water modulations of the original harmonics. M_4 and S_4 are the fourth-diurnal species at twice the frequency of the original harmonics M_2 and S_2. MS_4 and MS_f are the result of the interaction between M_2 and S_2.

2.3 Dynamic Tidal Theory

In the real world ocean tides do not resemble Equilibrium Tides for a number of reasons (e.g., *Hendershott*, 1981; *Pugh and Woodworth*, 2014):

1. The movement of water in the ocean must obey the physical laws given by the hydrodynamic equations. This means that, with the exception of the Southern Ocean and the Arctic basin, land masses prevent the tidal wave from circumnavigating the globe.

2. Tidal waves travel as shallow water waves in the Earth's oceans because they are limited by water depth and their speed is slower than the speed of the Moon generating them. They thus experience a lag with respect to their forcing.

3. The ocean basins have natural modes of resonance which influence their response to the the tidal forcing.

4. Water movements are subjected to deflection by the rotation of the Earth around its own axis, represented by the Coriolis acceleration in the hydrodynamic equations.

5. The solid Earth responds elastically to loading and unloading by tides, which can lead to both local and far field effects.

6. Water movement is affected by friction. This leads to energy losses

2.3.1 Long waves in a non-rotating system

Tidal waves travel as shallow water waves in the Earth's oceans, as their wave lengths are much greater than the water depth of the ocean which means that their propagation

is limited by water depth.

The wave length λ of a shallow-water wave is given by

$$\lambda = \frac{c}{\omega} \tag{2.26}$$

where c is the wave speed and the frequency is denoted by ω. Given that the amplitude of the wave is small compared to the water depth and the wave length is much greater than the water depth, the wave speed is (e.g., *Kundu*, 1990)

$$c = \sqrt{gD} \tag{2.27}$$

where g is the gravitational acceleration and D is the water depth. The currents are related to the sea-level displacement ζ:

$$u = \zeta\sqrt{g/D} \tag{2.28}$$

The latter two expressions can be derived from the solutions to the continuity and horizontal momentum equations. As tidal waves are long waves they travel non-dispersively and the motion of each tidal constituent can thus be represented separately.

2.3.2 Standing Waves and Resonance

In the ocean, waves cannot continuously travel as progressive waves but undergo reflection at sudden depth changes and coastal boundaries. The observed wave represents the combination of the incident and reflected wave. In the simplest case of a long channel, in which the wave is reflected from one end without loss of amplitude, the result of the combination of the waves is a standing wave. It has a nodes where amplitudes are zero alternating with antinodes where amplitudes a maximal, each separated by a distance of $\lambda/4$.

In a closed rectangular basin, e.g., a lake, with a length L and water depth D water movement occurs analogous to a pendulum, with two waves travelling in opposite directions and being perfectly reflected at either end. The natural period of oscillation (or resonance period) T_n of the basin is given by

$$T_n = \frac{2L}{\sqrt{gD}} \tag{2.29}$$

For the real world T_n will vary because water depths are mostly not uniform and basins are not rectangular. This gives rise to longitudinal and latitudinal seiches and in addition basins can have more than one node.

Standing waves also occur in basins which are open at one end at which they are forced with oscillating currents at the open boundary. In this case of forced oscillations the natural period T_{nf} is given by

$$T_{nf} = \frac{4L}{\sqrt{gD}} \tag{2.30}$$

In contrast to seiches, which, once initiated, continue until damped by friction, these forced oscillations die down once the mechanism forcing them is removed. If a system is forced close to its resonant period, large amplifications in amplitudes can occur (*Egbert et al.*, 2004). In nature perfect resonance tends not to occur as the incoming wave is not perfectly reflected at the end of the basin. Thus in most cases the outgoing wave is smaller than the incoming wave. This can be represented by a progressive wave superimposed on a standing wave.

2.3.3 Amphidromes

The behaviour of a progressive wave in a channel changes greatly when the rotation of the Earth is considered. The wave now becomes a Kelvin wave. The rotation of the Earth induces a deflection to the right (left) in the Northern (Southern) Hemisphere which is bounded by the wall of the channel on the right (left). A pressure-gradient is set up which continues to build until it is balanced by the geostrophic force of the rotation. The amplitude ζ decreases exponentially across the channel from its maximum value at the right-hand (left-hand) side of the channel as a function of the distance y offshore:

$$\zeta(y) = H_0 \mathrm{e}^{-fy/c} \tag{2.31}$$

$$u(y) = \sqrt{gD}\zeta(y) \tag{2.32}$$

where the f is the Coriolis parameter. The length scale of the decay is the Rossby radius given by f/c. At a distance $y = f/c$ the amplitude of the wave has fallen to $0.37H_0$. The motion of the currents is parallel to the propagation direction of the waves (see Figure 2.6). Note that Kelvin waves can only travel in one direction: in the Northern Hemisphere the coastline is always to the right of the propagation direction, in the Southern Hemisphere it is always on the left.

The case of a standing wave in a channel on a rotating system is of special interest in tidal applications. Away from the boundary, where the description of the processes taking place would require complicated mathematics, the waveforms can be represented

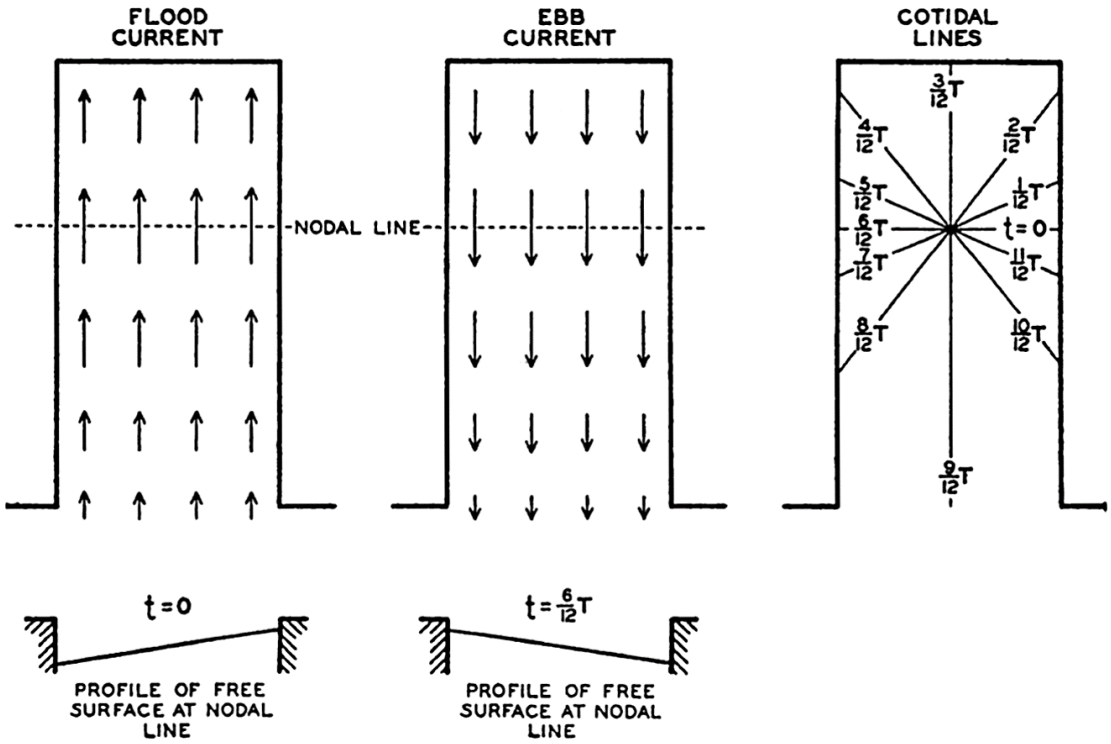

Figure 2.6: Schematic representation of oscillations in a channel with an open boundary resulting in the development of an amphidromic point. Figure from *Sverdrup* (1942).

by two Kelvin waves travelling along the channel in opposite directions. In contrast to the nodal line in the non-rotating case the wave now oscillates around a nodal point, or an amphidrome (see Figure 2.6). In the Northern (Southern) Hemisphere the wave rotates counter-clockwise (clockwise). The amplitudes increase from the nodal point (zero amplitude) outwards, with the largest amplitudes at the boundaries and the co-tidal lines radiate outward from the amphidrome.

If the reflected part of the wave is reduced in comparison to the incoming wave due to energy loss through friction, the amphidrome is shifted toward the left-hand boundary of channel (with the viewer looking into the channel). This process may shift the amphidrome onto land at which point it becomes known as a degenerate amphidrome. The co-tidal lines still centre at this point.

2.3.4 Hydrodynamic Equations

The dynamic theory of tides was cast into its modern form by Laplace in 1775-1776. He derived a set of hydrodynamic equations from the Navier-Stokes equations, commonly known as the Laplace Tidal Equations (LTEs), which are used as the basis for modern

tidal modelling (*Hendershott*, 1981; *Pugh*, 1996; *Pugh and Woodworth*, 2014). In the recent past these have been extended to include terms addressing frictional terms, energy losses to the internal tide and shallow Earth deformation (*Griffiths and Hill*, 2015). Most tidal models assume single-layer shallow-water dynamics (e.g., *Hendershott*, 1977; *Egbert et al.*, 2004):

$$\frac{\partial \mathbf{U}}{\partial t} + \mathbf{U} \cdot \nabla \mathbf{u} + \mathbf{f} \times \mathbf{U} = -a_H \nabla^2 \mathbf{U} - gH\nabla(\zeta - \zeta_{EQ} - \zeta_{SAL}) - \mathbf{F} \tag{2.33}$$

$$\frac{\partial \zeta}{\partial t} = -\nabla \cdot \mathbf{U} \tag{2.34}$$

where the ζ is the tidal elevation, t denotes time, $\mathbf{U}$ is the depth-integrated volume transport calculated as the velocity $\mathbf{u}$ multiplied by the water depth H, $\mathbf{f}$ is the Coriolis vector, a_H is the eddy viscosity, and $\mathbf{F}$ describes frictional or dissipative stresses. ζ_{EQ} is the equilibrium tide and ζ_{SAL} is an equilibrium-like tide term describing the effects of self-attraction and loading.

In the following sections the terms describing the equilibrium tide, forced by the full astronomic tide generating potential, self-attraction and loading, and frictional terms, will be discussed in more detail.

2.3.5 The yielding Earth

Not only the ocean but also the solid Earth is affected by the tidal forces. The solid Earth responds elastically to the tidal forces giving rise to the so-called Earth tides. Although small in comparison to the ocean tides, these effects can nevertheless be measured with sensitive instrumentation. There are two factors contributing to the Earth tides: the direct response of the Earth to the tidal forces, and the indirect response of the Earth to the ocean tidal loading and mass redistributions across the globe. Since the 1970s it has been recognised that calculations of the ocean tides must take the self-attraction and the Earth-loading of the tides into account (*Hendershott*, 1972) as these can alter the ocean tidal amplitudes by as much as 20% or more in some regions and cause phase shifts of up to 30° (*Gordeev et al.*, 1977).

The solid Earth tides can be divided into (a) the body tide, ζ_b, describing the direct response of the Earth to the tidal gravitational forces and (b) the radial-displacement ocean-load tide, ζ_l, describing the effects of the loading of the Earth's crust and the changes in mass distribution on the Earth due to tidal water movement in the oceans (*Hendershott*, 1981; *Ray*, 1998). In contrast to the oceans, the Earth is approximately in

static equilibrium with regards to the tide generating forces, as the longest normal modes of the solid Earth are much shorter than the tidal forcing frequencies. This means that the Earth's response to the tidal forcing occurs instantaneously. The observed ocean tide, ζ, can therefore be written as a combination of the geocentric tide, the displacement of the Earth's free surface, ζ_g, and the Earth tides (*Munk and Macdonald*, 1960; *Hendershott*, 1981; *Ray*, 1998):

$$\zeta = \zeta_g - \zeta_b - \zeta_l. \tag{2.35}$$

The body-tide response of the Earth to the tide generating forces are largely determined by its viscous properties of the Earth's interior described by the Love numbers h_n and k_n and the loading numbers h'_n and k'_n. This gives rise to an elastic surface distortion of an amplitude ζ_b (*Munk and Macdonald*, 1960; *Hendershott*, 1981; *Ray*, 1998):

$$\zeta_b = h_n \Omega / g. \tag{2.36}$$

The ocean load tide ζ_l is given by

$$\zeta_l = \sum_n \frac{h'_n U_n}{g} \tag{2.37}$$

where U_n is the n-th degree spherical harmonic component of the gravitational potential induced by the ocean loading ζn. The total gravitational potential of the ocean loading U is $\sum_n U_n$. U_n/g can be now be replaced so that ζ_l now becomes

$$\zeta_l = \sum n h'_n \alpha_n \zeta_n \tag{2.38}$$

$$\text{with } \alpha_n = \frac{3(\rho_w/\rho_e)}{2n+1} \tag{2.39}$$

where ρ_w and ρe represent the densities of sea water and the Earth, respectively.

The complete tidal potential Γ can now be written as the sum of the astronomical tidal potential Ω, the effect of the solid Earth yielding to Ω and the ocean self-attraction contribution and its resulting loading contribution:

$$\Gamma = \Omega + k_n \Omega + \sum_n g \alpha_n \zeta_n + \sum_n k'_n g \alpha_n \zeta_n. \tag{2.40}$$

The equilibrium tide ζ_{EQ} accounts for the Earth's body tide and ζ_{SAL} represents the equilibrium-like tide induced by the tide's self-attraction and loading. They are given by

$$\zeta_{EQ} = \frac{(1 + k_n - h_n)\Omega}{g}, \text{and} \tag{2.41}$$

$$\zeta_{SAL} = \sum_n (1 + k'_n - h'_n) \alpha_n \zeta_n. \tag{2.42}$$

In order to compute the latter term Green's functions can be constructed instead of using spherical harmonics (*Farrell*, 1972; *Ray*, 1998).

2.3.6 Internal tides and ocean mixing

So far, only barotropic tides have been considered, i.e. tides without a vertical structure, propagating along the air-sea interface. Baroclinic tides, also referred to as internal tides, are generated by the interaction of the barotropic tidal currents with the bottom topography of the oceans in stratified waters. The drag force exerted on the tidal flow through the displacement of the isopycnals results in the formation of internal waves at tidal frequencies in the ocean's interior (e.g., *Munk*, 1966; *Garrett and Munk*, 2007; *Munk and Wunsch*, 1998; *Egbert and Ray*, 2000; *Wunsch and Ferrari*, 2004; *Garrett and Kunze*, 2007). As for waves along the air-sea interface the restoring force for internal waves is gravity but its effect is reduced due to the very much smaller density differences between the different water layers in the ocean. Therefore, internal waves with amplitudes much greater than those of surface waves, or of the generating tide, can be observed, with amplitudes exceeding tens or even hundreds of metres (e.g. *Garrett and Kunze*, 2007; *Hall et al.*, 2011). Tidal conversion, i.e., the generation of internal tides take place along steep topographic features such as the continental shelf breaks, deep sea ridges, islands and sea mounts (e.g. *Bell*, 1975; *Egbert and Ray*, 2001) in both the deep ocean and shelf seas (*Garrett and Kunze*, 2007). In the deep oceans, where tidal currents tend to be weak, internal waves often have a similar frequency as the forcing astronomical tides close to their generation site. However as they propagate away through waters which are highly variable in their density stratification both temporally and spatially, their frequencies often shift away from the original astronomic forcing frequency (*Garrett and Kunze*, 2007). On the continental shelf, where tidal currents are generally much stronger, lee waves with much shorter frequencies are often generated (e.g., *Rippeth and Inall*, 2002). Internal tides can be detected from satellite imagery, showing that they can propagate across oceans for thousands of kilometers before they break (e.g., *Garrett and Munk*, 2007), causing turbulence and thus mixing (e.g., *Wunsch and Ferrari*, 2004). Therefore, the locations at which the barotropic surface tide loses energy to the internal tides (i.e. at steep topographic features and continental shelves) are not necessarily the same regions at which the energy from the internal tide is dissipated causing mixing (*Rudnick et al.*, 2003). The amount of energy converted from barotropic tides to internal tides is estimated to be approximately 30% of the total tidal energy dissipation in the ocean. Energy transfer between barotropic to baroclinic tides occurring mainly in the deep ocean where energy losses due to bottom friction are very small (*Egbert and Ray*,

2001; *Nycander*, 2005). The amount of energy lost to internal tides through internal wave drag also plays a role in determining the magnitude of the surface tides, which subsequently influences the strength of the internal tide (*Garrett and Kunze*, 2007).
In theoretical studies it has been shown that the formation of progressive internal waves should not be possible poleward of the critical latitude (74° for M_2 and 30° for K_1) due to the dependence of the wave speed on the wave frequency minus the Coriolis parameter. However, due to topographic interaction internal waves at semi-diurnal frequencies can be observed poleward of the critical latitude (*Pugh and Woodworth*, 2014). Internal tides play an important role in driving mixing across density interfaces in the deep ocean because their breaking causes turbulent mixing (*Munk*, 1966; *Munk and Wunsch*, 1998; *Egbert and Ray*, 2000; *Wunsch and Ferrari*, 2004; *Garrett and Kunze*, 2007; *Green and Nycander*, 2013). The importance of tidal mixing in the deep ocean for the large-scale ocean circulation was first recognised by *Munk* (1966). He established a model in which upwelling of cold water is balanced by downward mixing of heat into the ocean's interior thereby maintaining the observed stratification in the oceans. The energy for the mixing is supplied by wind and tides, with internal tides being especially of importance in the abyssal ocean (e.g., *Munk and Wunsch*, 1998; *Wunsch and Ferrari*, 2004; *St. Laurent and Garrett*, 2002; *MacKinnon and Winters*, 2005). It has been shown that mixing is not spatially uniform but occurs in distinct locations, especially over rough topography in the deep ocean (e.g., *Egbert and Ray*, 2001; *St. Laurent et al.*, 2003). A number of studies suggest that the spatial distribution of the mixing may be important for maintaining the large-scale ocean circulation (*Munk and Wunsch*, 1998; *Egbert and Ray*, 2001; *Wunsch and Ferrari*, 2004; *Jayne*, 2009). *Egbert and Ray* (2001) also speculate on the feedbacks between the structure of the ocean's interior, i.e. the level of stratification, and the tides. These interactions could be of importance in long term climate projections (see also *Green et al.* (2009) or *Schmittner et al.* (2015)).

2.3.7 Global tidal energy dissipation

The dissipation of tidal energy in the oceans takes place through two processes: firstly, by dissipation through bed friction on the shelf seas and, secondly, by losses of tidal energy to internal tides in the deep ocean. These energy losses have been investigated from satellite altimetry (*Egbert and Ray*, 2000, 2001), tidal models assimilating satellite altimetry and tide gauge data (e.g., *Egbert*, 1997; *Egbert and Ray*, 2003) or from tide

models (e.g., *Egbert et al.*, 2004; *Wilmes and Green*, 2014). For the principle semidiurnal M_2 tide, approximately a third of the energy is lost in the deep ocean and the remaining 70% in the shelf seas. For the principle diurnal K_1 constituent only 10% of the total energy dissipates in the deep ocean and the other 90% on shelf seas (*Egbert and Ray*, 2003).

These dissipative terms are included in Equation 2.33 as the term F which includes both energy losses through bed friction and conversion to internal waves.

Tidal energy dissipation throughout this work is calculated according to the methodology detailed in *Egbert and Ray* (2001). Ignoring the non-linear terms in Equation (2.33) and taking Equation (2.33) $\cdot \rho u$ and Equation (2.34) $\cdot \rho g \zeta$, the tidal energy balance is given by

$$\frac{\partial KE}{\partial t} + \frac{\partial PE}{\partial t} + \nabla \cdot P = \frac{\partial W}{\partial t} + D \tag{2.43}$$

where KE and PE are the kinetic and potential energy, P is the energy flux, W is the work done by the potential vertical and horizontal forces including the work done against the tidal potential, and the tidal energy dissipation is given by D. We assume that the energy density $\rho \frac{1}{2}(h\mathbf{u}^2 + g\zeta^2)$ is in steady state and

$$\langle \frac{\partial KE}{\partial t} \rangle = \langle \frac{\partial PE}{\partial t} \rangle = 0, \tag{2.44}$$

where $\langle\rangle$ denote the time averages. Taking time averages of Equation 2.43 gives the well-know equation for tidal energy dissipation (e.g., *Egbert and Ray*, 2001):

$$D = W - \nabla \cdot P. \tag{2.45}$$

The work W done by the tide is the sum of two work terms and their corresponding frictional losses. The terms are, firstly, work against the large-scale astronomic and body tide and, secondly, the work through self-attraction and loading effects. Each work term additionally has a term describing the frictional energy losses to the solid Earth. Taken together these give the work term W which is expressed as

$$W = g\rho_0 \langle \mathbf{U} \cdot \nabla \cdot (\zeta_{EQ} + \zeta_{SAL}) \rangle, \tag{2.46}$$

where $\langle$ and $\rangle$ denote the time averages and ρ is the mean ocean density.

The energy flux P is given by

$$P = g\rho_0 \langle \mathbf{U}\zeta \rangle. \tag{2.47}$$

Using tidal amplitudes and currents from either the TPXO data base (for validation) or from the model simulations it is therefore possible to calculate the dissipation rate for each constituent without the need to use parameterisations.
Instead of the indirect method detailed above estimating D from the W and $\nabla \cdot P$, dissipation due to bed friction and conversion to internal waves can also be evaluated separately. Energy losses to bed friction are given by

$$F_b = \rho_0 C_d |\mathbf{u}| \mathbf{u}^2, \tag{2.48}$$

where C_d is a dimensionless drag coefficient, with values typically around 0.0025 (*Egbert et al.*, 2004).
The energy losses to internal waves are more complicated to calculate and a number of different tidal conversion schemes have been suggested over the last decades (*Bell*, 1975; *Jayne and St Laurent*, 2001; *Llewllyn Smith and Young*, 2002; *Zaron and Egbert*, 2006; *Green and Nycander*, 2013; *Green and Huber*, 2013; *Buijsman et al.*, 2015). The conversion from barotropic to baroclinic tidal energy is generally parameterised with help of a linear internal wave drag scalar or tensor, C_{IT}. C_{IT} is in some form dependent on the buoyancy frequency of the ocean (indicating the level of stability or stratification of the water column), topographic roughness, and the Coriolis parameter. From C_{IT} dissipation due to internal wave drag $\mathbf{F}_{IT}$ can be estimated (*Buijsman et al.*, 2015) as

$$\mathbf{F}_{IT} = \rho_0 \mathbf{u} \cdot C_{IT} \cdot \mathbf{u}. \tag{2.49}$$

2.3.8 Present day global tides

The present day tidal amplitudes and phases for the principle semi-diurnal and diurnal constituents, M_2 and K_1, from the TPXO global tidal solution (see section 3.3) are shown in Figure 2.7. For both constituents a large number of amphidromic systems (see section 2.3.3) can be seen with the tidal waves normally circulating anti-clockwise around the amphidromes in the Northern Hemisphere and clockwise in the Southern Hemisphere. The tidal waves propagate as Kelvin waves.

The present day oceans are dominated by the semi-diurnal tides because the basin shapes allow for near-resonant properties at semi-diurnal forcing frequencies. This can be illustrated with a simple calculation (*Pugh and Woodworth*, 2014): taking an average basin length of 10000 km and a mean water depth and assuming that the tidal wave travels at 198 m/s (wave speed for depth limited waves in a water depth of 4000 m) it

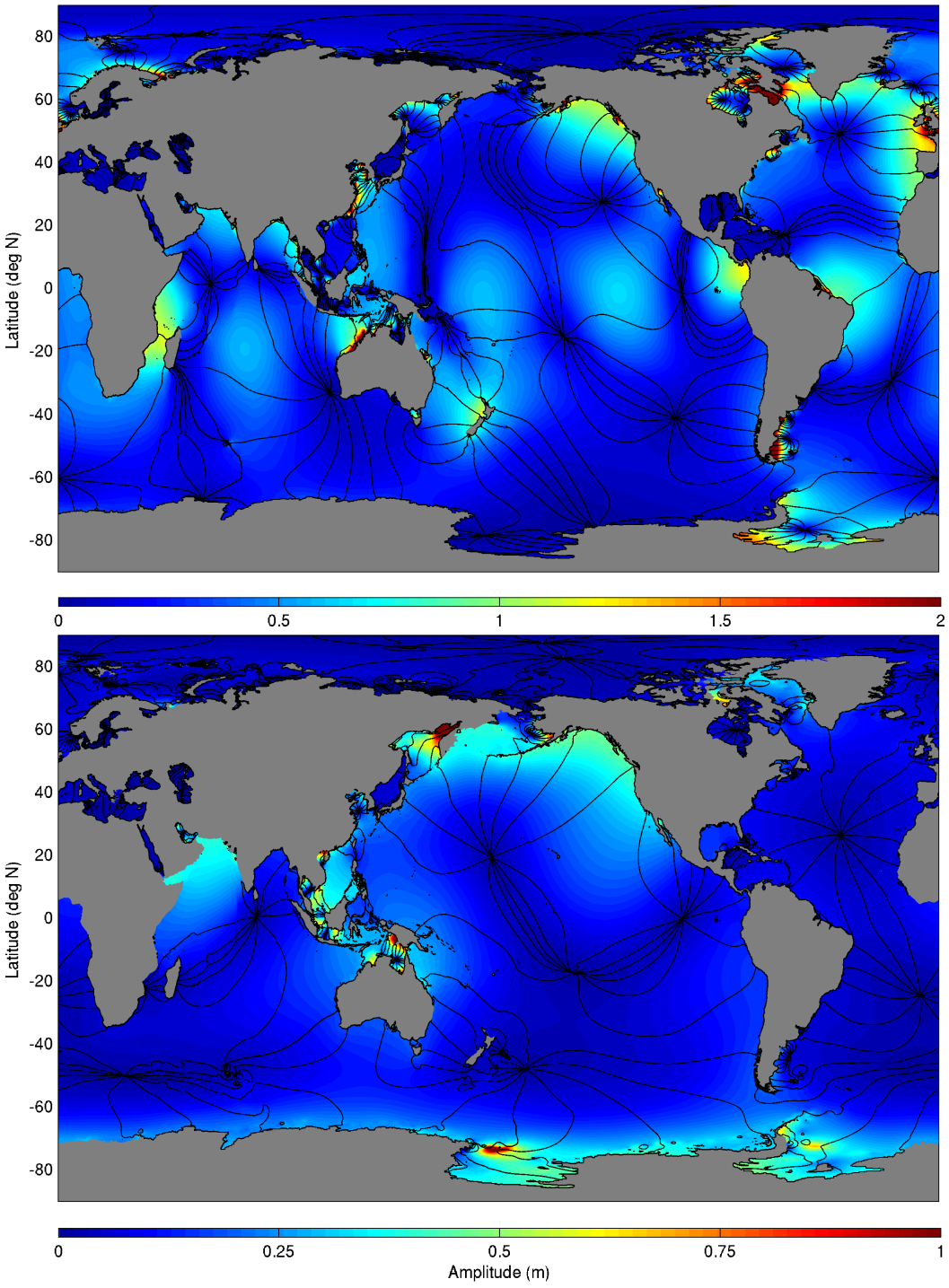

Figure 2.7: Present day tidal amplitudes from TPXO8. Top panel shows M_2, bottom panel K_1. The shading indicates amplitudes and the black lines are the phase lines.

would take a wave approximately 14 hours to travel from one end of the basin to the other.

In the Atlantic, the tidal wave propagates northwards along the coast of Brazil with large tidal ranges around the North Brazil Shelf, crosses the Atlantic to the central west African coastline and continues northwards along the margins of the European Shelf. In the North Atlantic energy is leaked onto the European Shelf where around 200 GW of tidal energy is dissipated (*Egbert and Ray*, 2000). Some energy is also lost to the amphidromic systems around Iceland. Very large tidal amplitudes can be observed throughout the Atlantic and in the Labrador Sea due to their resonant properties. As the wave propagates back southwards along the east coast of the US, amplitudes become much smaller. This is due to the energy losses in the North Atlantic region. For K_1, with exception of the Northern Labrador Sea tidal amplitudes are very small.

In the Pacific, the M_2 tides are still dominant but the K_1 tides also have considerable amplitudes in a number of locations. For M_2, large amplitudes can be seen in the Panama basin and along the northwest coast of the US together with large tides around New Zealand. The tidal wave propagates northward along the west coast of the US and southward along the west coast of Asia and east coast of Central and South America. The large tides and the anti-clockwise circulation around New Zealand are consistent with topographic trapping (*Bye and Heath*, 1975). For K_1, large tides are observed in the North Pacific, in the Sea of Okhosk, in the South China Sea and in the seas between Thailand, Indonesia and northwest Australia. The tidal wave travels clockwise heading northward along the west coast of the US and southward along east coast of Asia. In the South Pacific, the wave propagates northward along the east coast of Australia and southward along the west coast of central America. The large tides observed in the Indonesian Seas are consistent with a resonant Helmholtz oscillator (*Zu et al.*, 2008).

In the Indian Ocean, again, the M_2 tides display larger amplitudes than the K_1 tide. The K_1 dynamics are dominated by a large amphidromic system with anti-clockwise circulation in the central Indian Ocean, producing large amplitudes in the Arabian Sea. A degenerate amphidrome is located on the African side of the Mozambique Channel. For M_2 the dynamics are more complex. The amphidromic system located in southeastern basin produces a large semi-diurnal tidal range along the northwest coast of Australia and in the Timor Sea. The Bay of Bengal is too narrow for the development of an amphidrome. Instead the dynamics show similarities with a standing wave system with

northward propagation of the tidal wave both on the east and west coast of the Bay of Bengal and the tendency towards a degenerate amphidrome located on Sri Lanka. The Arabian Sea in contrast has a geometry that allows the formation of an amphidrome. Large tidal amplitudes can be seen in the Mozambique Channel. Nearly constant phases are observed throughout the channel due to a double standing wave system. In the central Indian Ocean a similar phenomenon can be seen with large amplitudes and nearly constant phases which is termed an anti-amphidrome and corresponds to an antinode in a standing wave system (*Pugh and Woodworth*, 2014).

The Southern Ocean and the Arctic basin are the only ocean basins which allow waters to circumnavigate the globe. For both constituents the tidal wave propagates westward around Antarctica, however, they have very different structures. For K_1, the tide resembles a zonal wavenumber 1 Kelvin wave with large amplitudes along all of the margins of the continent and enhancements in the Ross and Weddell Seas. Similar dynamics apply to the M_2 tide which has zonal wavenumber 2 or 3 structure. However considerable interaction occurs with the topographic features on the Antarctic margin, such as the Ross or Weddell Sea, due to the similar length scales of the topographic features and the wave. Therefore, the amplitudes along the coastline of Antarctica tend to be small but are strongly amplified in the Weddell Sea and in parts of the Ross Sea (*Griffiths and Peltier*, 2009). In the Arctic, both M_2 and K_1 tides are small at present day. For M_2 the Arctic is characterised by an amphidrome located in the centre of the Arctic basin. This results in an anticlockwise movement of the tidal wave around the basin. The largest amplitudes are observed in the adjoining seas such as the Greenland Sea and the Barents Sea.

2.4 How can sea-level changes alter tidal dynamics?

There are two different mechanisms by which secular sea-level changes alter tidal dynamics; firstly, by altering the resonant properties of the ocean, and secondly, by altering the propagation speed of the tidal wave, and hence the energy lost to friction, which subsequently leads to shifts in the position of amphidromic points.

2.4.1 Resonance

Large enhancements in amplitudes and dissipation occur when the tidal forcing frequency lies close to the natural period, T_{nf}, of an ocean basin. A change in sea-level can therefore

alter the natural period of a (simplified) ocean basin (T_{nf} is dependent on water depth; see Equation 2.30). For the case of the Patagonian Shelf an increase in sea-level would push the shelf sea closer to resonance for M_2 frequencies (*Carless et al.*, 2016). However, for the open ocean basins the mechanisms are not as straightforward as interaction occur between shelf seas and the open ocean. For an open ocean basin its resonant properties can be described using the concept of a damped harmonic oscillator (*Egbert et al.*, 2004). A simple forced damped harmonic oscillator is described by the equation

$$\partial^2\zeta_{tt} + \gamma\partial\zeta_t + \zeta = \sin(\omega t), \tag{2.50}$$

where ζ denotes the displacement, γ the damping coefficient and ω is the forcing frequency. The dissipation, ϵ, is given by

$$\epsilon = R[i\omega/(1-\omega^2 - i\gamma\omega)]. \tag{2.51}$$

From Figure 2.8 it is evident that an ocean basin which is forced by an oscillation with a frequency at or close to its resonant frequency and with minimal associated damping then the tidal amplitudes and associated tidal dissipation are strongly enhanced in the ocean basin. *Egbert et al.* (2004) used this concept to illustrate why tidal amplitudes and dissipation were strongly enhanced in the North Atlantic during the LGM. The LGM has resonant periods of 12.66, 12.8 and 14.4 hours (*Platzman*, 1975; *Platzman et al.*, 1981; *Müller*, 2008). The sea-level reduction of around 130m lead to a strong reduction in the damping exerted by the present-day shelf seas and therefore an enhancement in tidal amplitudes and associated dissipation during the LGM. During the deglacial period as the shelf seas flooded and the damping increased open ocean amplitudes in the North Atlantic strongly decreased (see Chapter 4 for a detailed description). These results are confirmed by *Arbic et al.* (2009) who show that the magnitude of the open ocean tides is controlled by the loss of tidal energy on the shelf seas and that the impacts of this interaction are particularly strong when both the open ocean and the adjoining shelf sea are close to resonance. Again, a sea-level change can lead to changes in the resonant properties of either the open ocean or the shelf sea (or both), modifying the nature of the interaction between the two.

2.5 Changes in propagation properties of the tidal wave

Taylor (1921) investigated the impacts of introducing a dissipative boundary on amphidromic systems in a frictionless semi-enclosed basin and showed that the loss of

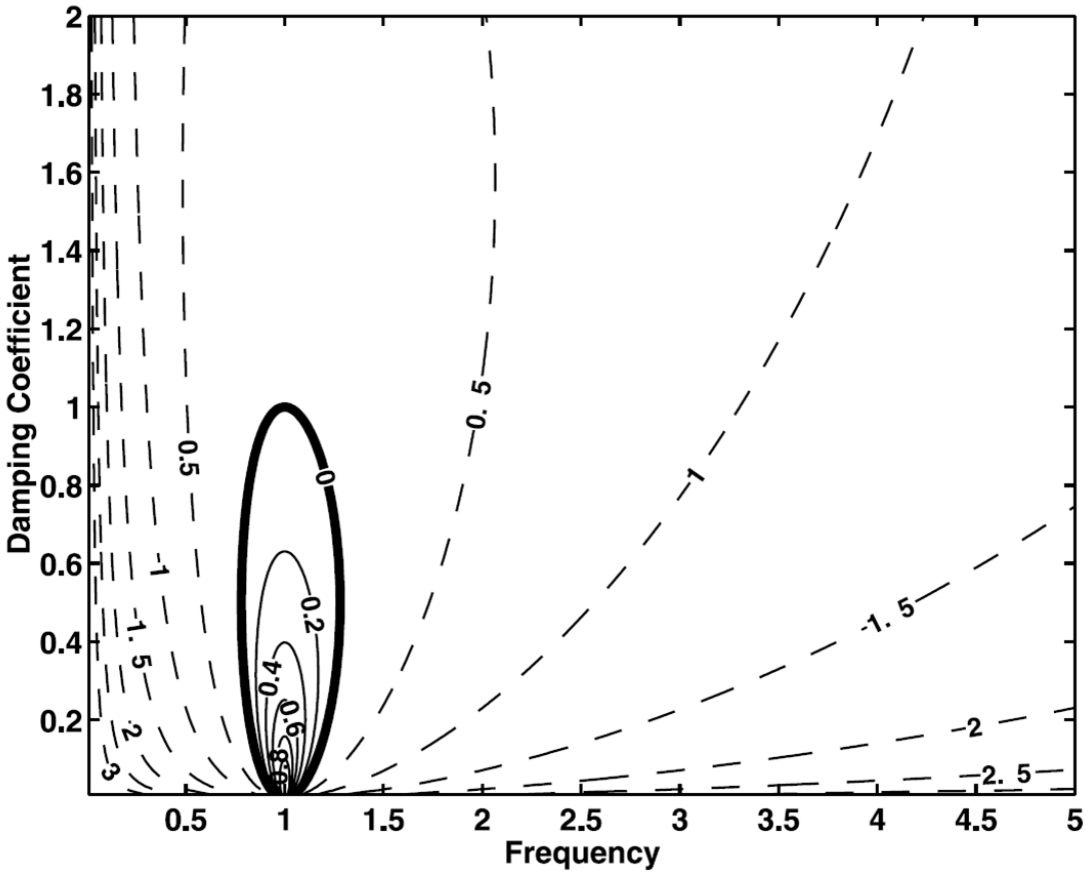

Figure 2.8: Dissipation rate in a forced damped harmonic oscillator plotted as $\log(\epsilon)$. γ denotes the damping coefficient, and ω_r/ω indicates the ratio between the resonant frequency and the forcing frequency. Figure from *Egbert et al.* (2004).

energy from the incident Kelvin wave at the boundary resulted in a displacement of the amphidromes to the left of the direction of travel of the incident wave and reduced amplitudes along the left-hand boundary of the basin. *Rienecker and Teubner* (1980) later included the effects of friction and demonstrated that the distance by which the amplitudes were displaced was dependent on the magnitude of the energy losses through friction and increases away from the dissipative boundary. Investigating the impacts of the springs-neap cycle *Pugh* (1981) demonstrated that significant movement of amphidromes occur between spring tides and neap tides due to larger proportionally larger amounts of energy being lost during spring tides during neap tides. This work also showed that the amount of energy lost at the head of the basin changes depending on the position in the springs-neap cycle and is lower as the tidal range increase. These factors highlight the non-linearity nature of the responses in this physical system.

A change in sea-level is therefore likely to affect amphidromic systems in basins not

close to resonance in a number of different ways. Increasing water depth will lead to an increase in the propagation speed of the tidal wave, and hence shift the amphidromic point towards the open boundary of the semi-enclosed basin. This shift should lead to an increase in the amplitudes at the dissipative end of the basin, hence a larger tidal range. The increase in tidal range also increases tidal currents. The energy losses due to friction are dependent on the cube of the tidal currents, hence more energy is lost due to friction. This in turn would shift the amphidromes to the left of the direction of propagation of the tidal wave, hence further increasing the amplitudes on the right side of the basin (with regards to the incident wave propagation direction). However, following *Pugh* (1981) the increase in tidal range should also decrease the proportion of tidal energy reflected by the dissipative boundary, leading to a further displacement of the amphidrome to the left of the incident wave travel direction.

2.6 The real world

However, the situations discussed here are highly idealised cases and in the real oceans amphidromic systems are likely not to behave in such a fashion for a number of reasons:

1. water depths are not equal throughout the ocean,
2. the semi-enclosed basins are not rectangular,
3. sea-bed roughness varies considerably across ocean basins, leading to different responses in dissipation and hence varying amphidrome displacements,
4. changes in self-attraction and loading of the Earth's surface are likely to occur due to the changes in tidal elevations, which then result in feedbacks with the large-scale tidal dynamics,
5. changes in resonant properties occur affecting amphidrome movement,
6. displacement of one amphidrome is likely to lead to a displacement of the neighbouring amphidrome,
7. the sea-level changes discussed in this work are in most cases globally non-uniform, resulting in additional complexities.

Therefore, it is concluded that the investigation of tidal changes in response sea-level changes is a highly complex subject matter and the responses expected will be very

different between different ocean basin and it is likely that is difficult to discern any one process responsible for a tidal change.

2.7 Summary

This chapter has given an overview of the basic tidal dynamics. The first part derived the tide-generating potential and the equilibrium tide, and discussed variations in orbital configuration of the Sun and the Moon leading to the description of a number of basic tidal constituents. This was done for the case of an idealised ocean with uniform water depth and no land masses. The second part looked at tidal dynamics in the real ocean and begins with the introduction of the shallow water equations. Thereafter concepts such as conversion of energy from the barotropic to the baroclinic tide are introduced, and the dissipation of tidal energy in the ocean is discussed and an overview over self attraction and loading is given. A description of the M_2 and K_1 tide in the present-day ocean is given. The chapter finishes with a discussion of the mechanisms behind changes in tidal dynamics in response to sea-level changes, and eludes on the reasons the responses are highly complex and non-linear in the real ocean.

Chapter 3

Tidal Modelling

3.1 A brief history and overview of global tidal modelling

Tidal modelling has a rich history, with the first successful attempts at modelling global ocean tides being made during the late 1970s (e.g *Pekeris and Accad*, 1969; *Parke and Hendershott*, 1980; *Schwiderski*, 1980). Using a hydrodynamic interpolation scheme, *Schwiderski* (1980) established the first true global ocean tide model at a 1° horizontal resolution by assimilating data from over 1700 tide gauges for the M_2 and K_1 tidal constituents. This model was considered state of the art, until GeoSat provided the first altimetric data sets in the late 1980s, enabling the establishment of global tidal dataset with equally good or better accuracy than *Schwiderski* (1980). With the launch of TOPEX/Poseidon in 1992, global tidal modelling progressed rapidly, firstly, due to the improved coverage of the new satellite system and secondly because of considerable advances in numerical tidal modelling and the availability of computing facilities (*Shum et al.*, 2014). Since the early 1990s knowledge about tidal dynamics has vastly improved. Considerable advances have been made in understanding the dissipation of tidal energy, the conversion of barotropic to baroclinic tides, and the wider role of tidal energy in the climate system. Measurements of the tides in critical areas such as the poles have become available from both GPS measurements (e.g., *Yuan et al.*, 1999; *Löfgren et al*, 2014) and polar satellite missions (*Stammer et al.*, 2014).

Three different types of tidal models can be distinguished: (a) empirical models that derive their data purely from the analysis of satellite altimetry data sets, (b) hydrodynamic models that assimilate data from satellite altimetry and/or tide gauges and (c) forward tidal models which compute the tides purely from the hydrodynamic equations. Empirical tide models such as EOT11 (*Savcenko and Bosch*, 2012) or OSU12 (*Fok*, 2012) use either least-squares harmonic analysis or the so-called response method to obtain empirical estimates of the tides from satellite altimetry without the need of a hydrodynamic model (*Savcenko and Bosch*, 2012). Assimilated tide models such as TPXO8 (*Egbert and Erofeeva*, 2002), FES2012 (*Carrère et al.*, 2012), or HAMTIDE (*Taguchi et al.*, 2014) interpolate altimetry and tide gauge data with help of barotropic hydrodynamic models solving the shallow water equations. These models assimilate data from numerous satellite missions over the past decades, e.g., TOPEX/Poseidon, Jason-1, Geosat Follow-On (GFO), Envisat and ERS-2, in order to obtain complete global coverage. Both types of models achieve accuracies of around 0.5 cm in the deep ocean and of less than 4 cm on the continental shelves when compared to tide gauges for M_2. Despite their high levels

of accuracy the models still have problems in coastal environments due to e.g., contamination of the satellite footprint by land, and issues accounting for air pressure and wind variability (*Vignudelli et al.*, 2005). In the high northern and southern latitudes seasonal ice coverage hampers data quality (see the review by *Stammer et al.*, 2014).

Unconstrained tidal models such as OTIS (*Egbert et al.*, 2004), HIM (*Hallberg and Rhines*, 1996) or STM-1B (*Griffiths and Peltier*, 2009) solve the linearised barotropic shallow water equations forced solely by the tidal potential. They include parameterisations for the conversion of barotropic tidal energy to internal tides. Self attraction and loading (SAL) is usually implemented following an iterative procedure such as suggested in *Egbert et al.* (2004). Models such as HYCOM (*Chassignet et al.*, 2007; *Arbic et al.*, 2010) or STORMTIDE (*Müller et al.*, 2012) are part of high resolution ocean models and run in three dimensions as opposed to two dimensions in the previously mentioned models. They are forced by the astronomic tidal potential and climatological wind fields. Surface buoyancy forcing is restored at regular intervals. These models resolve mesoscale eddies and low mode internal waves. SAL is included in parametrised form. These two groups of purely hydrodynamic models are able to simulate the tides with an accuracy of around 5 cm in the deep ocean and 25 cm in the shelf seas in comparison to satellite altimetry data and tide gauge data (*Stammer et al.*, 2014). The accuracy of these models depends to a very high degree on the quality of bathymetric data which leads to the large inaccuracies in the shelf seas.

In the following the discussion will focus on the barotropic forward tidal model OTIS and the global tidal model TPXO8 as these are the products used for to the subsequent studies.

3.2 OTIS

The Oregon State University Tidal Inversion Software consists of two components – a barotropic forward tidal model solving the hydrodynamic equations (*Egbert et al.*, 2004) (subsequently denoted as OTIS) and the inversion software that assimilates observational data into the model (*Egbert and Erofeeva*, 2002). The combined model is used to develop the global tidal model TPXO and this work uses the forward tidal model OTIS as a standalone software to simulate tides.

OTIS is widely used for both regional and global modelling of ocean tides, with studies covering aspects of tides in the past, present and future (*Egbert et al.*, 2004; *Green*,

2010; *Green and Huber*, 2013; *Green and Nycander*, 2013; *Rosier et al.*, 2014a; *Pelling and Green*, 2013; *Green and David*, 2013; *Wilmes and Green*, 2014). In comparison to other unconstrained purely hydrodynamic tidal models OTIS produces the high accuracies both in the open ocean and in coastal regions (*Stammer et al.*, 2014) and is computationally efficient to run. OTIS was therefore selected for this study.

3.2.1 The governing equations

OTIS solves the linearised shallow water equations (*Egbert et al.*, 2004) as developed in Chapter 2 or by *Hendershott* (1977) which are given by

$$\frac{\partial \mathbf{U}}{\partial t} + \mathbf{f} \times \mathbf{U} = -gH\nabla(\zeta - \zeta_{EQ} - \zeta_{SAL}) - \mathbf{F} \tag{3.1}$$

$$\frac{\partial \zeta}{\partial t} = -\nabla \cdot \mathbf{U}, \tag{3.2}$$

where $\mathbf{U}$ is the depth integrated volume transport, which is calculated as tidal current velocity $\mathbf{u}$ times water depth H. f is the Coriolis vector, g denotes the gravitational constant, ζ stands for tidal elevation and ζ_{SAL} denotes the tidal elevation due to self-attraction and loading, and ζ_{EQ} is the equilibrium tidal elevation. F represents frictional losses due to bottom drag and internal tide conversion. These equations are solved on an Arakawa C-grid, using explicit finite differences time stepping, with periodic forcing, followed by harmonic analysis of the steady state solution to obtain tidal elevations and transports (*Egbert et al.*, 2004, 1994). OTIS can be run with up to 8 constituents, though throughout this study most simulations are carried out for M_2 and K_1 only (and in addition for S_2 and O_1 in Chapter 4). This way the computational expense can be greatly reduced with only very minor losses in accuracy (*Egbert et al.*, 2004).

3.2.2 Dissipation terms

The dissipation $F = F_{IT} + F_B$ is a sum of terms of energy loss due to bottom friction (F_B) and the loss of energy to the internal tide (F_{IT}).

Bed friction, important for energy losses in shallow shelf seas, is implemented through through a quadratic friction term

$$F_B = C_d \mathbf{U} \left|\mathbf{u}\right| / H \tag{3.3}$$

where C_d is a dimensionless drag coefficient which commonly takes a value of 3×10^{-3}. Conversion of energy to internal waves is represented by a linear friction parameterisation

(*Zaron and Egbert*, 2006; *Green and Nycander*, 2013) with

$$F_{IT} = C_{IT}\mathbf{U} \tag{3.4}$$

where the internal wave drag coefficient is given by

$$C_{IT} = \Lambda H(\nabla H)^2 \frac{N_b \bar{N}}{8\pi^2 \omega} \tag{3.5}$$

where Λ is a scaling factor and N is the buoyancy frequency given by $N(z) = N_0 e^{z/1300}$ with $N_0 = 5.24 \times 10^{-3}$ and $z = 0$ at the sea surface. N_b denotes the value of $N(z)$ at the sea bed where $z = -H$. $\bar{N}$ is the vertical average of N over the water column calculated as $\bar{N} = 1300 N_0[1 - e^{-H/1300}]/H$ and ω denotes the frequency of the given tidal constituent. Equation 3.5 presents a slightly modified version of the formulation given in *Zaron and Egbert* (2006) ($C_{IT} = c_{BC}\frac{N_b(\nabla H)^2}{kH}$), in which the wave number k has been replaced by $k = \frac{\pi\omega}{\bar{N}H}$ (*Kundu*, 1990; *Green and Huber*, 2013; *Green and Nycander*, 2013).

3.2.3 Implementation of self-attraction and loading

The correction for self-attraction and loading in equation 3.1 is implemented as an equilibrium-like tide ζ_{SAL} (*Egbert et al.*, 2004) which is related to ζ by

$$\zeta_{SAL} = G_{SAL} * \zeta \tag{3.6}$$

where G_{SAL} is the SAL Green function (see Section 2.3.5 and *Ray* (1998) for more details). However, including this equation into equation 3.1 and evaluating it at each time step is not computationally feasible. Therefore, the SAL correction is added as an extra forcing term in order to avoid the explicit solution of the term.

In OTIS several different methodologies are available for the implementation of the SAL correction. Firstly, a prescribed SAL field can be used, e.g., for the present day tides the SAL field is calculated from one of the versions of the global tidal model TPXO. Secondly, a SAL correction can be implemented by the crude parametrisation suggested by *Pekeris and Accad* (1969) where the Green's function is replaced by a scalar β so that ζ_{SAL} becomes

$$\zeta_{SAL} = (1 - \beta)\zeta \tag{3.7}$$

with β commonly taking values of around 0.1. However, as shown by, e.g., *Ray* (1998), this parametrisation is too simplistic to capture the SAL effects in all locations of the

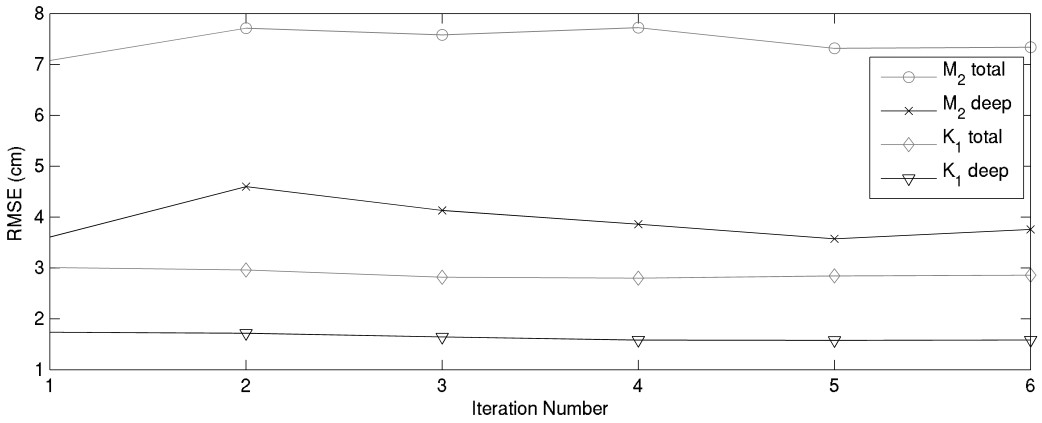

Figure 3.1: Root-mean square errors (RMSEs) of present-day amplitudes compared to TPXO8 for 6 SAL iterations. Iteration 1 has a prescribed present-day SAL field, iterations 2 to 5 calculate SAL according to Equation 3.8. The black crosses and triangular markers show open ocean (h $>$ 500 m) RMSEs for M_2 and K_1, respectively, and the grey circles and diamond markers show total ocean RMSEs for M_2 and K_1, respectively.

globe. The third methodology as implemented by *Egbert et al.* (2004), is an iterative scheme by which the elevations from iteration n, ζ^n, are used to evaluate SAL elevations for the nth iteration ζ^n_{SAL}. ζ^n_{SAL} is given by

$$\zeta_{SAL} = \beta\zeta + G'_{SAL} * \zeta \tag{3.8}$$

where, as previously a value of 0.1 is used for β. This scheme has the advantage that it leads to a rapid convergence of the solutions in contrast to previous schemes (see *Egbert et al.*, 2004).

3.2.4 Open boundary conditions

At coastal open boundaries zero normal flow is prescribed. At open ocean boundary nodes both elevation and velocity boundary conditions can be specified, though throughout this work elevation boundary conditions are used. They are prescribed from the TPXO6.2 database (see *Egbert and Erofeeva*, 2002, and section 3.3 for more details) at the northern open boundary.

3.2.5 Model setup

In this study OTIS is run at a horizontal resolution of $1/8° \times 1/8°$ which is a compromise between computational efficiency and numerical accuracy. *Egbert et al.* (2004) show that increasing the grid resolution of the model from $1/8°$ to $1/12°$ results only in very minor

improvements in the model accuracy. OTIS is run for the constituents M_2 and K_1 in a near global set up ranging from 86°S to 89°N. This means that the southern open boundary lies over the Antarctic continent, thus eliminating any errors at boundaries. At the northern open boundary elevation boundary conditions are prescribed (see section 3.2.4). The model is run with a time step of 1 s for 13 days of which the last 5 days are used for harmonic analysis with the inbuilt OTIS harmonic analysis software. Elevations are output as complex numbers taking the form $\zeta = A * \exp(i * \theta)$, where the amplitude A can be calculated as abs(ζ) and the phase as atan2(imag(ζ),real(ζ)).

In the standard setup four SAL iterations are carried out due to numerical reasons: As each iteration takes two days when run on eight cores, a simulation with four SAL iterations takes approximately eight days or 1536 computer hours. In Chapter 6, where we need the greatest accuracy, as very small signals are compared, we carry out a further two iterations. Figure 3.1 shows total and deep root-mean square errors of simulated M_2 and K_1 amplitudes compared to TPXO8 (see Section 3.3). The first iteration of the present-day run which is forced with the observed SAL field has a slightly higher accuracy for M_2 tidal amplitudes compared to the fourth iteration when the total ocean is compared. However, the difference for the deep ocean is much smaller. For K_1, the accuracy in both the total and deep ocean is greatest for iteration four and remains approximately constant for further iterations.

3.2.6 Bathymetries

The present-day bathymetric data is a composite bathymetry as in *Egbert et al.* (2004) based on the Smith and Sandwell database, v.14, (see *Smith and Sandwell*, 1997, and `http://www.topex.ucsd.edu/pub/global_topo_1min/` for the latest version) (SS) with bathymetry for the Arctic and Antarctic from the IBCAO, v.2, (see *Jakobsson et al.*, 2008, and `http://www.ngdc.noaa.gov/ mgg/bathymetry/arctic/` for the latest version) and ETOPO1 databases (see *Amante and Eakins*, 2009, and `http://www.ngdc.noaa.gov/mgg/global/`). Each dataset was interpolated to a common resolution of 1/8° × 1/8°, and then the datasets were merged over 5° latitude using linear weighting. IBCAO and SS overlap between 74°N and 79°N, and SS and ETOPO1 have a common grid between 65°S and 60°S.

Older bathymetric data bases, e.g. early versions of GEBCO, assume that all ice is grounded around Antarctica treating any ice that is present as grounded. However, in a

significant number of embayments in Antarctica, the ice draining the ice streams is floating on the water column as ice shelves. Ignoring water present under ice shelves leads to pronounced differences in the bathymetry (both for water depths and coastline shapes). Using this bathymetry for tide modelling leads to large changes in tidal dynamics. As the water depths under the ice shelves can be quite considerable, it is important to include these in the bathymetries that form the basis of the tidal model. Here, bathymetry data beneath ice shelves in Antarctica is found by reducing the bedrock water depth by the amount of water displaced by the overlying ice. Hereby it is assumed that the grounding line is located where the water depth is equal to the volume of water displaced by the ice. If the amount of water displaced by the ice is greater than the bedrock water depth, the ice is assumed to be fully grounded. The water depth in the vicinity of the ice sheets is therefore calculated as

$$d_w = \begin{cases} d_{br} - 0.9 \cdot h_i & \text{if} \quad 0.9 \cdot h_i < d_{br} \\ 0 & \text{if} \quad 0.9 \cdot h_i > d_{br} \end{cases} \tag{3.9}$$

where the h_i denotes ice thickness, d_{br} is bedrock depth and d_w is water column thickness. The factor 0.9 corrects for the reduced density of ice in comparison to water.

3.3 TPXO8

TPXO8 is the global tidal solution for elevations and barotropic currents (see Figure 2.7) used for validation throughout this work. TPXO8 is the most recent product in the series of TPXO global tidal datasets, with the first version published in 1994 (*Egbert et al.*, 1994) and since improved by *Egbert and Erofeeva* (2002). Data from satellites and tide gauges is assimilated into the hydrodynamic model OTIS using a representer-based approach. TPXO8 uses harmonically analysed along-track data from the Topex/Poseidon and Jason missions. In the Arctic and Antarctic, data from ERS/Envisat, together with tide gauge data, is added to achieve a good global coverage. TPXO8 includes over 30 regional high-resolution solutions for continental shelf areas and enclosed seas assimilating more detailed satellite data. These were then merged into a lower $1/30°$ horizontal resolution global solution.

TPXO8 uses a prescribed SAL correction calculated from the previous version TPXO6.2 and applies a linear bed friction parameterisation. In contrast to the purely hydrodynamic version of OTIS the inverse model solves the linearised shallow water equations in

the frequency domain by factorisation of a coefficient matrix. This is much faster than the original approach. Also, velocities are eliminated from the equations, bringing further improvements in computational efficiency. Data is assimilated with help of a representer approach whereby a weighted sum of the squared misfits between the observational data and the linearised shallow water equations is minimised (*Egbert and Erofeeva*, 2002). The latest version of TPXO, TPXO8, displays high levels of accuracy of 0.5 cm in the deep ocean and 3.5 cm in the shelf seas compared to observations. Slightly larger errors can be seen along coast lines and in the polar seas (*Stammer et al.*, 2014).

3.4 Summary

This chapter has given a brief overview of the history of large developments that have taken place from the 1980s when the first attempts at global tidal modelling were made through to the present where high resolution tidal models with global errors of less than 5 cm are available, and provided an overview the different tidal models currently available to simulate global tidal dynamics. In the next part the reasoning behind the choice of the tidal model OTIS for this study is explained, and a detailed technical description of OTIS is included. Here, a description of the model setup specific to this study is included. The last section of the chapter provides details on the global tidal solution TPXO8, which is used for validation of OTIS throughout this work.

Chapter 4

The evolution of tides and tidal dissipation over the past 21,000 years

4.1 Introduction

The 120–130 m ice-equivalent sea-level reduction during the Last Glacial Maximum (LGM; some 22,000–18,000 years before present; henceforth 22–18 kyr BP) had a significant impact on the tides on a variety of scales due to the exposure of the continental shelf seas (e.g *Egbert et al.*, 2004; *Arbic et al.*, 2004; *Uehara et al.*, 2006; *Griffiths and Peltier*, 2008, 2009; *Green*, 2010; *Hill et al.*, 2011; *Hall et al.*, 2012). This had pronounced effects on the tides, mainly by increasing the total amount of semi-diurnal tidal energy lost in the ocean during the LGM to levels far above present. Furthermore, most of this energy dissipated in the deep ocean and not in shallow shelf seas, as is the case today (*Egbert and Ray*, 2001). As the sea-level rose at the end of the glacial period, the present day shelf seas flooded and there was a subsequent shift in the tidal dissipation from the open ocean to the newly flooded shelf seas (e.g., *Egbert et al.*, 2004; *Uehara et al.*, 2006; *Green*, 2010). Here, we present new simulations of the evolution of the near-global tides from the LGM to the present. The purpose of this investigation is four-fold:

1. present the evolution of the global semidiurnal tides at higher temporal and spatial resolutions than previously reported (e.g., *Egbert et al.*, 2004; *Uehara et al.*, 2006; *Hill et al.*, 2011; *Hall et al.*, 2012),

2. describe the evolution of the diurnal tides from the LGM to the present,

3. investigate the sensitivity of the global tides at present and during the LGM to the location of ice sheet grounding lines, thus extending the work by *Griffiths and Peltier* (2009) and

4. comment on the implications of altered tidal dissipation for the large-scale ocean circulation.

Previous simulations of the palaeoocean tides show surprising results, with total globally integrated dissipation some 30% larger than at present and a larger fraction of this energy dissipating in the deep ocean (*Egbert et al.*, 2004; *Green*, 2010). The dissipation in the semi-diurnal band increased far more than that of the diurnal constituents (*Green*, 2010), which implies that the mechanism behind these shifts is tidal resonance (*Egbert et al.*, 2004; *Griffiths and Peltier*, 2008; *Arbic et al.*, 2009; *Green*, 2010). Removing the shelf seas effectively reduces the damping of the tides, which – when the ocean basin is close to resonance – leads to an increased tidal amplitude and associated dissipation of energy

(see *Egbert et al.*, 2004; *Green*, 2010, especially their Figs. 11 and 1, respectively). The present day North Atlantic has natural resonant periods of 12.66, 12.8 and 14.4 hours (*Platzman*, 1975; *Platzman et al.*, 1981; *Müller*, 2008). The exposure of shelf seas during the LGM removed the damping of the glacial ocean which explains why 'megatides' (tidal amplitudes in excess of 6 m) may have been present there during the LGM (e.g., *Uehara et al.*, 2006; *Arbic et al.*, 2007a; *Griffiths and Peltier*, 2008, 2009) and not at present. Furthermore, *Arbic et al.* (2009) and *Skiba et al.* (2013) show that adding a shelf ocean, which is close to resonance, to a deep ocean basin, that is also close to resonance, reduces the deep ocean tides of the ocean basin. This is analogous to when the European and Patagonian shelves flooded during the deglaciation after the LGM.

The extent of floating ice shelves in Antarctica and the bathymetries under the ice shelves are important in determining the regional tidal dynamics (*Griffiths and Peltier*, 2009; *Rosier et al.*, 2014a). However, there is an ongoing debate about the exact grounding line location of the Antarctic Ice Sheet during the LGM and the subsequent deglacial period. This is especially true for the Weddell Sea sector (see Fig. 4.1), where estimates range from an ice sheet grounded at the shelf margin (e.g., *Hall and Denton*, 2000; *Larter et al.*, 2012; *Anderson et al.*, 2002) to an only partially grounded ice sheet within the Weddell Sea, with strongly differing estimates over the timing of the initiation of deglaciation (e.g., *Stolldorf et al.*, 2012; *Hein et al.*, 2011; *Hillenbrand et al.*, 2012). For the Western Ross Sea, however, there is a general consensus that the ice sheet grounded at the present day shelf break during the LGM (e.g. *Anderson et al.*, 2002; *Domack et al.*, 1999; *Hall and Denton*, 2000; *McKay et al.*, 2008; *Livingstone et al.*, 2012). Although the behaviour of the ice masses in the Western Ross Sea has been extensively researched, ambiguity of both LGM extent and deglacial behaviour exists for the Eastern Ross Sea (e.g. *Shipp et al.*, 1999; *Anderson et al.*, 2002; *Mosola and Anderson*, 2006). *Griffiths and Peltier* (2009) investigate regional changes in the polar LGM tides in global tidal simulations in response to different grounding line positions of both the Antarctic Ice Sheet and the ice sheet occupying the Queen Elizabeth Islands in the Canadian Arctic. They show that grounding line shifts affect the tides in the vicinity of the respective ice sheets. In our simulations we extend the approach by *Griffiths and Peltier* (2009) and analyse the response in global tides to different grounding line positions of the Antarctic Ice Sheet from the LGM to the early Holocene.

There are several reasons to reinvestigate the tidal evolution over the last 21 kyr with

higher resolution and with the response of both semidiurnal and diurnal tides described. Changes in tidal dissipation can affect the large scale meridional overturning circulation (MOC), which has been shown to be sensitive to the input of mechanical energy in the deep ocean (e.g., *Huang*, 1999; *Johnson et al.*, 2008; *Green et al.*, 2009). Based on first order physical principles (e.g., *Stommel*, 1961), it is thus expected that the MOC during the LGM would have been stronger. Instead, most investigations point towards the MOC being more sluggish in the past, due to an increased freshwater input to the North Atlantic, which hampered the formation of North Atlantic Deep Water (e.g., *Broecker and Denton*, 1990; *Lenderink and Haarsma*, 1994; *Rahmstorf*, 2002; *Green et al.*, 2009). However, the increased energy input from tides during the LGM may have facilitated the recovery of the MOC at the end of any freshwater pulse (*Green et al.*, 2009; *Green and Bigg*, 2011). The very large tides reported in the Arctic and Labrador Sea during the LGM may also have been acting to destabilize the continental ice sheets (*Arbic et al.*, 2004; *Rosier et al.*, 2014a). Additionally, tides themselves are quite sensitive to the location of ice sheet grounding lines (*Griffiths and Peltier*, 2008, 2009; *Rosier et al.*, 2014a). The present simulations thus provide a new insight into the behaviour of the tides over the last 21 kyr at high resolution, and may form a basis for ocean mixing in further climate models simulations.

In order to provide better tidal estimates for the last 21 kyr, we re-run the model used by *Egbert et al.* (2004) but with a slightly modified set up. We include most of the Arctic, as opposed to cutting at 82°N, which adds information about tidal changes in the Arctic and reduces the influence of open boundary conditions on the tidal solution. We also include analysis of the K_1 tide – the focus of most previous studies has been on M_2 – and we investigate the sensitivity of the global tidal evolution to the location of the Antarctic grounding lines. Furthermore, we present results from time slices every 500–1000 years from the LGM to the present, thus exploring new features of the tides not reported previously. Previous global studies have either presented selected time slices with spatially high resolution (*Egbert et al.*, 2004; *Green*, 2010), coarse resolution studies with higher temporal resolution (*Thomas and Söndermann*, 1999; *Uehara et al.*, 2006) or have shown temporally and spatially highly resolved regional timeslices (*Uehara et al.*, 2006; *Hill et al.*, 2011; *Hall et al.*, 2012). To date only regional changes in tides in response to changes in the grounding line location and ice shelf extent of the Antarctic Ice Sheet have been examined (*Griffiths and Peltier*, 2009; *Rosier et al.*, 2014a). This

work is carried out with both a high temporal and spatial resolution and looks at the global impacts of changes in the grounding line in Antarctica. We begin by introducing the tidal model in the next section, including an overview of the different simulations. The results for both the M_2 and K_1 constituents from these simulations are presented in section 4.3 where we first explore the LGM state and then investigate the temporal evolution from the LGM to the present. Section 4.3.4 investigates the implications of the changes in tidal dissipation during the LGM on the MOC.

4.2 Tidal modelling

4.2.1 Model description

The Oregon State University Tidal Inversion Software (OTIS) has been used in several previous investigations to simulate global and regional tides in the past, present and future oceans (e.g., *Egbert et al.*, 2004; *Green*, 2010; *Pelling and Green*, 2013; *Green and Huber*, 2013). It provides a numerical solution to the shallow water equations, but the non-linear advection terms and the horizontal diffusion are neglected without loss of accuracy (*Egbert et al.*, 2004). The only forcing is the astronomic tide-generating force. Energy is dissipated through a quadratic bed-friction term and a linear tidal conversion scheme, representing the energy losses to internal tides. It is used in the setup described in Chapter 3.2.

We acknowledge that changes in stratification could be important for the LGM, but they have been studied elsewhere (e.g. *Egbert et al.*, 2004; *Griffiths and Peltier*, 2009) and our focus is on evaluating changes in tides due to shifts in the grounding line position. The establishment of a more accurate stratification is work in progress and not part of the scope of this study. The ocean may have been more stratified during the LGM, making N^2 up to a factor of two higher (*Green et al.*, 2009). In order to test for sensitivity of the results to changes in stratification we perform simulations of the LGM tides with IT drag multiplied by factors 0.5 and 2 in order to evaluate the sensitivity of dissipation to offsets in stratification.

The palaeotopography comes from ICE-5G (see *Peltier*, 2004, and `http://www.atmosp.physics.utoronto.ca/peltier/data.php` for the latest version), which has a $1^\circ \times 1^\circ$ resolution and is available in 500 or 1000 year time slices from the present to the LGM. For accuracy reasons, the runs were also made on a $1/8^\circ \times 1/8^\circ$ grid, with palaeobathymetries

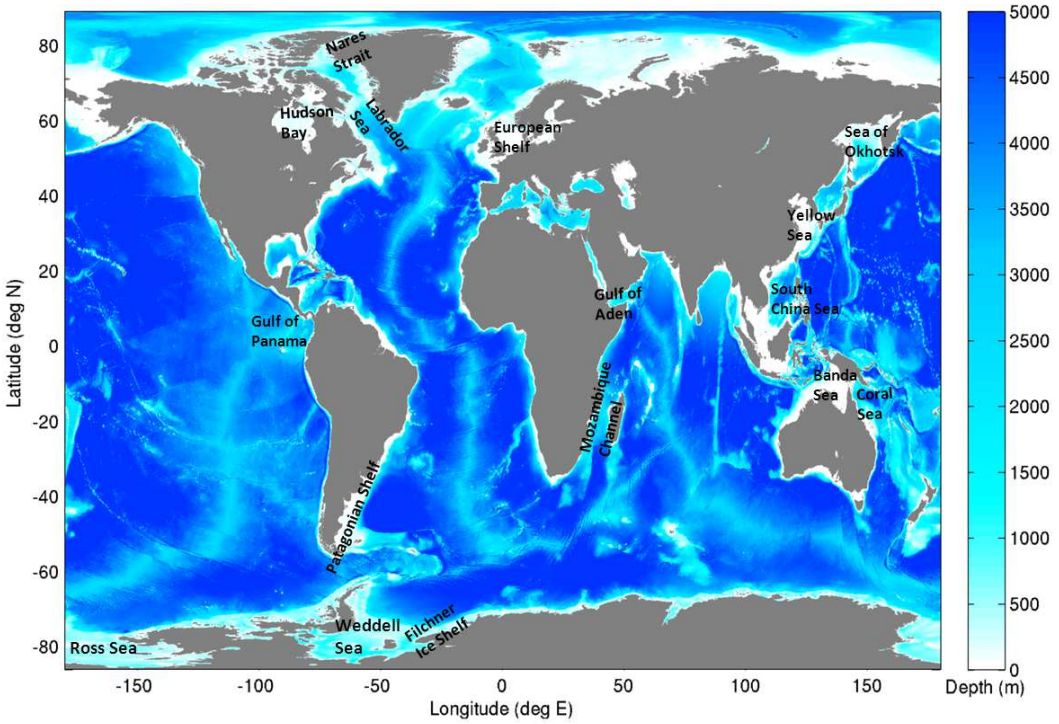

Figure 4.1: Present day bathymetry assembled from the Smith and Sandwell, v.14, IBCAO , v.2, and ETOPO1 databases. Regions mentioned in subsequent sections of this paper are marked on the map.

obtained following the methodology in *Egbert et al.* (2004): for each time-slice, the difference between the $1° \times 1°$ palaeobathymetry and the $1° \times 1°$ version of the present day (PD) bathymetry (see Chapter 3.2.6 for a description and Figure 4.1) was computed and then linearly interpolated to the PD 1/8° grid and added to the PD 1/8° bathymetry. This leads to sea-level adjustment consistent with the ICE-5G database, but with the necessary resolution to obtain reliable results.

The model grid thus has a fully-global longitudinal span and covers the globe between 86°S–89°N in latitude. At the northernmost boundary, an elevation boundary condition was applied using data from the TPXO7.2 database (see *Egbert and Erofeeva*, 2002, and `http://volkov.oce.orst.edu/tides/ global.html`). Simulations with a land-mass at the northernmost boundary were run for a few select time slices and did not change the results (e.g. *Egbert et al.*, 2004; *Arbic et al.*, 2009). We opted for the open boundary in the Arctic here. However, the fully-global simulations in *Griffiths and Peltier* (2008, 2009) suggest that the tide was almost an order of magnitude larger along 89°N during the LGM – a feature which must have been crucial to generate their megatides along the Arctic shelf. As described later, we therefore performed sensitivity simulations with

enhanced tidal amplitudes in our boundary conditions.

The present day runs are evaluated against the TPXO8 database, which was averaged from a $1/30° \times 1/30°$ to $1/8° \times 1/8°$ horizontal resolution and then interpolated using linear interpolation to the common latitude-longitude grid. Note that for computational reasons (model issues with high resolution files), we still use TPXO7.2 for the boundary conditions. The difference between the two databases is negligible along 89°N and should not impact on the results but TPXO8 is generally more accurate due to the increased resolution.

4.2.2 Grounding line scenarios

LGM to early Holocene (21 to 10 kyr BP) simulations are carried out for two extreme grounding line cases. This enables us to take the uncertainties of the reconstructions discussed in Section 4.1 into account and to provide a realistic range in which partially grounded cases could lie. The first case deals with grounded Antarctic ice shelves (ice in Weddell and Ross Sea grounded, henceforth referred to as 'GR'), whereas the second case uses floating Antarctic ice shelves (ice in Weddell and Ross Sea floating, 'FL'). For the GR case, all Antarctic ice given by the ice thickness data in the ICE-5G dataset is assumed to be grounded. For the FL case the change in ice thickness between the palaeo-slices and the present day case is added to the total water depth and only when the ice thickness exceeds the height of the water column is the ice grounded. Otherwise we assume that a floating ice shelf is present. The horizontal extent of the floating ice shelf is the same as for the grounded ice sheet. We do not specify the thickness of the ice shelves as it is the total water depth change, i.e. the eustatic and isostatic sea-level changes together with alterations water depth due to the displacement of water from the presence of ice shelves, and the location of the grounding line that are important for the tidal dynamics (e.g. *Griffiths and Peltier*, 2009; *Rosier et al.*, 2014a). Throughout the Holocene we assume the ice to have been ungrounded in the Weddell and Ross Sea and only the FL case is referred to for this period.

4.2.3 Simulations and computations

Runs are made for the present and for a number of palaeo time-slices between 21 kyr BP and 1 kyr BP using the relevant topography for each time-slice (the simulated ages are marked in Fig. 4.8). The simulation period for each run is 13 days, of which

the last 5 days are used for harmonic analysis of the modelled elevations and currents. Forcing consists of the astronomic tidal potential and prescribed elevations at the Arctic boundary for the M_2 and K_1 constituents. Additionally, runs are made for the LGM (21 kyr) and the present using M_2, S_2, K_1 and O_1 forcing with a 45-day run time and 30 day harmonic analysis. The S_2 signal responds very similarly to M_2, and O_1 is close to K_1 in response, so for computational economy we focus on M_2 and K_1 in the following. Model output consists of tidal amplitudes and phases, and volume transports and transport phases for each modelled constituent. In order to test for the sensitivity to variations in the elevation boundary conditions at the northern open boundary (89°N) we perform runs where the TPXO7.2 boundary conditions are multiplied by factors of 2, 4, and 8 for the 21 kyr time slice with grounded Antarctic ice sheets.
The dissipation of tidal energy is computed following the methodology in *Egbert and Ray* (2001) (see Chapter 2.3.7 for a description).

4.3 Global tidal dynamics

4.3.1 The control runs

The amplitude and dissipation fields for the PD control runs for M_2 and K_1 for both floating and grounded Antarctic ice shelves can be seen in Figs. 4.2 and 4.3. The different present-day scenarios are from now on referred to as pdM2fl (present day, M_2 constituent and floating ice shelves), pdM2gr (present day, M_2 constituent and grounded ice shelves) for M_2, and pdK1fl and pdK1gr for the K_1 results, respectively. Note that the grounded PD simulation is a sensitivity case, arising from some global topographic data bases not having including bathymetric data under the Antarctic ice shelves. The corresponding root mean square (RMS) amplitude errors, total and deep dissipation, and correlation coefficients between modelled and observed amplitudes are listed in Table 4.1.

Using TPXO8 as observations we obtain a RMS difference of less than 6.8 cm between the modelled M_2 tidal amplitudes for the floating ice shelf case (Fig. 4.2) and observed M_2 elevations. In water deeper than 500 m, the RMS difference is below 3.9 cm. This demonstrates a marked improvement to the simulations by *Egbert et al.* (2004). The correlation coefficient between pdM2fl and TPXO8 is $r = 0.95$, thus explaining 90% of the variance in TPXO8 which implies that we capture both the absolute tidal amplitudes and the structure of the tidal elevation relatively well. For the grounded ice sheet case,

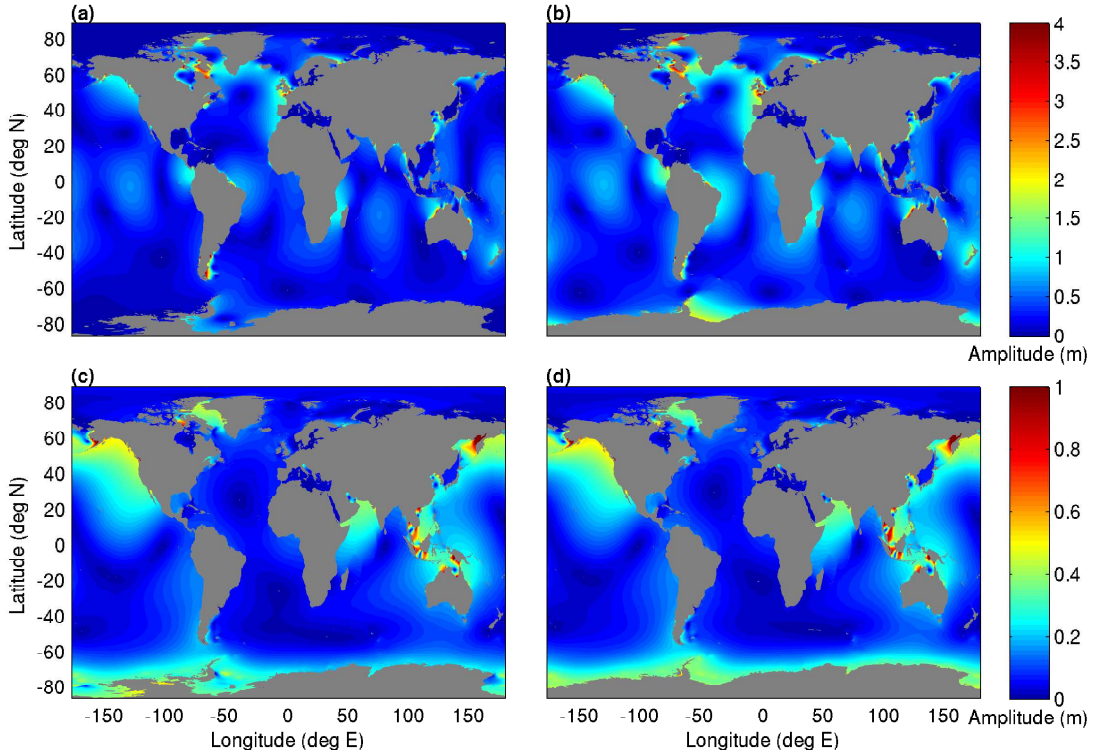

Figure 4.2: Present day M_2 amplitudes for (a) floating and (b) grounded Antarctic ice shelves, respectively; (c) and (d) same but for K_1

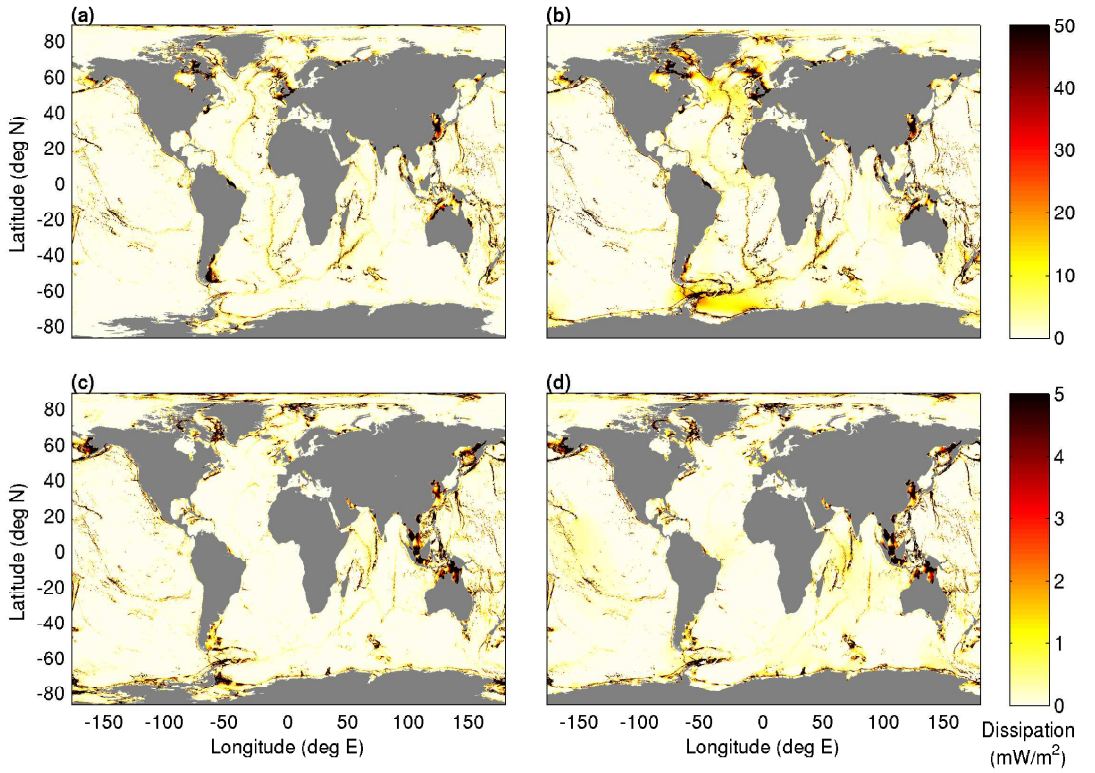

Figure 4.3: Same as Fig. 4.2 but for dissipation

pdM2gr, the RMS values are considerably higher, with 16.6 cm and 12.8 cm for the whole ocean and the deep ocean respectively. There is a marked offset in the tides around both Antarctica and in the North Atlantic region in this run. This highlights issues that occur when using inaccurate Antarctic bathymetries and incorrect grounding line positions of the ice sheets. The grounding of the ice shelves around Antarctica leads to a marked increase in amplitude of several meters around Antarctica and a northward shift of the nearby amphidromic points. This results in decreases in amplitudes along the south-east coast of South America and an increase along the central east coast (Fig. 4.2). The shift in amphidromic points propagates all the way into the North Atlantic, resulting in increased amplitudes in the Labrador Sea, the Nares Straits, and along the west coast of North America. In addition to the amplitude shifts caused by the blocking of the Weddell Sea, the grounded ice also acts as a wall, which reflects tidal energy back into the North Atlantic. Again, this results in a more energetic tidal field. These changes are also reflected in the dissipation field. Total M_2 dissipation for the FL case is 2.29 TW of which 0.96 TW (41%) takes place in the deep ocean (i.e., where $h > 500$ m). This compares very well with the deep dissipation from both TPXO8 (0.96 TW) and the estimates by *Egbert and Ray* (2001). It does however slightly underestimate the dissipation in shallow water, probably due to errors in the bathymetry. For the GR case, the dissipation increases considerably to 3.17 TW in total with 1.18 TW (37%) occurring in the deep ocean. Here, a shift in dissipation takes place from the Patagonian shelf into Drake Passage and the Atlantic part of the Southern Ocean. The North Atlantic becomes significantly more energetic, as seen from the amplitudes. This shows that a regional change in bathymetry can lead to significant alterations of global tidal dynamics.

The RMS error for pdK1fl is below 3 cm for the global tides and less than 1.8 cm for the deep ocean. The pattern correlation between TPXO8 and pdK1fl is $r = 0.93$ and our model result thus explains 86% of the variance in the TPXO8. For the grounded ice shelf case (pdK1gr) the RMS values are larger than for the floating case (pdK1fl), with values of 4.5 cm and 2.4 cm for the global and deep ocean, respectively. With grounded ice shelves the explained variance is reduced by 8%. For K_1, the difference between grounded and floating ice shelves is much less pronounced than for M_2, and the shifts in amplitude are local and confined to the proximity of Antarctica. For the GR case a pronounced decrease in dissipation can be seen in this region in comparison to the FL case, whereas only small changes occur throughout the remaining ocean. Total dissipation for the FL

Table 4.1: Comparison of present day simulations for grounded and floating ice shelves for M2 and K1, respectively, to TPXO8. Amplitude root mean square errors (RMSE) were calculated globally (1st column; total RMSE) and for the deep ocean (depths > 500 m; 2nd column; deep RMSE); the pattern correlations (3rd column; correlation coeff.) were obtained by simply correlating our elevation fields with the TPXO fields. The 4th and 5th columns show total and deep (> 500 m) dissipation, respectively.

Case	**tot. RMSE (cm)**	**deep RMSE (cm)**	**correlation coeff.**	**tot. dissip. (TW)**	**deep dissip. (TW)**
TPXO8 M2	–	–	–	2.393	0.957
TPXO8 K1	–	–	–	0.355	0.127
pdM2fl	6.671	3.866	0.947	2.291	0.957
pdM2gr	16.604	12.776	0.866	3.172	1.176
pdK1fl	2.838	1.771	0.926	0.380	0.174
pdK1gr	4.555	2.391	0.903	0.368	0.122

case is 0.38 TW with 45% of the dissipation taking place in the deep ocean giving a good fit with the TPXO8 data. For the grounded case, total dissipation does not change but the fraction of deep dissipation decreases to 33%. This is because dissipation previously occurring in the Weddell and Ross Seas is omitted, leading to increased amounts of energy on the Antarctic shelf and in the Indian Ocean.

4.3.2 Tidal evolution

In this section the evolution of the tides from 21 kyr BP to present is described for both M_2 and K_1, for each of the two grounding line scenarios. The LGM amplitude and dissipation fields can be seen in Figs. 4.4 and 4.5. The evolution of dissipation globally is shown in Fig. 4.8, and the corresponding basin wide dissipation is displayed in Fig. 4.7.

M_2 constituent

Global tidal dynamics at the LGM are strongly altered in comparison to the present day case for both scenarios. For both grounding line cases, strongly enhanced tidal amplitudes and dissipation can be seen throughout the Atlantic, around Antarctica, the Coral Sea, the Gulf of Aden, the area north of the Mozambique Channel and the Gulf of Panama (Fig. 4.4). These areas correspond to areas of increased dissipation rates (Fig. 4.5), and our results are consistent with those reported by *Egbert et al.* (2004) and

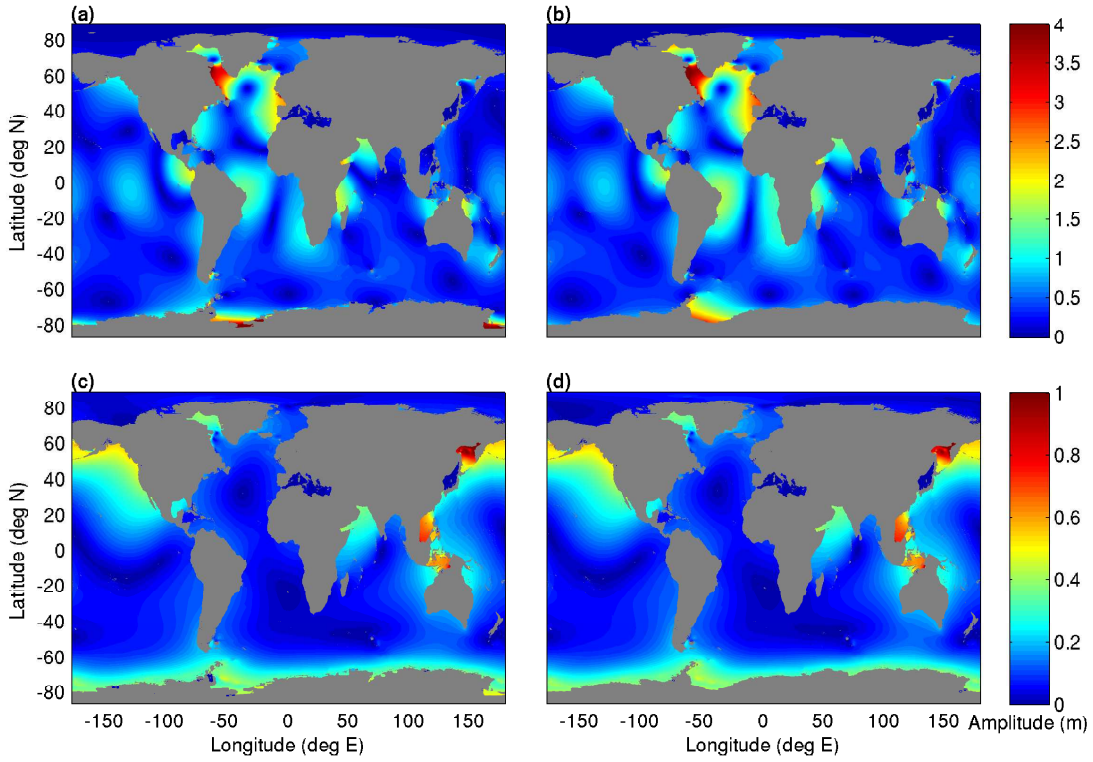

Figure 4.4: LGM (21 kyr BP) M_2 amplitudes for (a) floating, and (b) for grounded Antarctic ice sheets, respectively. (c) and (d) same as (a) and (b) but for K_1

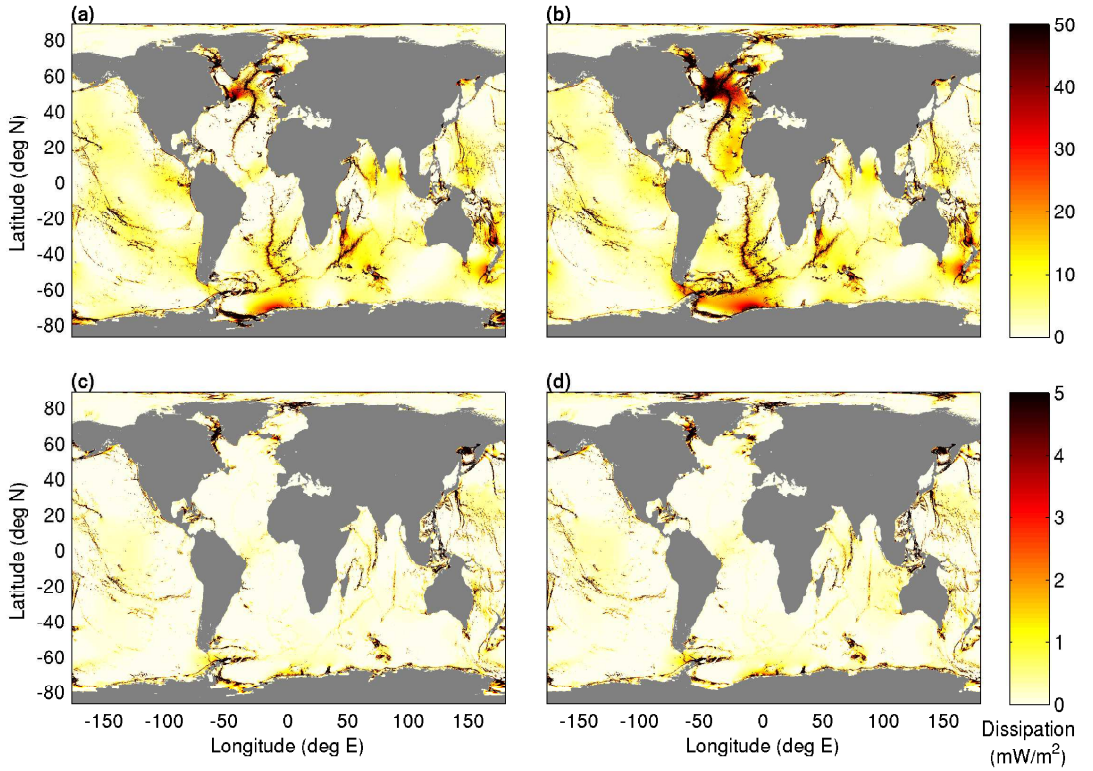

Figure 4.5: Same as Fig. 4.4 but for dissipation

Griffiths and Peltier (2008, 2009). However, considerable differences can also be seen between the two different grounding line scenarios in both amplitudes and dissipation rates. At 21 kyr BP, the main differences in amplitude and dissipation between the grounding line scenarios are found in the Atlantic (Fig. 4.7). In the South Atlantic and in the vicinity of Antarctica the smallest amplitudes are observed for the grounded ice shelf case. This is the scenario which generates the largest tidal amplitudes in the North Atlantic region with a maximum of 5.5 m in the Labrador Sea. Ungrounding the ice sheet in both the Weddell and Ross Seas reduces the amplitude in the North Atlantic considerably, with the maximum amplitudes in the Labrador Sea dropping to 4.1 m. However, due to the formation of a shallow shelf sea in the Weddell Sea, considerable semi-diurnal tidal amplitudes of up to 5.5 m can now also be seen here, and large tides can be observed in the Ross Sea. This corresponds to the results presented by *Griffiths and Peltier* (2009), who also find large changes in the regional Antarctic tides in response to grounding line shifts and report strongly enhanced tides in both the Ross and Weddell Sea for the LGM. They also find that the large tides in the Ross Sea disappear when the grounding line is advanced out towards the shelf break whereas the tides in the Weddell remain amplified with the grounding line shifts. These global differences in the tides due to grounding line changes are also reflected in the dissipation patterns which differ mainly in both the North and South Atlantic. Less energy is dissipated in the North Atlantic region as the Weddell Sea ice becomes ungrounded whereas for the South Atlantic the opposite is the case. The total M_2 dissipation estimates for the grounded case is 4.75 TW (GR), whereas the dissipation for the floating case is much lower at 4.05 TW (FL). The values mark an increase in dissipation compared to the FL present day case by between 1.8 TW (78%) and 2.5 TW (107%) for the lowest and highest case respectively. These values are in close correspondence to those previously reported (*Egbert et al.*, 2004; *Uehara et al.*, 2006; *Griffiths and Peltier*, 2008, 2009). The reason for these differences in dissipation rates between the two scenarios becomes evident from Fig. 4.5 (a) and (b). For the FL case, the North Atlantic region tidal amplitudes are reduced in comparison to the GR scenario and less dissipation takes place south of Greenland. For the GR case, the grounding of the entire ice in the Weddell Sea and the removal of the shelf sea occupying the Weddell Sea enhances the Atlantic tides and increases dissipation in the North Atlantic. This is the same mechanism as discussed in *Egbert et al.* (2004) and *Green* (2010) where the removal of the damping factor (in this case the shelf sea in the

Weddell Sea) in a basin that is in a near resonant state acts to enhance the dissipation in this system.

We do not find the LGM megatides in the Arctic which *Griffiths and Peltier* (2008, 2009) see in their fully global simulations. Their results show M_2 amplitudes which exceed 3 m around the margins of the Artic basin. We on the other hand find tides in the Arctic basin which are strongly amplified by up to a factor of five, however the absolute amplitudes changes are much smaller than those reported by *Griffiths and Peltier* (2008, 2009). Increasing the elevation boundary conditions at the open boundary at 89°N by a factor of two leads to a small increase in the Arctic tides, whereas a factor eight leads to an increase in amplitudes on the shelf close to the values reported by *Griffiths and Peltier* (2009). The increase in open boundary elevation also induces amplitudes near the North Pole which are consistent with those seen by *Griffiths and Peltier* (2009). However, we find that altering the boundary conditions in the centre of the Arctic has very little effect on the tides elsewhere on the globe outside the Arctic Basin. The amplitude differences generally do not exceed 5 cm and are restricted to areas where the tides were large during the LGM in the first place. The same applies for dissipation rates, where the factor 8 boundary condition simulation produces an increase in global dissipation by 5% with the changes being local and restricted to the Arctic.

Large shifts in the global patterns of both amplitude and dissipation take place during the transition from the LGM to present that differ for each of the two grounding line scenarios for the semi-diurnal tidal constituent. The changes during this period can be divided into four distinct phases over the time period under investigation:

21–16 kyr BP: Between 21 and 18 kyr BP both amplitudes and dissipation rates largely reflect the LGM state and remain fairly constant throughout the period. Dissipation occurs mainly in waters deeper than 500m, as most of the shelf seas were emergent during this period. Large tides can be observed in the Labrador Sea, along the European coast, and along the ice margins in the Weddell Sea. For both scenarios, the initial flooding of the shelf seas between 18 and 16 kyr BP leads to a slight drop in Labrador Sea amplitudes, accompanied by an increase of the amplitudes on the European shelf. The dissipation rates remain constant over this period.

16–10 kyr BP: As the shelf seas continue to flood, pronounced drops in amplitudes and dissipation can be seen for both grounding line scenarios, with dissipation

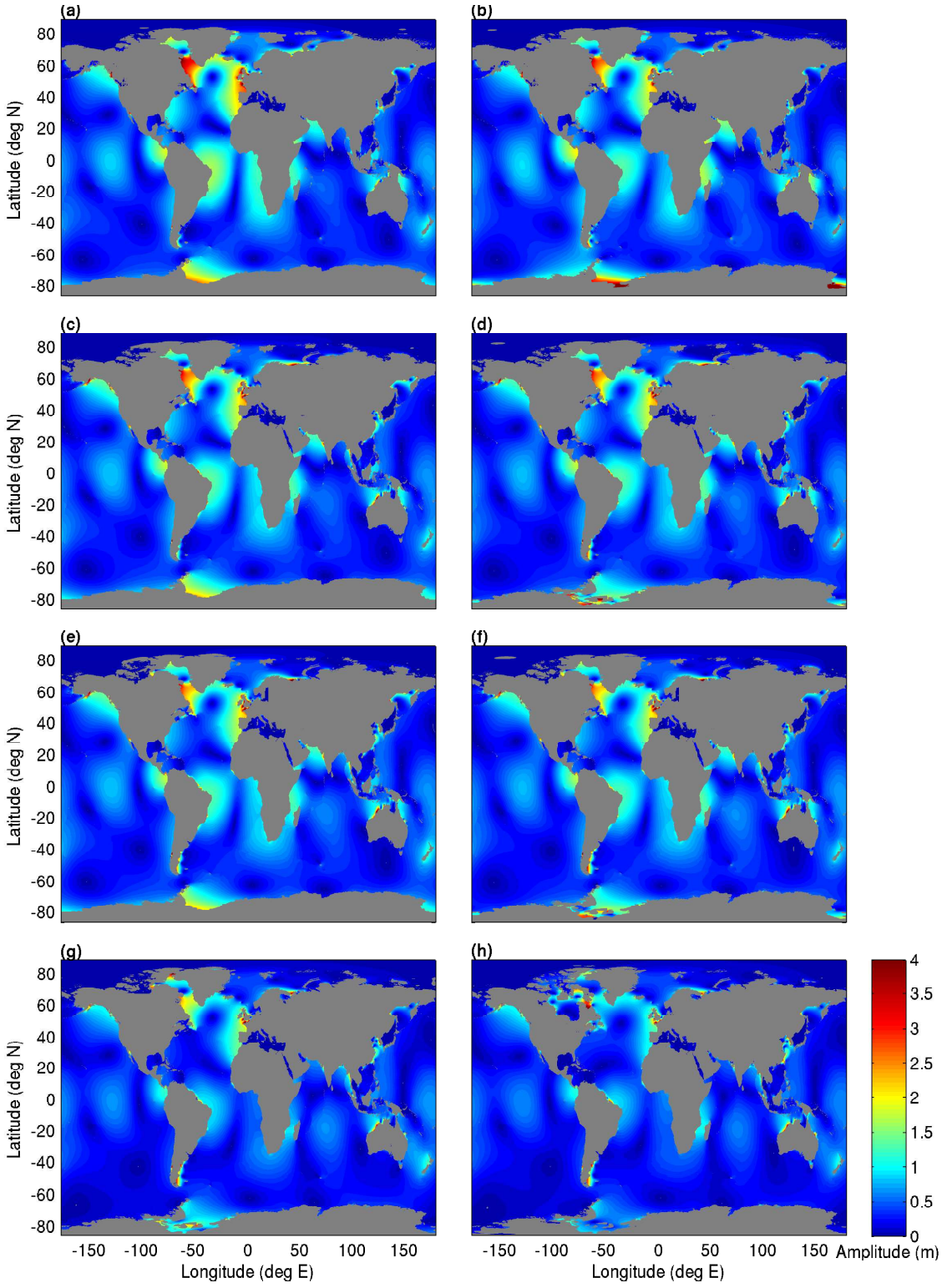

Figure 4.6: M_2 amplitudes at 14 kyr BP for (a) GR and (b) FL, at 11 kyr BP for (c) GR and (d) FL, at 10 kyr BP for (e) GR and (f) FL,and (g) 9 kyr BP and (h) 8 kyr BP for FL.

shifting from the deep ocean to the shelf seas. The changes in dissipation take place gradually and are more pronounced for the GR case, with total dissipation decreasing by 0.8 TW and deep dissipation by 1.8 TW. For the FL case the drops amount to 0.4 and 1.3 TW, respectively (Fig. 4.8). These figures correspond to the results presented by *Uehara et al.* (2006) who report decreases in dissipation of a very similar magnitude from simulations with a coarse resolution global tidal model for this time period. For the FL scenario, initially, the total dissipation remains fairly constant. A gradual decrease in amplitudes in the Labrador Sea can be seen commencing around 14 kyr BP corresponding to increased flooding of shelf seas which acts to reduce the deep dissipation rates. At this point, the dissipation in the Southern Ocean and South Atlantic also begin to drop. Meanwhile, dissipation in the North Pacific and the Indian Ocean increases due to the formation of new shallow seas. An especially pronounced drop in tidal amplitudes in the North Atlantic occurs between 12 and 11 kyr BP when the shelf area fraction increases by nearly 2% and parts of the Weddell and Ross Seas and the Patagonian Shelf flood. The flooding of these areas, which are all highly efficient dampers, consequently reduces the Atlantic tides and decreases dissipation. A large drop in dissipation can also be found in the North Pacific due to the flooding of the Yellow Sea. For the GR scenario both amplitudes and dissipation remain fairly constant in the North Atlantic region between 16 and 14 kyr BP, despite the large topographical changes. Decreases in dissipation can be seen in the Southern Ocean, South Atlantic and South Pacific. From 14 to 10 kyr BP pronounced changes in global tidal dynamics take place: tidal amplitudes in the Labrador Sea strongly decrease whereas large amplitudes can now be seen on the European Shelf. With the flooding of the shelf seas North Pacific and Indian Ocean dissipation initially increases, but for the Pacific the trend is reversed around 11.5 kyr, when sea-level rises abruptly.

10–8 kyr BP: The most pronounced drop in global dissipation takes place between 10 and 9 kyr BP for both grounding line cases – a result very similar to those in *Uehara et al.* (2006). For the FL scenario, large drops in amplitude occur throughout the Atlantic and Indian Oceans, as well as in the Weddell and Ross Sea where amplitudes decrease locally with over 1 m. These drops coincide with the partial opening of the Nares Strait and changes in water depth of over 50 m in both the Weddell and Ross Sea due to the melting of the ice occupying these

embayments (as given by changes in ICE-5G ice thicknesses). For the GR case we assume that the ice sheets in the Weddell and Ross Sea unground between 10 and 9 kyr BP. Consequently, the amplitude and dissipation rates follow the FL case from that point onwards. The ungrounding event may have taken place at an earlier or later stage, but the effects are very similar regardless the timing. The ungrounding of the ice sheet in the Weddell and Ross Seas leads to a large decrease of the global total dissipation. For the GR case, these drops take a very similar pattern as for the FL case in this time step, i.e. the dissipation decreases throughout the Atlantic, Indian Ocean and Southern Ocean, but it is strongly enhanced around Antarctica and slightly increased throughout the remaining ocean basins. These changes in dissipation are driven by large tidal amplitudes in the Weddell and Ross Seas, and pronounced drops in amplitudes in all of the large ocean basins. The largest changes in amplitude for the FL scenario take place between 9–8 kyr and coincide with the retreat of large parts of the Laurentide Ice Sheet (e.g. *Dyke and Prest*, 1987). The resulting extensive flooding led to an increase of the global shelf sea area by 2%, the largest increase over the simulation period. With the flooding of the Hudson Strait and Hudson Bay, amplitudes in the Labrador and Weddell Sea drop drastically (by up to 1.5 m for both cases) whereas an increase in amplitudes can be seen on the Patagonian Shelf. Large tidal amplitudes also appear in the newly formed Hudson and Nares Straits in the Canadian Arctic (Fig. 4.6 (g) and (h)).

8–0 kyr BP: The last 8000 years show only small variations of the M_2 tidal amplitudes, and, consequently, only minor changes in the dissipation rates. This is consistent with results presented by *Hill et al.* (2011) and *Hall et al.* (2012) who show that tides throughout the North Atlantic showed little change during this period. Therefore, this period is not discussed further.

K_1 constituent

The K_1 amplitudes and dissipation stand in contrast to the response of the M_2 tide. The K_1 amplitudes at the LGM very much resemble the present day tidal dynamics (see *Griffiths and Peltier*, 2009). Changes in K_1 occur on a local scale, whereas large global shifts take place for the M_2 tide. The most prominent shifts can be seen in the Pacific where the diurnal tidal constituent is dominant at present. Consequently, we see

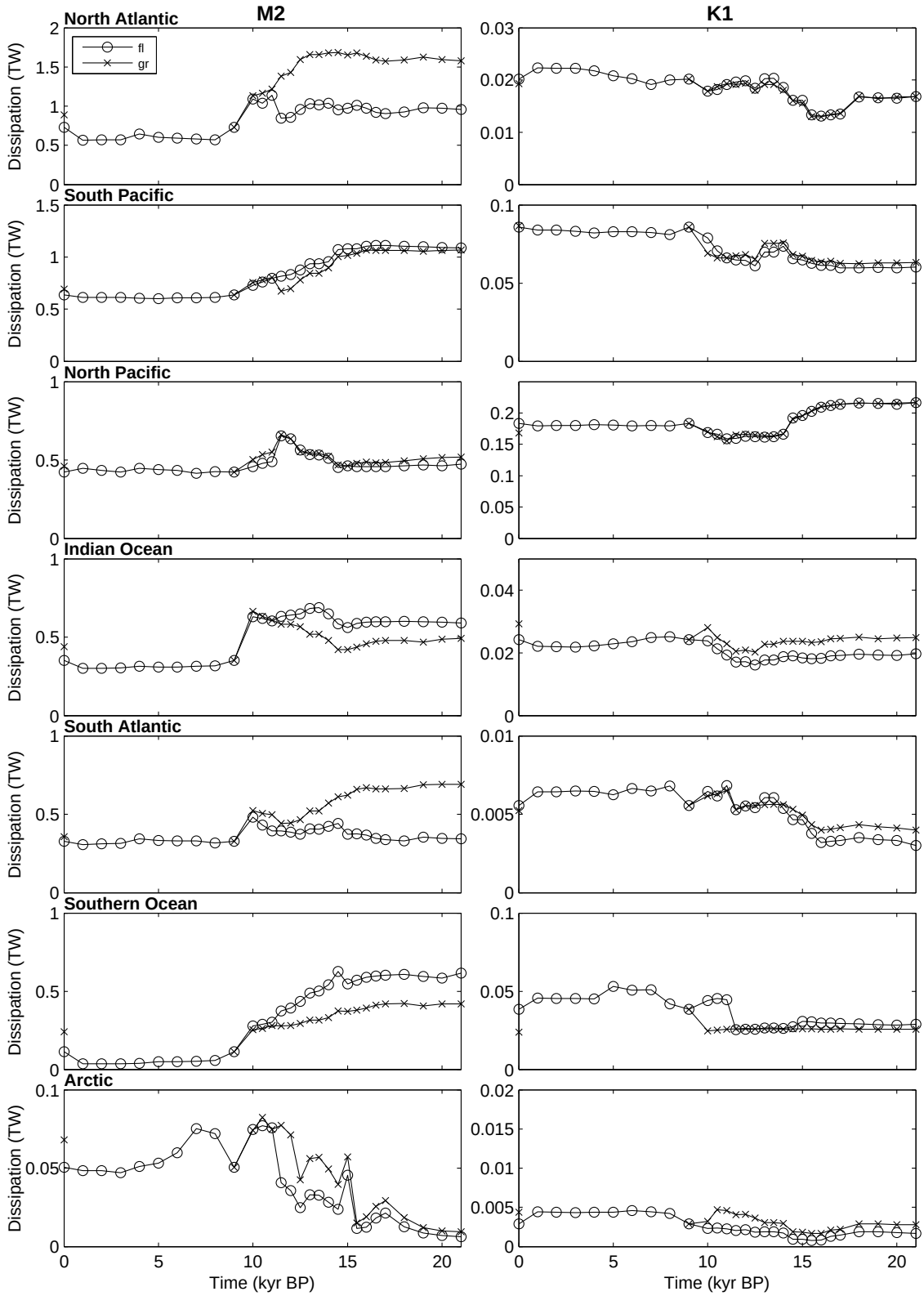

Figure 4.7: Regional total dissipation for M_2 and K_1 from 21 kyr BP to present for both GR (crosses) and FL scenarios (circles).

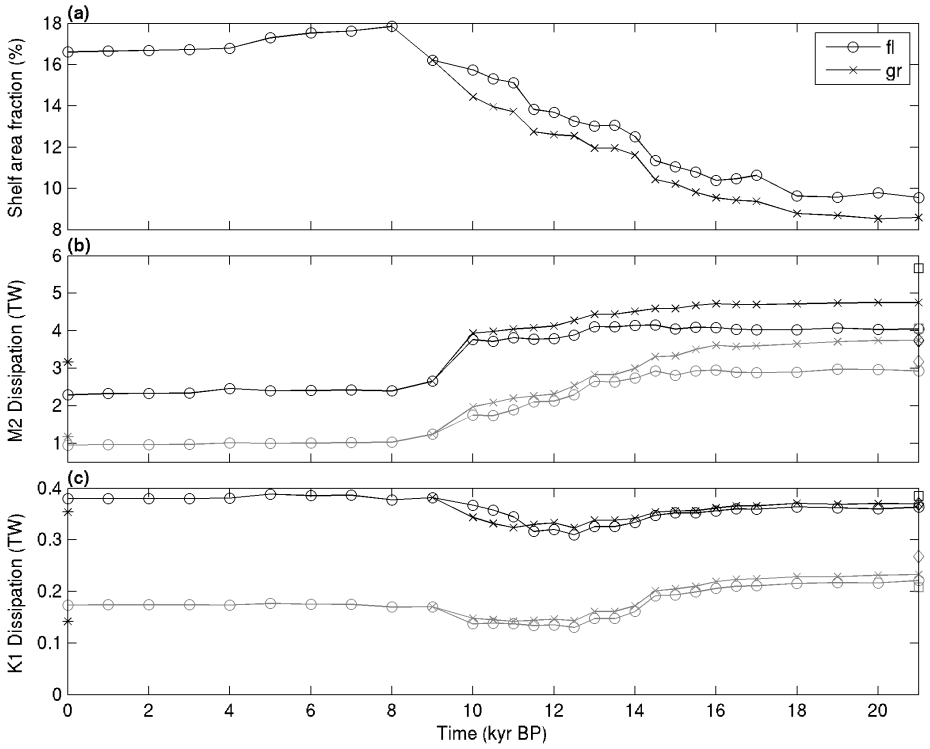

Figure 4.8: (a) Proportion of bathymetry that is shallower than 500m; total (black) and deep (> 500 m water depth, grey) dissipation for M_2 (b) and K_1 (c) for each GR (crosses) and FL (circles) grounding line scenarios. Squares and diamonds mark the dissipation values for IT drag multiplied by a factor of 0.5 and 2, respectively. The stars at 0 kyr BP give the dissipation values for the grounded PD ice sheet case.

changes in the Sea of Okhosk (SoO), the South China Sea (SCS) and the Banda Sea (BS). Changes in these regions have also been reported by *Uehara* (2005) and *Griffiths and Peltier* (2009). The amplitudes in the SCS and BS reach up to 1 m, and in the SoO amplitudes range up to 3 m – a pattern in contrast with PD conditions (*Zu et al.*, 2008; *Green and David*, 2013). As opposed to M_2, there are no major global differences between the different ice sheet grounding line scenarios for the LGM. The alterations in tidal dynamics are purely regional in the proximity of the respective grounding lines and the differences in global tidal amplitudes are less than 5 cm. The SCS, SoO and BS in the Pacific are also the locations in which the largest changes occur from the LGM to the Holocene. Again, in contrast to the semidiurnal tide, these shifts take place regionally, with no large changes in the global diurnal tidal dynamics during the past 21 kyr:

21–16 kyr BP: During this period the results from both grounding line scenarios largely resemble those during the LGM. Amplitudes in the SoO, SCS and BS remain high,

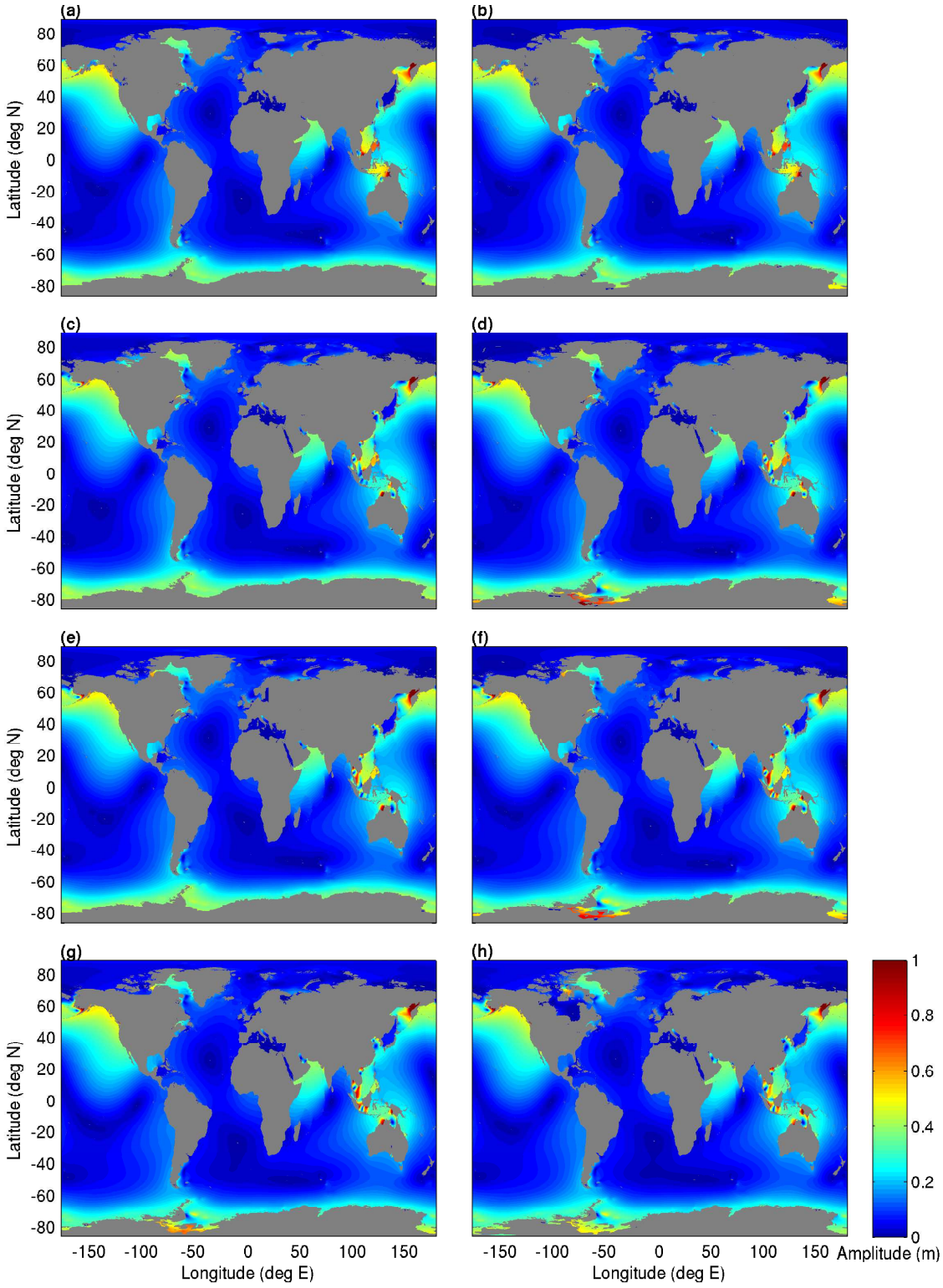

Figure 4.9: Same as Fig. 4.6 but for K_1 amplitudes.

and dissipation in the North and South Pacific stays at a constant level, not reacting to the initial small increase shelf area.

16–11 kyr BP: During this time period the largest regional shifts can be seen as shelf areas flood, thus altering local tidal dynamics. Again, the changes are confined to those basins in which the K_1 tidal constituent is dominant at present. Between 16 and 14.5 kyr BP a gradual decrease in dissipation can be seen in the North Pacific whereas for the South Pacific the dissipation rate increases slightly with the flooding of the shelf areas in the SCS and BS (Fig. 4.7). The decrease in the North Pacific is linked to a drop in amplitudes in the SoO and a confinement of large amplitudes to the Shelikhov Gulf as sea-level continues to increase. Between 14.5 and 14.0 kyr BP a stronger drop in amplitudes in the SoO, SCS and BS can be seen. This corresponds to the largest increase in sea-level (20 m in 500 years) during which the Gulf of Thailand and parts of the Australian shelf flood and a strong decrease in dissipation takes place for the North Pacific (Fig. 4.9 (a) and (b), and Fig. 4.7). The flooding of shelf areas results in a slight increase in dissipation in the South Pacific for both scenarios. The slight drop in dissipation in the South Pacific between 13 and 12 kyr BP coincides with further flooding of the shelf areas between Japan, China and Northern Australia. As the sea-level continues to rise, both scenarios gradually move towards the present day pattern (see Fig. 4.9 (c) and (d) and *Green and David*, 2013). Between 12 and 11 kyr BP for the FL scenario the ungrounding of the ice in the Weddell and Ross Sea results in an increase in dissipation in the Southern Ocean region, and considerable amplitudes of over 1 m can now be seen in the Weddell Sea.

11–0 kyr BP: No major changes in dissipation or amplitudes occur over this period. The small changes that can be seen again occur locally as the ice sheets gradually further unground and shallow seas are formed. Between 11 and 9 kyr BP a small increase of the dissipation rates for both scenarios can be seen, which is linked to the ungrounding of the Antarctic ice sheets occupying the Weddell and Ross Sea. This is more pronounced for the GR scenario due to the larger drop in ice volume in these embayments. A small decrease in Weddell Sea amplitudes can be seen between 10 and 8 kyr BP. In contrast to the semi-diurnal constituent the diurnal tides seem to have been unaffected by the large increase in sea-level between 9 and 8 kyr BP (Fig. 4.9 (g) and (h)).

4.3.3 Wider implications

The grounding line locations in the Weddell and Ross Seas appear to have a significant impact on the M_2 tidal dynamics, both regionally and globally (see *Rosier et al.*, 2014a, for possible future effects). The situation with grounded ice during the LGM gives a 1.5 times higher dissipation rate than the floating ice scenario, and was arguably the most likely configuration for the LGM. The enhanced LGM dissipation rates in the North Atlantic are thus not only due to regional resonance, but also caused by feedback effects from Antarctica. This also holds for the PD simulation: if the ice shelves ground at the PD ice front, tidal dissipation rates are enhanced by a factor of 1.4 in the Northern Hemisphere, but the impact is slightly suppressed compared to the glaciation. It must be noted that this latter case is the actual bathymetry in the first version of GEBCO and highlights the importance of using accurate bathymetric databases in tidal models. Why do K_1 and M_2 differ so strongly in their evolution from the LGM to present? In contrast to K_1, M_2 tides appear to be controlled by sea-level - today a large proportion of the tidal energy dissipates in shelf seas which were not present during the LGM. During the LGM, the North Atlantic region, the Coral Sea, the Gulf of Aden, the area north of the Mozambique Channel, and the Gulf of Panama are closer to resonance because the removal of the shelf seas acts to decrease the effective damping of the tide (*Egbert et al.*, 2004; *Green*, 2010). For the North Atlantic, continuing to lower sea-level does not increase amplitudes (Figure 4.10) or dissipation further, suggesting that the North Atlantic is as close to resonance as it can be at the LGM. However, resonance may not be the entire story: Antarctic grounding line location appears to play a significant role in controlling global amplitudes and dissipation rates and thus, global semi-diurnal tidal dynamics. In contrast, for K_1, the areas in which large amounts of dissipation occur today – the SoO and SCS – were present during the LGM and none of the large ocean basins are close to resonance at present and during the LGM (*Platzman et al.*, 1981). This therefore leads to little change between the LGM and the present and the responses seen are mechanistically not the same as for the M_2 constituent.

4.3.4 Implications for LGM Mixing and MOC

Despite numerous studies, the strength and structure of the large-scale MOC during the LGM remain a contended subject. The prevailing view is that in the MOC was more sluggish during the LGM and switched into a 'cold' mode and an 'off' state during Hein-

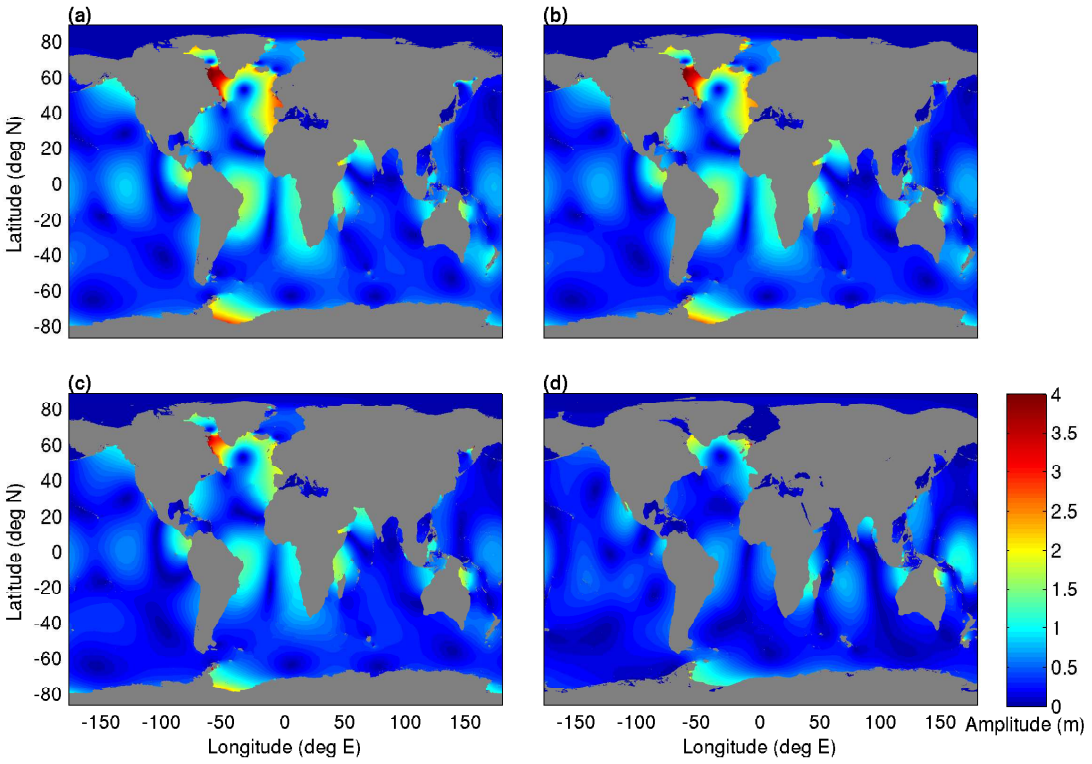

Figure 4.10: M_2 amplitudes for (a) the LGM, (b) the LGM with an additional sea-level decrease of (b) 50 m, (c) 100 m, and (d) 500m.

rich events (e.g., *Huang*, 1999; *Rahmstorf*, 2002; *Curry and Oppo*, 2005; *Liu et al.*, 2005; *Marchitto and Broecker*, 2006; *Otto-Bliesner et al.*, 2007; *Johnson et al.*, 2008; *Green et al.*, 2009). In the cold mode, in the glacial Atlantic, the northward transport of warm subtropical waters and the buoyancy driven deep-water formation the Nordic Seas were reduced. The upper 2000 m of the mid-and high latitude North Atlantic were occupied with Glacial North Atlantic Deep Water (GNADW) (e.g., *Duplessey et al.*, 1988; *Curry and Oppo*, 2005; *Lych-Stieglitz et al.*, 2007). This is the glacial equivalent of North Atlantic Deep Water, which in the present day ocean occupies the entire water column. Antarctic Bottom Water (AABW) extended much further northward and occupied the lower part of the water column in the glacial North Atlantic (e.g., *Rahmstorf*, 2002). This theory is based on tracers such as ^{14}C, $\delta^{13}C$ or Cd/Ca suggesting an increased ventillation age, shoaled northern source waters, and a stronger influx of AABW. These results have been backed by numerous modelling studies studies showing different ocean circulation configurations for the glacial ocean (e.g., *Stocker et al.*, 1992; *Otto-Bliesner et al.*, 2007; *Green et al.*, 2009). However, other more recent reconstructions of water mass properties and modelling studies argue towards a circulation that does not differ

greatly from its present day strength but advocate that the depth-extent of GNADW shoaled during the LGM (*McManus et al.*, 2004; *Lippold et al.*, 2005; *Ritz et al.*, 2013). The mechanical energy necessary to sustain the MOC at present day has been estimated at around 2 TW (e.g., *Wunsch and Ferrari*, 2004), with about 1 TW being supplied by the tide (e.g., *Egbert and Ray*, 2001) and the remainder by the wind, meso-scale eddies, and geothermal heat fluxes (e.g., *Huang*, 1999; *St. Laurent and Simmons*, 2006). The mechanical energy input drives turbulent vertical mixing which balances deep-water formation at high latitudes, maintains stable stratification in the oceans and drives upwelling of deep waters to the surface of the oceans (e.g., *Munk*, 1966; *Munk and Wunsch*, 1998; *Huang*, 1999; *St. Laurent and Simmons*, 2006). The rate of vertical mixing is expressed by the vertical diffusivity k_z which for the present-day ocean has been estimated at 1×10^{-5} m^2 s^{-1} for the surface ocean and at $1 - 10 \times 10^{-4}$ m^2 s^{-1} for the deep ocean (*St. Laurent and Simmons*, 2006). However, there are strong regional variations, especially over areas of rough topography (e.g., *Polzin et al.*, 1997; *Ledwell et al.*, 2000; *Wunsch and Ferrari*, 2004). It has been hypothesised that the much larger rates of tidal energy dissipation during the LGM may have increased vertical diffusivities and could have lead to a strengthing of the MOC (*Huang*, 1999; *Wunsch*, 2003; *Green et al.*, 2009; *Schmittner et al.*, 2015).

The impacts of altered tidal dissipation on ocean mixing and the MOC have previously been examined (*Montenegro et al.*, 2007; *Green et al.*, 2009). Using a coarse resolution tidal model *Montenegro et al.* (2007) obtain LGM internal tide energy fluxes, which are implemented in an intermediate complexity climate model. They report altered LGM diffusivities but no large effects of the altered tidal mixing on the LGM MOC. *Green et al.* (2009) find that increased diffusivities due to enhanced tidal mixing cannot counteract the increased freshwater forcing in the upper North Atlantic and the MOC remains more sluggish during the LGM. *Schmittner et al.* (2015) (see Appendix for the full study) re-investigate the implications of the altered tidal dynamics on ocean mixing and the global ocean MOC, using the tidal dissipation fields presented in this study as the basis their work. Using a higher-resolution tidal model (see this Methodology in this chapter), energy fluxes due to internal wave drag for the LGM are estimated. They are used as an input to a global tidal mixing parameterisation in the intermediate-complexity climate model UVic and the impact of altered tidal mixing on diffusivities and the global MOC during the LGM is investigated.

Schmittner et al. (2015) use OTIS in a similar setup as this study and simulate PD and LGM tidal dynamics for the four priniciple tidal constituents M_2, K_1, S_2 and O_1. These together account for 94% of the total dissipation in the PD ocean. The PD simulations use the same bathymetry as the PD control simulations presented earlier in this chapter. The LGM simulations are carried out with the LGM 'GR' bathymetry but with a vertical wall at the northern open boundary in order to eliminate any issues with open boundary conditions. The model was run with a simple $\beta = 0.1$ SAL-correction for computational reasons.

In addition to both a PD and a LGM simulation using the previously applied conversion parameterisation (see Methods section of this chapter and *Green and Nycander*, 2013) (which assumes horizontally uniform stratification) the model was re-run using spatially varying, vertically averaged stratification fields from the climate model, given by the bouyancy frequency $N(x, y, z)$. These were implemented into OTIS as spatially varying internal wave drag (C_{IT}) fields for both PD and LGM conditions in order to obtain estimates of the energy dissipation due to internal wave drag $\mathbf{F}_{IT}$. $\mathbf{F}_{IT}$ is calculated from Equation 2.49 (see Equation 3.5, where N_b is $N(x, y, z)$ at the sea bed and $\bar{N}$ is $N(x, y, z)$ averaged over the water column). The resulting $\mathbf{F}_{IT}$ fields are input into the climate model as tidal forcing.

The climate model UVic (*Schmittner and Egbert*, 2014) is a three-dimensional ocean circulation model, coupled to a one-layer energy-balance model of the atmosphere and a dynamic sea-ice model. The atmosphere model has prescribed top-of-the-atmosphere irradiance, wind stress, albedo and moisture advection forcing. This setup is a computationally highly efficient setup and permits long run times of 4500 years. It however excludes atmosphere-ocean feedbacks. The model is run for a pre-industrial PD state and an LGM state with prescribed ice-sheet extent, orbital parameters, and atmospheric CO_2 concentrations, and PD bathymetry is used in all simulations. Tidal mixing is included according to (*Schmittner and Egbert*, 2014) with the diapycnal diffusivity given by

$$k_v = k_{bg} + \frac{\Theta\epsilon}{N^2} \tag{4.1}$$

where k_{bg} is the background diffusivity which is set to $0.3 \times 10^{-4} m^2 s^{-1}$, $\Theta = 0.2$ is the mixing efficiency, and ϵ is the energy dissipation rate. ϵ is dependent on the energy flux from the barotropic to the internal tide, a vertical decay function, and a dissipation efficiency coefficient which is dependent on the critical latitude. In this equation k_{bg} is the

background diffusivity which also includes the effects of remotely dissipated tidal energy (e.g., internal waves breaking far from their generation site) and other mixing processes not considered here (e.g., wind and meso-scale eddies), $\Theta\epsilon$ denotes the rate by which tidal energy is dissipated, and N^2 gives a measure of the stability of the water column. The following simulations were carried out: PD_{PDmix} uses PD $\mathbf{F}_{IT}$ fields, LGM_{PDmix} uses LGM boundary conditions but PD $\mathbf{F}_{IT}$, and LGM_{LGMmix} uses LGM boundary conditions and LGM $\mathbf{F}_{IT}$. Results from the last 500 years of the simulations will be discussed.

The tide model results show that, in addition to the enhancement of tidal energy dissipation from a total of $\sim$ 3.7 TW at present to 5.8 TW for glacial conditions, $\mathbf{F}_{IT}$ increases by more than a factor of 3 from 1.3 TW to 4.7 TW. This is consistent with the shift of tidal energy dissipation from the shelf seas in PD to the deep ocean in LGM. This is due to the sea-level decrease of $\sim$ 130 m leading to a strong decrease in energy losses due to bottom friction. These increases occur mainly throughout the Atlantic (see Figure 4.11) as a consequence to changes in resonant properties (*Egbert et al.*, 2004; *Green*, 2010; *Wilmes and Green*, 2014).

When $\mathbf{F}_{IT}$ is mapped onto the climate model grid, the strongest enhancements in $\mathbf{F}_{IT}$ can be seen in the sub-thermocline and mid-depth layers, i.e. around 3000 m (Figure 4.12 a). Only small changes in stratification between the PD_{PDmix}, LGM_{PDmix} and LGM runs occur (Figure 4.12 b). However large increases in the vertical diffusivities can be seen for LGM_{LGMmix}, whereas diffusivities in LGM_{PDmix} closely resemble those of PD_{PDmix} (Figure 4.12). In the sub-thermocline and mid-depth regions, longitudinally averaged diffusivities increase by over 200% and global mean values for LGM are enhanced by a factor of three against PD and LGM_{PDmix}. These changes are especially pronounced for the Atlantic sector, whereas only small increases occur in the Indian Ocean and the Pacific shows no markable changes. Circumpolar Deep Water (CPDW) influx increases for the Indian Ocean but shows no change for the Atlantic or the Pacific.

When the climate model is forced with LGM boundary conditions but present-day tidal mixing (LGM_{PDmix}) strong decreases in the mid-depth Atlantic meridional overturning circulation (AMOC) can be seen, together with small decreases in the Pacific MOC (Figure 4.14). This is in agreement with previous modelling studies that show decreases in the AMOC using LGM boundary conditions (*Stocker et al.*, 1992; *Otto-Bliesner et al.*, 2007; *Green et al.*, 2009). In contrast, when tidal mixing is altered to reflect LGM tidal

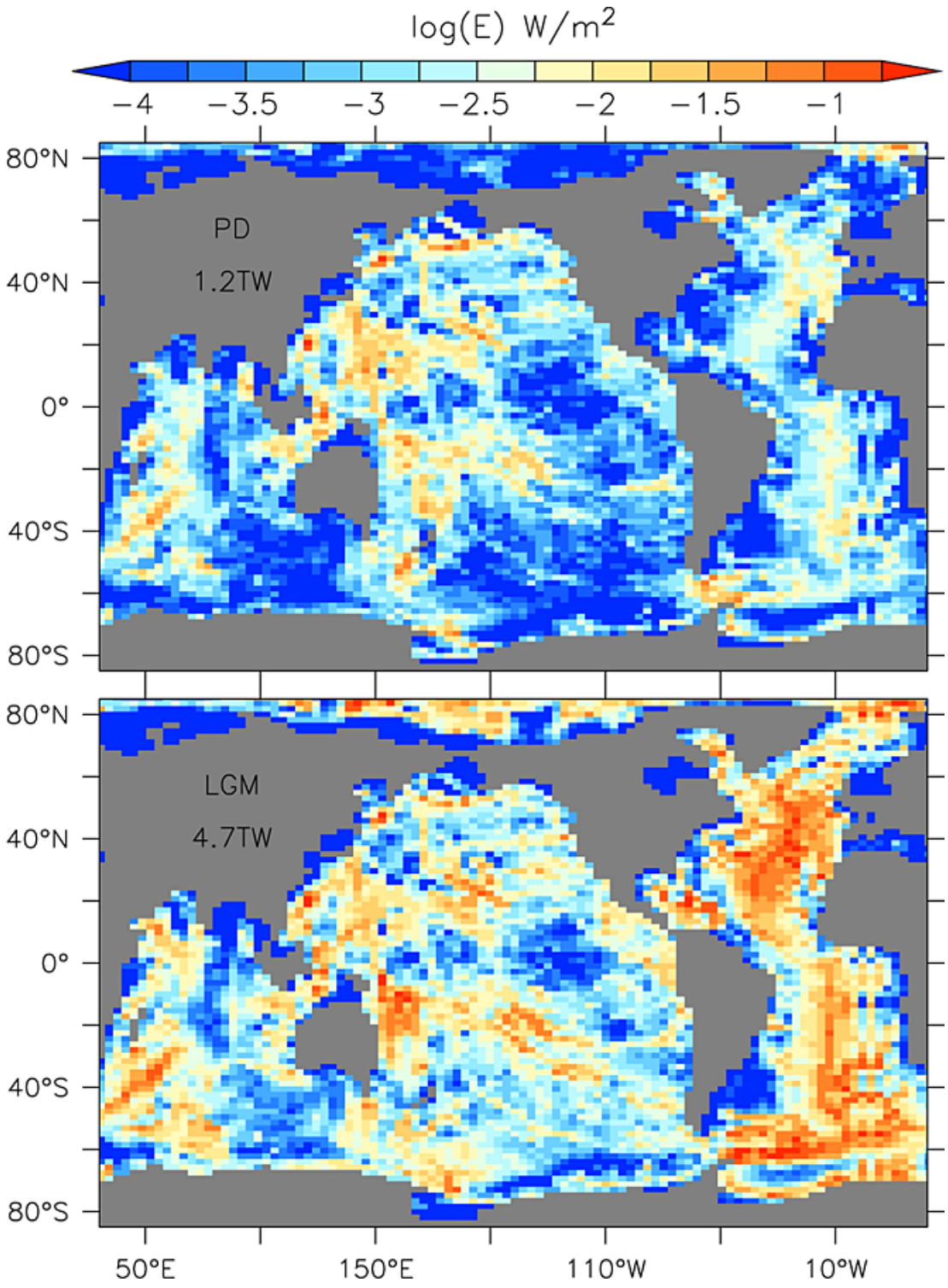

Figure 4.11: (a) PD and (b) LGM dissipation due to internal wave drag $\mathbf{F}_{IT}$ summed for the four tidal constituents M_2, S_2, K_1 and O_1. The numbers over Asia give the global integrals. Figure taken from *Schmittner et al.* (2015).

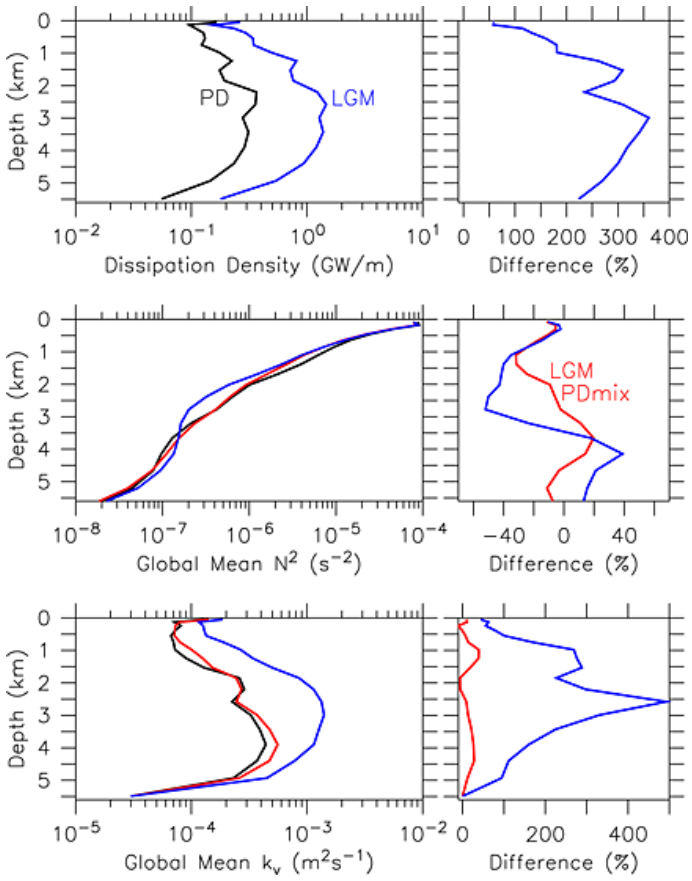

Figure 4.12: (Top) Horizontally integrated PD and LGM tidal dissipation density $\mathbf{F}_{IT}/\Delta z$ (Δz being model layer thickness), (middle) horizontally averaged buoyancy frequency squared (N^2) for PD_{PDmix} (black), LGM_{PDmix} (red) and LGM_{LGMmix} (blue) and (bottom) horizontally averaged diffusivities k_v for PD_{PDmix} (black), LGM_{PDmix} (red) and LGM_{LGMmix} (blue). (right) absolute values and (left) percentage changes relative to PD. Figure taken from *Schmittner et al.* (2015).

dynamics, large differences in ocean circulation can be seen. The AMOC strengthens to values close to PD and in the North Atlantic, the overturning cell occupies the entire water column. AABW influx also intensifies to values greater than PD. As in the Atlantic, the Pacific MOC also increases in strength. However the changes here are much smaller than in the Atlantic. The influx of CPDW into all ocean basins increases by around 25% into the Atlantic, the Indian Ocean and the Pacific. These results indicate that the changes in tidal mixing are of the same magnitude as the buoyancy forcing from the LGM boundary conditions in the Atlantic and are able to counteract the decreases in overturning in this ocean basin, but that in the Pacific and the Indian Ocean they strongly exceed the buoyancy forcing and result in a strengthened circulation.

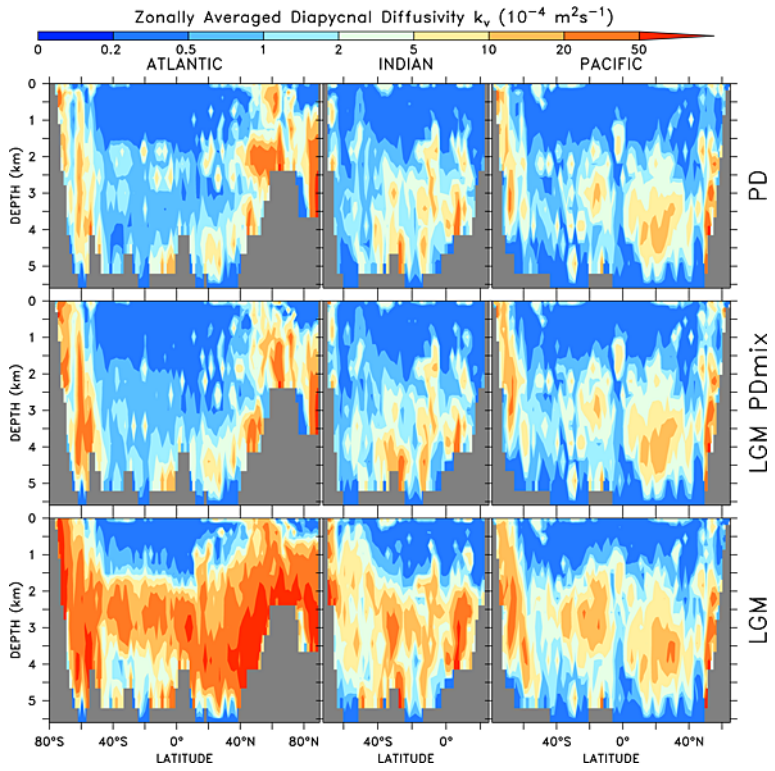

Figure 4.13: Horizontally averaged diapycnal diffusivities K_v for the Atlantic (left), Indian Ocean (centre) and Pacific (bottom). Values for PD_{PDmix} are shown at the top, LGM_{PDmix} in the middle and LGM_{LGMmix} at the bottom. Figure taken from *Schmittner et al.* (2015).

4.4 Discussion

With this work a detailed picture of the evolution of tides from the LGM to the present has been presented. Large alterations can be seen for the M_2 tidal constituent over this time period, as previously suggested by a number of studies (*Egbert et al.*, 2004; *Arbic et al.*, 2004; *Uehara et al.*, 2006; *Griffiths and Peltier*, 2009; *Green*, 2010), whereas for K_1 only small changes in the global tidal dynamics occur consistent with *Egbert et al.* (2004), *Uehara* (2005) and *Griffiths and Peltier* (2009).

In contrast to *Egbert et al.* (2004), who present time slices every 5000 years between LGM and present for M_2, here a much more detailed picture in 500 to 1000 year time intervals is provided. The model is run at a much higher spatial resolution than *Uehara et al.* (2006) who present 1000 year time slices for the same period. Our simulations differ somewhat from those by *Egbert et al.* (2004) and *Uehara et al.* (2006) in that their results suggest little change in global total dissipation between 15 and 10 kyr BP. In contrast, we find that, depending on the grounding line scenario, nearly half the decrease in

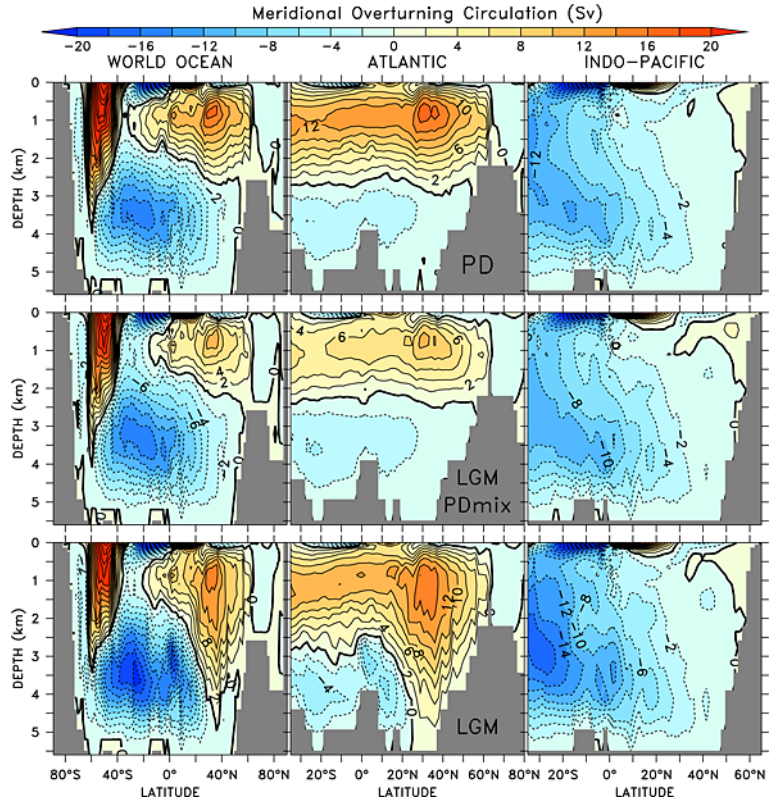

Figure 4.14: Meridional overturning stream circulation for the World Ocean (left), Atlantic (centre) and Indo-Pacific (right). Values for PD are shown at the top, LGM$_P Dmix$ in the middle and LGM at the bottom. Figure taken from *Schmittner et al.* (2015).

dissipation occurs during the transition from the LGM to the Holocene, due to the large bathymetric changes resulting from the deglaciation. Furthermore, the results by *Egbert et al.* (2004) provide no indication of the exact timing of the decrease in dissipation taking place between 10 and 5 kyr BP. Our simulations suggest that the largest changes in dissipation occur when the ice sheets occupying the Weddell and Ross Seas unground. This coincides both in timing and magnitude with the largest decreases in dissipation that *Uehara et al.* (2006) find. The largest shifts in global amplitudes take place between 9 and 8 kyr BP, when large parts of the Laurentide Ice Sheet disintegrated, resulting in large increases in sea-level and flooding of the Hudson Bay and Straits (e.g. *Clarke et al.*, 2003). *Hill et al.* (2011) also report large changes in tidal amplitudes along the east coast of middle and central America for this time period. According to our simulations, thereafter, only small changes in dissipation take place. These results highlight that the large changes in semidiurnal tides from the LGM to present did not occur linearly, but are intricately tied to the ice dynamics of the major ice sheets and their link to global sea-levels.

In contrast to *Griffiths and Peltier* (2008, 2009) we do not find megatides in the Arctic basin during the LGM in our normal set-up. Arctic tides in our simulations are enhanced by up to a factor of five along the north coast of Greenland and in the Canadian Basin, to values slightly smaller than reported by *Thomas and Söndermann* (1999) who find amplitudes of up to 70 cm. Stepwise increasing the TPXO7.2 elevation boundary conditions at 89°N by up to a factor of 10 (Figure 4.15) to match the amplitudes found at the same latitude by *Griffiths and Peltier* (2008, 2009) (this occurs at an amplification factor of eight), but not altering the grounding line location of the ice sheet covering the Queen Elisabeth Islands, enables us to reproduce the several metre amplitudes they find along the Arctic coastline. As *Griffiths and Peltier* (2008, 2009) use a truly global model, we conclude that the Arctic megatides reported by *Griffiths and Peltier* (2008, 2009) are a possible feature. These may have impacted Arctic mixing during the LGM. *Egbert et al.* (2004) carried out sensitivity experiments with the same model we use. They remark that neither changing the boundary conditions in the Arctic, placing a 'vertical wall' in the centre of the Arctic nor running the model in a truly global set-up with the North Pole shifted into Greenland alters the global tides outside the Arctic basin. This is supported by our boundary condition experiments. We find that even when boundary conditions are enhanced by a factor 10 this does not alter the tides outside the Arctic basin significantly.

Griffiths and Peltier (2008, 2009) use the ICE-5G v 1.3 palaeotopography reconstruction (based on the 2min ETOPO2 present-day bathymetry) interpolated to a grid spacing that ranges from 50km at the equator to 5km near the poles. In contrast, here the model is run with a bathymetry with a horizontal resolution of 12 km by 13.5 km at the equator, to 2 km by 13.5 km horizontal resolution in the centre of the Arctic Basin. The change in topography between present day and the past time slice is superimposed onto a present day bathymetry at 1/8° resolution, to retain present day topographical features.

Our results are consistent with the damped harmonic oscillator hypothesis presented by *Egbert et al.* (2004), and further explored by *Green* (2010). The removal of shelf seas during the LGM due to the 130 m sea-level drop reduces the damping and pushes the ocean closer to resonance. This effect is especially prominent in the North Atlantic. It can be seen that notable reductions in deep dissipation occur synchronously with flooding of shelf seas (e.g., at around 14 kyr BP when parts of both the Patagonian and the

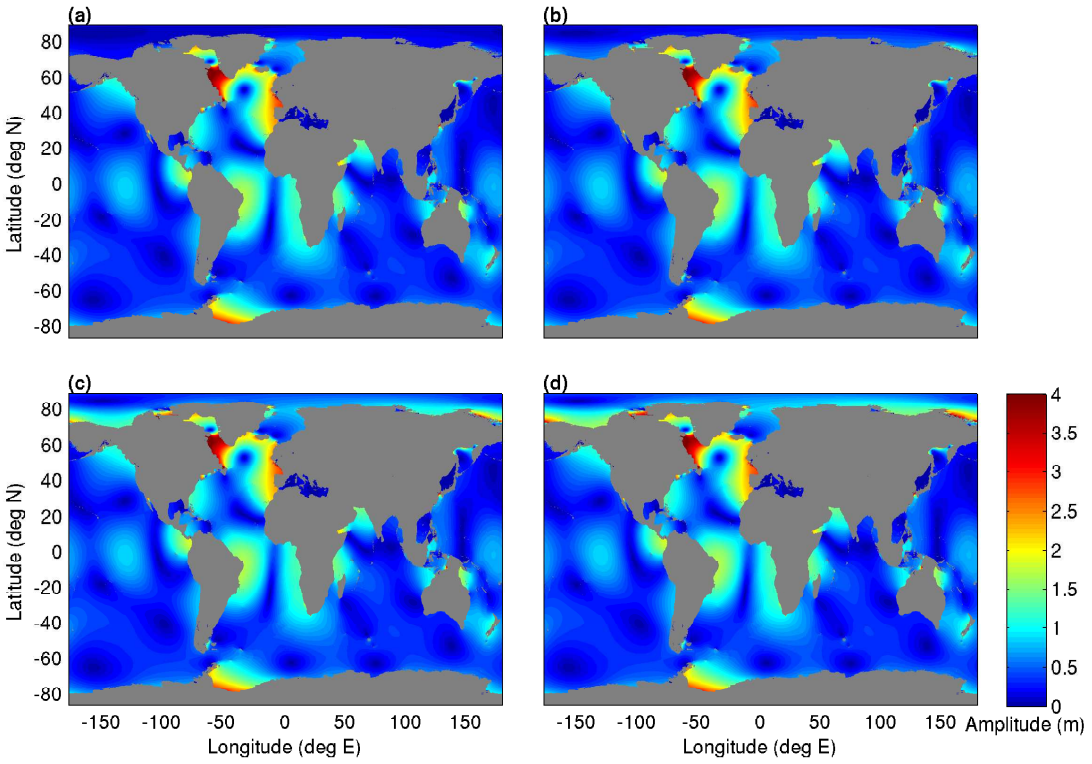

Figure 4.15: LGM M_2 amplitudes with Arctic open boundary boundary conditions from TPXO7.2 enhanced by a factor of (a) 2, (b) 4, (c) 8, and (d) 10.

European Shelf flood, or between 9 and 8 kyr BP when Hudson Bay and Strait flood), suggesting that the Atlantic is moved away from resonance. This result agrees with work by *Arbic et al.* (2009) who show that blocking each of these three shelves in a present day bathymetry acts to increase North Atlantic and, especially, Labrador Sea tides. We also show that altering the grounding line of the ice sheets in Antarctica not only has an effect on the regional tides (*Griffiths and Peltier*, 2009), but that significant changes in the global tides occur. A grounding line shift can also lead to notable changes in global dissipation. Our simulations therefore highlight the importance of improving the reconstructions for ice sheet extent and dynamics during the LGM and deglaciation. This is especially of interest, as it has been hypothesised that the large tides in the Labrador Sea may have influenced the breakup of the Laurentide Ice Sheet during the deglaciation, and may have been one of the mechanisms of rapid ice sheet discharge of the Heinrich events during the last glacial (e.g. *Arbic et al.*, 2004, 2008; *Griffiths and Peltier*, 2008, 2009). Similarly, we suggest that the large tides found in the Weddell Sea during the LGM, for the scenarios with floating ice, could have aided in breaking up and retreating the ice from the continental shelf. This hypothesis was also put forward by *Griffiths and*

Peltier (2009) who suggest that the Antarctic Ice Sheet may have experienced similar instability events as the Northern Hemisphere ice sheets. Recent work from cores around Antarctica (*Weber et al.*, 2011) indicates that the retreat of the Antarctic Ice Sheet from the shelf may have begun as early as 19.3 kyr BP in the south-eastern Weddell Sea. This is an area which corresponds to the locations in which our simulations suggest large tidal amplitudes during this period.

With this work the knowledge about the K_1 tidal dynamics between the LGM and the present has been extended. The LGM and the present were the only time slices that had been explored previously (e.g. *Griffiths and Peltier*, 2008, 2009; *Green*, 2010). In contrast to the semi-diurnal tides, the K_1 constituent experiences much less change between the LGM and present and between the individual time steps. Changes do not take place on a global scale but are confined to the regions in which K_1 tides are important at present, i.e., the North Pacific and especially the SoO, the SCS and the seas around Indonesia. Similar results were also reported by *Uehara* (2005) and *Griffiths and Peltier* (2009). Therefore, none of the dramatic shifts in dissipation that can be seen for M_2 appear for K_1. Nevertheless, considerable alterations in the tidal dynamics in these small basins can be seen. Some of these changes can be explained by shelf-blocking experiments (*Skiba et al.*, 2013). For example, blocking of the Sahul shelf enhances the tidal amplitudes in the SCS and the BS. Between 14 and 12 kyr BP, when the Sahul shelf begins to flood, it can be seen in our simulations that amplitudes in the Banda Sea strongly decrease. A very similar effect which is also explored by *Skiba et al.* (2013) is evident between 15 and 14 kyr BP when the Gulf of Tonkin begins to flood, and amplitudes in the South China Sea strongly decrease.

It has recently been suggested that the present tidal conversion parameterization may not be the best for this type of tidal model and that the one presented by *Nycander* (2005) gives the highest accuracy of the tidal simulation (*Green and Nycander*, 2013). There are, however, two issues with *Nycander* (2005)'s scheme. First, it requires a 3D stratification field for the entire ocean. For the present this is straightforward, and one could possibly use results from a palaeomodel for the LGM field, but we still lack relevant data for the other time slices between the LGM and PD. Furthermore, *Egbert et al.* (2004) showed that increasing the global conversion coefficient with factors between 0.5 and 4 had relatively small effects on the global dissipation rates during the LGM. This is to some extent supported by *Green and Huber* (2013), who show that during the early

Eocene (50 Ma), the abyssal M_2 dissipation rates were twice as large as at present, even though the vertical stratification was 3–4 times stronger than today. One could of course argue that we could use Nycander's scheme but with a slightly modified PD stratification all the way through. However, the second problem with using Nycander's parameterisation is that of resolution. The conversion coefficient C_{IT} in Eq. (3.5) must be computed with at least $1/30°$ resolution for Nycander's parameterisation to be accurate, which is far too detailed for the palaeo-slices. Consequently, we have to rely on other parameterisations at the moment. To obtain a likely range of the LGM dissipation rates and highlight the insensitivity, we repeated the sensitivity analysis by *Egbert et al.* (2004) and multiplied the conversion coefficient by a factor 0.5 or 2. There is an associated change in the abyssal dissipation – in both our results and those by *Egbert et al.* (2004) – but only with some 10–15% either way (see the diamonds and squares in Fig. 4.8 (b) and (c)). The changes in global average amplitudes lie in the order of 20% either way. This is because of the coupling in the model: when the IT drag is reduced, the velocity field may increase which leads to an increased dissipation and decreased amplitudes (and vice versa for an increased drag). These results show that the abyssal tidal dissipation rates are relatively insensitive to changes in hydrography. The modified IT drag runs presented give a quite probable range of palaeo-dissipation rates and amplitudes in the ocean.

The results from the climate model simulations are very different from the ones *Montenegro et al.* (2007) obtained using the same climate model but a tidal model with a much lower resolution. Their tide model indicates only small changes in LGM $\mathbf{F}_{IT}$, and they find that, subsequently, the LGM AMOC remains reduced, even when LGM tidal mixing is applied. In contrast, our tidal model and other higher resolution LGM tide studies (*Egbert et al.*, 2004; *Griffiths and Peltier*, 2009; *Green*, 2010; *Wilmes and Green*, 2014) indicate large changes in tidal dissipation between the present and the LGM.

A similar study carried out by *Peltier and Vettoretti* (2014), claiming to have identified the cause of Dansgaard-Oeschger Oscillations, investigates the LGM overturing circulation under different tidal mixing implementations. They however use vertical diffusivities that are of similar magnitude as PD values. The LGM k_v values in this study, however, are increased in comparison to the PD values by a factor of three. Using the low diffusivity values previous studies obtain, the LGM_{PDmix} simulation has an overturning circulation which is reduced in strength against the PD values.

The climate model used for this study has a coarse resolution and does not allow for feedbacks between atmosphere and ocean. These could play a role in modifying the glacial overturning circulation. Also, these simulations are not able to reproduce high abyssal salinities found by *Adkins et al.* (2002) which could point towards a stronger stratification in the glacial ocean. The impact of a changing stratification,N, is not straightforward to assess due to the opposite effects of N on dissipation and vertical diffusivities. However, further iterations with the tidal model in which the stratification from the LGM simulation is used to re-run the climate model shows only very minor changes in stratification, k_v, and the overturning circulation.

A variety of past studies have concluded that the MOC during the LGM was more sluggish with radiocarbon and other tracers pointing towards higher reservoir ages of the waters occupying the North Atlantic (e.g. *Lych-Stieglitz et al.*, 1999). However, a number of more recent publications have questioned the robustness of the proxies used (*Wunsch*, 2003; *Ritz et al.*, 2013; *Böhm et al.*, 2015). They infer from ^{231}Pa/^{230}Th ratios that the strength of the LGM MOC may have been only slighly decreased or even indistinguishable from that at present (*McManus et al.*, 2004; *Lippold et al.*, 2005; *Ritz et al.*, 2013). It has been hypothesised that a marked weakening of the MOC only occurred during so-called Heinrich events and at the termination of the last glacial (*McManus et al.*, 2004; *Ritz et al.*, 2013; *Böhm et al.*, 2015).

This study (*Schmittner et al.*, 2015) indicates that changes in tidal mixing are an important factor to be considered for the investigations of past and/or future climates and that the increases in the conversion of energy from the barotropic to the baroclinic tide may have played an important role in maintaining a vigorous MOC during the last glacial.

4.5 Conclusions

This work has investigated the impacts of the large-scale sea-level during the LGM on global tidal dynamics. Results from previous studies are reproduced which indicate that M_2 tidal amplitudes in the glacial North Atlantic may have exceeded amplitudes of 6 m and that tidal dissipation was strongly enhanced during the LGM. However, our work shows that the both amplitudes and dissipation in the North Atlantic are highly sensitive to the extent of the grounding lines of the ice sheets draining Antarctica. The changes in tidal dissipation during the LGM may have had a profound effect on

the large-scale overturing circulation during the last glacial counteracting the buoyancy forcing commonly believed to have lead to a more sluggish circulation during the last glacial. The results presented here suggest that the increased energy supply to the internal tide may have lead to a circulation that did not differ significantly in strength to today's circulation. Furthermore, our work shows that large adjustments in the M_2 tidal dynamics occurred over the deglacial period into the early Holocene but that tidal amplitudes remained fairly constant during the middle and late Holocene. In contrast to M_2, K_1 amplitudes and dissipation are hardly affected by the large sea-level adjustments occurring over the last 21,000 years.

Chapter 5

Global tidal trends over the 20^{th} and 21^{st} century

5.1 Introduction

The global mean sea-level trends have recently been quantified at 3.0 mm yr^{-1} since 1990 (*Church and White*, 2011; *Ray and Douglas*, 2011; *Church et al.*, 2013; *Hay et al.*, 2015) and at 1.7 mm yr^{-1} for the second half of the 20^{th} century (e.g., *Church and White*, 2011; *Ray and Douglas*, 2011; *Hay et al.*, 2015; *Church et al.*, 2013). It has been shown that these sea-level trends are spatially heterogenous and in some locations can vary by an order of magnitude from the mean trends and have the opposite sign (see e.g. *Church et al.*, 2013). Studies analysing both global (*Woodworth*, 2010; *Müller et al.*, 2011) and regional tide gauge data (*Ray*, 2006, 2009; *Jay*, 2009; *Müller*, 2011; *Devlin et al.*, 2014; *Zaron and Jay*, 2014) have found large-scale changes in tidal amplitudes for both diurnal and semi-diurnal tides, together with secular changes in tidal ranges, high and low and extreme water levels (*Flick et al.*, 2003; *Haigh et al.*, 2014; *Mawdsley et al.*, 2014, 2015) over the latter half of the 20^{th} and the beginning of the 21^{st} century. In some areas the tidal changes are of the same order of magnitude as the concurrent sea-level changes (e.g., *Müller et al.*, 2011).

To date, the cause of the large-scale tidal amplitude changes has remained unclear. For some locations it has been shown that changes in the local environmental settings, e.g., natural or man-made coastline changes or changing river discharge rates, can lead to readjusting local tidal dynamics (e.g., *Jay and Flinchem*, 1997; *Pelling et al.*, 2013b). For other locations, e.g. Hawaii, a link between changes in the baroclinic tide and the observed amplitude changes has been established (*Colosi and Munk*, 2006) or tidal changes have been attributed to resonant triad interactions (*Lamb*, 2007; *Devlin et al.*, 2014). A number of studies have hypothesised a link between mean sea-level changes and the observed tidal amplitude changes (*Müller et al.*, 2011; *Devlin et al.*, 2014), yet a clear link remains to be established. Previous studies on the impacts of large-scale mean sea-level changes have mainly focussed on much more extreme sea-level changes, for example, those between the Last Glacial Maximum and the present (e.g., *Arbic et al.*, 2004; *Uehara et al.*, 2006; *Arbic et al.*, 2008; *Griffiths and Peltier*, 2008, 2009; *Green*, 2010; *Wilmes and Green*, 2014). Others have examined regional tidal impacts of sea-level rise (e.g., *Ward et al.*, 2012; *Pickering et al.*, 2012; *Pelling et al.*, 2013a; *Luz Clara et al.*, 2015). *Müller et al.* (2011) model the observed tidal amplitude changes in response to glacio-isostatic adjustments and to sea-level increases. However they find that, in general, there is poor agreement between their model results and the observations. The best agreement

is found for the runs where observed spatially non-uniform sea-level trends are used as the forcing.

The aim of this chapter is to re-examine the link between the long-term amplitude trends measured by the tide gauges and the secular mean sea-level trends across the globe. Here a dataset that is both spatially and temporally more extensive than *Müller et al.* (2011) is used and an attempt to replicate the amplitude trends using the global tidal model OTIS is made. The first objective is to present a global distribution of amplitude and sea-level trends shown by the tide gauges and to compare the latter to spacial sea-level trends, which are deduced from satellite altimetry using the Colorado University Sea Level dataset (CU-SL; *Nerem et al.*, 2010). Secondly, in order to reproduce the observed tidal amplitude trends, OTIS is forced with both spatially uniform and non-uniform sea-level trends. The correspondence of the modelled and the observed tidal amplitude trends is evaluated and comments on the importance of spatially non-uniform sea-level trend fields are made. Thirdly, we postulate on the reasons why, in certain areas, our skills at reproducing the tidal changes are good, whereas in others regions we are unable to model the observed changes.

5.2 Methodology

5.2.1 Tide-gauge data

The analysed tide gauge data comes from *Mawdsley et al.* (2015) who analysed a subset of 220 tide gauges from the Global Extreme Sea Level Analysis (GESLA) dataset. The data has been quality controlled, with spikes removed, and datum changes accounted for. The dataset was split into mean sea-level (MSL), tidal components and a non-tidal residual. MSL was calculated by taking 30-day running means from the original sea-level data. Here, yearly averages of the hourly mean sea-level data are used. Yearly tidal amplitudes for 67 constituents from the timeseries without MSL were calculated, using the harmonic analysis software T_Tide (*Pawlowicz et al.*, 2002). This study uses the yearly amplitudes of the principle semi-diurnal and diurnal tidal constituents M_2 and K_1.

Here, a subset of 142 tide gauges from this dataset is selected which matches following criteria: at least 75% of the yearly amplitude data is existent, amplitude data is present after 2000 AD in order to generate an overlap with satellite data and at least 25 years

of data is present for each station. Tables 5.1 to 5.3 in the chapter appendix list the stations together with their location and the time period the records span.
In order to test the previously detailed analysis methods the amplitude and sea-level analysis was repeated for a small subset of tide gauges obtained from the UHSLC data set using the software package Tidal Analysis Software Kit (TASK) (*Bell et al.*, 1999). Using raw sea-level data sets and the different analysis method nearly identical mean amplitudes, and sea-level and amplitude trends were calculated. For the subset of tide-gauges also discussed by *Müller et al.* (2011) our trends closely correspond to the values found in their study.

5.2.2 Trend calculation

Sea-level and amplitude trends were calculated from the yearly MSL and amplitude data by linear regression under consideration of influences of a lag-1 year serial autocorrelation (see also *Müller* (2011) or *Mawdsley et al.* (2015)). Following *Yue et al.* (2002) the trends were calculated by

1. estimating the linear trend of original timeseries,
2. removing the linear trend from the dataset,
3. removing the lag-1 year autocorrelation from the detrended timeseries (in order to obtain the lag-1 year autocorrelation, a linear regression between the detrended time series and the time series shifted by one time step was calculated using the LinearModel.fit function in Matlab),
4. adding the trend calculated in step 1 to the residuals from step 3, and then
5. recalculating the trends.

For the amplitude data the 18.6-year nodal cycle was accounted for by least-squares fitting a harmonic with an 18.6-year period to the detrended dataset and removing it after after step 2 (see *Woodworth* (2010) or *Haigh et al.* (2011) for details on the importance of the nodal cycle). Trends are considered statistically significant when the regression coefficient differs significantly from zero, at a 95 % confidence level.
To make comparisons of the trends easier in the subsequent analysis, the trends were scaled up to reflect both 100 year changes and 1 m global average sea-level increases. Mean amplitudes were calculated from the entire tide-gauge data set.

No correction for glacio-isostatic adjustment (GIA) is applied to the sea-level trends because it is likely that the local tide trends are influenced by water depth changes from both vertical land movement and eustatic sea-level changes.

5.2.3 Tidal model and simulations

The tidal simulations were carried out with OTIS in the same setup as detailed in Chapter 3.2 and in *Wilmes and Green* (2014). For this study six SAL iterations were carried out because the sea-level changes with which the model is forced are small and changes in self attraction and loading are likely to be an important factor in the amplitude responses (*Müller et al.*, 2011). Sea-level changes were implemented into the model by adding (subtracting) the appropriate sea-level changes from the present-day bathymetry (see Chapter 3.2.6). The following simulations were carried out:

1. globally uniform sea-level increases of 1 m and 2 m;
2. globally uniform sea-level decreases of 1 m and 2 m;
3. simulations with spatially varying sea-level trends from the Colorado University sea-level (CU-SL) dataset (*Nerem et al.*, 2010).

Sea-level increases of 1 m and 2 m were chosen for this study for several reasons. Firstly, predicted sea-level changes over the next century are likely to lie within this range (*Church et al.*, 2013). Secondly, a large enough sea-level forcing is necessary to simulate a tidal signal that lies outside the model error. Additionally, the sea-level decrease simulations provide informations on whether tidal changes are primarily driven by regional or supra-regional changes.

The CU-SL dataset (see `http://sealevel.colorado.edu/content/map-sea-level-trends` to obtain the data) assembles sea-level data from the JASON-1 and 2, and the TOPEX/Poseidon satellite altimetry missions. It covers the period 1993 – 2015 AD. The altimetry data is analysed with an improved sea state bias correction, advanced inter-satellite calibration techniques and improved altimeter drift corrections. The dataset used here is not corrected for sea-level trends due to GIA-driven basin shape changes (*Nerem et al.*, 2010). Instead of scaling the trends to reflect a sea-level change over a given time period (e.g., 100 years) they were extrapolated to give globally average sea-level changes of 1 m and 2 m. This makes the non-uniform trend forcing comparable to the uniform forcing.

In areas where no CU-SL data was present, the global average sea-level change was substituted. We note that the tide gauge MSL trends include sea-level changes due to GIA which are not seen by the satellites.

5.3 Assumptions and Limitations

In this study tide-gauge data from the 20^{th} and extending into the 21^{st} century is being compared to tide model results from simulations with 1 m and 2 m sea-level increases. It is necessary to apply a sea-level forcing of this magnitude in order for results to lie outside the model error, and also the predicted sea-level increases over the coming century lie within this range (*Church et al.*, 2013). In comparing the tide-gauge data with the model trends we assume that the amplitude trends are linearly related to the sea-level increases occurring over the 20^{th} and extending into the 21^{st} century, an will remain so with future sea-level increase. A number of studies have questioned this assumption, however, this was generally of more importance when very large sea-level increases (e.g., 10 m) were considered (*Pickering et al.*, 2012). Furthermore the the tide-gauge data is compared to tide model simulations in which sea-level trends from satellite altimetry covering the period 1993-2015 were extrapolated to reflect global mean 1 m and 2 m sea-level increases. This approach assumes that the signals in the spatial variability of the sea-level trends are governed by long-term trends and not by interannual variability. Figure 5.1 shows that there are clearly signals of interannual variability present (ENSO variability can be seen, together with ocean current and eddy variability). However, sea-level signal from satellite altimetry is the best, currently available, long-term record of large-scale sea-level variations. In addition, forcing the model with large-scale varying sea-level increases allows the assessment whether the regional variability in the sea-level is important for the estimation of tidal changes or if tidal changes are mainly driven by the global mean increases.

5.4 Results

5.4.1 Tide gauge data

Sea-level trends

The analysis of the mean sea-level data (Tables 5.1 to 5.3 in the chapter appendix) shows a general increase in sea-level across the stations analysed. Of the 142 tide gauges analysed, 111 stations are experiencing significant changes in sea-level, 98 of which showing increasing sea-levels and 13 displaying decreases. The average change in sea-level is 17.6 cm per century when all tide gauges are included. This corresponds well to previous estimates given by, e.g., *Church and White* (2011) or the IPCC-AR5 report (*Church et al.*, 2013). A spatial comparison between the sea-level trends from the tide gauges and the CU-SL trends shows good coherence (see Figure 5.1). Both the tide gauges and the satellite altimetry data show significant increases in sea-level along the east coast of the US and on the European Shelf. The exception is the Scandinavian coast, which is influenced by GIA processes. Significant increases in sea-level also occur along the west coast of the Pacific and most of the Australian coastline. The western central Pacific is characterised by increases in sea-level, whereas the eastern central and southern Pacific generally sees small decreases in sea-level which also show up in the tide gauge data but are only significant along the South American coastline. The southern parts of the west coast of the US are experiencing small but significant increases in sea-level whereas in the northern parts sea-level is decreasing. This signal is present both in the tide gauge and in the satellite altimetry data. The satellite trends, however, strongly underestimate the magnitude of the sea-level decreases in this area. The tide gauges show decreases of nearly 10 mm yr^{-1} whereas the maximum drops in the CU-SL data amount to 2 mm yr^{-1}.

Nerem et al. (2010) note that there is a significant correlation between mean sea-level variations and ENSO. This ENSO-characteristic pattern (see, e.g., *Landerer*, 2008) also shows up in the regional CU-SL sea-level trends, with larger in increases in sea-level in the western central Pacific and smaller or negative changes in the central western Pacific.

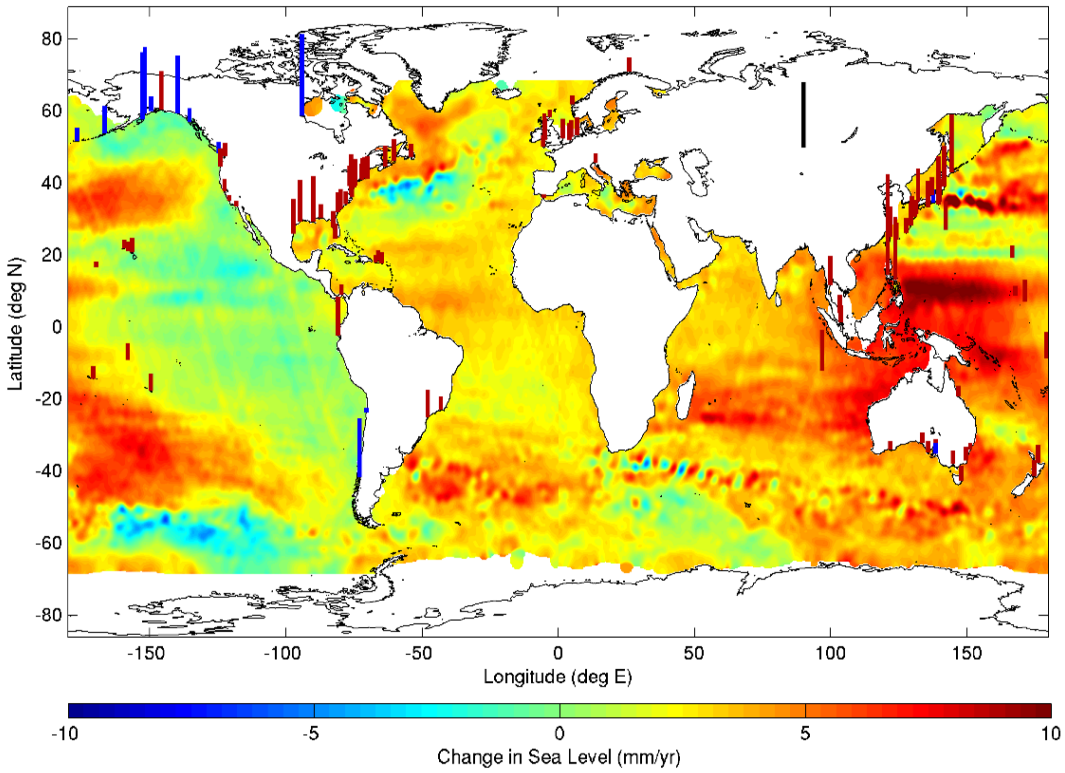

Figure 5.1: CU-SL trends shaded with sea-level trends captured by the tide gauges overlain as bars. The length of the bar displays the magnitude of the sea-level trends and red shading indicates a positive sea-level trend and blue a negative trend. The black reference bar in the centre of the Asian continent shows a trend of 10 mm yr^{-1}. Only stations with significant trends are shown.

Amplitude trends

The amplitude trends are spatially much less homogeneous than the sea-level trends for both M_2 and K_1 (see Figure 5.2). Nearly 70% of the tide gauges show statistically significant changes in M_2 tidal amplitudes with 63 stations displaying significant increases and 35 showing significant decreases in amplitudes. For K_1, in contrast, only 36% of the tide gauges show significant changes in amplitudes over the observational period. At 39 stations K_1 amplitudes are increasing and at 16 stations they are decreasing.

For M_2, the stations in the central eastern Pacific and along the north west coast of the US generally show increasing tidal ranges with the exception of two tide gauges on the central western US coast displaying decreasing amplitudes. The positive signal continues westward through the central Pacific. The stations located around Japan show decreased tidal amplitudes, whereas in the southern Yellow Sea, the Indonesian Seas and along the

north east coast of Australia amplitudes increase. The south east coast of Australia shows significant negative amplitude trends.

On the European Shelf the signal is highly heterogeneous with stations in close proximity displaying opposite trends. The stations in the Irish Sea generally have positive trends, whereas the western North Sea amplitudes show decreases, paired with increases in the eastern parts.

Along the eastern US coast the signals are similarly heterogeneous. In the Gulf of Florida all stations, apart from one, have positive amplitude trends. The increases continue northward of Florida. North of Delaware Bay the tide signals become negative up to New York City, whereas in the Gulf of Maine the tide gauge amplitude trends turn positive. The Bay of Fundy shows decreasing tidal amplitudes.

For K_1, the most prominent large-scale changes in amplitude are seen throughout the Pacific. The stations in the northern part of Japan show decreasing amplitudes whereas in the southern part they are rising. The southern parts of the East China Sea are characterised by increasing amplitudes. The Gulf of Thailand has a strongly negative amplitude trend whereas at Singapore the opposite signal is measured. The tide gauges along south east Australia generally show increasing amplitudes. Brisbane, on the east coast of Australia, has a small negative amplitude signal. Across the Tasman Sea, Wellington NZ shows increasing K_1 amplitudes. The stations in the western central Pacific do not display coherent signals – both increasing and decreasing trends can be observed. In contrast, the western central Pacific is dominated by small, positive amplitude trends. This signal continues along the north west coast of the US where the majority of stations display significant positive trends. Large, positive amplitudes can also be seen in the Gulf of Florida extending northward along the southern west coast of the US. In the north, the signals become smaller and less homogeneous. On the European Shelf, only two stations show significant trends: at Newlyn (UK) where amplitudes are increasing and at Heimsjoe on the Norwegian coast where they are decreasing. In the South Atlantic, Ushuia (Argentina) is the only tide gauge displaying a significant (negative) amplitude trend.

The M_2 the magnitude of the observed trends are generally much larger than for K_1. For the semi-diurnal constituent trends in most locations lie between 1 and 10 cm/century with the average trends lying around 5 cm/century. This makes the M_2 trends around or above 25% of the observed sea level trends assuming an increase of 18 cm over the last

century (see Figure 5.7 in the appendix of this chapter) and around 10% of the mean amplitude at most locations. The largest spatially consistent absolute trends occurring on the European Shelf with a few outliers e.g., in Hudson Bay, at Wilmington, US or Puerto Montt, Chile. For K_1 the absolute changes are much smaller. In most locations the trends do not exceed 5 cm/century or 5% of the corresponding MSL change. As for M_2, these changes correspond to approximately 10% of the mean amplitudes. For M_2, this result suggests that tide trends are of a magnitude where they need to be considered alongside of MSL increase. If the tide changes scaled linearly with MSL changes, the in the case of 1 m sea-level rise this could lead to changes in the order 25 cm in tidal amplitude at a number of different stations. This estimate could further increase when other constituents were included.

5.4.2 Simulations

In the following section we attempt to match the observed amplitude trends with the changes simulated by the tidal model. First, the performance of the tidal model at each of the tide gauge locations is evaluated. Figure 5.3 and Figure 5.6 in the chapter appendix show a comparison of the observed tidal amplitudes at each station with the simulated present-day tidal amplitudes (Figure 5.4 a and b for M_2 and K_1, respectively) and the assimilated TXPO8 global barotropic tidal solution. On average the non-assimilated tidal model OTIS has a root-mean square error (RMSE) of 14.0 cm against the M_2 tidal amplitudes measured by the tide gauges, whereas for TXPO8 the RMSE drops to 6.6 cm. Using statistical means to evaluate the performance of the models results in considerable bias towards tide gauge stations with poor performance. This can be shown by the calculations of the medians which have values of 4.8 cm and 1.8 cm, for OTIS and TPXO8, respectively. The tidal amplitudes simulated with the tidal model OTIS have a median error of 12% and for TPXO8 they lie at 5%. For OTIS, excluding the four tide gauge stations with errors greater than two standard-deviations from the mean leads to a reduction in the mean RMSE by 25%.

For K_1, the RMSEs lie at 7.0 cm for OTIS and at 6.3 cm for TPXO8 tide gauge amplitudes. In contrast to M_2, where the RMSEs are biased by a few outlying points, the distribution is much smoother for K_1, and removing datapoints that lie outside of two or three standard deviations of the mean only marginally changes the mean RMSE. Also, both OTIS and TPXO8 show the largest errors at the same stations which again stands

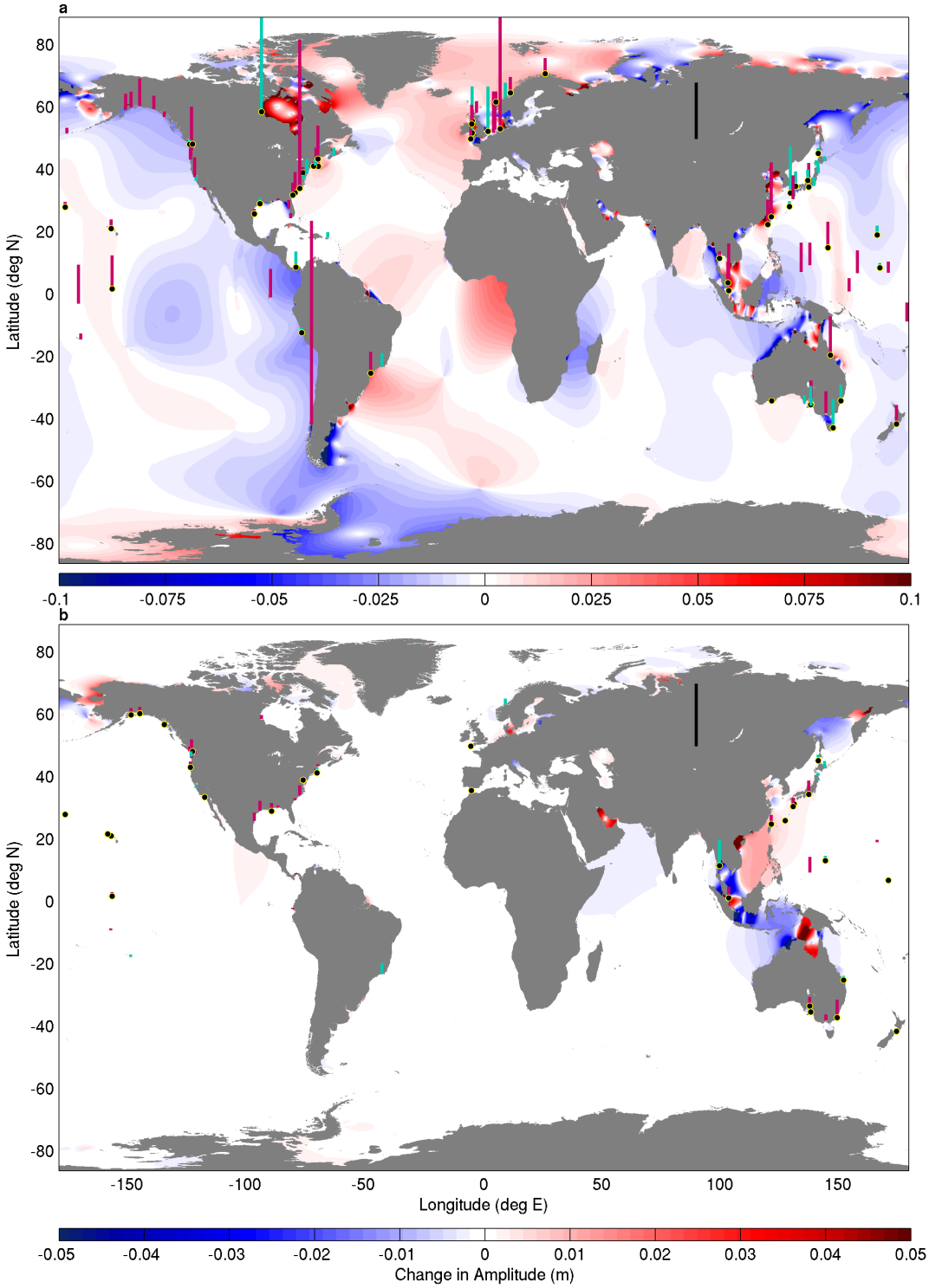

Figure 5.2: Simulated tidal amplitude change in response a non-uniform sea-level change of a global mean of 1 m with observed tidal amplitude trends overlain. The length of the bar displays the magnitude of the amplitude trends and magenta shading indicates a positive amplitude trend and turquoise a negative trend. The black reference bar in the centre of the Asian continent shows a trend of 10 cm/century. Only stations with significant trends are shown. The black and yellow dots indicate the stations at which the sign of the observed amplitude trends corresponds to the sign of the model trends. Panel (a) shows the changes for M_2, panel (b) the changes for K_1.

in contrast to M_2. On average, OTIS and TPXO8 have errors of 36% and 14% of the mean amplitudes, respectively.

Generally, the stations showing larger absolute errors also have larger relative errors, however, in some cases a small absolute error can produce a large relative error when mean amplitudes are large and vice versa. For the stations with a larger percentage error the offset in OTIS is much greater than TPXO8, indicating that the low resolution model is not able to resolve complex tidal dynamics. There is no apparent clustering of poorly performing stations in a certain region.

For the non-uniform sea-level scenario (Figure 5.4 c) amplitudes increase throughout the Atlantic with local exceptions on the Patagonian and European Shelves, and in the Gulf of Florida. The Weddell Sea is dominated by an amplitude decrease whereas changes of the opposite sign take place in the Ross Sea. Amplitudes along the east coast of the Pacific generally decrease with the exception of the southernmost part of the US coast. Amplitudes increase in the Bering Sea and the northern and southern central Pacific. Decreases can be seen in the Sea of Okhotsk continuing southward along the Japanese coastline and into the central Pacific. Amplitudes increase in the Yellow Sea and in the Indonesian seas together with decreases east of Borneo. The amplitude changes around Australia are fairly complex: in the north in the Arafura Sea amplitudes increase, whereas along the north eastern coastline they decrease. Amplitudes increase in the Tasman Sea but decrease to the west of Australia. Around the southwest increases can be seen but amplitudes decrease along the north east coast. Throughout the Indian Ocean and along the margins of Antarctica amplitudes generally increase. The exceptions are the southern tip of India and the east coast of Africa.

For M_2, the amplitude changes from the realistic sea-level forcing are generally similar to those using a uniform forcing. There are small regional differences between the scenarios with the non-uniform and the uniform sea-level forcing (Figure 5.4 f). These are most prominent along the margins of the Pacific. However the discrepancies are mostly restricted to offsets in the magnitude of the amplitude responses but not their sign. In the western Pacific the differences are most likely related to the larger-than-average sea-level changes in this area in the non-uniform sea-level change scenario. Differences in magnitude of the changes can also be seen off the north west American coast, where the amplitude changes in the non-uniform sea-level change scenario are much reduced against the uniform case. In this area, sea-level decrease due to glacial rebound is taking

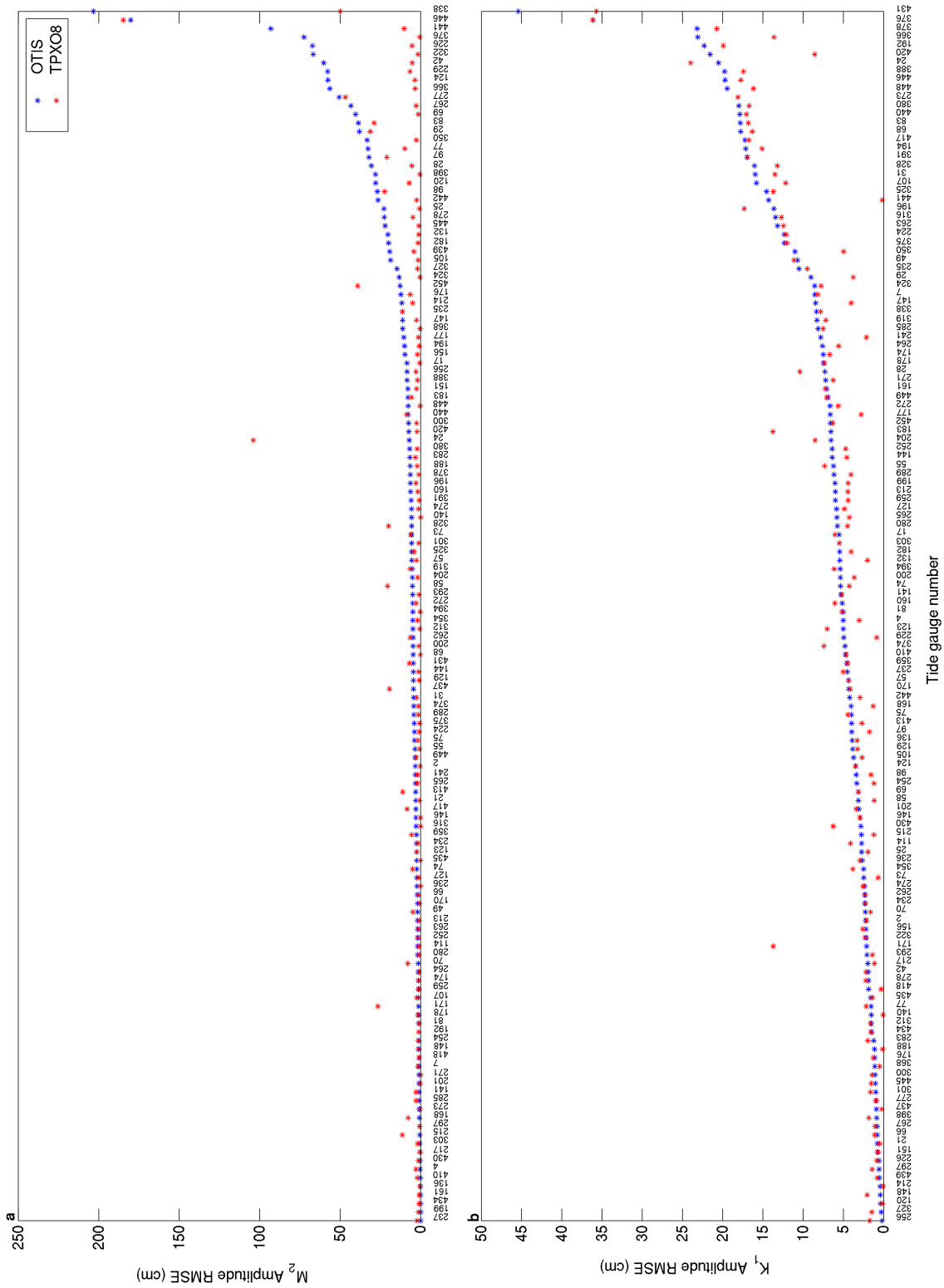

Figure 5.3: Root-mean square error between tidal amplitudes determined from the TG data and amplitudes given by the present-day control simulation and those by the TPXO8 global tidal solution. Panel (a) shows values for M_2, panel (b) values for K_1. Units are cm.

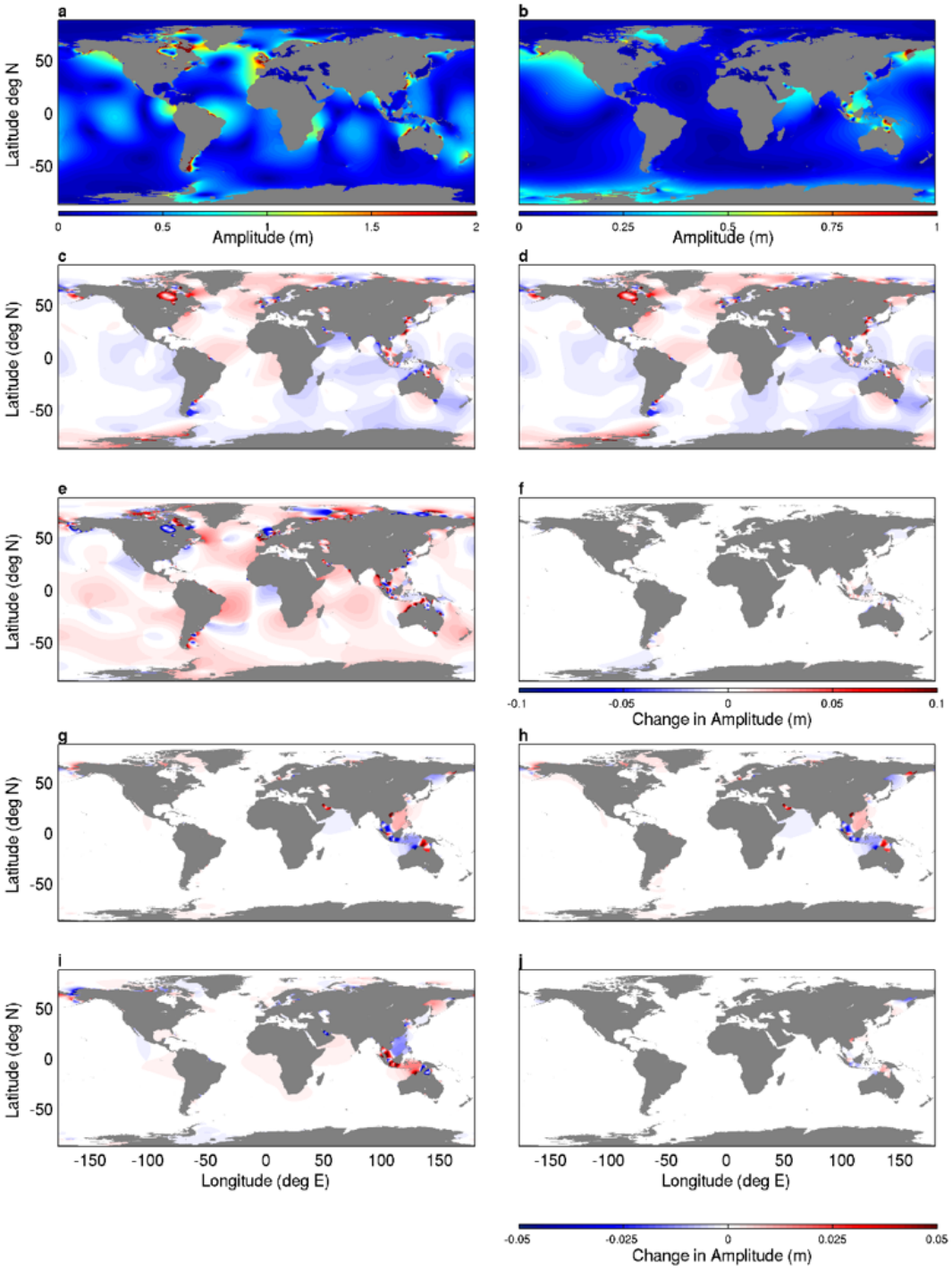

Figure 5.4: Panels a and b show simulated present-day amplitude for M_2 and K_1, respectively. M_2 amplitude changes in response to (c) a uniform 1 m sea-level change, (d) a non-uniform sea-level change with a global average of 1 m, and (e) a globally uniform sea-level decrease of 1 m. Panel (f) shows the difference between (c) and (d). Panels (g) to (j) same as (c) to (f) but for K_1.

place on a large enough scale to possibly affect tidal wave propagation. Elsewhere on the globe, the variations in the sea-level forcing have little impact on the modelled tidal amplitude changes. This is because the spatial variability in the non-uniform sea-level forcing is too small to impact the propagation of the tidal wave. This results in only small differences between the uniform and non-uniform scenarios away from the margins of the Pacific.

For K_1, the model suggests only small changes in tidal amplitudes in response to the sea-level changes and again, both scenarios show very similar amplitude trends (see Figures 5.4 g and h). The largest changes occur along the margins of the western Pacific, with large drops in the western part of the Sea of Okhotsk and increases in eastern part, together with increases in the Bering Sea. In the Indonesian seas amplitudes generally decrease but there are some large localised increases in amplitudes. Amplitudes increase in the South China Sea and Arafura Sea. Around Antarctica and throughout the Atlantic and the adjoining shelf seas the changes are very small. Slight increases in amplitudes can be seen in the Labrador Sea and Nares Strait. For the uniform sea-level increase scenario, the amplitude changes are generally slightly smaller in the Indonesian and China Seas than for the non-uniform scenario. Elsewhere across the globe the differences are very small (see Figure 5.4 l).

For each tide gauge station with a significant amplitude trend, amplitude response functions from the model simulations were determined (see Figures 5.8 – 5.10 for M_2 and Figures 5.11 – 5.12 in the chapter appendix) in order to investigate at which locations the model is able to capture the observed amplitude trends. For locations with negative sea-level trends, the observed amplitude trends were compared to the simulations with global uniform sea-level drops. However in the majority of cases these also matched the trends suggested by the non-uniform sea-level change scenario.

For 67 out of 93 tide gauge stations with a significant trend and where a correspondence could clearly be determined, the sign of the simulated tidal changes match with the simulations. This means that in more than 70% of the cases the model is able to predict the sign of the amplitude change correctly (see Figure 5.1 a). On the European Shelf, at 10 out of 13 stations, the modelled amplitude changes have the same sign as the observed trends. Along the east coast of the US and in the Gulf of Florida 13 of 20 tide gauges show trend signs that correspond to the modelled amplitude signals. The stations at which the observed trends do not match the model are generally located in

areas of complex coastal bathymetric settings, i.e. inlets, estuarine systems or bays. This possibly reflect issues with the relatively coarse resolution model simulating tides in complex topography. Only four tide gauges are present for South America, half of which are in agreement with the model. For Japan and Taiwan, the modelled and observed amplitude trends correspond well, with 14 out of 15 tide gauges having matching trend signs. A good correlation can also be seen in the Indonesian Seas. In the Pacific open ocean 11 of 15 tide gauges show agreement with the model. For this area, stations that do not agree lie close to regions where switches in sign of the amplitude trends are predicted by the model.

The west coast of the US is the only area where the model fails to reproduce the observed tidal amplitude trends. The modelled amplitude changes only agree with the sign at three of the 13 tide gauge stations. The modelled large-scale changes along the west coast of the US have the opposite sign to the observed trends, which are generally positive. A large proportion of the stations along the (north-)west coast of the US show decreasing sea-level trends. Neither the sea-level drop simulations nor the non-uniform simulations can simulate amplitude changes with the correct sign. However, the sea-level drop simulation does predict an increase in open ocean M_2 amplitudes for this area (see Figure 5.4 e). This problem could be arising from a number of issues: the sea-level decreases are much larger, especially along the north west coast of the US than acknowledged in the CU-SL dataset. This is because GIA signals are not included in this data set leading to an incorrect sea-level forcing being used. A further problem is that the sea-level decreases are local but with further-field sea-level increases. This means that the regional amplitude trends are probably a result of both local sea-level changes but also of changes in further-field tidal dynamics. Therefore, this interaction would not be captured by the simulations with globally uniform sea-level decreases. Furthermore, most tide gauge stations lie in complex topographical environments, e.g. inlets, again making it hard to capture the correct dynamics in a low resolution model. Also the shelf in this area is very narrow and may not be resolved correctly, leading to mismatches.

For a number of stations the predicted magnitudes of the amplitude changes match the observed changes very well (see, e.g., stations 29 (Baltimore USA), 57 (Cananeia BRA), 77 (Churchill CAN), 196 (Kuantan MSY), or 200 (Kushiro JPN) in Figures 5.8 – 5.10 in the chapter appendix). Generally, though, the model tends to underestimate the magnitude of the amplitude changes in comparison to the observed trends by $\sim 50\%$ to 75%

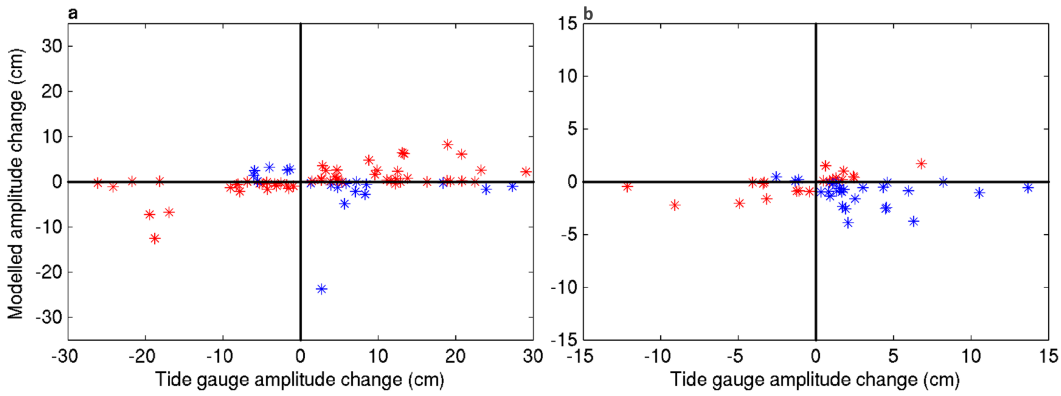

Figure 5.5: Simulated amplitude changes from the 1 m non-uniform sea-level change simulation plotted against the observed amplitude changes scaled to reflect a local sea-level change of 1 m. For locations with negative sea-level changes the amplitude changes from the uniform -1 m sea-level change simulation were taken and plotted against the observed change scaled to reflect a -1 m sea-level change. The dots plotted in red show stations at which the signs of observed and modelled trends correspond, the blue shading indicates locations at which this is not the case. Only stations with significant amplitude trends are shown. Panel (a) shows M_2 amplitude changes, panel (b) K_1 changes.

(see Figure 5.5 a). However, scaling the observed tidal amplitude trend to reflect the response to a 1 m sea-level change may skew the 'observed' values towards the larger magnitudes.

For K_1, in contrast to M_2, the model shows much less skill in reproducing the observed amplitude trends (see Figure 5.1 b). For only 22 of 56 tide gauges the observed amplitude trends correspond to the sign of the modelled changes meaning that the model is able to show the correct trend at less than 40% of the locations. Apart from two stations in the south, the modelled trends do not match the observed trends either in the northern part of Japan or in the southern areas. In the central Pacific five of 10 stations correspond to the the model trend and along the Australian coastline the modelled trends fit the observations at four of five stations. Along the west coast of North and Central America the skill is better, with six of 11 trends corresponding between observations and models. In the Gulf of Florida two of the four stations match the modelled changes. Along the Atlantic coast of the US only two of six stations have the same trends. Two of the three stations on the European coast showing significant trends match the modelled trends.

As for M_2, the model generally underestimates the magnitude of the amplitude changes for K_1 (see Figure 5.5 b).

5.5 Discussion

With this study it has been attempted to reproduce the recent M_2 and K_1 amplitude changes obtained from 142 tide gauge stations using a global tide model. We used both observed sea-level changes from the CU-SL datasets and globally uniform sea-level increases and decreases as the forcing.

For both M_2 and K_1, the signs and magnitudes of the amplitude trends are in close agreement to previously published tidal amplitude trend data (*Jay*, 2009; *Woodworth*, 2010; *Müller et al.*, 2011). Despite using a slightly different subset of tide gauges, which includes more stations than *Müller et al.* (2011) used, but fewer than *Woodworth* (2010), the spatial patterns in the different ocean basins agree very well. Here, in contrast to the previously mentioned studies, only stations where amplitude trends are statistically significant are discussed. This results in fewer stations being included in the analysis but these stations should reflect changes which are different from natural variability.

As in *Müller et al.* (2011) the tide model was forced with using the latest CU-SL trend dataset (2015 version) in order to reproduce the observed amplitude trends. In contrast to *Müller et al.* (2011) who carry out this simulation at $1/2°$ horizontal resolution and perform SAL iterations, here, the tidal model is run at $1/8°$ horizontal resolution and six SAL iterations are carried out for all simulations. In the central and western Pacific, the spatial patterns of change agree largely with *Müller et al.* (2011) (see their Figure 11 f for M_2). However, there are pronounced regional differences, e.g. in the north east Pacific, throughout the Atlantic or the Southern Ocean. These could be due to model resolution, differing SAL implementations, an effect of the different versions of the CU-SL forcing being used, or the contrasting extrapolation methodologies applied. *Müller et al.* (2011) also discuss the differences in amplitude responses throughout the SAL iteration. The changes in self-attraction and loading with small sea-level changes are likely to be of similar magnitude as the tidal amplitude changes themselves, any errors in the SAL estimations leading to quite large offsets. These issues could be contributing to the erroneous signal in the northeast Pacific. Further SAL iterations, which are in progress, could possibly address these issues.

Using non-uniform sea-level forcing results in only very small differences to the uniform forcing. This is probably due to the regional variations in the sea-level forcing which occur on too small a spatial scale to impact the large-scale tidal dynamics. Hence, the changes in tidal dynamics are mainly driven by the global mean sea-level changes.

For M_2, the modelled tidal amplitude changes correspond very well to the sign of the tide gauge amplitude trends with over two thirds of the modelled trends having the same sign as the observations. The exception is the north west coast of the US, where the issues are probably due to the CU-SL sea-level forcing not showing the large sea-level decreases seen in the tide-gauges. If the not-matching tide gauges in this area are excluded from the analysis, the global amplitude trend correspondence rate increases to over 75%. This suggests that for most stations analysed, mean sea-level changes could play an important role in driving the secular semi-diurnal tidal changes. There is also a very good spatial agreement between the Greater Diurnal Tidal Range (GDTR) trends shown by *Mawdsley et al.* (2015) (see their Figure 7 c) and our M_2 amplitude trends. This suggests that firstly, the GDTR trends are driven by changes in the semi-diurnal tide and secondly, the GDTR trends are caused by the same forcing mechanism, which is proposed here to be global mean sea-level changes.

For approximately 10% of the stations the model is also able to represent the magnitude of the changes fairly accurately. At most stations the observed amplitude trends are however underestimated by the model. There is a number of possible reasons for this. First, the amplitude changes could be driven by other processes in addition to the mean sea-level changes. Second, the model is being run at $1/8°$ horizontal resolution and tide gauges are often located along complex coastlines with, e.g., inlets, estuaries or fjords, which cannot be captured by a low resolution model setup. Third, the tide gauge amplitude trends are being scaled up to fit a global mean sea-level increase of 1 m in order to make them comparable to the 1 m sea-level rise simulations which is a considerable extrapolation. This will exacerbate any existing uncertainties or errors in the tide gauge amplitude and sea-level trend estimates. A further possibility would have been to force the model with the observed sea-level trends, which average to a mean change of less than 20 cm. However, using a such small forcing would make it hard to distinguish changes from model errors.

For stations such as Astoria or Wilmington which are located at river mouths it has been suggested that the amplitude trends could reflect local changes in, for example, river discharge rather than large-scale patterns (*Müller*, 2011; *Matte et al.*, 2014).

The near-global CU-SL trend dataset generally corresponds well to the sea-level trends obtained from the tide gauges. It shows very similar spatial variability both in magnitude and sign compared to the data obtained from satellite altimetry. One exception is the

north west coast of the US, where the tide gauges show strongly negative sea-level trends which are not present in the CU-SL data. This is because the satellite data does not include vertical land movement due to GIA processes. This issue could be contributing to the inability of the model to reproduce the observed increases in the M_2 amplitudes in this region. At any given point, a change in tidal amplitudes will be driven by both regional changes in sea-level, i.e. in this area a decrease in sea-level, but also the large-scale changes, i.e. the global increase in sea-level. For this area, the large-scale sea-level change patterns throughout the Pacific show good correspondence with the tide gauge trends but the regional trends do not match. It is likely that this issue cannot be addressed by using global sea-level decrease scenarios because these change the sign of the large-scale forcing. A further possibility could be that ignoring GIA processes could be hampering the results. GIA induces sea-level changes through a number of mechanisms: postglacial and recent ice loss removes loading from the Earth's surface causing vertical land movement through viscous processes in the Earth's interior; ice loss leads to changes in gravitational attraction due to past and recent ice loss, and the changes in mass distribution on the Earth result in rotational changes (*Pugh and Woodworth*, 2014). However, in an additional simulation, forced by both the relative sea level changes from present-day GIA (see *Peltier*, 2004, and `http://www.atmosp.physics.utoronto.ca/ peltier/data.php` for the data) together with the large-scale sea-level changes from CU-SL (not shown), no large changes in the amplitude responses in the northeast Pacific can be seen. This suggests that either our model is not able to resolve the dynamics of the very narrow shelf in this region or that other processes are driving the tidal changes. Recent melting of Alaskan glaciers has lead to a relative sea-level decrease in the north east Pacific due to gravitational and Earth rotational effects (*Bamber et al.*, 2010). These effects are not included either in the CU-SL dataset or in the GIA forcing. Additionally, the addition of fresh water from the Alaskan glaciers into the north east Pacific could lead to stratification changes altering the propagation properties of the tides in this region.

For K_1, in contrast to M_2, the model is not able to reproduce the amplitude changes. This, in part, could be due to a much smaller percentage of stations showing significant changes in amplitudes, resulting in a much lower signal to noise ratio. The model error for K_1 lies at around 3 cm and only few stations amplitude trends exceed values of 2 cm/century. Stations with significant trends are mainly located in the Pacific and along the east coast of the US whereas elsewhere on the globe K_1 amplitude trends are negligi-

ble. However, in comparison to M_2, the amplitude changes are also much smaller, both in absolute magnitude and in percentage terms, and the model error at many locations by far exceeds the observed amplitude changes. Furthermore, a number of areas such as the Indonesian seas, the Persian Gulf, the Sea of Okhotsk, or the Antarctic embayments, which at present have large K_1 tides and thus where prominent changes could be expected to occur have a poor tide gauge coverage. As for M_2, the north west coast of the US shows significant amplitude increases which the model however is not able to simulate. In part, this may be due to the previously discussed issues with sea-level trends in this area. However, for K_1, the trends are also very small in this area leading to greater uncertainties. A further reason why the model is not capturing the trends is that the errors in the open ocean dynamics are too large and thus the responses to the sea-level changes do not reflect the actual changes occurring. Alternatively, the amplitude changes could be driven by different processes such as local or large-scale changes in stratification or ocean circulation patterns, both of which exhibit back effects on the ocean tides. As for M_2, in the locations where the sign of the modelled trend does agree with the sign of the observed amplitude changes, the model strongly underestimates the magnitude of the changes. This suggests that the model is not capturing some of the changes in the dynamics correctly and that there may be other factors influencing the amplitude changes apart from sea-level alterations.

This study highlights the need for a denser tide gauge network with stations located in more remote and in less developed parts of the globe. Our results call for more open-ocean gauges so the tide gauge network can represent a truly global picture of the changes occurring throughout the different ocean basins. This would also enable assessment whether trends at a single tide gauge reflect large-scale patterns or purely local dynamical changes.

Carrying out simulations at higher spatial resolution, e.g. 1/15°, 1/20° or even 1/30° horizontal resolution, may lead to improved accuracy and solve some of the problems with resolving complex coastlines. However, this method would be computationally much more expensive for a global setup, especially if SAL iterations are carried out. A solution to improve computational efficiency could be to carry out high-resolution regional simulations as previously done by e.g. *Ward et al.* (2012), *Pickering et al.* (2012), *Pelling et al.* (2013a) or *Luz Clara et al.* (2015). These would be forced by a lower resolution global simulation providing boundary conditions, so that regional changes are still driven

by a combination of large-scale and local shifts in the tidal dynamics.

For M_2, these results suggest that the global sea-level changes play an important role in driving the observed changes and that M_2 tidal amplitudes display a strong sensitivity to both regional and global sea-level changes. For K_1, in contrast, it was not possible to show a link between the observed sea-level changes and the observed amplitude changes. This indicates that further research is necessary to establish the reasons for the observed changes in the diurnal tidal dynamics. In future, more extensive datasets will show whether the link hypothesised for M_2 holds over time and higher-resolutions simulations may address model issues in topographically complex coastal zones.

Bot the tide-gauge data and the model results indicate that tidal amplitudes are sensitive to sea-level changes. This bears direct consequences for the planning of coastal protection as the tidal amplitude changes in some location amount to a considerable fraction of the the corresponding mean sea-level changes. It has, however, also been shown that the phase of the tide affects the propagation of storm surges (*Horsburgh and Wilson*, 2007). Storm surge modelling for future climates scenarios has generally assumed that tidal dynamics will remain unaltered (e.g., *Lowe and Gregory*, 2005). This work, in contrast suggests that global changes in tidal dynamics could occur with future sea-level increases invalidating this assumption. Furthermore, this work, once again, highlights the importance of considering changes in the tides in future climate scenarios as they represent one of the main drivers of day-to-day sea-level variability.

5.6 Conclusions

Sea-level change is likely to be one of the most destructive aspects of global warming, and the results presented here emphasise that mean sea-level changes could also act as a driver of changes in the tides and hence alter sea-level variability. This work adds to the body of evidence indicating that even relatively moderate sea-level increases can evoke global changes in the tides. The simulations presented here suggest that sea-level changes could at least partially be driving the globally observed 20^{th} and 21^{st} century M_2 amplitude trends, which in many locations exceed 20% of the observed mean sea-level changes occurring over the same time period. For K_1, the amplitude trends are of much smaller magnitude, and the simulations were not able to reproduce the trends, possibly due to the large uncertainty in the trends.

5.7 Data Acknowledgement

We are grateful to Dr. Robert Mawdsley and Dr. Ivan Haigh for providing amplitude and mean sea-level data as published in *Mawdsley et al.* (2015). The original tide gauge data comes from the GESLA dataset which was initiated by Philip Woodworth (NOC Liverpool, UK) and John Hunter (Antarctic Climate & Ecosystems Cooperative Research Centre Australia). Extensions to the dataset were provided by: University of Hawaii Sea Level Center, National Oceanographic and Atmospheric Authority, British Oceanographic Data Centre, Marine Environmental Data Service, Canada; Bureau of Meteorology, Australia; and Norwegian Mapping Authority.

5.8 Appendix

Table 5.1: Tide-gauge stations used for this study. The station numbers refer to the station numbers in the GESLA data set. Start year and End year give the range of the records. M2 Amp and K1 Amp refer to the present-day mean M_2 and K_1 tidal amplitudes at each station as measured by the tide gauges, respectively. Stars mark trends that are significant at the 95% level.

	Station		Lat	Lon	Start Year	End Year	Sea Level Trend (cm/100yr)		M2 Amp (cm)	M2 Trend (cm/100yr)		K1 Amp (cm)	K1 Trend (cm/100 yr)	
2	Abashiri	JPN	44.0	144.3	1968	2008	18.25	*	17.2	-0.30		22.1	-0.12	
4	Aburatsu	JPN	31.6	131.4	1961	2009	20.85	*	52.9	-1.54	*	17.8	0.28	*
7	Adak	USA	51.9	-176.6	1950	2002	-19.39	*	19.4	0.94	*	28.7	0.21	
17	Antofagasta	CHL	-23.7	-70.4	1945	2003	-7.12	*	37.2	-0.06		8.8	-0.11	
21	Argentia	CAN	47.3	-54.0	1971	2007	20.11	*	67.4	-0.92		8.3	-0.88	
24	Astoria	USA	46.2	-123.8	1925	2008	-3.47		93.9	7.83	*	23.6	2.97	*
25	Atlantic City	USA	39.4	-74.4	1911	2004	41.04	*	58.6	0.21		7.5	0.13	
28	Balboa	PAN	9.0	-79.6	1907	2005	16.12	*	183.2	-2.73	*	3.9	0.15	*
29	Baltimore	USA	39.3	-76.6	1902	2012	31.79	*	14.7	0.90	*	5.3	0.20	*
31	Bamfield	CAN	48.8	-125.1	1969	2010	1.66		94.5	0.30		25.1	0.00	
42	Boston	USA	42.4	-71.1	1921	2011	27.68	*	136.9	2.65	*	11.5	0.24	*
49	Bundaberg	AUS	-24.9	152.3	1966	2009	1.75		87.1	1.43		11.7	-0.62	*
55	Callao	PER	-12.1	-77.2	1970	2010	-10.61		23.4	-0.83	*	7.2	-0.09	
57	Cananeia	BRA	-25.0	-47.9	1954	2005	42.52	*	36.6	3.74	*	11.4	-0.38	
58	Cape May	USA	39.0	-75.0	1965	2004	41.92	*	70.8	-2.53	*	8.4	0.06	
66	Ceuta	ESP	35.9	-5.3	1944	2003	5.19	*	30.3	-0.08		2.1	-0.21	*
68	Charleston OR	USA	43.3	-124.3	1978	2010	4.72		81.1	1.96	*	24.6	0.85	*
69	Charleston SC	USA	32.8	-79.9	1921	2010	31.22	*	76.6	3.64	*	7.7	0.28	*
70	Charlotte Amalie	VIR	18.3	-64.9	1978	2005	10.16		4.2	-0.14		6.1	0.17	
73	Chesapeake Bay	USA	37.0	-76.1	1975	2013	60.92	*	37.8	-0.83	*	4.6	0.13	
74	Chichijima	JPN	27.1	142.2	1975	2011	43.91	*	28.4	-0.34		12.1	-0.38	
75	Christmas Island	KIR	2.0	-157.5	1974	2003	-1.48		26.3	5.90	*	3.8	0.63	*
77	Churchill	CAN	58.8	-94.2	1961	2002	-125.77	*	153.0	-23.64	*	3.7	0.59	*
81	Cocos Island	AUS	-12.1	96.9	1985	2010	63.90	*	30.8	0.48		9.0	-0.35	
83	Cordova	USA	60.6	-145.8	1964	2001	58.78	*	144.3	4.88	*	30.4	1.01	*
97	Delfzijl	NDL	53.3	6.9	1970	2005	28.38	*	133.8	21.87	*	9.3	0.48	
98	Den Helder	NDL	53.0	4.7	1970	2005	24.98	*	65.1	5.98	*	10.1	0.60	
105	Duck Pier	USA	36.2	-75.7	1978	2012	47.29	*	47.8	-0.65		5.7	-0.35	
107	Dutch Harbour	USA	53.9	-166.5	1982	2010	-41.59	*	27.1	-0.87		22.8	-0.47	
114	Esperance	AUS	-33.9	121.9	1965	2011	12.85	*	10.5	0.57	*	13.4	0.14	
120	Fishguard	GBR	52.0	-5.0	1963	2006	33.96	*	136.0	-8.21	*	7.9	-0.36	
123	Fort Denison	AUS	-33.9	151.2	1914	2006	9.15	*	51.4	-2.81	*	9.7	0.03	
124	Fort Pulaski	USA	32.0	-80.9	1935	2007	30.16	*	100.8	2.17	*	7.9	0.21	
127	French Frigate Shoal	USA	23.9	-166.3	1974	2002	16.78		9.7	0.72		6.7	0.40	
129	Funafuti	TUV	-8.5	179.2	1977	2007	39.72	*	57.5	3.36	*	5.3	0.24	
132	Galveston Pier	USA	29.3	-94.8	1904	2005	64.60	*	8.7	-0.98	*	11.2	1.56	*
136	Geraldton	AUS	-28.8	114.6	1963	2001	13.46		7.3	-0.06		12.5	0.01	
140	Grand Isle	USA	29.3	-90.0	1980	2013	70.83	*	1.3	-0.01		11.2	1.27	*
141	Apra Harbour	GUM	13.4	144.7	1948	2002	5.92		22.1	-0.46		11.6	-0.72	*
144	Hachinohe	JPN	40.5	141.5	1980	2010	40.63	*	30.7	-1.26	*	17.9	-0.44	*
146	Hakodate	JPN	41.8	140.7	1964	2005	1.55		21.9	-0.69	*	10.3	0.15	
147	Halifax	CAN	44.7	-63.6	1919	2009	31.65	*	63.0	-1.38	*	4.8	0.02	
148	Hamada	JPN	34.9	132.1	1984	2012	51.53	*	8.1	-2.56	*	8.8	0.23	
151	Heimsjoe	NOR	63.4	9.1	1969	2000	0.74		77.9	-2.51	*	5.4	-0.90	*

Table 5.2: Table 5.1 continued.

156	Hoek van Holland	NDL	52.0	4.1	1970	2005	26.86	*	79.2	7.34 *	10.7	0.87
160	Honningsvaag	NOR	71.0	26.0	1970	2002	21.80	*	86.7	2.73 *	3.0	-0.34
161	Honolulu	USA	21.3	-157.9	1905	2011	14.05	*	16.5	1.56 *	8.1	0.11 *
168	Ishigaki	JPN	24.3	124.2	1969	2012	26.37	*	43.9	0.61	17.0	0.22
170	Johnston Island	USA	16.7	-169.5	1947	2000	7.83	*	26.3	0.42	3.4	0.00
171	Johor Baharu	MYS	1.5	103.8	1983	2010	25.68	*	87.2	8.33 *	30.5	1.75 *
174	Kahului	USA	20.9	-156.5	1950	2008	21.82	*	18.4	0.14	9.6	0.01
176	Kanton	KIR	-2.8	-171.7	1972	2001	-0.01		36.8	6.92 *	2.1	0.09
177	Kaohsiung	TWN	22.6	120.3	1980	2012	18.54		17.9	4.31 *	16.1	0.87
178	Kapingamarangi	FSM	1.1	154.8	1978	2002	18.95		16.9	2.33 *	12.4	-1.32
182	Keelung	TWN	25.1	121.7	1980	2005	46.25	*	22.3	9.60 *	15.5	1.40 *
183	Kelang	MYS	3.1	101.4	1983	2009	16.63		137.9	0.46	3.8	1.45
188	Key West	USA	24.6	-81.8	1913	2011	23.17	*	17.5	0.91 *	8.9	0.02
192	Ko Lak	THA	11.8	99.8	1985	2010	44.22	*	6.2	1.16 *	33.8	-4.02 *
194	Kodiak Island	USA	57.7	-152.5	1975	2003	-103.72	*	96.7	1.27	25.9	0.35
196	Kuantan	MYS	4.0	103.4	1983	2010	27.94	*	52.6	3.66 *	36.2	-1.30
199	Kushimoto	JPN	33.5	135.8	1961	2010	40.38	*	45.7	-0.91	16.6	0.07
200	Kushiro	JPN	43.0	144.4	1963	2009	89.68	*	29.1	-0.82 *	19.3	-1.11 *
201	Kwajalein	USA	8.7	167.7	1946	2007	15.31	*	47.1	-0.81 *	6.5	-0.08
204	La Libertad	ECU	-2.2	-80.9	1949	2008	59.10	*	77.6	0.15	2.9	0.19 *
213	Legaspi	PHL	13.2	123.8	1984	2004	97.15	*	52.9	-1.48	11.1	-0.76
214	Lerwick	GBR	60.2	-1.1	1959	2008	5.54		58.0	-0.30	7.9	-0.15
215	Lewes	USA	38.8	-75.1	1957	2010	35.72	*	60.0	-2.12 *	8.2	0.35
217	Lime Tree Bay	VIR	17.7	-64.8	1982	2009	17.94	*	1.4	0.59	6.4	-0.10
224	Los Angeles	USA	33.7	-118.3	1923	2011	8.17	*	51.5	0.39 *	21.8	0.21 *
226	Lowestoft	GBR	52.5	1.8	1964	2012	30.31	*	69.8	-7.93 *	13.8	-0.43
229	Maaloey	NOR	61.9	5.1	1969	2003	13.96	*	57.8	1.80 *	5.0	-0.19
234	Magueyes Island	PRI	18.0	-67.0	1965	2010	12.10	*	0.7	0.23	5.4	0.13
235	Maisaka	JPN	34.7	137.6	1968	2010	-20.27	*	31.4	4.22 *	12.3	2.13 *
236	Majuro	PHL	7.1	171.4	1968	2006	33.23	*	52.1	1.95 *	5.3	-0.37 *
237	Malakal	PLW	7.3	134.5	1969	2007	0.98		51.9	5.21 *	14.7	0.58
241	Manila	PHL	14.6	121.0	1984	2005	155.29	*	19.0	1.39	27.8	3.51
252	Mera	JPN	34.9	139.8	1965	2007	35.63	*	35.7	-1.54 *	18.3	-0.13
254	Midway	USA	28.2	-177.4	1947	2005	5.27		11.8	0.86 *	5.5	0.23 *
256	Millport	GBR	55.7	-4.9	1978	2003	5.12		112.1	2.06 *	9.7	0.46
259	Miyakejima	JPN	34.1	139.5	1964	2010	74.34	*	34.4	0.39	17.5	-0.51
262	Montauk	USA	41.0	-72.0	1959	2005	33.51	*	28.7	-0.58 *	4.9	-0.24
263	Monterey	USA	36.6	-121.9	1973	2012	8.45		49.3	-0.77 *	23.1	-0.27 *
264	Nagasaki	JPN	32.7	129.9	1963	2004	20.91	*	82.7	-8.30 *	20.0	-0.06
265	Naha	JPN	26.2	127.7	1966	2010	22.79	*	57.6	0.20	15.9	0.41 *
267	Nantucket	USA	41.3	-70.1	1965	2010	34.66	*	43.6	1.62 *	8.4	-0.29
271	Nawiliwili	USA	22.0	-159.4	1954	2012	13.18	*	14.9	-0.07	8.4	0.22 *
272	Naze	JPN	28.4	129.5	1957	2004	34.86	*	56.5	-0.88 *	15.3	0.24
273	Neah Bay	USA	48.4	-124.6	1934	2010	-17.65	*	78.4	-0.76 *	30.4	0.79 *
274	New London	ISA	41.4	-72.1	1938	2008	22.68	*	36.0	0.74 *	5.1	-0.25
277	Newlyn	GBR	50.1	-5.5	1915	2008	17.22	*	171.1	1.70 *	5.4	0.19 *
278	Newport	USA	41.5	-71.3	1930	2006	25.41	*	51.0	-1.02 *	4.9	-0.17
280	Nishinoomote	JPN	30.7	131.0	1965	2008	22.84	*	58.5	4.20 *	17.9	1.36 *
283	North Sydney	CAN	46.2	-60.3	1969	2008	33.38	*	36.8	0.69	8.3	0.41
285	Noumea	NCL	-22.3	166.4	1967	2002	1.02		40.6	0.49	6.6	-0.05
289	Ofunato	JPN	39.1	141.7	1965	2010	51.79	*	30.7	-0.92 *	18.7	-0.21 *
293	Pago Pago	ASM	-14.3	-170.7	1948	2007	19.88	*	37.2	1.06 *	2.8	0.11
297	Papeete	PYF	-17.5	-149.6	1975	2008	26.21	*	6.4	-0.34	1.6	-0.35 *
300	Cook Islands	COK	-9.0	-158.1	1977	2007	25.14	*	9.4	-0.91	1.2	0.28 *

Table 5.3: Table 5.1 continued.

301	Pensacola	USA	30.4	-87.2	1923	2008	20.87	*	1.8	0.27	*	12.7	0.27	*
303	Pohnpei	FSM	7.0	158.2	1974	2003	17.91		27.2	4.03	*	9.8	0.31	
312	Port Isabel	USA	26.1	-97.2	1977	2011	53.40	*	6.4	0.78	*	13.2	1.31	*
316	Port San Luis	USA	35.2	-120.8	1948	2002	8.82	*	49.2	0.29		22.4	0.06	
319	Port Adelaide	AUS	-34.9	138.6	1940	2000	21.78	*	49.5	4.13	*	17.1	0.17	
322	Portland	USA	43.7	-70.2	1910	2005	17.89	*	135.6	5.85	*	11.2	0.25	*
324	Port Lincoln	AUS	-34.7	135.9	1965	2003	17.92	*	24.1	-1.45	*	16.9	0.27	
325	Port Lonsdale	AUS	-35.1	138.5	1962	2003	-16.87	*	44.8	-3.28	*	10.4	-0.43	*
327	Port Patrick	GBR	54.8	-5.1	1968	2007	25.17	*	134.0	3.36	*	9.9	-0.28	
328	Port Pirie	AUS	-33.2	138.0	1941	2001	-0.85		49.4	0.13		27.8	1.35	*
338	Puerto Montt	CHL	-41.5	-73.0	1980	2001	-90.08	*	186.9	36.20	*	15.6	1.32	
350	Rio de Janeiro	BRA	-22.9	-43.1	1963	2005	20.67	*	33.2	-2.38	*	11.0	-1.69	*
354	Roervik	NOR	64.9	11.3	1969	2010	-9.47		78.7	2.75	*	4.7	-0.06	
359	Saipan	MNP	15.2	145.7	1978	2003	7.00		19.3	4.55	*	11.4	0.51	
366	San Francisco	USA	37.8	-122.5	1897	2012	18.87	*	56.4	3.45	*	23.1	0.00	
368	San Juan	USA	18.5	-66.1	1977	2009	16.01	*	15.5	-0.89	*	7.5	-0.49	
374	Santa Cruz	ECU	-0.8	-90.3	1978	2008	6.40		64.4	5.01	*	1.6	0.02	
375	Santa Monica	USA	34.0	-118.5	1973	2006	13.31		50.9	0.55		21.9	-0.34	
376	Seattle	USA	47.6	-122.3	1901	2012	20.11	*	107.1	-0.03		46.1	0.42	*
378	Seldovia	USA	59.4	-151.7	1975	2005	-102.87	*	222.7	2.77	*	34.5	0.41	
380	Seward	USA	60.1	-149.4	1967	2004	-22.60	*	119.9	2.76	*	28.9	1.03	*
388	Sitka	USA	57.1	-135.3	1938	2011	-21.18	*	110.6	0.98	*	28.0	0.40	*
391	South Beach	USA	44.6	-124.0	1967	2012	22.84	*	88.7	1.61	*	26.5	0.09	
394	Spring Bay	AUS	-42.6	147.9	1985	2010	23.28	*	29.9	-5.06	*	9.5	-0.36	
398	St Petersburg	USA	27.8	-82.6	1946	2008	25.41	*	16.2	1.44	*	14.7	0.13	
410	Tauranga	NZL	-37.7	176.2	1984	2006	27.93	*	70.4	-1.99		1.3	-0.23	
413	Thevenard	AUS	-32.1	133.7	1966	2013	15.60	*	29.8	0.05		13.9	0.30	
417	Townsville	AUS	-19.3	146.8	1959	2012	16.93	*	73.6	6.86	*	16.4	0.28	
418	Toyama	JPN	36.8	137.2	1967	2011	27.12	*	6.2	-1.86	*	5.4	-0.19	
420	Trieste	ITA	45.7	13.8	1970	2004	15.27	*	26.6	0.34		5.3	-0.19	
430	Victor Harbour Victoria	AUS	-35.6	138.6	1965	2001	8.08		13.2	-1.47	*	13.9	0.29	
431	Harbour	CAN	48.4	-123.4	1909	2010	7.20	*	37.2	0.28	*	37.6	0.45	*
434	Wake Island	USA	19.3	166.6	1950	2005	19.37	*	27.9	-1.61	*	4.9	0.33	*
435	Wakkanai	JPN	45.4	141.7	1967	2012	27.00	*	2.4	-0.90	*	6.5	-0.92	*
437	Wellington	NZL	-41.3	174.8	1944	2007	23.97	*	48.2	3.30	*	3.2	0.36	*
439	Wick	GBR	58.4	-3.1	1965	2006	10.77	*	101.5	2.03	*	11.5	-0.22	
440	Willapa Bay	USA	46.7	-124.0	1972	2009	16.26	*	96.5	-0.98		26.1	-0.80	*
441	Williamstown	AUS	-37.9	144.9	1966	2004	19.80	*	23.1	3.83	*	6.8	0.91	*
442	Wilmington	USA	34.2	-78.0	1935	2010	19.44	*	57.5	26.42	*	5.9	1.59	*
445	Woods Hole	USA	41.5	-70.7	1957	2005	24.45	*	23.0	-0.22		6.4	-0.82	*
446	Wyndham	AUS	-36.9	149.6	1966	2002	20.50	*	230.3	6.44		33.7	2.80	*
448	Yakutat	USA	59.5	-139.7	1961	2007	-88.71	*	112.5	2.38	*	28.3	0.25	
449	Yap	FSM	9.5	138.1	1969	2002	-11.14		39.9	4.01	*	11.9	2.49	*
452	Zanzibar	TZA	-6.2	39.2	1984	2009	-5.48		120.8	-0.94		11.1	0.02	

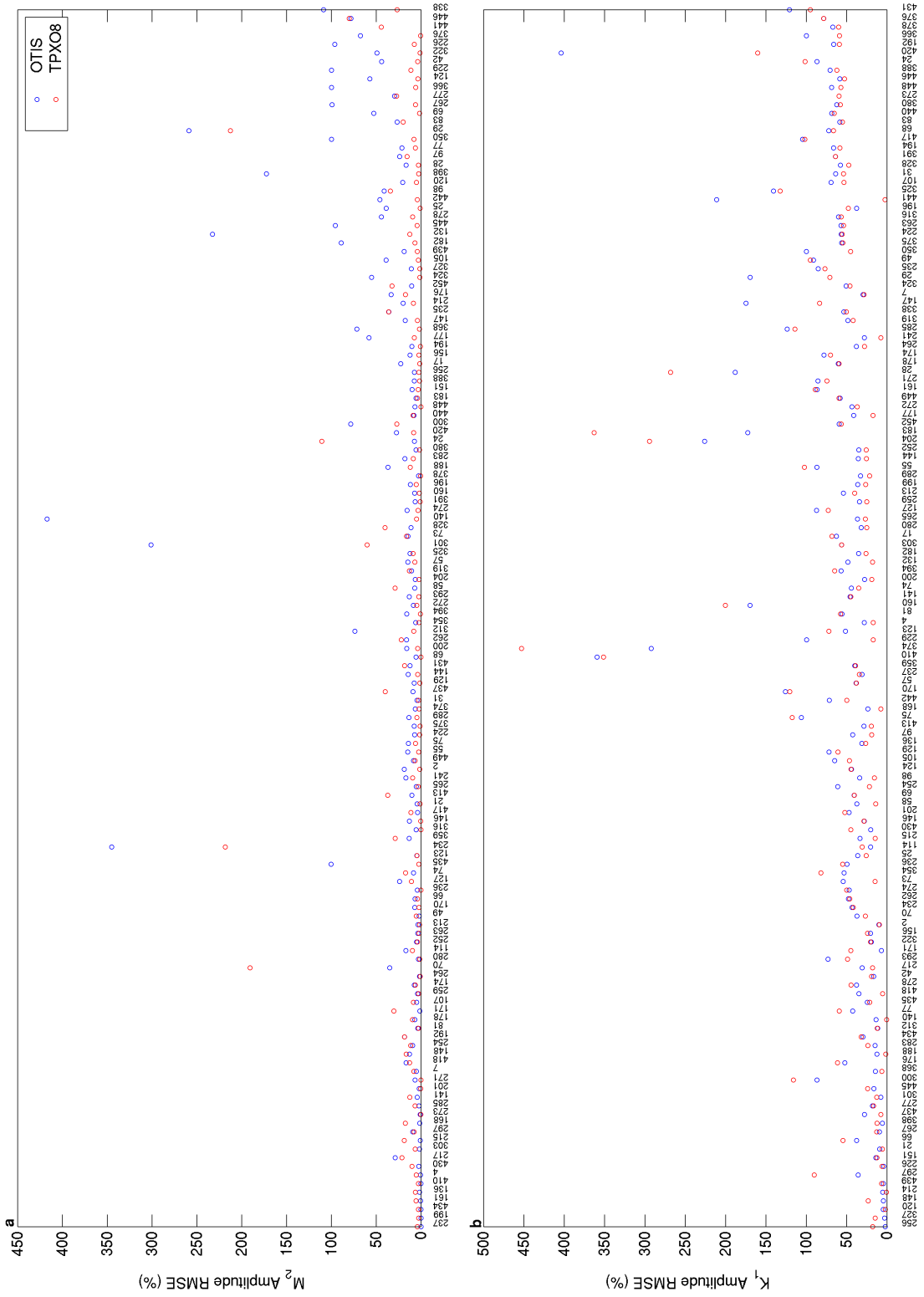

Figure 5.6: Percentage root-mean square error between tidal amplitudes determined from the TG data and amplitudes given by the present-day control simulation and those by the TPXO8 global tidal solution. Panel (a) shows values for M_2, panel (b) values for K_1. Units are %

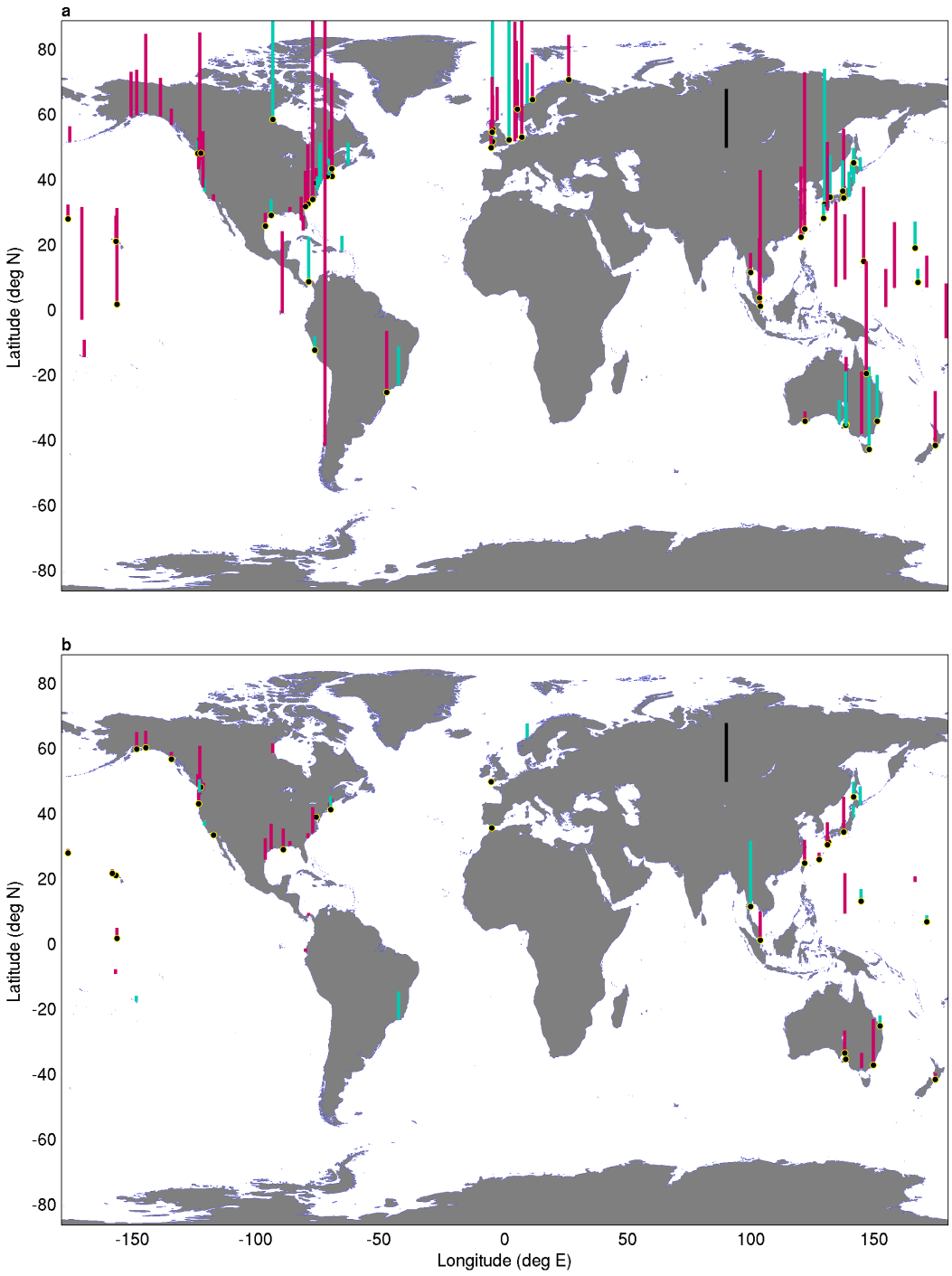

Figure 5.7: Observed tidal amplitude trends shown as percentage of 18 cm SL increase over the 20^{th} century. The length of the bar displays the magnitude of the amplitude trends and magenta shading indicates a positive amplitude trend and turquoise a negative trend. The black reference bar in the centre of the Asian continent shows a trend of 20%/century. Only stations with significant trends are shown. The black and yellow dots indicate the stations at which the sign of the observed amplitude trends corresponds to the sign of the model trends. Panel (a) shows the changes for M_2, panel (b) the changes for K_1.

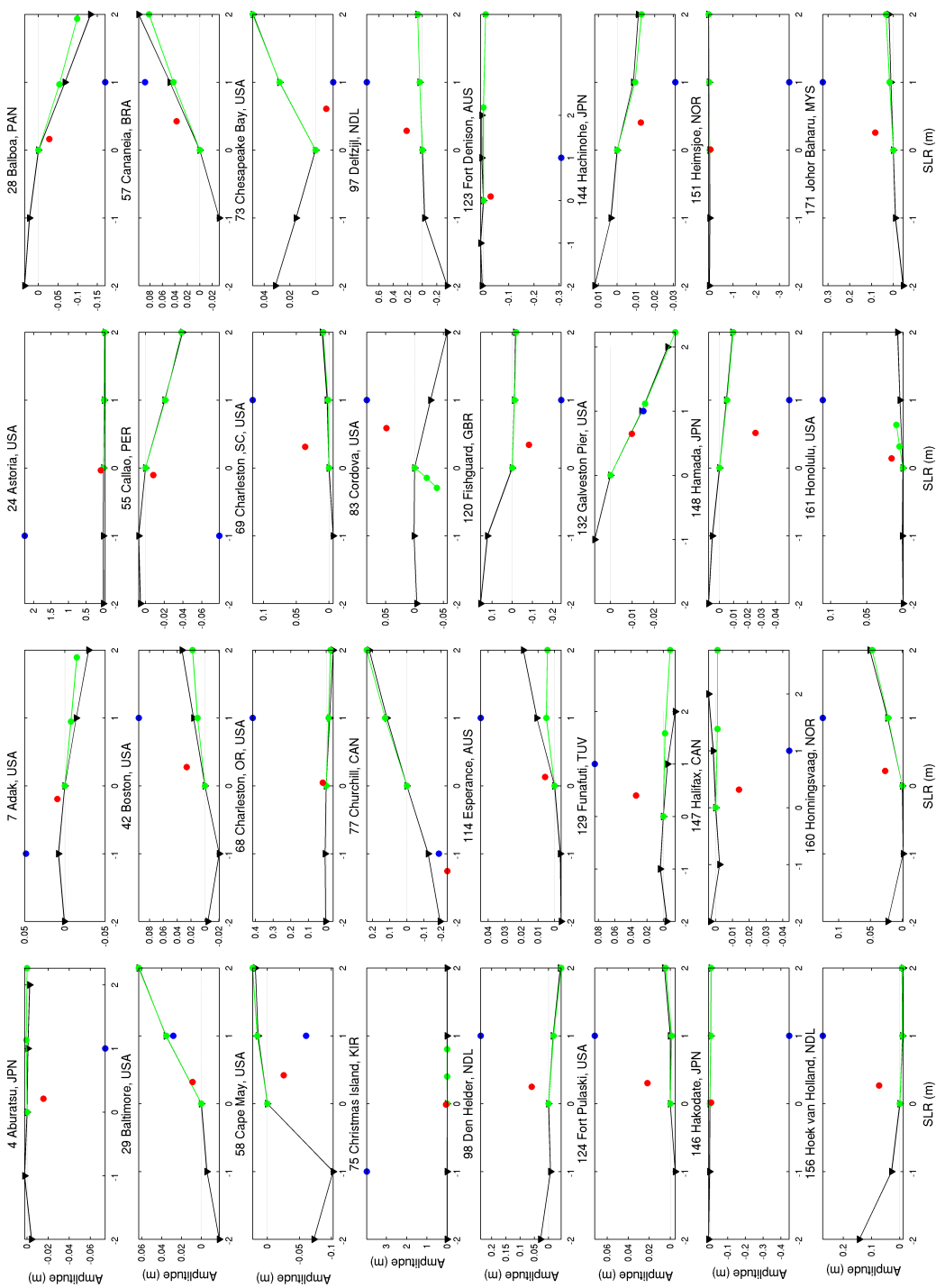

Figure 5.8: M_2 amplitude response functions as simulated by OTIS for TG locations with significant amplitude trends. The black dots show the amplitude changes for globally uniform -2 m, -1 m, 0 m, 1 m, and 2 m sea-level change simulations. The green dots show simulated amplitude responses to the non-uniform sea-level changes of 1 m and 2 m. For the latter simulations the amplitude response is plotted against the actual local sea-level change which can differ from the global mean. The blue dot shows the observed amplitude change per century plotted against sea-level change per century. The red dot shows observed amplitude change scaled to 1 m sea-level change. For locations with negative sea-level change the latter have been scaled again a sea-level change of -1 m.

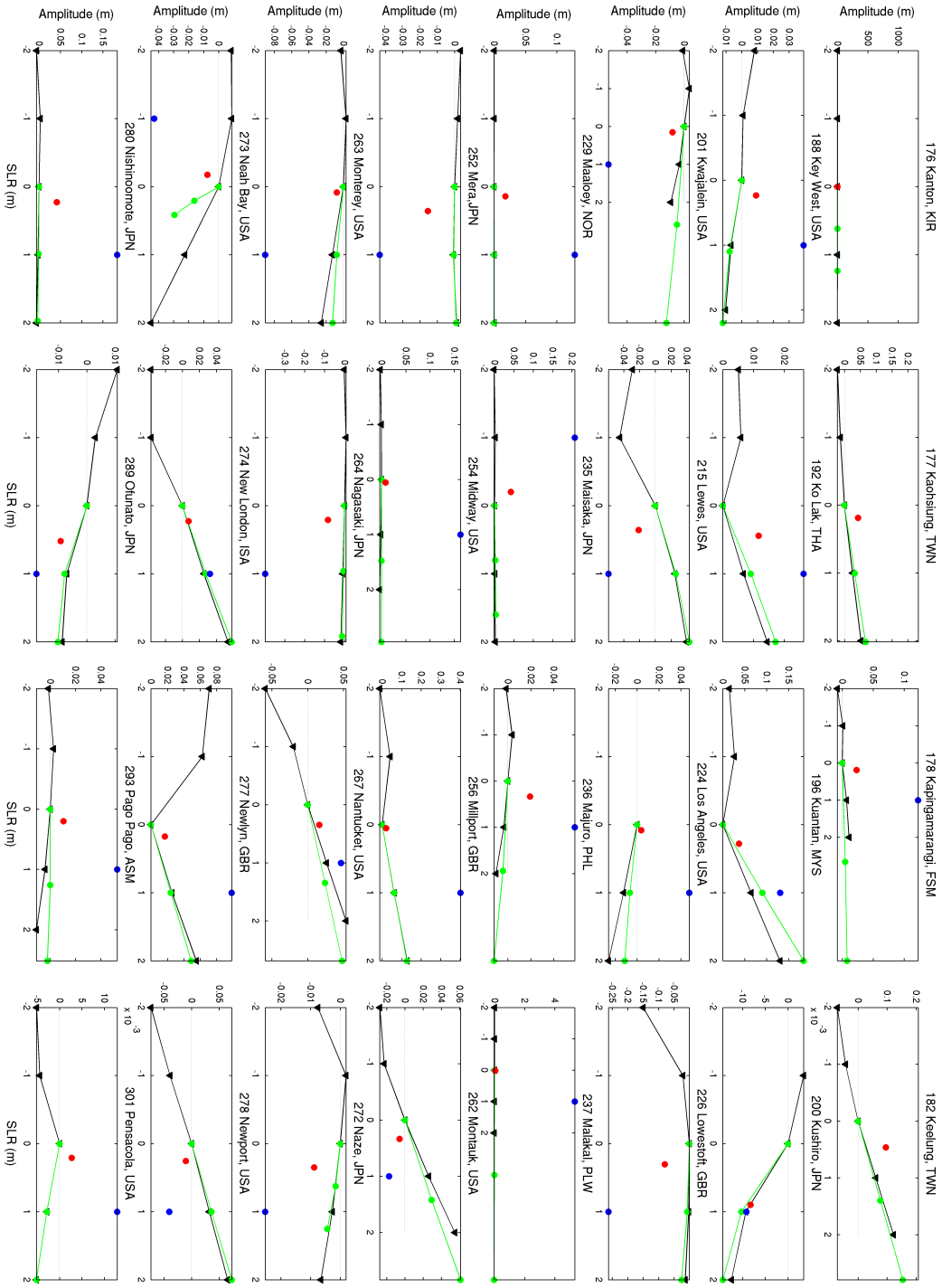

Figure 5.9: Same as Figure 5.8.

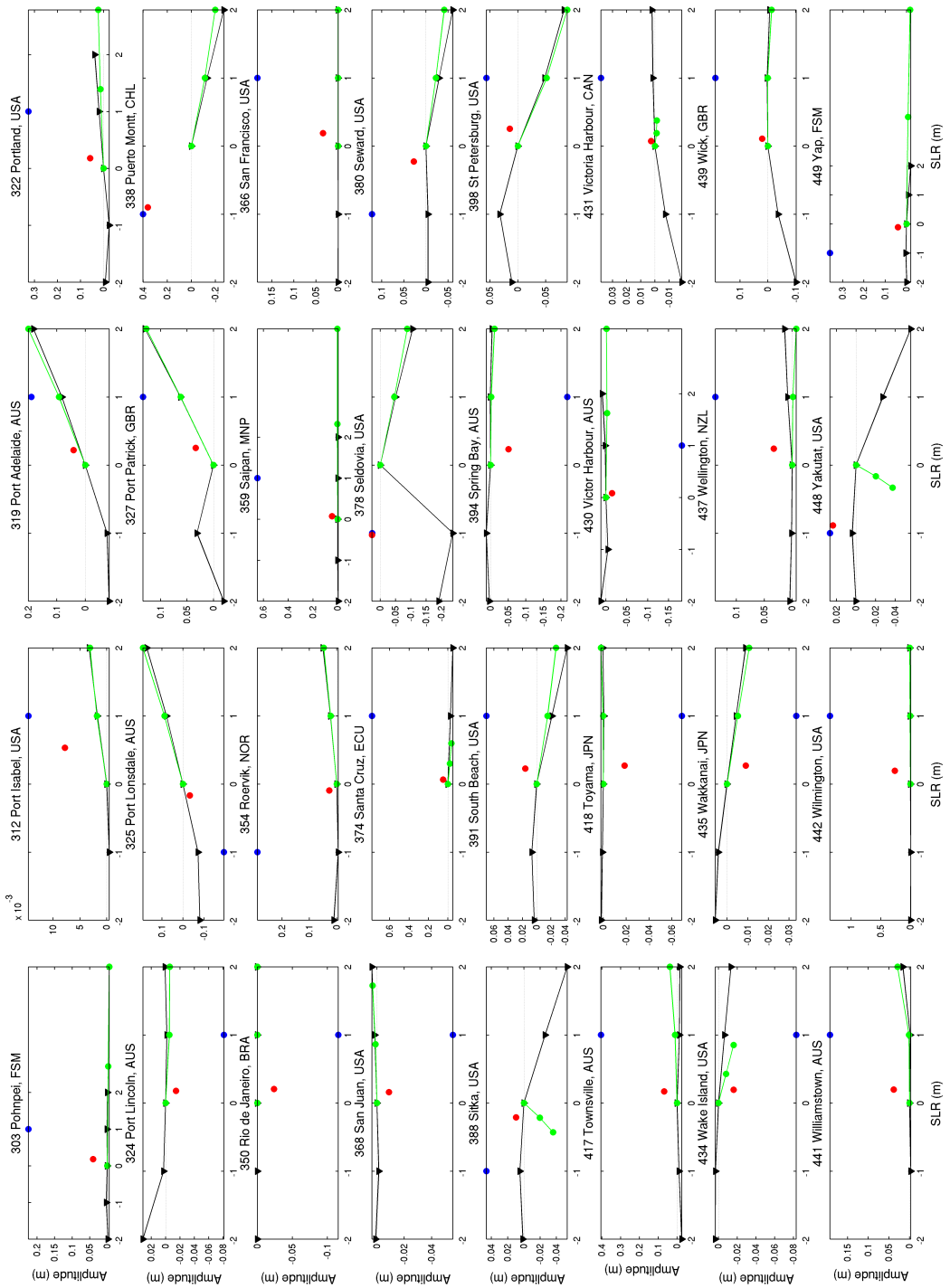

Figure 5.10: Same as Figure 5.8.

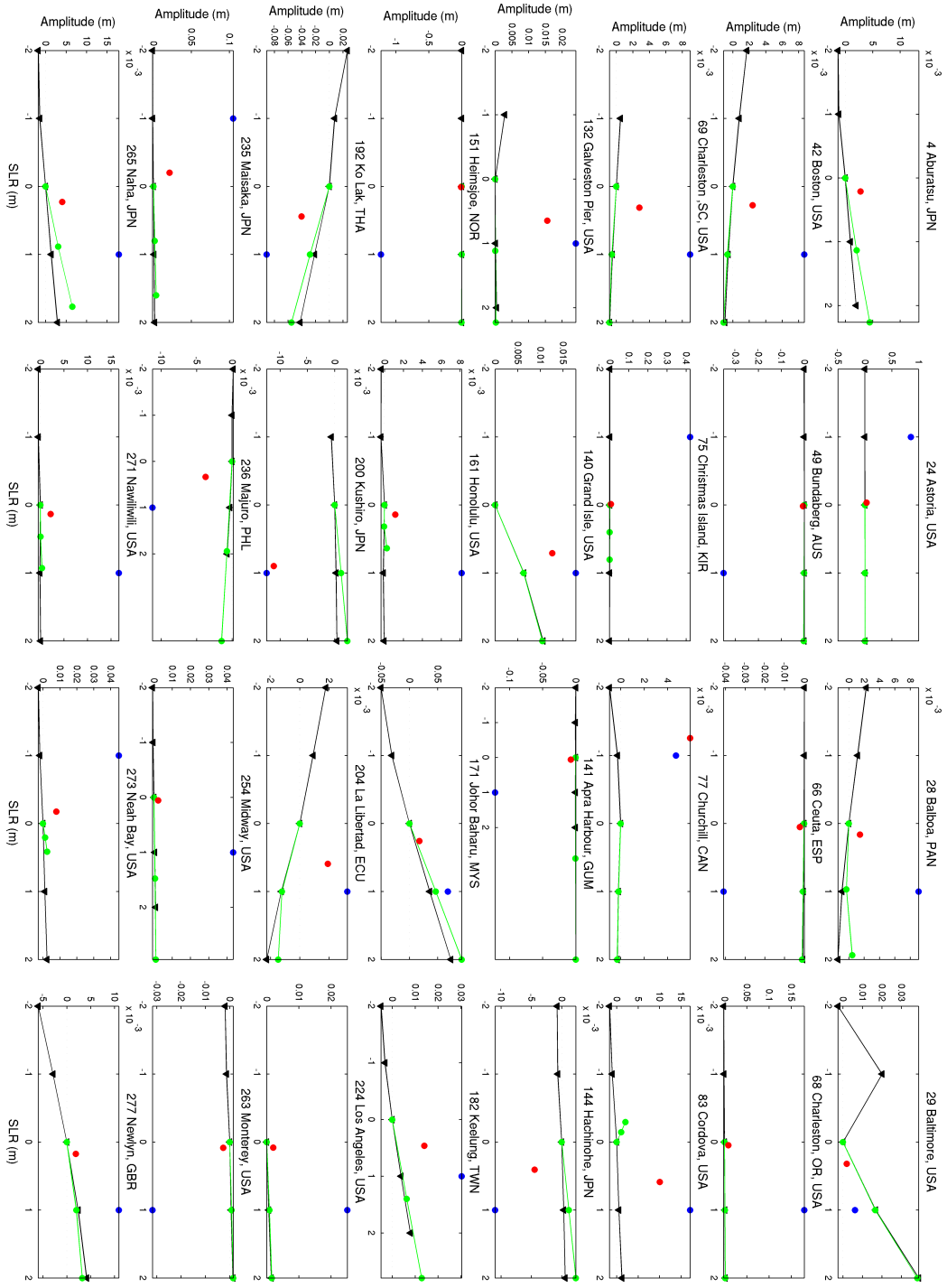

Figure 5.11: Same as Figure 5.8 but for K_1.

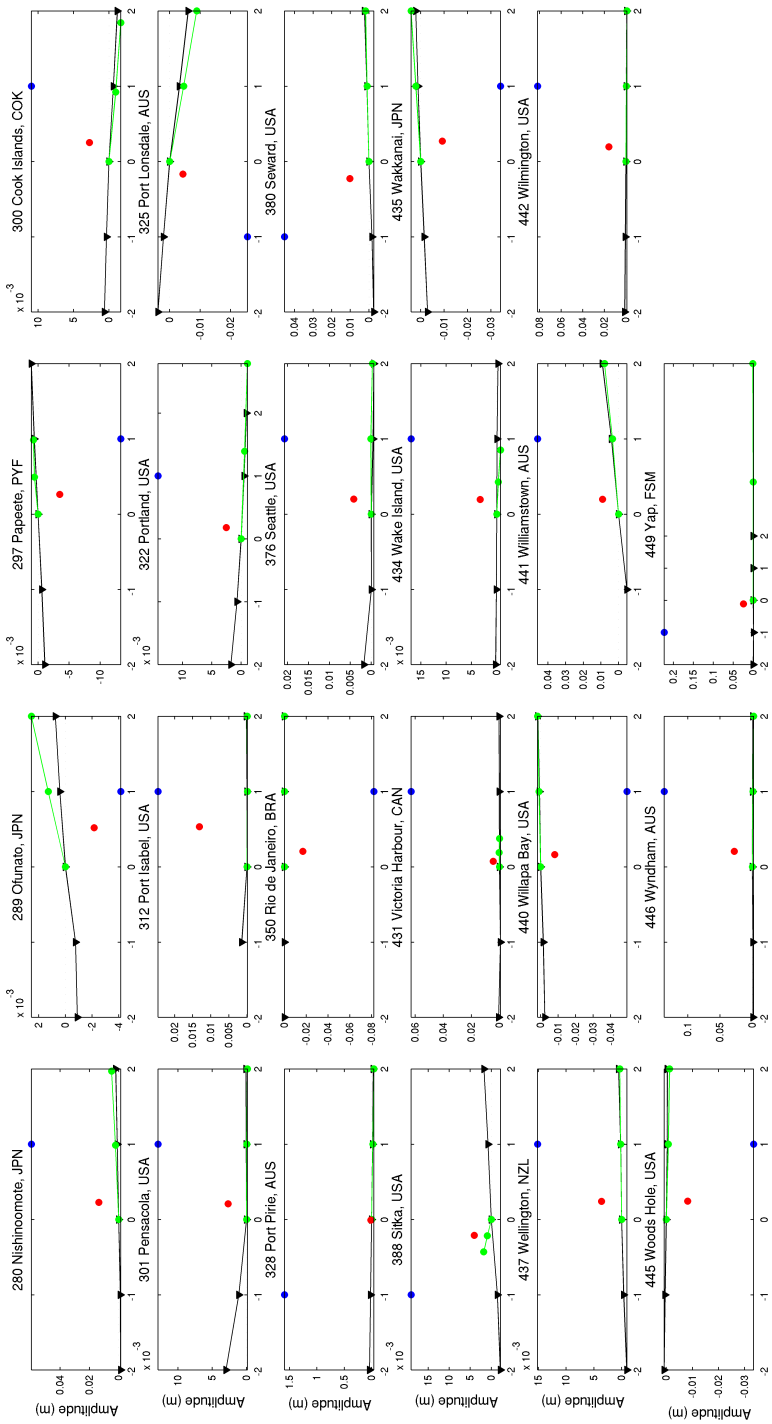

Figure 5.12: Same as Figure 5.8 but for K_1.

Chapter 6

Global marine impacts of large-scale ice-sheet collapses

6.1 Introduction

Tides play an important role in the global climate system. Approximately half of the energy necessary to sustain the large-scale meridional ocean overturning circulation (MOC) is provided by the tide (e.g., *Munk and Wunsch*, 1998). At rough bathymetric features energy is transferred from the barotropic tide to internal waves which subsequently break and cause mixing in the interior of the ocean (*Egbert and Ray*, 2000; *Ledwell et al.*, 2000). Vertical mixing balances deep water formation and influences the strength of the MOC, and thus supports a key pathway for the redistribution of heat, momentum and freshwater across the globe (e.g., *Wunsch and Ferrari*, 2004). For the Last Glacial Maximum (LGM), when sea-level was 120 m lower than at present, it has been suggested that altered tidal processes due to the sea-level decrease could have modified the structure of the MOC (see **?**, and Chapter 4 for a detailed description).

Tides control shelf-sea primary production in temperate and polar regions by determining the locations of tidal mixing fronts in temperate and polar shelf seas (e.g., *Pingree et al.*, 1978; *Holligan et al.*, 1984; *Simpson and Sharples*, 2012). Tidal mixing fronts are interfaces between seasonally stratified, nutrient depleted and fully mixed, nutrient rich waters. Their location is determined by the balance between heating from the sun and mixing by the tide and the wind (*Simpson and Hunter*, 1974). Mixing fronts sustain the highest levels of primary productivity and associated secondary productivity in shelf seas as nutrients are resupplied here (e.g., *Sharples and Holligan*, 2006). This makes these areas valuable fishing grounds (e.g., *Simpson and Sharples*, 2012). Furthermore, the partitioning between seasonally stratified and fully mixed waters in temperate and polar shelf seas influences the uptake of CO_2 in form of dissolved inorganic carbon from the atmosphere and the storage of organic carbon from biological activity (*Tsunogai et al.*, 1999; *Thomas et al.*, 2004). The organic and inorganic carbon can be subsequently exported off the shelf into the deep ocean by horizontal advection or isopycnal mixing. This process is known as the continental shelf pump (*Tsunogai et al.*, 1999; *Thomas et al.*, 2004; *Rippeth et al.*, 2008).

In coastal areas tides are the main driver of sea-level variability on hourly to daily time scales. They therefore influence the structure of near-shore and intertidal ecosystems, and determine coastal morphology. They do not only induce rapid sea-level changes themselves, but the phase of the tide also modifies propagation properties of storm surges (*Horsburgh and Wilson*, 2007).

Because tides propagate as shallow-water waves they are strongly affected by water-depth (sea-level) changes that alter the propagation speed of the tidal wave and can change resonant properties (see, e.g., *Green*, 2010). However, investigations of the impact of sea-level changes on tides have mostly focussed on the LGM (e.g., *Egbert et al.*, 2004; *Griffiths and Peltier*, 2009; *Green*, 2010; *Wilmes and Green*, 2014) or on regional responses to future sea-level rise (*Ward et al.*, 2012; *Pickering et al.*, 2012; *Pelling et al.*, 2013a; *Pelling and Green*, 2013; *Luz Clara et al.*, 2015).

It has been hypothesised that during the Last Interglacial (∼125 kyr BP; LIG) a collapse of the West Antarctic Ice Sheet (WAIS) may have taken place (*Raymo and Mitrovica*, 2012) and that parts of the Greenland Ice Sheet (GIS) melted (e.g., *Kopp*, 2009). However, recent studies highlight that ice sheet collapses could also occur in future. Recent investigations of the glaciers draining the WAIS have show widespread grounding line retreat (*Rignot et al.*, 2014; *Joughin et al.*, 2014) together with increased ice discharge rates (*Pritchard and Vaughan*, 2007; *Mouginot et al.*, 2014) over the last decades. This gives rise to a strongly negative mass balance (*Harig and Simons*, 2015). As the WAIS is predominately a marine-based ice sheet and inherently unstable (*Clark and Lingle*, 1977; *Oppenheimer*, 1998; *Bamber et al.*, 2009; *Gomez et al.*, 2010; *Joughin et al.*, 2014) it has been suggested that these trends may be linked to the early phases of a marine ice-sheet instability, possibly leading to a collapse of marine sectors of the WAIS in the coming centuries or millennia (*Joughin et al.*, 2014; *Mouginot et al.*, 2014). Similarly, for the Greenland Ice Sheet (GIS), a number of studies have reported increased ice mass loss rates over the past decades (*Velicogna*, 2009; *Velicogna et al.*, 2014) and regionally increased flow speeds (*Rignot and Kanagaratnam*, 2006; *Moon et al.*, 2012). It has been suggested that if a certain warming threshold is crossed, a full melting of the ice sheet could occur (*Gregory et al.*, 2004; *Robinson et al.*, 2012). A full collapse of an ice sheet would induce globally heterogeneous sea-level changes, due to the loss of the gravitational attraction of the ice sheet, changes in loading of the Earth's crust and perturbations in the Earth's rotation (*Clark and Lingle*, 1977; *Milne and Mitrovica*, 1996; *Mitrovica et al.*, 2009; *Gomez et al.*, 2010) (see Figure 6.1). Despite recent work (*Clark and Lingle*, 1977; *Mitrovica et al.*, 2009; *Gomez et al.*, 2010; *Mitrovica et al.*, 2011) showing highly heterogeneous sea-level change rates which, regionally, can have the opposite sign to the global average, and could therefore influence the tidal response to the sea-level changes, the global response of tides to large-scale, glacially-mediated sea-level changes in both the

future climate and during the LIG has yet to be investigated.

Our aims in this chapter are to demonstrate how collapses of the WAIS or the GIS affect tidal processes, and to highlight the importance of tides in the climate system. We deliberately collapse the entire ice sheets as this gives an indication of the extremes in responses. All intermediate ice sheet melt cases are likely to evoke tidal changes that lie between the present-day case and the extremes. First, we describe the changes in tidal amplitudes induced by gravitationally self-consistent sea-level changes following the removal of each the WAIS and GIS (Figure 6.1), and address implications for coastal flooding. Next, we illustrate the global consequences of the changes in the associated dissipation of tidal energy in the oceans, and postulate impacts on ocean mixing and shelf sea biogeochemical cycles.

6.2 Methods

6.2.1 Simulations

We carry out three sets of numerical tidal model simulations, using OTIS, to reach these goals: (1) a present day control simulation of the global M_2 tide (henceforth 'Control'; Figure 6.2a); (2) a simulation with a collapsed WAIS (denoted 'NoWAIS'); and (3) a simulation with a collapsed GIS (denoted 'NoGIS').

OTIS was run in the same setup as described in Chapter 3.2. NoWAIS and NoGIS use bathymetries in which the ice is removed and replaced by bedrock (see Figure 6.1a for NoWAIS). The sea-level changes following collapses of each ice sheet (Figure 6.1b and c), with equivalent eustatic values (EEVs) of 5 m and 7 m for WAIS and GIS, respectively, are computed using a gravitationally self-consistent sea-level theory. It takes into account deformation of an elastic Earth model, changes in Earth rotation, and migrating shorelines (*Gomez et al.*, 2010). For comparison we also perform tidal simulations with spatially uniform sea-level increases of 5 m and 7 m to reinvestigate the validity of previous uniform sea-level rise studies (e.g., *Ward et al.*, 2012; *Pickering et al.*, 2012; *Luz Clara et al.*, 2015). The model was run for both M_2 and K_1, however K_1 is not elaborated on here, because the changes in tidal amplitudes and the associated tidal dissipation are local and of small magnitude.

6.2.2 Bathymetry and sea-level model

Global bathymetric data from *Wilmes and Green* (2014) (see also Section 3.2.6 for details) is used as input to the tidal model for the Control scenario. For the NoWAIS and NoGIS scenarios, the ice in West Antarctica and on Greenland, respectively, is removed and replaced by bedrock data from the ETOPO1 database (*Amante and Eakins*, 2009) in each bathymetry. Predicted sea-level changes for collapses of the WAIS or GIS are then added to this initial bathymetry to produce the bathymetry used in the tidal modelling keeping the land-ocean boundaries constant apart from in the ice-sheet collapse locations.

The implementation of sea-level change in tidal models, i.e. whether new land is allowed to flood or the land-sea configuration is held constant, can lead to large differences in tidal responses (*Pelling et al.*, 2013a; *Ward et al.*, 2012). Here, we assume that areas experiencing large tidal changes are or will be protected by flood defences as is the case for the European Shelf (*Pelling et al.*, 2013a). Consequently, we do not flood new grid cells. We have performed simulations allowing inundation and find that the global patterns are very similar to the simulations presented here. There are local differences, which are evident in some shelf seas, however the global, open ocean patterns correspond well. Considering the fairly low resolution of the tidal model (with respect to the complexity of coastal flooding) we therefore suggest that the differences between 'flooding' and 'no-flooding' are best addressed in high-resolution regional studies.

The calculations of sea-level change following the full collapse of the WAIS and GIS were performed using the sea-level theory and algorithm described in detail in *Gomez et al.* (2010). This theory includes gravitational self-consistency, elastic deformation of the solid Earth, changes in the rotation of the Earth. It allows for migrating shorelines and the inundation with water of sectors freed of marine-based ice. Calculations are performed up to spherical harmonic degree and order 512, and elastic and density structure of the solid Earth is given by the Preliminary Reference Earth Model (PREM) (*Dziewonski and Anderson*, 1981). The prediction for the NoWAIS scenario comes directly from *Gomez et al.* (2010), while the prediction for the NoGIS scenario was calculated applying the same procedure. The current scenarios represent instantaneous sea-level responses to full ice-sheet collapses. Future work will involve consideration of time-incremented ice-sheet removal over a range of timescales and the incorporation of a viscoelastic Earth model.

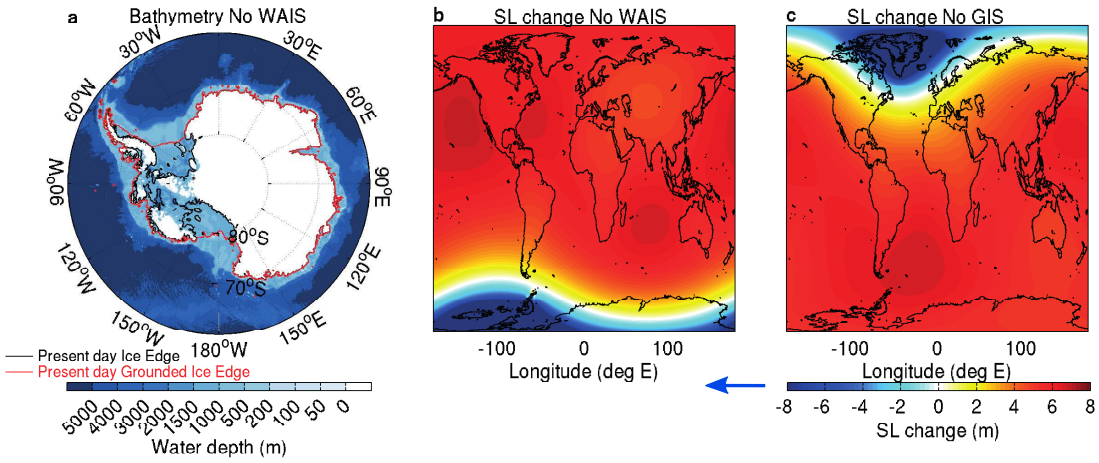

Figure 6.1: (a) Antarctic bathymetry with WAIS removed. The white shading indicates land areas or areas of ice higher than the sea surface height; the black line shows the extent of grounded ice in the Control simulation; the red line indicates the maximum extent of ice including ice shelves, (b) sea-level change in response to a WAIS collapse, (c) sea-level change in response to a collapse of the GIS. For (b) and (c) the black contour marks the land ocean boundary. For (b) and (c) the blue arrow on the colour bar indicates that the sea-level decrease in proximity to the ice-sheet collapse location saturates the colour bar (the maximum decreases amount to 87m (NoWAIS) and 88m (NoGIS)).

In addition, we prepare uniform sea-level rise bathymetries where sea-level is increased by 5 m and 7 m, respectively, against the Control bathymetry, and land-ocean boundaries are held constant.

6.2.3 Analysis

The Control amplitudes were evaluated against the TPXO8 database (*Egbert and Erofeeva*, 2002) using a root-mean square error (RMSE), calculated as the sum of the latitudinally weighted square differences between the Control simulation and TPXO8. For M_2 we achieve a global RMSE of 7.7 cm, which in the deep ocean (water depth $h > 500$ m) drops to 3.8 cm. Control dissipation is 2.34 TW in total and 0.77 TW for the deep ocean, consistent with values from TPXO8 (with total and deep dissipation being 2.39 TW and 0.96 TW).

The open ocean amphidrome locations are determined with the help of an algorithm which finds the minima in amplitudes in the open ocean and determines the locations at which the phase differences are greatest. Taken together these two criteria give the locations of the amphidromes.

The Simpson-Hunter Stratification Parameter k was calculated following *Simpson and Hunter* (1974) as $k = h/u^3$, where h is water depth and u is tidal current velocity. A value of $log_{10}(k) = 2.5$ was used to mark the transition between mixed and stratified waters as was done by *Simpson and Pingree* (e.g., 1978) or *Luz Clara et al.* (2015), with $log_{10}(k) > 2.5$ representing stratified waters and $log_{10}(k) < 2.5$ mixed waters.
Dissipation was computed as the difference between the work done by the tide producing force and the divergence of the energy flux following *Egbert and Ray* (2001) (see also Section 2.3.7).

6.3 Results

6.3.1 Amplitudes

Large changes in M_2 amplitudes can be seen in both the NoWAIS and NoGIS simulations. In the NoWAIS case (Figure 6.2b), tidal amplitudes of up to 1 m occur in the new West Antarctic ocean basin, together with increases of nearly 0.5 m over the central Ross Sea. Amplitudes also increase throughout the Pacific, particularly in the Panama Basin (up to 0.2 m), along the west coast of the US, in the Bering Sea (up to 1.2 m), along the Asian coast of the Pacific (up to 0.65 m) and along the north Australian coast. Slight decreases in amplitudes can be seen west of New Zealand. The Atlantic sector sees reductions in tidal amplitudes of up to 1.2 m throughout the North Atlantic, with the exception of Hudson Bay, and with larger than present tides in the southern basin, especially on the Patagonian Shelf.

Overall, the NoGIS simulation shows a similar picture, although there are regional differences between the NoGIS and NoWAIS simulations (Figure 6.2c). The amplitude enhancements throughout the Pacific are larger than in NoWAIS due to larger sea-level changes in the NoGIS simulation. The largest differences between NoGIS and NoWAIS are found around Antarctica where, in the NoGIS case, the amplitude differences are small because local bathymetry remains the same. Pronounced differences are also seen throughout the Atlantic, where sea-level changes vary strongly between scenarios. In the Atlantic, for NoGIS, greater amplitude increases occur on the Patagonian Shelf than in NoWAIS, but we also see more pronounced decreases throughout the North Atlantic, including Hudson Bay. Furthermore, the response on the European Shelf is much weakened in comparison to NoWAIS. Overall, amplitudes increase along 59% and 57% of the

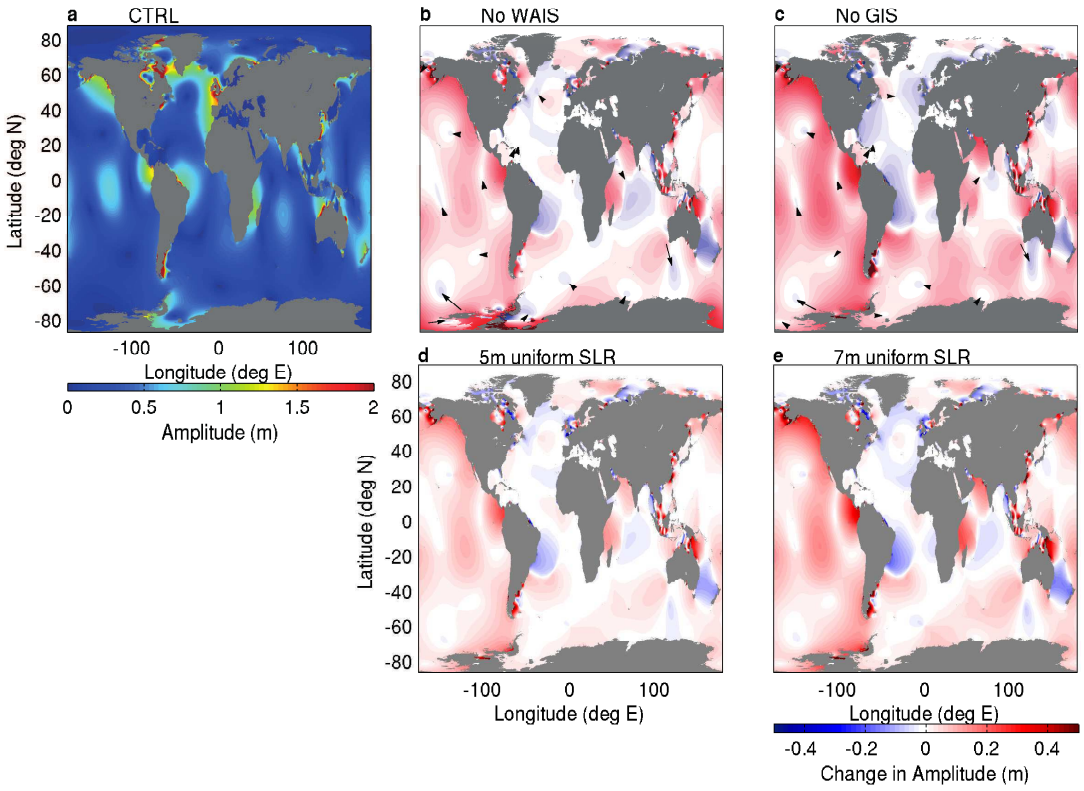

Figure 6.2: (a) Present day M_2 amplitudes for the Control simulation. (b-e) M_2 amplitude changes in response to (b) the removal of the WAIS (NoWAIS), (c) the removal of the GIS (NoGIS), (d) uniform 5 m sea-level increase and (e) uniform 7 m sea-level increase. For (b) and (c) the black arrows indicate shifts of open ocean amphidromes, with arrows pointing from the amphidrome location in the Control simulation to their location in the NoWAIS and NoGIS, respectively.

coastline for NoWAIS and NoGIS, respectively, whereas 36% and 38% of the coastline experience decreases.

Solutions of the Taylor problem for shelf-sea tides (*Rienecker and Teubner*, 1980; *Pelling et al.*, 2013a) show that the increased propagation speed of the tidal wave with sea-level rise shifts amphidromes towards areas of enhanced dissipation. A shift of one amphidrome then triggers movement of the adjacent amphidromic points (see the diagram in *Pelling et al.*, 2013a). For the NoWAIS case the removal of the ice sheet results in an eastward shift of the southernmost amphidromic point located in the Ross Sea, subsequently triggering a northwest shift of the neighboring amphidrome (Figure 6.2b). The open ocean amphidromes in the Central and North Pacific shift north- and westward towards areas of enhanced dissipation in the West and North Pacific (see Figure 6.4b). This is induced by changes in the propagation properties of the tidal wave due to the

sea-level increases. For the NoGIS scenario the changes in the Central and North Pacific mirror those in the NoWAIS case but differ close to Antarctica as dissipation changes here are much smaller (Figure 6.2c and Figure 6.4c). In the South Atlantic the northwestward migration of the amphidrome between South Africa and central South America results in decreases in amplitudes over the Amazon Shelf. In the North Atlantic the small northwestward shift of the amphidromic point south of Greenland in the NoWAIS case and the eastward shift in the NoGIS scenario are responsible for the considerable amplitude changes in this near-resonant region. Consequently, the increased dissipation on the Patagonian Shelf seen in both scenarios, and for NoWAIS also in the Weddell Sea sector (see Table 6.3.1 and Figure 6.4), reduces dissipation in the North Atlantic and its adjoining shelf seas. This is analogous to the tidal changes occurring between the LGM and the Holocene when sea-level rose and shelf seas progressively flooded reducing open ocean dissipation (*Wilmes and Green*, 2014).

These results highlight that tidal amplitude changes at a given location are related to both local and far field sea-level changes, and, in particular for the case of NoWAIS, to the inundation of sectors freed of marine-based ice (Figure 6.1a). In proximity of the ice sheet the sea-level changes are opposite in sign and an order of magnitude or more greater than the EEV (Figure 6.1b and c). For example, in Figure 6.1b showing WAIS collapse with an EEV of 5 m, sea-level falls in the WAIS region by up to 87 m. Note that sea-level changes in the proximity of ice loss are highly dependent on the geometry and amount of ice removed (*Mitrovica et al.*, 2011). Also the predictions in Figure 6.1b and c are computed for the scenarios in which the WAIS and GIS fully collapse. This result leads to very different responses of the tides between the NoWAIS and the NoGIS cases in the polar regions. This aspect is not taken into account when using the traditional uniform sea-level rise scenarios. Furthermore, in areas where the predicted sea-level change corresponds to the EEV of the respective ice sheet, the tidal response still differs from the uniform case (Figure 6.2d and e), showing that local (shelf sea) tidal responses are influenced by far-field dynamics. These results emphasize the importance of using geographically variable sea-level change scenarios, as opposed to the traditional approach of applying globally uniform sea-level increases. Furthermore, these finding highlight the importance of using 'correct' boundary conditions that take the global changes into account when performing high-resolution regional studies.

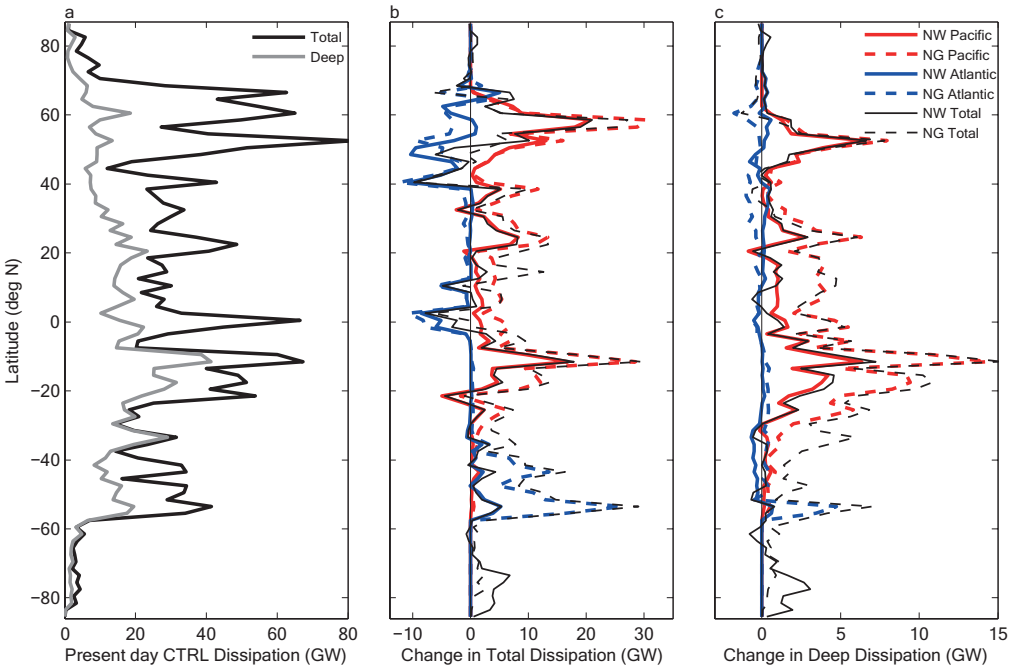

Figure 6.3: (a) Longitudinally integrated M_2 tidal dissipation summed over 2° of latitude for smoothing purposes for total dissipation (black) and deep dissipation (grey, $h > 500$ m). Change in longitudinally integrated M_2 tidal dissipation due to the ice-sheet removal for (b) total dissipation and (c) deep dissipation. Solid lines indicate the NoWAIS simulation, dotted lines the NoGIS simulation. Black shows total changes, blue Atlantic only and red Pacific only.

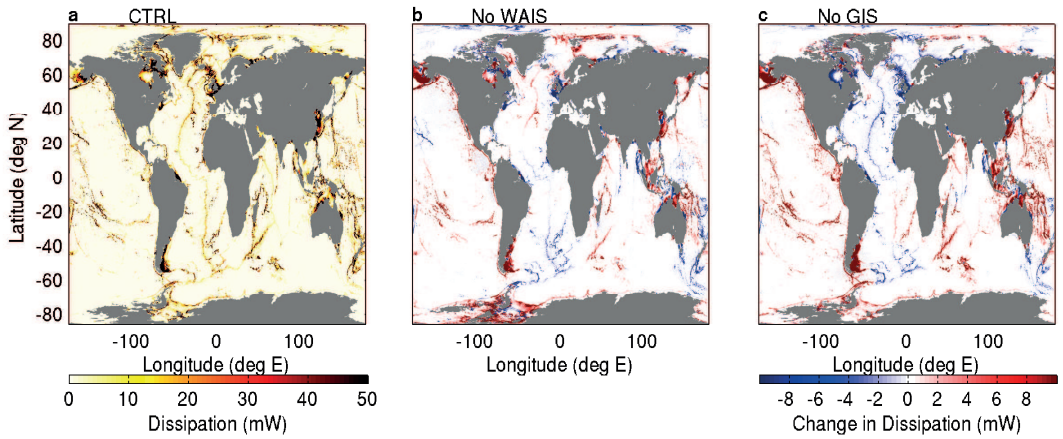

Figure 6.4: (a) Present day M_2 dissipation for the Control simulation. M_2 dissipation changes in response to (b) the removal of the WAIS (NoWAIS), and (c) the removal of the GIS (NoGIS).

Table 6.1: Shelf-sea dissipation and stratification changes. The left three columns give M_2 tidal dissipation in shallow waters ($h < 500$ m) for selected shelf regions for the Control simulation, the NoWAIS simulation and the NoGIS simulation. Units are Gigawatts. The values in brackets give the percentage changes in dissipation for NoWAIS and NoGIS. The right two columns give the change in extent of waters which remain well mixed due to tidal mixing and so are not subjected to seasonal stratification. Units are %. No values for stratification changes are given for the Amazon Shelf as its oceanographic regime is dominated by freshwater fluxes.

	Shelf dissipation [GW] (% change)					Mixed water extent (% change)	
	Control	NoWAIS		NoGIS		NoWAIS	NoGIS
Global	1570	1350	(-14)	1490	(-5)	-20	-23
Amazon Shelf	78	59	(-24)	52	(-33)	–	–
Bering Sea	63	119	(89)	140	(122)	52	62
China Seas	167	195	(17)	223	(34)	-24	-30
European Shelf	127	102	(-20)	111	(-13)	3	-4
Patagonian Shelf	101	120	(18)	188	(86)	-12	32

6.3.2 Dissipation

Pronounced changes in tidal energy dissipation occur throughout the different ocean basins in response to the changes in tidal processes (Figures 6.4 and 6.3, and Table 6.3.1). In the following "deep" ("shelf") refers to water depths deeper (shallower) than 500 m. The total (deep) globally-integrated dissipation rate from the M_2 tide increases from 2.28 TW (1.02 TW) in Control to 2.46 TW (1.11 TW) in NoGIS and 2.74 TW (1.25 TW) in NoWAIS. For both NoWAIS and NoGIS these changes are mainly due to enhanced dissipation in the Pacific (Figure 6.3b), especially around the Bering Sea (approximately 55° N). There, shelf dissipation increases by 90% and 120% for NoWAIS and NoGIS, respectively (Table 6.3.1). Increases also occur north-east of Australia (15° S) and in the China Seas (20° N) (∼20% and 40%, respectively). With the exception of the Patagonian Shelf (55° S), where 90% more energy is dissipated in NoGIS than in the Control simulation, dissipation generally drops throughout the Atlantic in both NoWAIS and NoGIS. This includes decreases on the Amazon Shelf (5° N), in the Bay of Fundy (40° N), and on the European Shelf (50° N). Interestingly, deep-water dissipation (Figure 6.3c) in the Atlantic shows little change for either collapse case, whereas strong

increases occur throughout the Pacific. The main locations for enhanced deep-water dissipation are the Coral Sea north-east of Australia (20° S – 0° S), the Izu-Bonin-Mariana Arc south of Japan (25° N), and the Aleutian Ridge to the south of the Bering Sea (50° N), and also in the West Antarctic ocean basin for NoWAIS. Again in NoGIS, larger changes can be seen than in NoWAIS compared to the Control.

The changes in shelf-sea dissipation are predicted to lead to changes in the extent of seasonal stratification in a number of temperate and polar shelf seas (see Table 6.3.1 and Figure 6.5). Calculation of the Simpson-Hunter stratification parameter shows that the mixing front locations and lengths change in most shelf seas examined in both scenarios, and that pronounced changes in the extent of mixed water occur. Globally, the spatial extent of permanently mixed waters decreases by around 20%, corresponding to an increase in stratified waters for both scenarios, but across the different shelf seas the patterns are highly heterogeneous. For example, in the Bering Sea the extent of mixed waters increases by over 50% whereas for the China Seas, decreases of around 25% and 30% occur in NoWAIS and NoGIS, respectively.

6.4 Discussion

The impact of possible future large-scale ice sheet collapses on the tides and tidally-driven processes has been investigated. Our results show prominent global changes in both tidal dynamics and tidally-driven processes in response to the removal of the WAIS and the GIS. These results are applicable both for changes that may occur in a warming world but also for the LIG which is often considered an analogy for our climate system in the next millennia (e.g., *Church et al.*, 2013).

Large amplitude changes occur on most coastlines which are heterogenous in nature. Together with the mean sea-level changes they are expected to considerably alter coastal ecosytems and morphology. The considerable changes in amplitudes could hamper reconstructions of LIG sea-level as sea-level index points often rely on tidal amplitudes not varying in magnitude (e.g., *Scourse*, 2013).

The increased deep-water dissipation rates seen for the central and northern Pacific may affect ocean dynamics, climatic patterns, and as a consequence biogeochemical cycles. The enhancements in the Pacific and the Southern Ocean region may intensify abyssal diapycnal mixing and thus influence the overturning circulation in the Pacific and the Antarctic Circumpolar Current (*Munk and Wunsch*, 1998; *Egbert and Ray*, 2001). This

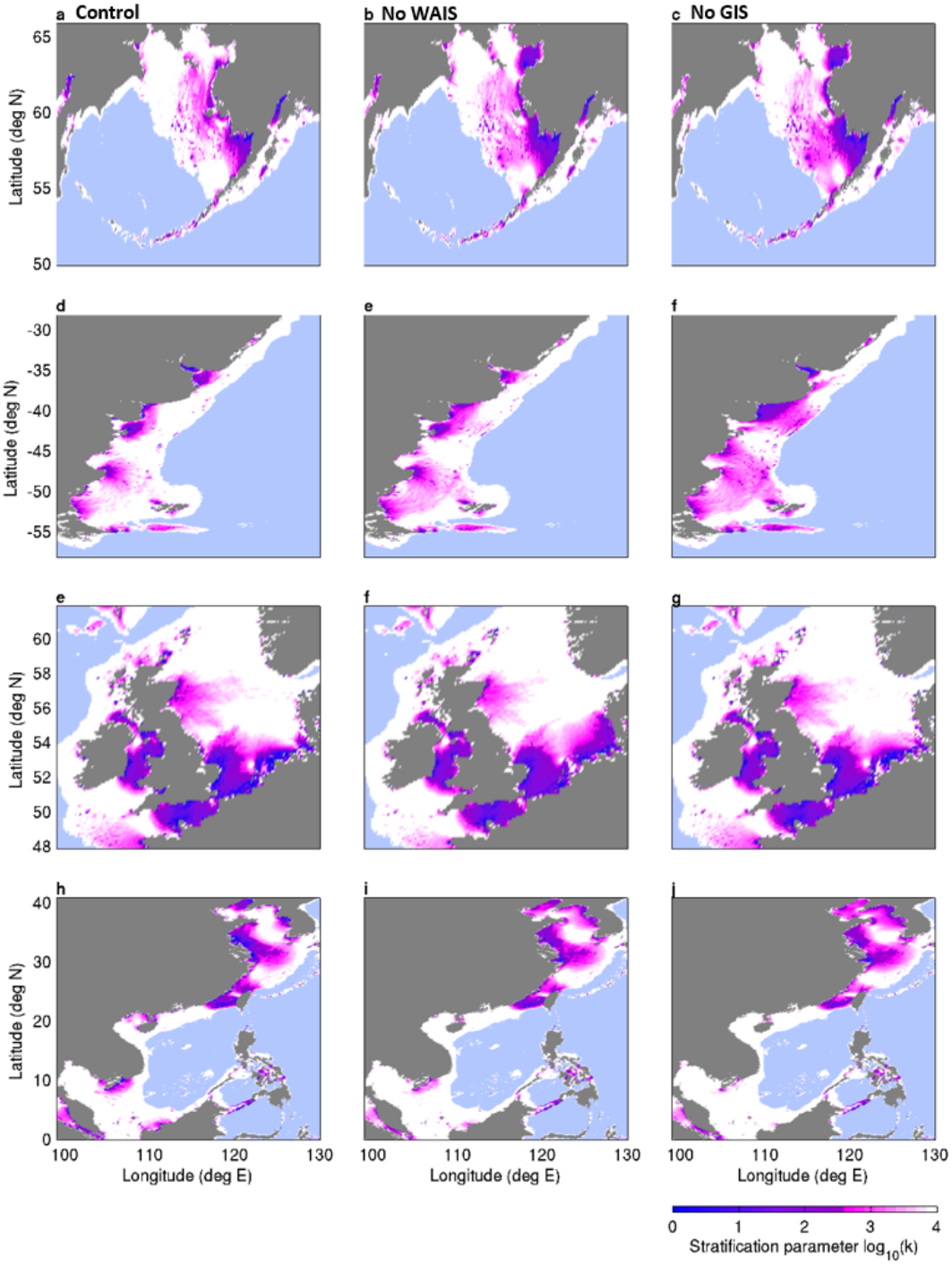

Figure 6.5: Stratification parameter $\log_{10}$(k) calculated for M_2 for CTRL (left column), NoWAIS (central column), and NoGIS (right column). The light blue shading marks areas deeper than 500 m. Values below 2.5 indicate fully mixed water, values above seasonally stratified waters. Areas displayed are (a) - (c) the Bering Sea, (d) - (f) the Patagonian Shelf, (g) - (i) the European Shelf and (j) - (l) the China Seas.

would affect heat and momentum transfer across the globe, as has been hypothesized to have occurred during the LGM (*Green et al.*, 2009; *Schmittner et al.*, 2015) and Eocene (*Green and Huber*, 2013). Prominent changes in dissipation also occur around the Indonesian Seas. Here, at present, the Indonesian Throughflow (ITF) transports heat and freshwater into the Indian Ocean (*Sprintall et al.*, 2009). Links between the ITF and the climate patterns ENSO and the Indian Ocean Dipole have been suggested (e.g., *Zhou et al.*, 2015). Changes in the tides in this area could lead to modifications in the strength and structure of the ITF with possible feedbacks for supraregional climate modes. We therefore argue that long-term simulations of ocean-climate scenarios, irrespective of time period, should take changes in tidally-driven mixing into account.

The large changes in the level of tidal energy dissipation in the shelf seas will result in profound local changes in water column structure with potential downstream impacts for fisheries and the global carbon cycle. Primary productivity in tidally-dominated seasonally stratified shelf seas is strongly influenced by the location of tidal mixing fronts. These separate seasonally stratified waters from water which remains fully mixed throughout the year. Tidal mixing fronts support very high levels of biological productivity, slightly lower values are found in seasonally stratified areas, and productivity is generally low in fully mixed waters (*Pingree et al.*, 1978; *Holligan et al.*, 1984). The changes in the geographical extent of seasonal stratification in temperate and polar shelf seas will thus change shelf-wide primary productivity levels. Consequently, both the changes in productivity and the distribution of shelf sea water masses could modify the strength of the shelf sea carbon pump (*Tsunogai et al.*, 1999; *Thomas et al.*, 2004; *Rippeth et al.*, 2008). Changes in primary productivity will have implications for shelf sea ecosystem structure (*Simpson and Sharples*, 2012). Despite a global increase in the geographical extent of seasonal stratification, regional changes are highly heterogeneous (see Table 6.3.1 and Figure 6.5). For example, in the Bering Sea, home to a globally-important fishery (*FAO*, 2014), the extent of stratification is predicted to shrink whilst in the Yellow and East China Seas levels increase. On the Patagonian Shelf, another fishery of global importance, large shifts in the location of the mixing fronts occur for both scenarios.

We have assumed that global ocean stratification remains unaffected by the addition of meltwater from the ice sheets. However, large additions of freshwater could lead to changes in ocean stratification altering the propagation of the barotropic tide and the generation of internal waves. The latter could have feedbacks for internal mixing.

6.5 Conclusions

This work illustrates and highlights the importance of tides in the global climate system. We have shown that the sea-level changes from large-scale ice-sheet collapses have the potential to substantially alter global tidal dynamics resulting in large amplitude changes across most of the globe. However, not only changes in amplitude are of importance: Our results suggest that the changes in tidal dynamics could have important downstream effects altering the position and length of tidal mixing fronts in seasonally stratified temperate and polar shelf sea, thus altering shelf-sea biogeochemistry and leading to changes in the global carbon cycle. Furthermore, changes in tidal dissipation could affect alter the amount of energy supplied to the internal tide which is important for mixing in the ocean's interior. This mixing in part drives large-scale ocean currents which have a strong influence on global climate patterns. We therefore conclude that past and future changes in the tides due to large-scale sea-level change have the potential not only to alter sea-level variability but could also lead to important feedbacks in the climate system. It is therefore suggested that tidal changes driven by sea-level changes should be considered in climate projections. Our results also emphasise the need for high-resolution regional tide studies addressing local impacts of sea-level changes on tides, better descriptions of the mechanisms behind these changes, and their feedbacks with components of the climate system.

Chapter 7

Discussion and Conclusions

7.1 Discussion and Outlook

With this work the impact of large-scale climatologically driven sea-level changes on the global tides has been explored. It has been shown that tides are highly sensitive even to the relatively small sea-level changes that are being observed at present and that changes in the global tidal dynamics can occur on a large range of timescales.

For both the past sea-level low-stand during the LGM and the possible future ice sheet collapse scenarios, increases in M_2 tidal amplitudes occur across large parts of the globe, albeit in different areas and for different reasons. During the LGM, tidal amplitudes were much greater in the Atlantic than at present. This was due to changes in the resonant properties of the Atlantic during the LGM. The 130 m sea-level drop led to the exposure of most shelf seas where a large part of tidal energy is lost at present. This reduced the damping properties of the ocean basin which is close to resonance at semi-diurnal tidal frequencies at present and led to strongly enhanced amplitudes and dissipation in the LGM ocean (see, e.g., *Egbert et al.*, 2004; *Green*, 2010; *Wilmes and Green*, 2014). The sea-level drop showed very little effect in the Pacific compared the large increases in amplitudes seen in the Atlantic. Large parts of the Pacific are not close to resonance at present for semi-diurnal frequencies (e.g., *Platzman et al.*, 1981) and were, as the research presented here suggests, also not in the past. In contrast to the Atlantic, the shelf seas in the Pacific are much narrower and occupy much less area than in the Atlantic, meaning that the shape of the ocean basin changes much less in the Pacific than in the Atlantic, when large sea-level changes occur.

In the ice sheet-collapse scenarios, in contrast, the strongest increases in tidal amplitudes can be seen in the Pacific. They, however, occur due to changes in the propagation properties of the tidal waves due to increased sea-level and not due to resonance effects as in the Atlantic during the LGM. The altered tidal wave properties cause shifts of most amphidromic points throughout the Pacific, leading to increased amplitudes along most Pacific coast lines. The North Atlantic, for both WAIS and GIS collapses, shows small decreases in amplitudes and dissipation which is consistent with the North Atlantic being pushed away from resonance as sea-level further increases. These results agree well with the amplitude trends observed from the tide-gauge data. Large changes in the M_2 tidal amplitudes are occurring over most areas on the globe where data is available. In some locations the amplitude trends are nearly as large as the mean sea-level trends occurring in conjunction.

The analysis of the tide-gauge data indicates that, at least for M_2, part of the observed global amplitude trends can be explained with the large-scale sea-level changes occurring at present. This implies that sea-level increases can be considered a driver of large-scale changes in tidal dynamics. However, it appears that the tidal model underestimates the changes in amplitudes. This suggests that further processes may be contributing to the tidal changes such as changes in the internal tide (*Zaron and Jay*, 2014), changes in local coastal morphology (*Pelling et al.*, 2013b), or changing interactions with other tidal constituents (*Devlin et al.*, 2014) that have not been considered in this study.

In contrast to M_2, K_1 tides show a very low sensitivity to the range of sea-level change explored in this study. Neither the large sea-level adjustments seen during the deglacial period, nor future sea-level increases result in global changes in the K_1 tide. The changes mainly occur in the shelf seas in which the K_1 tide is large at present, i.e. the Sea of Okhotsk, the South China Sea, the Indonesian seas, and the Bering Sea, but the open ocean changes are small. This is due to none of the large ocean basins being close to resonance at diurnal frequencies at present (see e.g., *Platzman et al.*, 1981; *Green*, 2010). The observed tidal amplitude trends for K_1 are much smaller than for M_2 and occur at a much smaller proportion of stations analysed.

Chapters 5 and 6 have included simulations with both uniform and spatially varying sea-level changes. The simulations in Chapter 5 forced with the CU-SL sea-level changes show only small, localised differences to the uniform runs. In contrast, the results in Chapter 6 display large differences between the uniform and the non-uniform simulations. The CU-SL sea-level trends are spatially highly heterogenous, whereas the fingerprints used in Chapter 6 are spatially much more consistent. The fingerprints show pronounced decreases in sea-level over a large region close to the ice sheet and large increases away from the ice sheet. For those investigating the tidal response of large-scale sea-level changes this highlights the importance of considering non-uniform sea-level changes when the variations in sea-level exceed supraregional scales rather than simply applying the global mean sea-level change.

The considerable amplitude variations are also important for the reconstructions of past sea-levels. Sea-level index points (SLIPs) are sedimentary structures, fossil organisms, or archaeological features whose origin is primarily driven by sea-level at the point of deposition (*Shennan*, 2015). Often SLIPs do not record mean sea-level. Instead, for example, they document mean spring high tide levels. Most studies using SLIPs as indicators

assume tidal ranges that do not vary over time (see e.g., *Scourse*, 2013). However, this work and other studies (*Egbert et al.*, 2004; *Griffiths and Peltier*, 2009; *Green*, 2010) show that in the recent past, considerable changes in tidal amplitudes have occurred and are occurring at present (e.g., *Woodworth*, 2010; *Mawdsley et al.*, 2015) invalidating this assumption (e.g., *Shennan*, 2015). Furthermore, in the case of the LGM, the tidal changes, are actually driven by sea-level changes, further complicating the reconstructions of past sea-levels.

The work presented in Chapter 7 is not only of relevance for the future but also for the past: reconstructions of sea-level during the past interglacial have suggested that global mean sea-level may have been over 6 m higher than at present (see e.g., *Kopp*, 2009). It has been hypothesised that partial melting or a full collapse of the WAIS may have significantly contributed to the sea-level highstand (*Raymo and Mitrovica*, 2012; *Bradley et al.*, 2012) together with partial melting of the Greenland Ice Sheet (*Kopp*, 2009). Global climate has been estimated to have been around 2°C warmer than at present (*Church et al.*, 2013), a value which may be reached by the end the year 2100 (*Pachauri*, 2014). This indicates that collapses of the WAIS may have occurred in the past and could be a possible future phenomenon. This work shows that a collapse of the WAIS would have induced profound changes in the global tides with implications not only for shelf sea dynamics, and thus primary productivity, with possible back effects for CO_2 concentrations, but also open ocean dynamics which may not only be important in the future but also in the past.

Changes in the tides have the potential to alter a large range of oceanic processes. Changes in the amount of tidal energy dissipated in the oceans can alter the amount of vertical mixing occurring in the deep ocean with potential feedbacks on open ocean circulation. This supports previous speculation (*Munk and Wunsch*, 1998; *Green et al.*, 2009) that the increase in tidal dissipation during the LGM had the potential to counteract the processes slowing the MOC during the LGM reported in a number of modelling studies (e.g., *Stocker et al.*, 1992). Increased tidal mixing rates could also have provided a mechanism for the rapid resumption of the MOC to full strength after large fresh water inputs during the Heinrich events during the LGM (e.g., *Green et al.*, 2009). These mechanisms could also be important in the future. Decreased tidal dissipation in the Atlantic region, as seen for the melting of the GIS, and to smaller extent for the WAIS, combined with an increased freshwater input from the melting ice sheet could lead to a

reduction of the strength of the overturning.

Changes in the energy input from the tides are not only important in the open ocean but also in shelf seas. Despite their surface area being small ($\sim$ 9% of the surface of the ocean), their account for nearly $1/5^{th}$ of the oceanic primary productivity (*Simpson and Sharples*, 2012) with 90% of the global fish catches coming from shelf seas and the shelf break (*Pauly*, 2002). Oceanic primary productivity leads to the fixture of CO_2 into organic matter, part of which is subsequently exported to the deep ocean (*Tsunogai et al.*, 1999; *Thomas et al.*, 2004; *Simpson and Sharples*, 2012). It has been estimated that 47% of the particulate organic carbon export to the deep ocean occurs in shelf seas (*Jahnke*, 2010). In many shelf seas physics and biochemistry are heavily influenced by the tide (e.g., *Simpson and Sharples*, 2012). *Simpson and Bowers* (1981) show that the modulations of the tides over the spring-neap cycle can lead to considerable displacements of tidal mixing fronts. The changes in tidal dynamics with changing sea-levels in some areas are much greater than spring-neap modulations and therefore large shifts in mixing front positions are to be expected. These would subsequently lead to alterations in primary productivity levels and shelf sea biogeochemistry, and hence would have implications for fisheries and carbon export to the deep ocean. Here, these processes are discussed for the future large-scale ice sheet collapses, however they are likely to have played a role during the LGM or the last interglacial, and may have lead to feedbacks with other processes in the climate system.

It is therefore suggested that for ocean and climate studies on timescales in which significant alterations of the tides could occur, these changes need to be taken into account, both for the open ocean and for shelf seas. This would, for example, mean including changes in tidal mixing into modelling studies such as previously done by some studies (e.g., *Schmittner et al.*, 2015; *Green*, 2010; *Montenegro et al.*, 2007; *Herold*, 2014).

A number of studies have suggested that ice sheet dynamics of the glaciers draining the Antarctic Ice Sheets are influenced by tides. It has been shown that flow speeds of the ice streams are modulated at tidal frequencies (e.g., *Anandakrishnan*, 2003) and that tides lead to the flexing of the floating part of the ice sheets, the ice shelves (e.g., *Vaughan*, 1995). It has been hypothesised that changes in the tides along the ice sheet margins could be a mechanism inducing large-scale ice sheet discharge (*Arbic et al.*, 2004) as periodically occurred during the LGM (e.g., *Heinrich*, 1988). Our simulations show that so-called megatides occurred along the margins of both the Laurentide and the Antarctic

Ice Sheet during the LGM, suggesting that there is indeed the possibility of the feedback between ice sheets and tides. However, this is only possible if floating ice was present along the edge of the ice sheet, as is the case for present-day Antarctica. Sensitivity tests of Antarctic ice sheet dynamics show that the pressure from future climate warming could lead to a strong reduction of ice shelf area (*Winkelmann et al.*, 2013). This is expected to cause feedbacks on the regional tides possibly causing further ice shelf retreat (*Rosier et al.*, 2014a). Our simulations for the collapses of the WAIS and GIS each indicate further enhancements in tidal amplitudes along the margins of Antarctica due to increasing sea-levels, which could lead to a further destabilisation of the ice sheets. Future work should investigate feedbacks between tide and ice sheet dynamics such as done in a simplified case for the present (*Rosier et al.*, 2014a).

For numerical reasons the simulations here have been carried out on a $1/8° \times 1/8°$ horizontal resolution so that the dynamics in the large open ocean basins could be captured. In order to carry out studies that would be useful to policymakers or coastal engineers planning coastal defense structures on shelf seas, much higher accuracies would be necessary.

However, studies solely running tidal models for specific shelf sea areas such as the European Shelf (*Ward et al.*, 2012; *Pickering et al.*, 2012; *Pelling et al.*, 2013a) or the Patagonian Shelf (*Luz Clara et al.*, 2015) and investigating the response of the tides to global mean sea-level changes run into a couple of problems. One key assumption is that large-scales open ocean tides with which these authors forced their tidal models at the domain boundaries do not change with altered sea-levels. Here it is shown that this is not the case. Even moderate global sea-level changes of 1 m result in considerable changes in the open ocean tides. *Arbic and Garrett* (2010) and *Skiba et al.* (2013) show that there are considerable interactions between shelf and open ocean tides and these are expected to play a role with changes in tidal dynamics induced by sea-level changes. A further issue arising with studies solely focussing on shelf seas is that, in contrast to global studies, changes in the self attraction and loading cannot be included. *Müller et al.* (2011) show that considerable changes in the tidal response occur throughout the SAL iterations.

One solution to these problems would be to carry out nested studies where high resolution regional setups are forced with open ocean tidal dynamics taking the large-scale tidal changes into account. A further compromise would be to run the tidal model at,

e.g. a global horizontal resolution of $1/15°$, instead of $1/30°$ which at present is feasible for shelf areas only. A further possibility would be to us a finite element or volume flexible mesh approach. Future work on shelf seas should also take the non-linear dynamics into account which are neglected in the present study.

Friction between the motion of the water by the tide and the Earth's surface slows the Earth's rotation which causes an offset of the tidal bulge from the Earth-Moon axis. The graviational torque between the tidal bulge and the Moon leads to a transfer of energy from the Earth's orbital motion to the rotation of the Moon. This results in an acceleration of the Moon's orbital motion, together with a decrease in the Earth's day length (see e.g., *Cartwright*, 1999). According to Keppler's third law, the increase in angular momentum of an orbiting body leads to its recession away from the main body and a transfer of its kinetic energy to potential energy with respect to the main body. For the Earth-Moon system this results in an increase of the distance of the Moon from the Earth and a slowing of the Moon's orbital motion (see e.g., *Brosche and Sündermann*, 1978). The recession rate is therefore directly dependent on global tidal dissipation rates (see e.g., *Cartwright*, 1999). To date the history of the Moon's recession rate since its formation at around 4.5 Gyr (*Kleine et al.*, 2005) is largely unconstrained (*Waltham et al.*, 2015).

Milankovitch et al. (1941) hypothesised that the long-term variations in the Earth's orbit, taken together as the variations from the Earth's eccentricity, precession, and obliquity, result in changes in climate patterns. Since then, the onset of glaciations have been linked to Milankovitic cycles (e.g., *Hays et al.*, 1976). However, both precession and obliquity cycles are dependent on the Earth-Moon configuration and therefore the history of these climate cycles is tied to the evolution of the Earth-Moon system (*Waltham et al.*, 2015). Most studies estimating past climate cycles have assumed either a constant lunar recession rate (*Berger et al.*, 1992) or a constant tidal dissipation rate (*Laskar*, 2004).

However the work presented here together with studies such as *Green and Huber* (2013) or *Egbert et al.* (2004), suggest that tidal dissipation may have strongly varied in the geological past. *Green and Huber* (2013) suggest that globally integrated tidal dissipation rates may have been as low as 1.4 TW during the Eocene. This work shows that during the LGM, tidal dissipation may have increased to 5.8 TW, around 2 TW more than at present. Changes as 'small' as a collapse of the WAIS, with a corresponding

mean sea-level change of 5 m, can evoke a 15% change in M_2 dissipation over timescales of thousands of years. Over geological timescales, much larger sea-level changes and changes in continental configuration over Earth's history have occurred. These would be expected to result in much greater changes in tidal dissipation, as can be seen for the LGM. This also has implications for the calculation of past climate cycles as with large variations in the Earth's tidal dissipation in the past previous estimates of the precession and obliquity cycles harbour considerable uncertainties (see e.g., *Waltham et al.*, 2015).

7.2 Conclusions

Ocean tides are an important physical phenomenon affecting a large range of processes both in the ocean and the climate system. For a large range of coastal, open ocean and climate processes it is not only mean sea-level that is important but most crucially also its variability. Here it has been shown that tides are highly sensitive to large-scale sea-level changes on a large variety of time scales, and that global tidal responses can be seen for even the relatively small present day sea-level changes. Sea-level changes alter the propagation properties of the tidal wave in the ocean and can induce changes in the resonant properties in the ocean. These processes lead to changes in tidal amplitudes and dissipation which are especially prominent for the semi-diurnal tidal constituent M_2, whereas K_1 changes are mostly regional. It has been illustrated that tidal changes can have a wide range of impacts such as altering the large-scale oceanic MOC, or inducing changes in shelf sea productivity and hence affecting carbon export to the deep ocean. It is concluded that sea-level changes on different timescales can lead to large changes in global tidal dynamics. These have the potential to induce feedbacks in both the climate system, alter ecosystems, and have important impacts for societies and economics.

Bibliography

Adkins, J. F., K. McIntyre, and D. P. Schrag. (2002), The salinity, temperature, and δ18O of the glacial deep ocean, *Science*, *298*, 1769–1773, doi:10.1126/science.1076252.

Amante, C., and B. W. Eakins (2009), ETOPO1 1 Arc-Minute Global Relief Model: Procedures, Data Sources and Analysis, NOAA Technical Memorandum NESDIS NGDC-24, *National Geophysical Data Center, NOAA*, 19 pp., doi:10.7289/V5C8276M.

Anandakrishnan, S., D. E. Voigt, R. B. Alley, and M. A. King (2003), Ice stream D flow speed is strongly modulated by the tide beneath the Ross Ice Shelf, *Geophysical Research Letters*, *30*, 1361, doi:10.1029/2002GL016329.

Anderson, J. B., S. S. Shipp, A. L. Lowe, J. S. Wellner, and A. B. Mosola (2002), The Antarctic Ice Sheet during the Last Glacial Maximum and its subsequent retreat history: a review, *Quaternary Science Reviews*, *21*, 49–70, doi:10.1016/S0277-3791(01)00083-X.

Arbic, B. K., D. R. Macayeal, J. X. Mitrovica, and G. A. Milne (2004), Palaeoclimate: ocean tides and Heinrich events., *Nature*, *432*, 460.

Arbic, B. K., P. St-Laurent, G. Sutherland, and C. Garrett (2007a), On the resonance and influence of the tides in Ungawa Bay and Hudson Strait, *Geophysical Research Letters*, *34*, L17,606, doi: 10. 1029/2007GL030,845.

Arbic, B. K., J. X. Mitrovica, D. R. MacAyeal, and G. A. Milne (2008), On the factors behind large Labrador Sea tides during the last glacial cycle and the potential implications for Heinrich events., *Paleoceanography*, *23*, PA3211, doi:10.1029/2007PA001,573.

Arbic, B. K., R. H. Karsten, and C. Garrett (2009), On tidal resonance in the global ocean and the back-effect of coastal tides upon open-ocean tides, *Atmosphere-Ocean*, *47*, 239–266, doi:10.3137/OC311.2009.

Arbic, B. K. and C. Garrett (2010), A coupled oscillator model of shelf and ocean tides. *Continental Shelf Research*, *30*, 564–574, doi:10.1016:/j.csr.2009.07.008.

Arbic, B. K., A. J. Wallcraft, and E. J. Metzger (2010), Concurrent simulation of the eddying general circulation and tides in a global ocean model, *Ocean Modelling*, *32*, 175–187, doi:10.1016/j.ocemod.2010.01.007.

Bamber, J. L., R. E. M. Riva, B. L. A. Vermeersen, and A. M. LeBrocq (2009), Reassessment of the potential sea-level rise from a collapse of the West Antarctic Ice Sheet., *Science*, *324*(5929), 901–903, doi:10.1126/science.1169335.

Bamber, J., and R. Riva (2010), The sea level fingerprint of recent ice mass fluxes, *The Cryosphere*, *4*(4), 621–627.

Bell, T. H. (1975), Topographically generated internal waves in the open ocean, *Journal of Geophysical Research*, *80*(3), 320–327.

C. Bell, J. M. Vassie, P. L. Woodworth (1999), POL/PSMSL Tidal Analysis Software Kit 2000 (TASK-2000). Permanent Service for Mean Sea Level, CCMS Proudman Oceanographic Laboratory, pp. 20

Bentley, M. J., C. O. Cofaigh, J. B. Anderson, H. Conway, B. Davies, A. G. C. Graham, C.-D. Hillenbrand, et al. (2014), A community-based geological reconstruction of Antarctic Ice Sheet deglaciation since the Last Glacial Maximum, *Quaternary Science Reviews*, *100*, 1–9.

Berger A., M. F. Loutre, and J. Laskar (1992), Stability of the astronomical frequencies over the Earth's history for paleoclimate studies, *Science*, *255*, 560–566.

Bindoff, N. L., et al. (2007), *Observations: Oceanic Climate Change and Sea Level. The Physical Science Basis. Contribution of Working Group I to the Fourth Assessment Report of the Intergovernmental Panel on Climate Change [Solomon, S., D. Qin, M. Manning, Z. Chen, M. Marquis, K.B. Av (eds.]*, pp. 387–432, Cambridge University Press, Cambridge, UK, and New York, NY, USA.

Böhm, E., J. Lippold, M. Gutjahr, M. Frank, P. Blaser, B. Antz, J. Fohlmeister, N. Frank, M. B. Andersen, and M. Deininger (2015), Strong and deep Atlantic meridional overturning circulation during the last glacial cycle, *Nature*, *517*(7532), 73–76, doi:10.1038/nature14059.

Bollmann, M., and et, al (2010), *World Ocean Review: Living with the oceans*, 236 pp., Maribus GmbH, Hamburg, Germany.

Bradley, S. L., M. Siddall, G. A. Milne, V. Masson-Delmotte, and E. Wolff (2012), Where might we find evidence of a Last Interglacial West Antarctic Ice Sheet collapse in Antarctic ice core records?, *Global and Planetary Change*, *88–89*, 64–75,doi: 10.1016/j.gloplacha.2012.03.004.

Broecker, W. S., and G. H. Denton (1990), What drives glacial cycles, *Scientific American*, *262*, 48–56.

Brosche, P., Sündermann, J., *Tidal friction and the Earth's rotation*, 242 pp., Springer, Berlin-Heidelberg-New York.

Buijsman, M. C., B. K. Arbic, J. A. M. Green, R. W. Helber, J. G. Richman, J. F. Shriver, P. G. Timko, A. Wallcraft (2015), Optimizing internal wave drag in a forward barotropic model with semidiurnal tides, *Ocean Modelling*, *85*, 42–55, doi: 10.1016/j.ocemod.2014.11.003.

Bye, J. A. T. and R. A. Heath (1975), The New Zealand semidiurnal tide, *Journal of Marine Research*, *33*, 423–442.

Carless, S. J., J. A. M. Green, H. E. Pelling, S-B. Wilmes (2016), Effects of future sea-level rise on tidal processes on the Patagonian Shelf, *Journal of Marine Science*, *submitted for publication.*

Carlson, A. E., and P. U. Clark (2012), Ice sheet sources of sea level rise and freshwater discharge during the last deglaciation, *Reviews of Geophysics*, *50*, RG4007, doi: 10.1029/2011RG000371.

Cartwright, D. E. (1999), *Tides – A scientific history*, Cambridge University Press.

Chassignet, E. P., H. E. Hurlburt, O. M. Smedstad, G. R. Halliwell, P. J. Hogan, A. J. Wallcraft, R. Baraille, and R. Bleck (2007), The HYCOM (HYbrid Coordinate Ocean Model) data assimilative system, *Journal of Marine Systems*, *65*, 60–83, doi:10.1016/j.marsys.20-05.09.016.a

Church, J. A., J. M. Gregory, P. Huybrechts, M. Kuhn, K. Lambeck, M. T. Nhuan, D. Qin, P. L. Woodworth (2001), *Changes in sea level*, In: Houghton, J. T., Ding,

Y., Griggs, D. J, Noguer, M., van der Linden, P., Dai, X., Maskell, K., Johnson, C. I. (eds), Climate change 2001: The Scientific Basis. Contribution of working group 1 to the third assessment report of the intergovernmental panel on climate change, Cambridge University Press, Cambridge.

Church, J. A. and N. J. White (2011), Sea-level rise from the late 19th to the early 21st Century, *Surveys in Geophysics*, *32*, 585–602, doi:10.1007/s10712-011-9119-1.

Church, J. A., et al. (2013), Sea Level. Climate Change 2013, In: Stocker, T.F., D. Qin, G.-K. Plattner, M. Tignor, S.K. Allen, J. Boschung, A. Nauels, Y. Xia, V. Bex and P.M. Midgley (eds.), *The Physical Science Basis. Contribution of Working Group I to the Fifth Assessment Report of the Intergovernmental Panel on Climate Change*, pp. 1137–1216, Cambridge University Press, Cambridge, UK, and New York, NY, USA doi:10.1017/ CBO9781107415324.026.

Clark, J. A., and C. S. Lingle (1977), Future sea-level changes due to West Antarctic ice sheet fluctuations, *Nature*, *269*(5625), 206–209, doi:10.1038/269206a0.

Clark, J. A., and A. C. Mix (1977), Ice sheets and sea level of the Last Glacial Maximum, *Quaternary Science Reviews*, *21*, 1–7, doi:10.1016/S0277-3791(01)00118-4.

Clarke, G., D. Leverington, J. Teller, and A. Dyke (2003), Paleoclimate. Superlakes, megafloods, and abrupt climate change., *Science*, *301*(5635), 922–3, doi: 10.1126/science.1085921.

Clark, P. U., A. S. Dyke, J. D. Shakun, A. E. Carlson, J. Clark, B. Wohlfarth, J. X. Mitrovica, S. W. Hostetler, and A. M. McCabe (2009), The Last Glacial Maximum, *Science*, *325*(5941), 710–714, doi:10.1126/science.1172873.

Carrère, L., F. Lyard, M. Cancet, A. Guillot, and L. Roblou (2012), FES 2012: A new global tidal model taking advantage of nearly 20 years of altimetry, *paper presented at The Symposium 20 Years of Progress in Radar Altimetry*, Venice.

Colosi, J. A., and W. Munk (2006), Tales of the venerable Honolulu tide gauge, *Journal of Physical Oceanography*, *36* 967–996.

Curry, W. B., and D. W. Oppo (2005), Glacial water mass geometry and the distribution of δ^{13}C of ΣCO2 in the western Atlantic Ocean, *Paleoceanography*, *20*, PA1017, doi: 10.1029/2004PA001021.

Devlin, A. T., D. A. Jay, S. A. Talke, and E. D. Zaron (2014), Can tidal perturbations associated with sea level variations in the western Pacific Ocean be used to understand future effects of tidal evolution?, *Ocean Dynamics*, doi:10.1007/s10236-014-0741-6:1-28.

Domack, E. W., E. A. Jacobson, S. Shipp, and J. B. Anderson (1999), Late Pleistocene-Holocene retreat of the West Antarctic Ice-Sheet system in the Ross Sea: Part 2–Sedimentologic and stratigraphic signature, *Geological Society of America Bulletin*, *111*(10), 1517–1536, doi:10.1130/0016-7606(1999)111.

Doodson, A. T. (1922), The harmonic development of the tide-generating potentia, *Proceedings of the Royal Society*, *A100*, 305–329.

Duplessy, J. C., N. J. Shackleton, R. G. Fairbanks, L. Labeyrie, D. Oppo, and N. Kallel (1988), Deepwater source variations during the last climatic cycle and their impact on the global deepwater circulation, *Paleoceanography*, *3*(3), 343–360, doi: 10.1029/PA003i003p00343.

Dyke, A. S., and V. K. Prest (1987), Late Wisconsinan and Holocene History of the Laurentide Ice Sheet, *Géographie physique et Quaternaire*, *41*(2), 237, doi: 10.7202/032681ar.

Dziewonski, A. M., and D. L. Anderson (1981), Preliminary reference Earth model, *Physics of the Earth and Planetary Interiors*, *25*(4), 297–356, doi:10.1016/0031-9201(81)90046-7.

Egbert, G. D., A. F. Bennet, and M. G. G. Foreman (1994), Topex/Poseidon tides estimated using a global inverse model, *Journal of Geophysical Research*, *99*, 24,821–24,852.

Egbert, G. D. (1997), Tidal data inversion: Interpolation and inference, *Progress in Oceanography*, *40*(1), 53–80.

Egbert, G. D., and R. D. Ray. (2000), Significant dissipation of tidal energy in the deep ocean inferred from satellite altimeter data, *Nature*, *405*(6788), 775–778.

Egbert, G. D., and R. D. Ray (2001), Estimates of M2 tidal energy dissipation from Topex/Poseidon altimeter data, *Journal of Geophysical Research*, *106*, 22,475–22,502.

Egbert, G. D., and S. Y. Erofeeva (2002), Efficient inverse Modeling of barotropic ocean tides, *Journal of Atmospheric and Oceanic Technology*, *19*, 183–204.

Egbert, G. D., and R. D. Ray (2003), Deviation of long-period tides from equilibrium: kinematics and geostrophy, *Journal of Physical Oceanography*, *33*(4), 822–839.

Egbert, G. D., B. G. Bills, and R. D. Ray (2004), Numerical modeling of the global semidiurnal tide in the present day and in the last glacial maximum, *Journal of Geophysical Research*, *109*, C03,003, doi:710.1029/2003JC001,973.

FAO (2014), The State of World Fisheries and Aquaculture 2014, Rome, pp. 223.

Farrell, W. E. (1972), Deformation of the Earth by surface loads, *Reviews of Geophysics*, *10*(3), 761–797, doi:10.1029/RG010i003p00761.

Flick, R., J. Murray, and L. Ewing (2003), Trends in United States Tidal Datum Statistics and Tide Range, *Journal of Waterway, Port, Coastal, Ocean Engineering*, *129(4)*, 155–164.

Fok, H. S. (2012), Ocean tides modeling using satellite altimetry, *Geodetic Science Rep. No. 501*, Ohio State Univ., Columbus.

Garrett, C., and E. Kunze (2007), Internal tide generation in the deep ocean, *Annual Reviews of Fluid Mechanics*, *39*, 57–87.

C Garrett, and W Munk (1979), Internal Waves in the Ocean, *Annual Review of Fluid Mechanics*, *11*, 339–369, doi: 10.1146/annurev.fl.11.010179.002011.

Gomez, N., J. X. Mitrovica, M. E. Tamisiea, and P. U. Clark (2010), A new projection of sea level change in response to collapse of marine sectors of the Antarctic Ice Sheet, *Geophys. J. Int.*, *180*(2), 623–634, doi:10.1111/j.1365-246X.2009.04419.x.

Gordeev, R. G., B. A. Kagan, and E. V. Polyakov (1977), The effects of loading and self-attraction on global ocean tides: the model and the results of a numerical experiment, *Journal of Physical Oceanography*, *7* (2), 161–170.

Green, J. A. M. (2010), Ocean tides and resonance, *Ocean Dynamics*, *60*(5), 1243–1253, doi:10.1007/s10236-010-0331-1.

Green, J. A. M., and G. R. Bigg (2011), Impacts on the global ocean circulation from vertical mixing and a collapsing Ice Sheet, *Journal of Marine Research*, *69*, 1–24.

Green, J. M., and T. W. David (2013), Non-assimilated tidal modeling of the South China Sea, *Deep Sea Research Part I: Oceanographic Research Papers*, *78*(null), 42–48, doi:10.1016/j.dsr.2013.04.006.

Green, J. A. M., and M. Huber (2013), Tidal dissipation in the early Eocene and implications for ocean mixing, *Geophysical Research Letters*, *40*(11), 2707–2713, doi:10.1002/grl.50510.

Green, J. A. M., and J. Nycander (2013), A Comparison of Tidal Conversion Parameterizations for Tidal Models, *Journal of Physical Oceanography*, *43*(1), 104–119, doi:10.1175/JPO-D-12-023.1.

Green, J. A. M., C. L. Green, G. R. Bigg, T. P. Rippeth, J. D. Scourse, and K. Uehara (2009), Tidal mixing and the Meridional Overturning Circulation from the Last Glacial Maximum, *Geophysical Research Letters*, *36*, L15,603, doi: 10.1029/2009GL039,309.

Gregory, J. M., P. Huybrechts, and S. C. B. Raper (2004), Climatology: threatened loss of the Greenland ice-sheet, *Nature*, *428*(6983), 616, doi:10.1038/428616a.

Griffiths, S. D., and W. R. Peltier (2008), Megatides in the {Arctic Ocean} under glacial conditions, *Geophysical Research Letters*, *35*, L08,605, doi:10.1029/2008GL033,263.

Griffiths, S. D., and W. R. Peltier (2009), Modeling of polar ocean tides at the Last Glacial Maximum: amplification, sensitivity, and climatological implications, *Journal of Climate*, *22*, 2905–2924, doi:10.1175/2008JCLI2540.1.

Griffiths, S. D., and D. F. Hill (2015), Tidal modeling, In: I. Shennan, A. J. Long and B. P. Horton (eds.) *Handbook of Sea-Level Research*, John Wiley and Sons, Ltd, Chichester, UK, doi:10.1002/9781118452547.ch29

Gudmundsson, G. H. (2011), Ice-stream response to ocean tides and the form of the basal sliding law, *The Cryosphere*, *5*(1), 259–270, doi:10.5194/tc-5-259-2011.

Haigh, I. D., M. Eliot, and C. Pattiaratchi (2011), Global influences of the 18.61 year nodal cycle and 8.85 year cycle of lunar perigee on high tidal levels, *Journal of Geophysical Research*, *116*, C06025, doi:10.1029/2010JC006645.

Haigh, I. D., E. M. S. Wijeratne, L. R. MacPherson, C. B. Pattiaratchi, M. S. Mason, R. P. Crompton, and S. George (2014), Estimating present day extreme total water

level exceedance probabilities around the coastline of Australia: tides, extra-tropical storm surges and mean sea level, *Climate Dynamics*, *42*, 121–138.

Hall, B. L., and G. H. Denton (2000), Extent and Chronology of the Ross Sea Ice Sheet and the Wilson Piedmont Glacier along the Scott Coast at and Since the Last Glacial Maximum, *Geografiska Annaler Series A Physical Geography*, *82A*, 337–363, doi:10.1111/1468-0459.00128.

Hall, R. A., J. M. Huthnance, and R. G. Williams (2011), Internal tides, nonlinear internal wave trains, and mixing in the Faroe-Shetland Channel, *Journal of Geophysical Research*, *116*, C03008, doi:10.1029/2010JC006213.

Hall, G. F., D. F. Hill, B. Horton, S. E. Engelhart, and W. R. Peltier (2012), A high-resolution study of tides in the Delaware Bay: Past conditions and future scenarios, *Geophysical Research Letters*, doi:10.1029/2012GL054675.

Hallberg, R. W., and P. B. Rhines (1996), Buoyancy-driven circulation in an ocean basin with isopycnals intersecting the sloping boundary, *Journal of Physical Oceanography*, *26*, 913–940.

Harig, C., and F. J. Simons (2015), Accelerated West Antarctic ice mass loss continues to outpace East Antarctic gains, *Earth and Planetary Science Letters*, *415*, 134–141, doi:10.1016/j.epsl.2015.01.029.

Hay, C. C., E. Morrow, R. E. Kopp and J. X. Mitrovica (2012), Probabilistic reanalysis of twentieth-century sea-level rise, *Nature*, *517*, 481–484, doi:10.1038/nature14093.

Hays, J. D., J. Imbrie, N. J. Shackleton (1976), Variations in the Earth's Orbit: Pacemaker of the Ice Ages?, *Science*, *198*(4316), 528–53, doi: 10.1126/science.194.4270.1121.

Hein, A. S., C. J. Fogwill, D. E. Sugden, and S. Xu (2011), Glacial/interglacial ice-stream stability in the Weddell Sea embayment, Antarctica, *Earth and Planetary Science Letters*, *307*(1-2), 211–221, doi:10.1016/j.epsl.2011.04.037.

Heinrich, H. (1988), Origin and consequences of cyclic ice rafting in the northeast Atlantic Ocean during the past 130 000 years, *Quaternary Research*, *29*, 143–152.

Hendershott, M. C. (1972), The Effects of Solid Earth Deformation on Global Ocean Tides, *Geophysical Journal International*, *29*(4), 389–402, doi:10.1111/j.1365-246X.1972.tb06167.x.

Hendershott, M. C. (1977), Numerical models of ocean tides, *The Sea vol. 6*, Wiley Interscience Publication, pp. 47–89.

Hendershott, M. C. (1981), Long waves and ocean tides. In:, B. A. Warren and C. Wunsch (eds.), *Evolution of Physical Oceanography. Scientific Surveys in Honor of Henry Stommel*, pp. 292–341, The MIT Press, Cambridge.

Herold N., J. Buzan, M. Seton, A. Goldner, J. A. M. Green, R. D. M'uller, P. Markwick, and M. Huber (2014), A suite of early Eocene (55 Ma) climate model boundary conditions,*Geoscientific Model Development*, *7*, 2077–2090.

Hilbert, D. and S. Cohn-Vossen (1999), *Geometry and the Imagination*, Chelsea, New York pp. 2–3.

Hill, D., S. Griffiths, W. Peltier, B. Horton, and T. Tornqvist (2011), High-resolution numerical modeling of tides in the western {Atlantic, Gulf of Mexico, and Caribbean Sea} during the {Holocene}, *Journal of Geophysical Research*, *in press*, doi:10.1029/2010JC006,896.

Hillenbrand, C.-D., M. Melles, G. Kuhn, and R. D. Larter (2012), Marine geological constraints for the grounding-line position of the Antarctic Ice Sheet on the southern Weddell Sea shelf at the Last Glacial Maximum, *Quaternary Science Reviews*, *32*, 25–47, doi:10.1016/j.quascirev.2011.11.017.

Holligan, P., P. Williams, D. Purdie, and R. Harris (1984), Photosynthesis, respiration and nitrogen supply of plankton populations in stratified, frontal and tidally mixed shelf waters, *Marine Ecology Progress Series*, *17*, 201–213, doi:10.3354/meps017201.

Horsburgh, K. J., and C. Wilson (2007), Tide-surge interaction and its role in the distribution of surge residuals in the North Sea, *Journal of Geophysical Research*, *112*(C8), C08,003, doi:10.1029/2006JC004033.

Huang, R. X. (1999), Mixing and energetics of the oceanic thermohaline circulation, *Journal of Physical Oceanography*, *29*, 727–746.

Jakobsson, M., R. Macnab, L. Mayer, R. Anderson, M. Edwards, J. Hatzky, H. W. Schenke, and P. Johnson (2008), An improved bathymetric portrayal of the Arctic Ocean: Implications for ocean modeling and geological, geophysical and oceanographic analyses, *Geophysical Research Letters*, *35*(7), 1–5, doi:10.1029/2008GL033520.

Jahnke, R. A. (2010), *Global Synthesis 1*, In: Carbon and Nutrient Fluxes in Continental Margins, Springer Berlin Heidelberg, pp. 597-615.

Jay, D. A. and E. P. Flinchem (1997), Interaction of fluctuating river flow with a barotropic tide: A demonstration of wavelet tidal analysis methods, *Journal of Geophysical Research*, *102*, 5705–5720, doi:10.1029/2008GL036185.

Jay, D. A. (2009), Evolution of tidal amplitudes in the eastern Pacific Ocean, *Geophysical Research Letters*, *36*, L04603, doi:10.1029/2008GL036185.

Jayne, S. R., and L. C. St Laurent (2001), Parameterizing tidal dissipation over rough topography, *Geophysical Research Letters*, *28*, 811–814.

Jayne, S. R. (2009), The impact of abyssal mixing parameterizations in an ocean general circulation model, *Journal of Physical Oceanography*, *39*(7), 1756–1775.

Jevrejeva, S., J. C. Moore, A. Grinsted, A. P. Matthews, G. Spada (2014), Trends and acceleration in global and regional sea levels since 1807, *Global and Planetary Change*, *113*, 11–22, doi:10.1016/j.gloplacha.2013.12.004.

Johnson, G. C., S. G. Purkey, and J. M. Toole (2008), Reduced Antarctic meridional overturning circulation reaches the North Atlantic Ocean, *Geophysical Research Letters*, *35*, 1–5.

Joughin, I., B. E. Smith, and B. Medley (2014), Marine ice sheet collapse potentially under way for the Thwaites Glacier Basin, West Antarctica., *Science (New York, N.Y.)*, *344*(6185), 735–738, doi:10.1126/science.1249055.

Kleine T., H., Palme, K. Mezger, and A. N. Halliday (2005), Hf-W chronometry of lunar metals and the age and early differentiation of the Moon, *Science*, *310*, 1671–1674.

Kopp, R. E., F. J. Simons, J. X. Mitrovica, A. C. Maloof and Michael Oppenheimer (2009), Probabilistic assessment of sea level during the last interglacial stage, *Nature*, *462*(7275), 863–867.

Kundu, P. K. (1990), Fluid Mechanics, *Academic Press*, pp. 638.

Lamb, K. G. (2007), Tidally generated near-resonant internal wave triads at a shelf break, *Geophysical Research Letters*, *34*(18), L18607, doi:10.1029/2007GL030825.

Landerer, F. W., J. H. Jungclaus, and J. Marotzke (2008), El Niño-Southern Oscillation signals in sea level, surface mass redistribution, and degree-two geoid coefficients, *Journal of Geophysical Research*, *113*, C08014, doi:10.1029/2008JC004767.

Laplace, P. S. (1799), Mécanique céleste, Paris.

Larter, R. D., A. G. Graham, C.-D. Hillenbrand, J. A. Smith, and J. A. Gales (2012), Late Quaternary grounded ice extent in the Filchner Trough, Weddell Sea, Antarctica: new marine geophysical evidence, *Quaternary Science Reviews*, *53*, 111–122, doi:10.1016/j.quascirev.2012.08.006.

Laskar J., P. Robutel, F. Joutel, M. Gastineau, A. C. M. Correia, and B. Levrard (2004), A long-term numerical solution for the insolation quantities of the Earth, *Astronomy and Astrophysics*, *428*, 261–285.

Ledwell, J. R., E. T. Montgomery, K. L. Polzin, .L C. St Laurent, R. W. Schmitt, and J. M. Toole (2000), Evidence for enhanced mixing over rough topography in the abyssal ocean, *Nature*, *403*, 179–182, doi:10.1038/35003164.

Lenderink, G., and R. J. Haarsma (1994), Variability and multiple equilibria of the thermohaline circulation, associated with deep water formation, *Journal of Physical Oceanography*, *24*, 1480–1493.

Lippold, J., Y. L., R. Francois, S. E. Allen, J. Gherardi, S. Pichat, B. Hickey, and H. Schulz (2012), Strength and geometry of the glacial Atlantic Meridional Overturning Circulation, *Nature Geoscience*, *5*, 813–816, doi:10.1038/ngeo1608.

Liu, Z., S.-I. Shin, R. S. Webb, W. Lewis, and B. L. Otto-Bliesner (2005), Atmospheric CO2 forcing on glacial thermohaline circulation and climate, *Geophysical Research Letters*, *32*, L02706, doi:10.1029/2004GL021929.

Livingstone, S. J., C. Ó Cofaigh, C. R. Stokes, C.-D. Hillenbrand, A. Vieli, and S. S. Jamieson (2012), Antarctic palaeo-ice streams, *Earth-Science Reviews*, *111*(1-2), 90–128, doi:10.1016/j.earscirev.2011.10.003.

Llewellyn Smith, S. G., and W. R. Young (2002), Conversion of the barotropic tide, *Journal of Physical Oceanography*, *32*(5), 1554–1566.

Löfgren, J. S., R. Haas, H.-G. Scherneck (2014), Sea level time series and ocean tide analysis from multipath signals at five GPS sites in different parts of the world, *Journal of Geodynamics*, *80*, 66–80, doi:10.1016/j.jog.2014.02.012.

Lowe, J. A., and J. M. Gregory (2005), The effects of climate change on storm surges around the United Kingdom., *Philosophical transactions. Series A, Mathematical, Physical, and Engineering Sciences*, *363*(1831), 1313–1328, doi: 10.1098/rsta.2005.1570.

Luz Clara, M., C. G. Simionato, E. D'Onofrio, and D. Moreira (2015), Future Sea Level Rise and Changes on Tides in the Patagonian Continental Shelf, *Journal of Coastal Research*, *313*, 519–535, doi:10.2112/JCOASTRES-D-13-00127.1.

Lynch-Stieglitz, J., W. B. Curry, and N. Slowey (1999), Weaker Gulf Stream in the Florida straits during the last glacial maximum, *Nature*, *402*(6762), 644–648, doi: 10.1038/45204.

Lynch-Stieglitz, J., J. F. Adkins, W. B. Curry, T. Dokken, I. R. Hall, J. C. Herguera, J. J-M. Hirschi et al. (2007), Atlantic meridional overturning circulation during the Last Glacial Maximum, *Science*, *316*(5821), 66–69, doi:10.1126/science.1137127.

MacAyeal, D. R. (1984), Thermohaline circulation below the Ross Ice Shelf: A consequence of tidally induced vertical mixing and basal melting, *Journal of Geophysical Research*, *89*(C1), 597–606, doi:10.1029/JC089iC01p00597.

MacAyeal, D. R. (1984), Thermohaline circulation below the Ross Ice Shelf: A consequence of tidally induced vertical mixing and basal melting, *Journal of Geophysical Research*, *89*(C1), 597, doi:10.1029/JC089iC01p00597.

MacKinnon, J. A., and K. B. Winters (2005), Subtropical catastrophe: Significant loss of low-mode tidal energy at 28.9°, *Geophysical Research Letters*, *32*, L15605, doi: 10.1029/2005GL023376.

Makinson, K., P. R. Holland, A. Jenkins, K. W. Nicholls, and D. M. Holland (2011), Influence of tides on melting and freezing beneath Filchner-Ronne Ice Shelf, Antarctica, *Geophysical Research Letters*, *38*(6), 6–11, doi:10.1029/2010GL046462.

Marchitto, T. M., and W. S. Broecker (2006), Deep water mass geometry in the glacial Atlantic Ocean: A review of constraints from the paleonutrient proxy Cd/Ca, *Geochemistry, Geophysics, Geosystems*, *7*(12), Q12003, doi:10.1029/2006GC001323.

Matte,P., D. A. Jay, and Y. Scretan (2014), *Nonstationary Tidal Harmonic Analysis Using NS_ TIDE: Application to the Columbia and St. Lawrence Rivers*, Proceedings of the 17th Physics of Estuaries and Coastal Seas (PECS) conference, Porto de Galinhas, Pernambuco, Brazil.

Mawdsley, R. J., I. D. Haigh, N. C. Wells (2014), *Global changes in tidal high water, low water and range*, In: Green, A.N. and Cooper, J.A.G. (eds.), Proceedings 13th International Coastal Symposium (Durban, South Africa), *Journal of Coastal Research*, *70*, 343–348.

Mawdsley, R. J., I. D. Haigh, and N. C. Wells (2015), Global secular changes in different tidal high water, low water and range levels, *Earth's Future*, *3*(2), 66–81, doi: 10.1002/2014EF000282.

McKay, R., G. Dunbar, T. Naish, P. Barrett, L. Carter, and M. Harper (2008), Retreat history of the Ross Ice Sheet (Shelf) since the Last Glacial Maximum from deep-basin sediment cores around Ross Island, *Palaeogeography, Palaeoclimatology, Palaeoecology*, *260*(1-2), 245–261, doi:10.1016/j.palaeo.2007.08.015.

McManus, J. F., R. Francois, J-M. Gherardi, L. D. Keigwin, and S. Brown-Leger (2004), Collapse and rapid resumption of Atlantic meridional circulation linked to deglacial climate changes, *Nature*, *428*(6985), 834–837, doi:10.1038/nature02494.

Milankovitch, M. (1998) [1941], Canon of Insolation and the Ice Age Problem, Belgrade: Zavod za Udzbenike i Nastavna Sredstva. ISBN 86-17-06619-9.; see also "Astronomical Theory of Climate Change"

Milne, G. A., and J. X. Mitrovica (1996), Postglacial sea-level change on a rotating Earth: first results from a gravitationally self-consistent sea-level equation, *Geophysical Journal International*, *126*(3), F13–F20, doi:10.1111/j.1365-246X.1996.tb04691.x.

Mitrovica, J. X., N. Gomez, and P. U. Clark (2009), The sea-level fingerprint of West Antarctic collapse., *Science*, *323*(5915), 753, doi:10.1126/science.1166510.

Mitrovica, J. X., N. Gomez, E. Morrow, C. Hay, K. Latychev, and M. E. Tamisiea (2011), On the robustness of predictions of sea level fingerprints, *Geophysical Journal International*, *187*(2), 729–742, doi:10.1111/j.1365-246X.2011.05090.x.

Moon, T., I. Joughin, B. Smith, and I. Howat (2012), 21st-century evolution of Greenland outlet glacier velocities., *Science*, *336*(6081), 576–578, doi:10.1126/science.1219985.

Montenegro, A., M. E., A. J. Weaver, and S. R. Jayne (2007), Response of a climate model to tidal mixing parameterization under present day and last glacial maximum conditions, *Ocean Modelling*, *19*(3), 125–137, doi:10.1016/j.ocemod.2007.06.009.

Mosola, A. B., and J. B. Anderson (2006), Expansion and rapid retreat of the West Antarctic Ice Sheet in eastern Ross Sea: possible consequence of over-extended ice streams?, *Quaternary Science Reviews*, *25*(17-18), 2177–2196, doi: 10.1016/j.quascirev.2005.12.013.

Mouginot, J., E. Rignot, and B. Scheuchl (2014), Sustained increase in ice discharge from the Amundsen Sea Embayment, West Antarctica, from 1973 to 2013, *Geophysical Research Letters*, *41*(5), 1576–1584, doi:10.1002/2013GL059069.

Müller, M. (2008), Synthesis of forced oscillations, Part I: Tidal dynamics and the influence of the loading and self-attraction effect, *Ocean Modelling*, *20*(3), 207–222, doi:10.1016/j.ocemod.2007.09.001.

Müller, M., B. K. Arbic, and J. X. Mitrovica (2011), Secular trends in ocean tides: Observations and model results, *Journal of Geophysical Research*, *116*(C5), C05013, doi:10.1029/2010JC006387.

Müller, M., B. K. Arbic, and J. X. Mitrovica (2011), Secular trends in ocean tides: Observations and model results, *Journal of Geophysical Research*, *116*(C5), C05013, doi:10.1029/2010JC006387.

Müller, M. (2011), Rapid change in semi-diurnal tides in the North Atlantic since 1980, *Geophysical Research Letters*, *38*, L11602, doi:10.1029/2011GL047312.

Müller, M., J. Y. Cherniawsky, M. G. G. Foreman, and J.-S. von Storch (2012), Global map of M2 internal tide and its seasonal variability from high resolution ocean circulation and tide modeling, *Geophysical Research Letters*, *39*, L19607, doi: 10.1029/2012GL053320.

Munk, W. H., G. J. Macdonald (1960), *The rotation of the earth: a geophysical discussion*, Cambridge University Press, pp. 323.

Munk, W. H. (1966), Abyssal recipes, *Deep Sea Research and Oceanographic Abstracts*, *13*(4), 707–730, doi:10.1016/0011-7471(66)90602-4.

Munk, W., and C. Wunsch (1998), Abyssal recipes II: energetics of tidal and wind mixing, *Deep Sea Research Part I Oceanographic Research Papers*, *45*(12), 1977–2010, doi:10.1016/S0967-0637(98)00070-3.

Nerem, R. S., D. P. Chambers, E. W. Leuliette, G. T. Mitchum, and B. S. Giese (1999), Variations in global mean sea level associated with the 1997–1998 ENSO event: Implications for measuring long term sea level change, *Geophysical Research Letters*, *26*(19), 3005–3008.

Nerem, R. S., E. Leuliette, and A. Cazenave (2006), Present-day sea-level change: A review, *Comptes Rendus Geoscience*, *338*, 1077–1083.

Nerem, R. S., D. Chambers, C. Choe, and G. T. Mitchum (2010), Estimating Mean Sea Level Change from the TOPEX and Jason Altimeter Missions, *Marine Geodesy*, *33*, 435.

Newton, I. (1687), Philosophiae Naturalis Principia Mathematica.

Nicholls, R. J., and A. Cazenave (2010), Sea-Level Rise and Its Impact on Coastal Zones, *Science*, *328*(5985), 1517–1520, doi:10.1126/science.1185782.

Nicholls-Lee, R. F., and S. R. Turnock (2008), Tidal energy extraction: renewable, sustainable and predictable, *Science Progress*, *91*(1), 81–111, doi: 10.3184/003685008X285582.

Nycander, J. (2005), Generation of internal waves in the deep ocean by tides, *Journal of Geophysical Research*, *110*, C10,028, doi:10.1029/2004JC002,487.

Otto-Bliesner, B. L., C. D. Hewitt, T. M. Marchitto, E. Brady, A. Abe-Ouchi, M. Crucifix, S. Murakami, and S. L. Weber (2007), Last Glacial Maximum ocean thermohaline circulation: PMIP2 model intercomparisons and data constraints, *Geophysical Research Letters*, *33*, 435.

Oppenheimer, M. (1998), Global warming and the stability of the West Antarctic Ice Sheet, *Nature*, *393*(6683), 325–332, doi:10.1038/30661.

Pachauri, R. K., et al. (2014), *Climate Change 2014: Synthesis Report. Contribution of Working Groups I, II and III to the Fifth Assessment Report of the Intergovernmental Panel on Climate Change*, Pachauri, R. and L. Meyer (eds.), Geneva, Switzerland, IPCC, 151 pp.

Parke, M. E., and M. C. Hendershott (1980), M2, S2, K1 models of the global ocean tide on an elastic earth, *Marine Geodesy*, *3*, 379–408.

Pawlowicz, R., B. Beardsley, and S. Lentz (2002), Classical tidal harmonic analysis including error estimates in MATLAB using T_TIDE, *Computers and Geosciences*, *28*, 929–937.

Pelling, H. E., and J. A. Mattias Green (2013), Sea level rise and tidal power plants in the Gulf of Maine, *Journal of Geophysical Research: Oceans*, *118*(6), 2863–2873, doi:10.1002/jgrc.20221.

Pelling, H. E., J. A. M. Green, and S. L. Ward (2013), Modelling tides and sea-level rise: To flood or not to flood, *Ocean Modelling*, *63*, 21–29, doi: 10.1016/j.ocemod.2012.12.004.

Pelling, H. E., K. Uehara, and J. A. M. Green (2013), The impact of rapid coastline changes and sea level rise on the tides in the Bohai Sea, China, *Journal of Geophysical Research*, *118*, 3462–3472, doi:10.1002/jgrc.20258.

Peltier, W. R. (2004), Global glacial isostacy and the surface if the ice-age earth: The ICE-5G (VM2) model and Grace, *Annual Review of Earth and Planetary Sciences*, *32*, 111–149.

Peltier, W. R. (2007), Postglacial coastal evolution: Ice-ocean-solid Earth interactions in a period of rapid climate change, *Geological Society of America Special Papers*, *426*, 5–28, doi:10.1130/2007.2426(02).

Vettoretti, G., and W. R. Peltier (2014), Interhemispheric air temperature phase relationships in the nonlinear Dansgaard-Oeschger oscillation, *Geophysical Research Letters*, *42*, 1180–1189, doi:10.1002/2014GL062898.

Pekeris, C. L. and Accad, Y. (1969), Solution of Laplace's equations for M_2 tide in the world oceans, *Phil. Trans. R. Soc. Lond.*, *265*, 413–436.

Perillo, G. M. E. (1995), *Geomorphology and sedimentology of estuaries*, 471 pp., Elsevier, Amsterdam, New York.

Pfeffer, W. T., J. T. Harper, and S. O'Neel (2008), Kinematic Constraints on Glacier Contributions to 21st-Century Sea-Level Rise, *Science*, *321*, 1340–1342. doi: 10.1126/science.1159,099.

Pickering, M., N. Wells, K. Horsburgh, and J. Green (2012), The impact of future sea-level rise on the European Shelf tides, *Continental Shelf Research*, *35*, 1–15, doi: 10.1016/j.csr.2011.11.011.

Pingree, R., P. Holligan, and G. Mardell (1978), The effects of vertical stability on phytoplankton distributions in the summer on the northwest European Shelf, *Deep Sea Research*, *25*(11), 1011–1028, doi:10.1016/0146-6291(78)90584-2.

Platzman, G. W. (1975), Normal modes of the Atlantic and Indian Oceans, *Journal of Physical Oceanography*, *5*, 201–221.

Platzman, G. W., G. A. Curtis, K. S. Hansen, and R. D. Slater (1981), Normal modes of the world ocean 2. Description of modes in the periods range 8 to 80 hours, *Journal of Physical Oceanography*, *11*, 579–603.

Pauly, D., V. Christensen, S. Guenette, T. J. Pitcher, U. R. Sumaila, C. J. Walters, R. Watson, D. Zeller (2002), Towards sustainability in world fisheries, *Nature*, *418*, 689–695.

Polzin, K. L., J. M. Toole, J. R. Ledwell, and R. W. Schmitt (1997), Spatial variability of turbulent mixing in the abyssal ocean, *Science*, *276*, 93–96.

Pritchard, H. D., and D. G. Vaughan (2007), Widespread acceleration of tidewater glaciers on the Antarctic Peninsula, *Journal of Geophysical Research*, *112*(F3), F03S29, doi:10.1029/2006JF000597.

Pugh, D. T. (1981), Tidal amphidrome movement and energy dissipation in the Irish Sea. *Geophysical Journal International*, *67*(2), 515–527.

Pugh, D. T. (1996), *Tides, surges and mean sea-level (reprinted with corrections)*, John Wiley & Sons Ltd.

Pugh, D. T., and Woodworth, P. L. (2014), *Sea-level science: understanding tides, surges tsunamis and mean sea-level changes*, Cambridge University Press, pp. 407.

Rahmstorf, S. (2002), Ocean circulation and climate during the past 120,000 years, *Nature*, *419*, 207–214.

Ray, R. D. (1998), Ocean self-attraction and loading in numerical tidal models, *Marine Geodesy*, *21*(3), 181–192.

Ray, R. D. (2006), Secular changes of the M2 tide in the Gulf of Maine, *Continental Shelf Research*, *26*, 422–427.

Ray, R. D. (2009), Secular changes of the solar semidiurnal tide of the western North Atlantic Ocean, *Geophysical Research Letters*, *36*, L19601.

Ray, R. D. and B. C. Douglas (2011), Experiments in reconstructing twentieth-century sea levels, *Progress in Oceanography*, *91*(4), 496–515.

Raymo, M., and J. .X. Mitrovica (2012), Collapse of Polar Ice Sheets During the Stage 11 Interglacial, *Nature*, *483*, 453–456.

Rienecker, M. M., and M. D. Teubner (1980), A note on frictional effects in Taylor's problem, *Journal of Marine Research*, *38*(2), 183–191.

Rignot, E., and P. Kanagaratnam (2006), Changes in the velocity structure of the Greenland Ice Sheet, *Science*, *311*(5763), 986–690, doi:10.1126/science.1121381.

Rignot, E., J. Mouginot, M. Morlighem, H. Seroussi, and B. Scheuchl (2014), Widespread, rapid grounding line retreat of Pine Island, Thwaites, Smith, and Kohler glaciers, West Antarctica, from 1992 to 2011, *Geophysical Research Letters*, *41*(10), 3502–3509, doi:10.1002/2014GL060140.

Rippeth, T. P. and M. E. Inall (2002), Observations of the internal tide and associated mixing across the Malin Shelf, *Journal of Geophysical Research*, *107*(C4), 3028.

Rippeth, T. P., J. D. Scourse, K. Uehara, and S. McKeown (2008), Impact of sea-level rise over the last deglacial transition on the strength of the continental shelf CO2 pump, *Geophysical Research Letters*, *35*, L24604, doi:10.1029/2008GL035880.

Ritz, S. P., T. F. Stocker, J. O. Grimalt, L. Menviel, and A. Timmermann (2013), Estimated strength of the Atlantic overturning circulation during the last deglaciation, *Nature Geoscience*, *6*(3), 208–212, doi:10.1038/ngeo1723.

Robinson, A., R. Calov, and A. Ganopolski (2012), Multistability and critical thresholds of the Greenland ice sheet, *Nature Climate Change*, *2*(6), 429–432, doi:10.1038/nclimate1449.

Rosier, S. H. R., J. A. M. Green, J. D. Scourse, and R. Winkelmann (2014), Modeling Antarctic tides in response to ice shelf thinning and retreat, *Journal of Geophysical Research: Oceans*, *119*(1), 87–97, doi:10.1002/2013JC009240.

Rosier, S. H. R., G. H. Gudmundsson, and J. A. M. Green (2014), Insights into ice stream dynamics through modelling their response to tidal forcing, *The Cryosphere*, *8*, 1763–1775, doi:10.5194/tc-8-1763-2014.

Rudnick, D. L., T. J. Boyd, R. E. Brainard, G. S. Carter, G. D. Egbert, M. C. Gregg, P. E. Holloway et al. (2003), From tides to mixing along the Hawaiian Ridge, *Science*, *301*(5631), 355–357, doi:10.1126/science.1085837.

Savcenko R., and W. Bosch (2012), EOT11a - Empirical Ocean Tide Model From Multi-Mission Satellite Altimetry, *DGFI Report No. 89*.

Schmittner, A., and G.-D. Egbert (2014), An improved parameterization of tidal mixing for ocean models, *Geoscientific Model Development*, *7*, 211–224, doi:doi:10.5194/gmd-7-211-2014.

Schmittner, A., J. A. M. Green, and S.-B. Wilmes (2015), Glacial ocean overturning intensified by tidal mixing in a global circulation model, *Geophysical Research Letters*, *42*(10), 4014–4022, doi:10.1002/2015GL063561.

Schwiderski, E. W. (1980), On charting global ocean tides, *Reviews in Geophysics*, *18*(1), 243–268, doi:10.1029/RG018i001p00243.

Source, J. D. (2013), *Quaternary Sea Level and Palaeotidal Changes: A Review of Impacts on, and Responses of, the Marine Biosphere in Oceanography and Marine Biology*, An Annual Review (Book 51), CRC Press, 468 pp.

Sharples J. and P. M. Holligan (2006), Interdisciplinary processes in the Celtic Seas, In: Robinson A. R., Brink K. H. (eds), *The Sea*, vol. 14B, Cambridge, MA, Harvard University Press; pp. 1003-1031.

Shennan, I. (2015), Handbook of sea-level research: framing research questions, In: I. Shennan, A. J. Long and B. P. Horton, *Handbook of Sea-Level Research*, John Wiley and Sons, Ltd, Chichester, UK, doi:10.1002/9781118452547.ch29

Shepherd, A., E. R. Ivins, A. Geruo, V. R. Barletta, M. J. Bentley, S. Bettadpur, K. H. Briggs, et al. (2012), A reconciled estimate of ice-sheet mass balance, *Science*, *338*(6111), 1183–1189.

Shum, C. K., P. L. Woodworth, O. B. Andersen, G. D. Egbert, O. Francis, C. King, S. M. Klosko, C. Le Provost, X. Li, J.-M. Molines, M. E. Parke, R. D. Ray, M. G. Schlax, D. Stammer, C. C.Tierney, P. Vincent, and C. I. Wunsch (1997), Accuracy assessment of recent ocean tide models, *Journal of Geophysical Research*, *102*, 25,173–25,194.

Shipp, S., J. B. Anderson, and E. W. Domack (1999), Late Pleistocene-Holocene retreat of the west Antarctic ice-sheet system in the ross sea: part 1– geophysical results, *Geological Society of*, *111*, 1486–1516, doi:10.1130/0016-7606(1999)111<1486.

Simpson, J. H., and J. Hunter (1974), Fronts in the Irish Sea, *Nature*, *250*, 404–406, doi: 10.1038/250,404a0.

Simpson, J. H., and R. D. Pingree (1978), Shallow sea fronts produced by tidal stirring, In: Bowman, M. J. and W. E. Esaias, *Oceanic fronts in coastal processes*, Springer Berlin Heidelberg, pp. 29–42.

J. H. Simpson and D. Bowers (1981), Models of stratification and frontal movement in shelf seas, *Deep Sea Research Part A. Oceanographic Research Papers*, *28*(7), 727–738, doi:10.1016/0198-0149(81)90132-1.

Simpson, J. H., and J. Sharples (2012), *Introduction to the Physical and Biological Oceanography of Shelf Seas*, 448 pp., Cambridge University Press, Cambridge.

Skiba, A. W., L. Zeng, B. K. Arbic, M. Müller, and W. J. Godwin (2013), On the Resonance and Shelf/Open-Ocean Coupling of the Global Diurnal Tides, *Journal of Physical Oceanography*, *43*(7), 1301–1324, doi:10.1175/JPO-D-12-054.1.

Smith, W. H., and D. T. Sandwell (1997), Global Sea Floor Topography from Satellite Altimetry and Ship Depth Soundings, *Science*, *277*(5334), 1956–1962, doi: 10.1126/science.277.5334.1956.

Sprintall, J., S. E. Wijffels, R. Molcard, and I. Jaya (2009), Direct estimates of the Indonesian Throughflow entering the Indian Ocean: 2004–2006, *Journal of Geophysical Research*, 114, C07001, doi:10.1029/2008JC005257.

Stammer, D., et al. (2014), Accuracy assessment of global barotropic ocean tide models, *Reviews of Geophysics*, *52*(3), 243–282, doi:10.1002/2014RG000450.

Stammer, D., A. Cazenave, R. M. Ponte, and M. E. Tamisiea (2013), Causes for contemporary regional sea level changes, *Annual Review of Marine Science*, *5*, 21–46, doi:10.1146/annurev-marine-121211-172406.

Stewart, R. H. (2009), *Introduction to the Physical and Oceanography*, 345 pp., Orange Grove Books.

St. Laurent, L., and C. Garrett (2002), The Role of Internal Tides in Mixing the Deep Ocean, *Journal of Physical Oceanography*, *32*, 2882–2899.

St. Laurent, L. S., S. Stringer, C. Garrett, and D. Perrault-Joncas (2003), The generation of internal tides at abrupt topography, *Deep Sea Research Part I: Oceanographic Research Papers*, *50*(8), 987–1003.

St. Laurent, L. and H. Simmons (2006), Estimates of power consumed by mixing in the ocean interior, *Journal of Climate*, *19*, 4877–4890, doi:10.1175/JCLI3887.1.

Stocker, T. F., D. G. Wright, and W. S. Broecker (1992), The influence of high-latitude surface forcing on the global thermohaline circulation, *Paleoceanography*, *7*(5), 529–541, doi:10.1029/92PA01695.

Stolldorf, T., H.-W. Schenke, and J. B. Anderson (2012), LGM ice sheet extent in the Weddell Sea: evidence for diachronous behavior of Antarctic Ice Sheets, *Quaternary Science Reviews*, *48*, 20–31, doi:10.1016/j.quascirev.2012.05.017.

Stommel, H. M. (1961), Thermohaline convection with two stable regimes, *Tellus*, *13*, 224–230.

Stommel H. M. (1966), *The gulf stream: A physical and dynamical description*, 248 pp., Cambridge University Press, Cambridge.

Sverdrup, H. U. (1942), *The Oceans, Their Physics, Chemistry, and General Biology*, 1087 pp., Prentice Hall, New York.

Taguchi, E., W. Zahel, and D. Stammer (2014), Inferring deep ocean tidal energy dissipation from the global high-resolution data-assimilative HAMTIDE model, *Journal of Geophysical Research: Oceans*, *119*, 4573–4592, doi:10.1002/2013JC009766.

Taylor, G., (1921), Tidal oscillations in gulfs and rectangular basins, *Proceedings of the London Mathematical Society*, *20*, 148–181.

Thomas, M., and J. Söndermann (1999), Tides and tidal torques of the world ocean since the last glacial maximum, *Journal of Geophysical Research*, *104*, 3159–3183.

Thomas, H., Y. Bozec, K. Elkalay, and H. J. W. de Baar (2004), Enhanced open ocean storage of CO2 from shelf sea pumping, *Science*, *304*(5673), 1005–1008, doi: 10.1126/science.1095491.

Timmermann, A., S. McGregor, and F.-F. Jin (2010), Wind Effects on Past and Future Regional Sea Level Trends in the Southern Indo-Pacific, *Journal of Climate*, *23*, 4429–4437, doi:10.1175/2010JCLI3519.1.

Tsunogai, S., S. Watanabe, and T. Suto (1999), Is there a 'continental shelf pump' for the absorption of atmospheric CO_2?, *Tellus*, *51B*, 701–712, doi:10.1034/j.1600-0889.1999.t01-2-00010.x.

Uehara, K. (2005), Changes of ocean tides along Asian coasts caused by the post glacial sea-level change, in *Mega-Deltas of Asia: Geological Evolution and Human Impact*, edited by Z. Chen, Y. Saito, and S. L. Goodbred Jr., pp. 227—-232, China Ocean Press.

Uehara, K., J. D. Scourse, K. J. Horsburgh, K. Lambeck, and A. P. Purcell (2006), Tidal evolution of the northwest European shelf seas from the Last Glacial Maximum to the present, *Journal of Geophysical Research*, *111*, C09,025, doi: 10. 1029/2006JC003,531.

Vaughan, D. G. (1995), Tidal flexure at ice shelf margins, *Journal of Geophyical Research*, *100*(B4), 6213–6224, doi:10.1029/94JB02467.

Velicogna, I. (2009), Increasing rates of ice mass loss from the Greenland and Antarctic ice sheets revealed by GRACE, *Geophysical Research Letters*, *36*, doi: 10.1029/2009GL040222.

Velicogna, I., T. C. Sutterley, and M. R. van den Broeke (2014), Regional acceleration in ice mass loss from Greenland and Antarctica using GRACE time-variable gravity data, *Geophysical Research Letters*, *41*(22), 8130–8137, doi:10.1002/2014GL061052.

Vermeer, M., and S. Rahmstorf (2009), Global sea level linked to global temperature, *Proceedings of the National Academy of Sciences of the United States of America*, *106*, 21,527–21,532.

Vignudelli, S., P. Cipollini, L. Roblou, F. Lyard, G. P. Gasparini, G. Manzella, and M. Astraldi (2005), Improved satellite altimetry in coastal systems: Case study of the Corsica Channel (Mediterranean Sea), Geophys. Res. Lett., 32, L07608, doi:10.1029/2005GL022602.

Waltham, D. (2015), Milankovitch Period Uncertainties and Their Impact On Cyclostratigraphy, *Journal of Sedimentary Research*, *85*(8), 990–998, doi: 10.2110/jsr.2015.66.

Wakelin, S. L., P. L. Woodworth, R. A. Flather, and J. A. Williams (2003), Sea-level dependence on the NAO over the NW European Continental Shelf, *Geophysical Research Letters*, *30*, 1403, doi:10.1029/2003GL017041.

Ward, S. L., J. A. M. Green, and H. E. Pelling (2012), Tides, sea-level rise and tidal power extraction on the European shelf, *Ocean Dynamics*, doi:10.1007/s10236-012-0552-6.

Ward, S. L., J. A. M. Green, and H. E. Pelling (2012), Tides, sea-level rise and tidal power extraction on the European shelf, *Ocean Dynamics*, doi:10.1007/s10236-012-0552-6.

Weber, M. E., W. Ricken, P. U. Clark, G. Kuhn, S. W. Hostetler, and J. X. Mitrovica (2011), Interhemispheric Ice-Sheet Synchronicity During the Last Glacial Maximum, doi:10.1126/science.1209299.

Wilmes, S.-B., and J. A. M. Green (2014), The evolution of tides and tidal dissipation over the past 21,000 years, *Journal of Geophysical Research: Oceans*, pp. 4083–4100, doi:10.1002/2013JC009605.

Winkelmann, R., A. Levermann, K. Frieler, M. A. Martin (2012), Uncertainty in future solid ice discharge from Antarctica, *The Cryosphere Discussions*, *6*, 673–714, doi: 10.5194/tcd-6-673-2012.

Woodworth, P. L. (2010), A survey of recent changes in the main components of the ocean tide, *Continental Shelf Research*, *30*, 1680–1691, doi:10.1016/j.csr.2010.07.002.

Wunsch, C. (2003), Determining paleoceanographic circulations, with emphasis on the Last Glacial Maximum, *Quaternary Science Reviews*, *22*, 371–385, doi:10.1016/S0277-3791(02)00177-4.

Wunsch, C. and R. Ferrari (2004), Vertical mixing, energy and the general circulation of the oceans, *Annual Review of Fluid Mechanics*, *36*, 281–314, doi: 10.1146/annurev.fluid.36.050802.122121.

Yuan, L., B- F. Chao, X. Ding, and P. Zhong (2013), The tidal displacement field at Earth's surface determined using global GPS observations, *Journal of Geophysical Research, Solid Earth*, *118*, 2618–2632, doi:10.1002/jgrb.50159.

Yue, S., P. Pilon and G. Cavadias (2002), Power of the Mann-Kendall and Spearman's rho tests for detecting monotonic trends in hydrological series, *Journal of Hydrology*, *259*, pp. 254–271.

Zaron, E. D., and G. D. Egbert (2006), Estimating open-ocean barotropic tidal dissipation: The Hawaiian Ridge, *Journal of Physical Oceanography*, *36*, 1019–1035.

Zaron, E. D., and D. A. Jay (2014), An analysis of secular change in tides at open-ocean sites in the Pacific, *Journal of Physical Oceanography*, *44(7)*, 1704–1726.

Zhou, Q., W. Duan, M. Mu, and R. Feng (2015), Influence of positive and negative Indian Ocean Dipoles on ENSO via the Indonesian Throughflow: Results from sensitivity experiments, *Advances in Atmospheric Sciences*, *32*(6), 783–793.

Zu, T., J. Gan, and S. Y. Erofeeva (2008), Numerical study of the tide and tidal dynamics in the South China Sea, *Deep Sea Research Part I: Oceanographic Research Papers*, *55*(2), 137–154, doi:10.1016/j.dsr.2007.10.007.

Chapter 8

Appendix

AGU PUBLICATIONS

JGR

Journal of Geophysical Research: Oceans

RESEARCH ARTICLE
10.1002/2013JC009605

The evolution of tides and tidal dissipation over the past 21,000 years

S.-B. Wilmes[1] and J. A. M. Green[1]

[1]School of Ocean Sciences, College of Natural Sciences, Bangor University, Menai Bridge, UK

Key Points:
- M2 tidal amplitudes and dissipation were strongly enhanced during the LGM
- Changes in the LGM K1 tides were confined to areas where K1 dominates today
- The deglacial M2 tides were closely linked to ice sheet groundling line locations

Correspondence to:
S.-B. Wilmes,
s.wilmes@bangor.ac.uk

Citation:
Wilmes, S.-B., and J. A. M. Green (2014), The evolution of tides and tidal dissipation over the past 21,000 years, *J. Geophys. Res. Oceans*, *119*, doi:10.1002/2013JC009605.

Received 11 NOV 2013
Accepted 13 JUN 2014
Accepted article online 16 JUN 2014

Abstract The 120 m sea-level drop during the Last Glacial Maximum (LGM; 18–22 kyr BP) had a profound impact on the global tides and lead to an increased tidal dissipation rate, especially in the North Atlantic. Here, we present new simulations of the evolution of the global tides from the LGM to present for the dominating diurnal and semidiurnal constituents. The simulations are undertaken in time slices spanning 500–1000 years. Due to uncertainties in the location of the grounding line of the Antarctic ice sheets during the last glacial, simulations are carried out for two different grounding line scenarios. Our results replicate previously reported enhancements in dissipation and amplitudes of the semidiurnal tide during LGM and subsequent deglaciation, and they provide a detailed picture of the large global changes in M_2 tidal dynamics occurring over the deglaciation period. We show that Antarctic ice dynamics and the associated grounding line location have a large influence on global semidiurnal tides, whereas the diurnal tides mainly experience regional changes and are not impacted by grounding line shifts in Antarctica.

1. Introduction

The 120–130 m ice-equivalent sea-level reduction during the Last Glacial Maximum (LGM; some 22,000–18,000 years before present; henceforth 22–18 kyr BP) had a significant impact on the tides on a variety of scales due to the exposure of the continental shelf seas [e.g., *Egbert et al*., 2004; *Arbic et al*., 2004; *Uehara et al*., 2006; *Griffiths and Peltier*, 2008, 2009; *Green*, 2010; *Hill et al*., 2011; *Hall et al*., 2013]. The main effect on the tides was the increase of the total amount of semidiurnal tidal energy lost in the ocean during the LGM to levels far above present. Furthermore, the main part of this energy dissipated in the deep ocean and not in shallow shelf seas as is the case today [*Egbert and Ray*, 2001]. As the sea-level rose at the end of the glacial period the present-day shelf seas flooded and there was a subsequent shift in the tidal dissipation from the open ocean to the newly flooded shelf seas [e.g., *Egbert et al*., 2004; *Uehara et al*., 2006; *Green*, 2010]. Here we present new simulations of the evolution of the near-global tides from the LGM to the present. The purpose of this investigation is threefold: (i) to present the evolution of the global semidiurnal tides at higher temporal and spatial resolutions than previously reported [e.g., *Egbert et al*., 2004; *Uehara et al*., 2006; *Hill et al*., 2011; *Hall et al*., 2013], (ii) to describe the evolution of the diurnal tides from the LGM to the present, and (iii) to investigate the sensitivity of the global tides at present and during the LGM to the location of ice sheet grounding lines, thus extending the work by *Griffiths and Peltier* [2009].

Previous simulations of the paleoocean tides show surprising results, with total globally integrated dissipation some 30% larger than at present and a larger fraction of this energy dissipating in the deep ocean [*Egbert et al*., 2004; *Green*, 2010]. The dissipation in the semidiurnal band increased far more than that of the diurnal constituents [*Green*, 2010], which implies that the mechanism behind these shifts is tidal resonance [*Egbert et al*., 2004; *Griffiths and Peltier*, 2008; *Arbic et al*., 2009; *Green*, 2010]. Removing the shelf seas effectively reduces the damping of the tides, which—when the ocean basin is close to resonance—leads to an increased tidal amplitude and associated dissipation of energy [see *Egbert et al*., 2004; *Green*, 2010, especially their Figures 11 and 1, respectively]. The present-day North Atlantic has natural resonant periods of 12.66, 12.8, and 14.4 h [*Platzman*, 1975; *Platzman et al*., 1981; *Müller*, 2008], which explains why there may have been megatides present there during the LGM [e.g., *Uehara et al*., 2006; *Arbic et al*., 2007; *Griffiths and Peltier*, 2008, 2009]. Furthermore, *Arbic et al*. [2009] and *Skiba et al*. [2013] show that adding a shelf ocean which is close to resonance to a deep ocean basin that is also close to resonance reduces the deep ocean tides of the ocean basin; this is analogous to when the European and Patagonian shelves flooded during the deglaciation after the LGM.

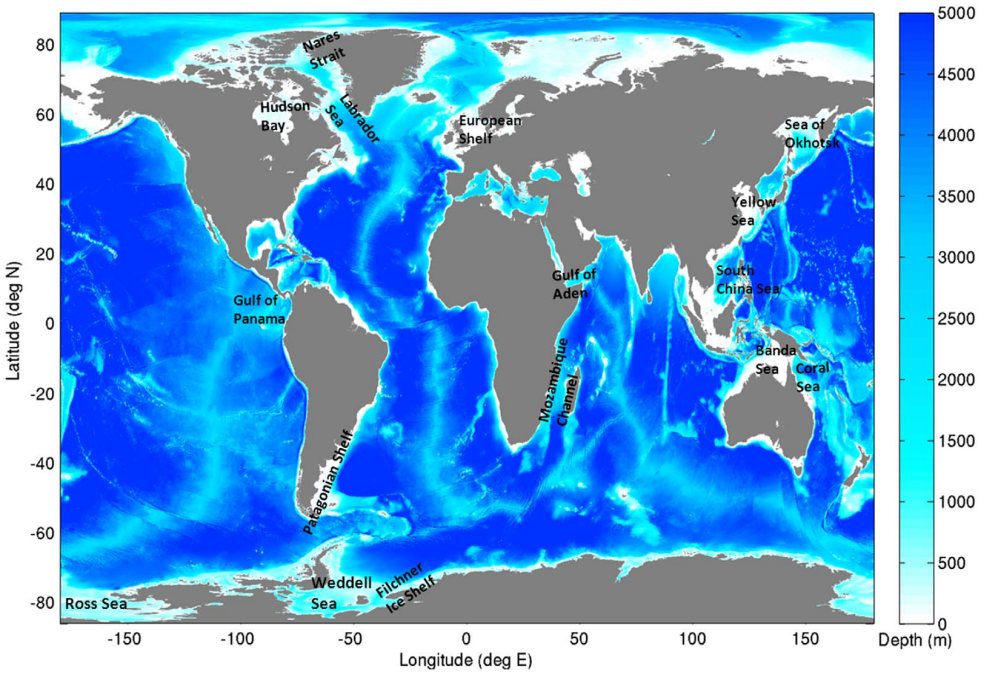

Figure 1. Present-day bathymetry assembled from the Smith and Sandwell, v.14, IBCAO, v.2, and ETOPO1 databases. Regions mentioned in subsequent sections of this paper are marked on the map.

The bathymetry under and the extent of floating ice shelves in Antarctica are important in determining the regional tidal dynamics [*Griffiths and Peltier*, 2009; *Rosier et al*., 2014]. However, there is an ongoing debate about the exact grounding line location of the Antarctic Ice Sheet during the LGM and the subsequent deglacial period. This is especially true for the Weddell Sea sector (see Figure 1), where estimates range from an ice sheet grounded at the shelf margin [e.g., *Hall and Denton*, 2000; *Larter et al*., 2012; *Anderson et al*., 2002] to an only partially grounded ice sheet within the Weddell Sea, with strongly differing estimates over the timing of the initiation of deglaciation [e.g., *Stolldorf et al*., 2012; *Hein et al*., 2011; *Hillenbrand et al*., 2012]. For the Western Ross Sea, however, there is a general consensus that the ice sheet grounded at the present-day shelf break during the LGM [e.g., *Anderson et al*., 2002; *Domack et al*., 1999; *Hall and Denton*, 2000; *McKay et al*., 2008; *Livingstone et al*., 2012]. Although the behavior of the ice masses in the Western Ross Sea has been extensively researched, ambiguity of both LGM extent and deglacial behavior exists for the Eastern Ross Sea [e.g., *Shipp et al*., 1999; *Anderson et al*., 2002; *Mosola and Anderson*, 2006]. *Griffiths and Peltier* [2009] investigate regional changes in the polar LGM tides in global tidal simulations in response to different grounding line locations of both the Antarctic Ice Sheet and the ice sheet occupying the Queen Elizabeth Islands in the Canadian Arctic and show that grounding line shifts affect the tides in the vicinity of the respective ice sheets. In our simulations, we extend the approach by *Griffiths and Peltier* [2009] and analyze the response in global tides to different grounding line positions of the Antarctic Ice Sheet from the LGM to the early Holocene.

There are several reasons to reinvestigate the tidal evolution over the last 21 kyr with higher resolution and with the response of both semidiurnal and diurnal tides described. Changes in tidal dissipation can affect the large scale meridional overturning circulation (MOC), which has been shown to be sensitive to the input of mechanical energy in the deep ocean [e.g., *Huang*, 1999; *Johnson et al*., 2008; *Green et al*., 2009]. Based on first-order physical principles [e.g., *Stommel*, 1961], it is thus expected that the MOC during the LGM would be stronger. Instead, most investigations point toward the MOC being more sluggish during in the past due to an increased freshwater input to the North Atlantic, which hampered the formation of North Atlantic Deep Water [e.g., *Broecker and Denton*, 1990; *Lenderink and Haarsma*, 1994; *Rahmstorf*, 2002; *Green et al*., 2009]. However, the increased energy input from tides during the LGM may have facilitated the recovery of the MOC at the end of any freshwater pulse [*Green et al*., 2009; *Green and Bigg*, 2011]. The very large

tides reported in the Arctic and Labrador Sea during the LGM may also have been acting to destabilize the continental ice sheets [*Arbic et al*., 2004; *Rosier et al*., 2014], and tides themselves are quite sensitive to the location of ice sheet grounding lines [*Griffiths and Peltier*, 2008, 2009; *Rosier et al*., 2014]. The present simulations thus provide a new insight into the behavior of the tides over the last 21 kyr at high resolution, and may form a basis for mixing in further climate models simulations.

In order to provide better tidal estimates for the last 21 kyr, we rerun the model used by *Egbert et al*. [2004] but with a slightly modified setup. We include most of the Arctic, as opposed to cutting at 82°N. We also include analysis of the K_1 tide, and we investigate the sensitivity of the global tidal evolution to the location of the Antarctic grounding lines. Furthermore, we present results from time slices every 500–1000 years from the LGM to the present, thus exploring new features of the tides not reported previously. Previous global studies have either presented selected time slices with spatially high resolution [*Egbert et al*., 2004; *Green*, 2010], coarse resolution studies with higher temporal resolution [*Thomas and Sündermann*, 1999; *Uehara et al*., 2006] or have shown temporally and spatially highly resolved regional timeslices [*Uehara et al*., 2006; *Hill et al*., 2011; *Hall et al*., 2013]. To date only regional changes in tides in response to changes in the grounding line location and ice shelf extent of the Antarctic Ice Sheet have been examined [*Griffiths and Peltier*, 2009; *Rosier et al*., 2014], whereas this study is carried out with both a high temporal and spatial resolution and looks at the global impacts of changes in the grounding line in Antarctica. We begin by introducing the tidal model in the next section, including an overview of the different simulations. The results for both the M_2 and K_1 constituents from these simulations are presented in section 3 where we first explore the LGM state and then investigate the temporal evolution from the LGM to the present.

2. Tidal Modeling

2.1. Model Description

The Oregon State University Tidal Inversion Software (OTIS) has been used in several previous investigations to simulate global and regional tides in the past, present, and future oceans [e.g., *Egbert et al*., 2004; *Green*, 2010; *Pelling and Green*, 2013; *Green and Huber*, 2013]. It provides a numerical solution to the shallow water equations, but the nonlinear advection terms and the horizontal diffusion are neglected without loss of accuracy [*Egbert et al*., 2004]. The only forcing is the astronomic tide-generating force, and energy is dissipated through a quadratic bed-friction term and a linear tidal conversion scheme representing the energy losses to internal tides. We thus solve

$$\frac{\partial \mathbf{U}}{\partial t} + f \times \mathbf{U} = -gh\nabla(\eta - \eta_{SAL}) + \mathbf{F}_b + \mathbf{F}_w + \mathbf{\Theta} \tag{1}$$

$$\frac{\partial \eta}{\partial t} = -\nabla \cdot \mathbf{U} \tag{2}$$

where $\mathbf{U} = \mathbf{u}h$ is the depth-integrated volume transport given by the velocity $\mathbf{u}$ times the water depth h, $\mathbf{f}$ is the Coriolis vector, η and η_{SAL} the tidal elevation and the self-attraction and loading elevation, respectively, $\mathbf{F}$ is the dissipative stress from bed friction (subscript b) and tidal conversion (subscript w), respectively, and $\mathbf{\Theta}$ is the astronomic tide-generating force. Self-attraction and loading (SAL) was implemented through the iterative scheme suggested by *Egbert et al*. [2004], and four iterations are performed for each simulation period.

The bed-friction is parameterized using a standard quadratic law: $\mathbf{F}_b = C_d \mathbf{U}|\mathbf{u}|/h$, where $C_d = 3 \times 10^{-3}$ is a drag coefficient, and $\mathbf{u}$ is the total velocity vector for all the tidal constituents. The tidal conversion term, F_w, is a vector given by

$$\mathbf{F}_w = C|\nabla h|^2 \frac{N_h \bar{N}}{8\pi^2 \omega}\mathbf{U} \tag{3}$$

where $C = 50$ is a scaling factor, ∇h the horizontal gradient of the topography, N the buoyancy frequency, N_h is the value of N at the seabed, $\bar{N}$ the average of N over depth of the entire water column, and ω the tidal

frequency. This is a slightly modified version of that given by *Zaron and Egbert* [2006] as described by *Green and Nycander* [2013]. It assumes a horizontally uniform abyssal stratification which is parameterized by the buoyancy frequency N through $N(z)=N_0\exp\left(\frac{-z}{1{,}300}\right)$ with $N_0 = 5.24 \times 10^{-3}$. We acknowledge that changes in stratification could be important for the LGM, but they have been studied elsewhere [e.g., *Egbert et al*., 2004; *Griffiths and Peltier*, 2009] and our focus is on evaluating changes in tides due to shifts in the grounding line position. The establishment of a more accurate stratification is work in progress and not part of the scope of this paper. N^2 may have been a factor 2 higher during the LGM [*Green et al*., 2009]. In any case, our present results are conservative since we use a reduced vertical stratification for the LGM. In order to test for sensitivity of the results to changes in stratification we perform simulations of the LGM tides with IT drag multiplied by factors 0.5 and 2 in order to evaluate the sensitivity of dissipation to offsets in stratification.

The PD bathymetric data, used as the basis for all simulations, are a conglomerate of the Smith and Sandwell database, v.14, [see *Smith and Sandwell*, 1997, and topex.ucsd.edu/pub/global_topo_1min for the latest version] (SS) and Arctic and Antarctic bathymetries from IBCAO, v.2, [see *Jakobsson et al*., 2008, and http://www.ngdc.noaa.gov/mgg/bathymetry/arctic/downloads.html] and ETOPO1 databases [see *Amante and Eakins*, 2009, and http://www.ngdc.noaa.gov/mgg/global/], respectively (Figure 1). All data sets were averaged to 1/8° × 1/8° horizontal resolution and then linearly interpolated to a common latitude-longitude grid. In the southern part of the domain, ETOPO1 and SS are merged from 65° to 60° S using linear weighting. The same methodology is applied in the subpolar north where SS and IBCAO are merged between 74° and 79° N.

The paleotopography comes from ICE-5G [see *Peltier*, 2004, and http://www.atmosp. physics.utoronto.ca/peltier/data.php for the latest version], which has a 1° × 1° resolution and is available in 500 or 1000 year time slices from the present to the LGM. For accuracy reasons, the runs were also made on a 1/8° × 1/8° grid, with paleobathymetries obtained following the methodology in *Egbert et al*. [2004]: for each time slice, the difference between the 1° × 1° paleobathymetry and the 1° × 1° version of the present-day (PD) bathymetry was computed and then linearly interpolated to the PD 1/8° grid and added to the present-day 1/8° bathymetry. This leads to sea-level adjustment consistent with the ICE-5G database, but with the necessary resolution to obtain reliable results. The model grid thus has a fully global longitudinal span and covers the globe between 86°S and 89°N in latitude. At the northernmost boundary, an elevation boundary condition was applied using data from the TPXO7.2 database [see *Egbert and Erofeeva*, 2002, and http://volkov.oce.orst.edu/tides/global.html]. Simulations with a landmass at the northernmost boundary were done for a few select time slices and did not change the results [e.g., *Egbert et al*., 2004; *Arbic et al*., 2009], and we opted for the open boundary in the Arctic here. However, the fully global simulations in *Griffiths and Peltier* [2008, 2009] suggest that the tide was almost an order of magnitude larger along 89°N during the LGM—a feature which must have been crucial to generate their "megatides" along the Arctic shelf. As described later, we therefore performed sensitivity simulations with enhanced tidal amplitudes in our boundary conditions.

The present day runs were evaluated against the TPXO8 database which was averaged from a 1/30° × 1/30° to 1/8° × 1/8° horizontal resolution and then interpolated using linear interpolation to the common latitude-longitude grid. Note that for computational reasons, we still use TPXO7.2 for the boundary conditions—the difference between the two databases is negligible along 89°N and should not impact on the results—but, TPXO8 is generally more accurate due to the increased resolution.

2.2. Grounding Line Scenarios

LGM to early Holocene (21–10 kyr BP) simulations were carried out for two extreme grounding line cases in order to take the uncertainties of the reconstructions discussed in section 1 into account and to provide a realistic range in which "partially" grounded cases could lie. The first case deals with grounded Antarctic ice shelves (ice in Weddell and Ross Sea grounded, henceforth referred to as "GR"), whereas the second case uses floating Antarctic ice shelves (ice in Weddell and Ross Sea floating, "FL"). For the GR case all Antarctic ice given by the ice thickness data in the ICE-5G data set is assumed to be grounded. For the FL case the change in ice thickness between the paleo-slices and the present-day case is added to the total water depth and only when the ice thickness exceeds the height of the water column is the ice grounded; otherwise we assume that a floating ice shelf is present. The horizontal extent of the floating ice shelf is the same as for

the grounded ice sheet. We do not specify the thickness of the ice shelves as it is the total water depth change, i.e., the eustatic and isostatic sea level changes together with alterations water depth due to the displacement of water from the presence of ice shelves, and the location of the grounding line that are important for the tidal dynamics [e.g., *Griffiths and Peltier*, 2009; *Rosier et al*., 2014]. Throughout the Holocene we assumed the ice to have been ungrounded in the Weddell and Ross Sea and only the FL case is referred to for this period.

2.3. Simulations and Computations

Runs were made for the present and for a number of paleo time slices between 21 kyr BP and 1 kyr BP using the relevant topography for each time slice (the simulated ages are marked in Figure 7). The simulation period for each run was 13 days, of which the last 5 days were used for harmonic analysis of the modeled elevations and currents. Forcing consisted of the astronomic tidal potential and prescribed elevations at the Arctic boundary for the M_2 and K_1 constituents. Runs were made for the LGM (21 kyr) and the present using M_2, S_2, K_1, and O_1 forcing, using a 45 day run time with 30 day harmonic analysis, but the S_2 signal responds very similarly to M_2, and O_1 is close to K_1 in response, so for computational economy we focus on M_2 and K_1 in the following. Model output consists of tidal amplitudes and phases, and volume transports and transport phases for each modeled constituent. In order to test for the sensitivity to variations in the elevation boundary conditions at the northern open boundary (89°N) we performed runs where the TPXO7.2 boundary conditions were multiplied by factors of 2, 4, and 8 for the 21 kyr time slice with grounded Antarctic ice sheets.

The dissipation of tidal energy was computed following the methodology in *Egbert and Ray* [2001]. By taking $\mathbf{u}\cdot(1) + \eta g$ (2) and introducing the energy density $\rho_0 0.5[h\mathbf{u}^2 + g\eta^2]$ which is assumed to be in steady state, the well-known expression for tidal dissipation D (in W m^{-2}) can be derived (after taking a time-average):

$$D = W - \nabla \cdot \mathbf{P} \tag{4}$$

Here, the work rate, W, and the divergence of the energy flux, $\mathbf{P}$, are defined as

$$W = g\rho_0 \langle \mathbf{U} \cdot \nabla(\eta_{eq} + \eta_{SAL}) \rangle \tag{5}$$

$$\mathbf{P} = g\rho_0 \langle \mathbf{U}\eta \rangle \tag{6}$$

in which $\langle\rangle$ denote the time-averages. Using tidal amplitudes and currents from either the TPXO data base (for validation) or from the model simulations it is therefore possible to calculate the dissipation rate for each constituent without the need to use parameterizations.

3. Global Tidal Dynamics

3.1. The Control Runs

The amplitude and dissipation fields for the PD control runs for M_2 and K_1 for both floating and grounded Antarctic ice shelves can be seen in Figures 2 and 3. The different present-day scenarios are from now on referred to as pdM2fl (present day, M_2 constituent and floating ice shelves), pdM2gr (present day, M_2 constituent and grounded ice shelves) for M_2, and pdK1fl and pdK1gr for the K_1 results, respectively. Note that the grounded PD simulation is a sensitivity case brought on by some global topographic data bases not having any bathymetry under the Antarctic ice shelves. The corresponding root mean square (RMS) amplitude errors, total and deep dissipation, and correlation coefficients between modeled and observed amplitudes are listed in Table 1.

Using TPXO8 as observations we obtain a RMS difference of below 6.8 cm between the modeled M_2 tidal amplitudes for the floating ice shelf case (Figure 2) and observed M_2 elevations, whereas in water deeper than 500 m, the RMS difference is below 3.9 cm, which shows a marked improvement to the simulations by *Egbert et al*. [2004]. The correlation coefficient between pdM2fl and TPXO8 is $r = 0.95$, thus explaining 90% of the variance in TPXO8 which implies that we capture both the absolute tidal amplitudes and the

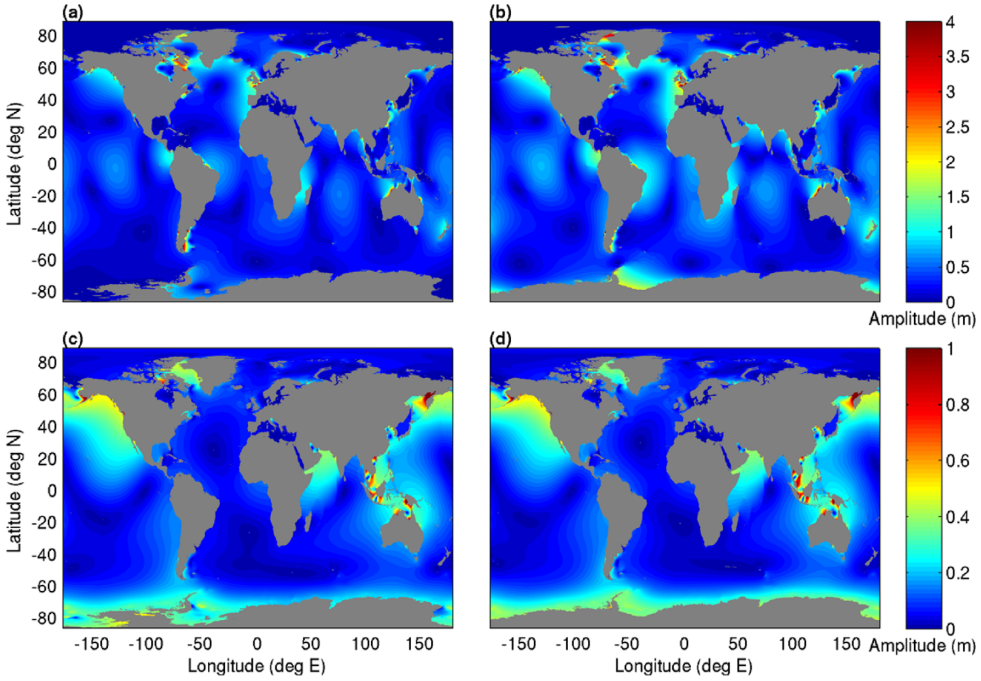

Figure 2. Present-day M_2 amplitudes for (a) floating and (b) grounded Antarctic ice shelves, respectively; (c) and (d) same but for K_1.

structure of the tidal elevation relatively well. For the grounded ice sheet case, pdM2gr, the RMS values are considerably higher with 16.6 and 12.8 cm for the whole ocean and the deep ocean, respectively. There is a marked offset in the tides around both Antarctica and in the North Atlantic region in this run, thus

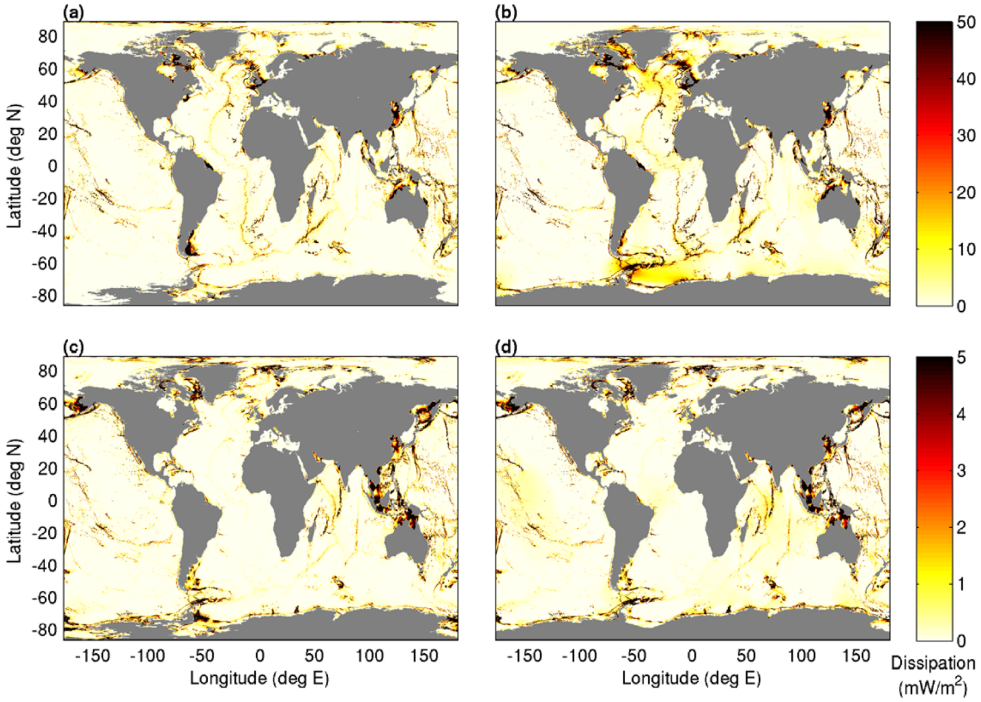

Figure 3. Same as Figure 2 but for dissipation.

Table 1. Comparison of Present-Day Simulations for Grounded and Floating Ice Shelves for M2 and K1, Respectively, to TPXO8[a]

Case	Total RMSE (cm)	Deep RMSE (cm)	Correlation Coefficient	Total Dissipation (TW)	Deep Dissipation (TW)
TPXO8 M2				2.393	0.957
TPXO8 K1				0.355	0.127
pdM2fl	6.671	3.866	0.947	2.291	0.957
pdM2gr	16.604	12.776	0.866	3.172	1.176
pdK1fl	2.838	1.771	0.926	0.380	0.174
pdK1gr	4.555	2.391	0.903	0.368	0.122

[a]Amplitude root mean square errors (RMSE) were calculated globally (first column; total RMSE) and for the deep ocean (depths > 500 m; second column; deep RMSE); the pattern correlations (third column; correlation coefficient) were obtained by correlating our elevation fields with the TPXO fields. The fourth and fifth columns show total and deep (>500 m) dissipation, respectively.

highlighting issues when using inaccurate Antarctic bathymetries and incorrect grounding line positions of the ice sheets. The grounding of the ice shelves around Antarctica leads to a marked increase in amplitude of several meters around Antarctica and a northward shift of the nearby amphidromic points, resulting in decreases in amplitudes along the south-east coast of South America and an increase along the central east coast (Figure 2). The shift in amphidromic points propagates all the way into the North Atlantic resulting in increased amplitudes in the Labrador Sea, the Nares Straits, and along the west coast of North America. In addition to the amplitude shifts by the blocking of the Weddell Sea, the grounded ice also acts as a wall which reflects tidal energy back into the North Atlantic, again resulting in a more energetic tidal field. These changes are also reflected in the dissipation field. Total M_2 dissipation for the FL case is 2.29 TW of which 0.96 TW (41%) takes place in the deep ocean (i.e., where $h > 500$ m). This compares very well with the deep dissipation from both TPXO8 (0.96 TW) and the estimates by *Egbert and Ray* [2001], but gives a very slight underestimate of the dissipation in shallow water, probably due to errors in the bathymetry. For the GR case, the dissipation increases considerably to 3.17 TW total and 1.18 TW (37%) deep dissipation, respectively. Here, a shift in dissipation occurring from the Patagonian shelf into Drake Passage and the Atlantic part of the Southern Ocean takes place, and the North Atlantic becomes significantly more energetic as seen from the amplitudes. This shows that a regional change in bathymetry can lead to significant alterations of global tidal dynamics.

The RMS error for pdK1fl is below 3 cm for the global tides and less than 1.8 cm for the deep ocean. The pattern correlation between TPXO8 and pdK1fl is $r = 0.93$ and our model result thus explains 86% of the variance in the TPXO8. For the grounded ice shelf case (pdK1gr), the RMS values are larger than for the floating case (pdK1fl), with values of 4.5 and 2.4 cm for the global and deep ocean, respectively. With grounded ice shelves the explained variance is reduced by 8%. For K_1, the difference between grounded and floating ice shelves is much less pronounced as for M_2 and the shifts in amplitude are local and confined to the proximity of Antarctica. For the GR case a pronounced decrease in dissipation can be seen in this region in comparison to the FL case, whereas only small changes occur throughout the remaining ocean. Total dissipation for the FL case is 0.38 TW with 45% of the dissipation taking place in the deep ocean giving a good fit with the TPXO8 data. For the grounded case total dissipation does not change but the fraction of deep dissipation decreases to 33%, as dissipation previously occurring in the Weddell and Ross Seas is omitted, and the Antarctic shelf and the Indian Ocean become more energetic.

3.2. Tidal Evolution

In this section, the evolution of the tides from 21 kyr BP to present is described for both M_2 and K_1 for each of the two grounding line scenarios. The LGM amplitude and dissipation fields can be seen in Figures 4 and 5. The evolution of dissipation globally is shown in Figure 7, and the corresponding basin wide dissipation is displayed in Figure 6.

3.2.1. M_2 Constituent

Global tidal dynamics at the LGM are strongly altered in comparison to the present-day case for both scenarios. For both grounding line cases, strongly enhanced tidal amplitudes and dissipation can be seen throughout the Atlantic, around Antarctica, the Coral Sea, the Gulf of Aden, the area north of the Mozambique Channel, and the Gulf of Panama (Figure 4). These areas correspond to areas of increased dissipation rates (Figure 5), and our results are consistent with those reported by *Egbert et al*. [2004] and *Griffiths and Peltier* [2008, 2009]. However, considerable differences can also be seen between the two different

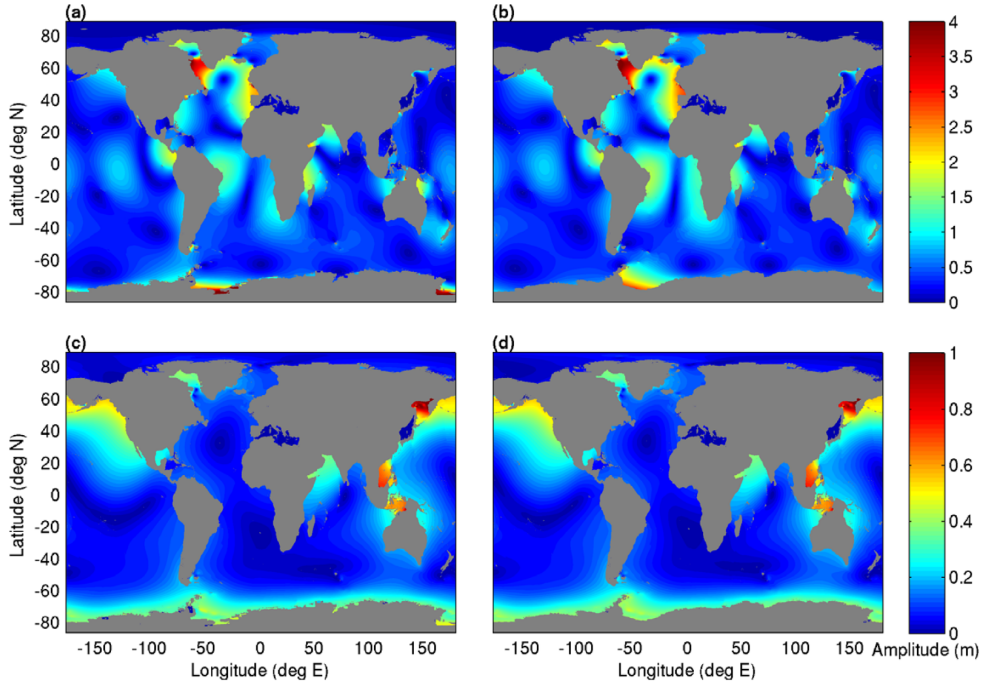

Figure 4. LGM (21 kyr BP) M_2 amplitudes for (a) floating and (b) for grounded Antarctic ice sheets, respectively. (c) and (d) same as Figures 4a and 4b but for K_1.

grounding line scenarios in both amplitudes and dissipation rates. At 21 kyr BP, the main differences in amplitude and dissipation between the grounding line scenarios are found in the Atlantic (Figure 6). In the South Atlantic and in the vicinity of Antarctica, the smallest amplitudes are observed for the grounded ice shelf case—the scenario which generates the largest tidal amplitudes in the North Atlantic region with a maximum of 5.5 m in the Labrador Sea. Ungrounding the ice sheet in both the Weddell and Ross Seas reduces the amplitude in the North Atlantic considerably, with the maximum amplitudes in the Labrador Sea dropping to 4.1 m. However, due to the formation of a shallow shelf sea in the Weddell Sea, considerable semidiurnal tidal amplitudes of up to 5.5 m can now also be seen here, and large tides can be observed in the Ross Sea. This corresponds to the results presented by *Griffiths and Peltier* [2009], who also find large changes in the regional Antarctic tides in response to grounding line shifts and report strongly enhanced tides in both the Ross and Weddell Sea for the LGM. They also find that the large tides in the Ross Sea disappear when the grounding line is advanced out toward the shelf break whereas the tides in the Weddell remain amplified with the grounding line shifts. These global differences in the tides due to grounding line changes are also reflected in the dissipation patterns which differ mainly in both the North and South Atlantic. Less energy is dissipated in the North Atlantic region as the Weddell Sea ice becomes ungrounded whereas for the South Atlantic the opposite is the case. The total M_2 dissipation estimates for the grounded case is 4.75 TW (GR), whereas the dissipation for the floating case is much lower at 4.05 TW (FL). The values mark an increase in dissipation compared to the FL present-day case by between 1.8 TW (78%) and 2.5 TW (107%) for the lowest and highest case, respectively. These values are in close correspondence to those previously reported [*Egbert et al*., 2004; *Uehara et al*., 2006; *Griffiths and Peltier*, 2008, 2009]. The reason for these differences in dissipation rates between the two scenarios becomes evident from Figures 5a and 5b. For the FL case the North Atlantic region tidal amplitudes are reduced in comparison to the GR scenario and less dissipation takes place south of Greenland. For the GR case, the grounding of the entire ice in the Weddell Sea and the removal of the shelf sea occupying the Weddell Sea enhances the Atlantic tides and increases dissipation in the North Atlantic. This is the same mechanism as discussed in *Egbert et al*. [2004] and *Green* [2010] where the removal of the damping factor (in this case the shelf sea in the Weddell Sea) in a basin that is in a near resonant state acts to enhance the dissipation in this system.

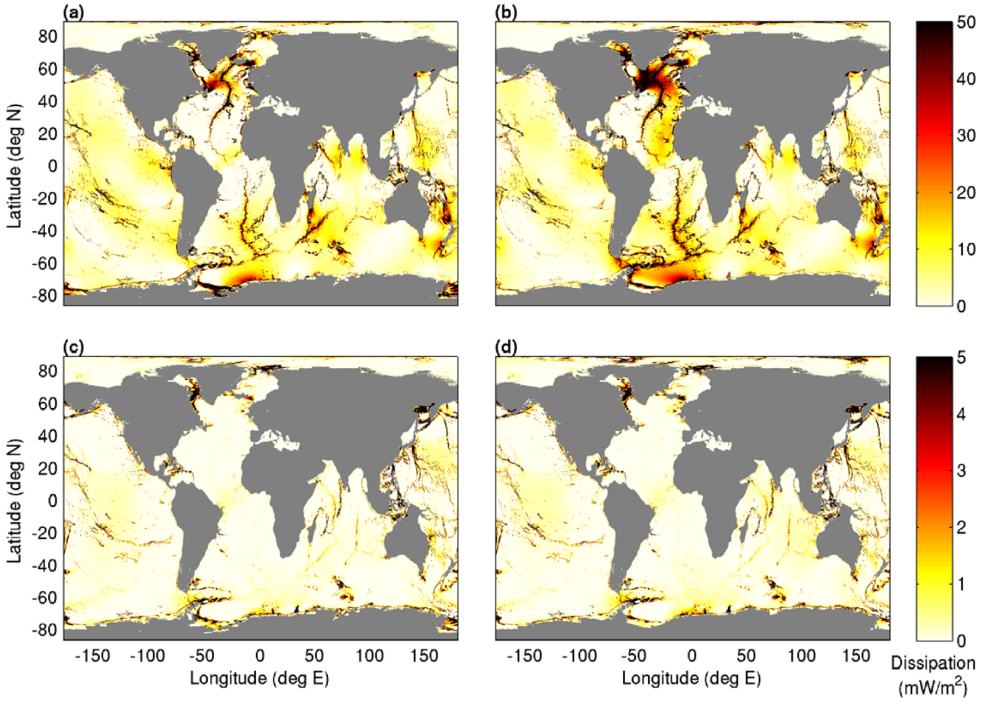

Figure 5. Same as Figure 4 but for dissipation.

We do not find the LGM "megatides" in the Arctic which *Griffiths and Peltier* [2008, 2009] see in their fully global simulations. Their results show M_2 amplitudes which exceed 3 m around the margins of the Artic basin, whereas we find tides in the Arctic basin which are strongly amplified by up to a factor of 5, but the absolute amplitudes are much smaller than those reported by *Griffiths and Peltier* [2008, 2009]. Increasing the elevation boundary conditions at the open boundary at 89°N by a factor of 2 leads to a small increase in the Arctic tides, whereas a factor 8 leads to an increase in amplitudes on the shelf close to those reported by *Griffiths and Peltier* [2009]. This also induces amplitudes along our boundary at 89°N which are consistent with those seen in *Griffiths and Peltier* [2009]. However, we find that altering the boundary conditions in the center of the Arctic has very little effect on the tides elsewhere on the globe outside the Arctic Basin, and changes are restricted to areas where the tides are large already and lie in the order of up to 5 cm. The same applies for dissipation rates, where the factor 8 boundary condition simulation produces an increase in global dissipation by 5% with the changes being local and restricted to the Arctic.

Large shifts in the global patterns of both amplitude and dissipation take place during the transition from the LGM to present that differ for each of the two grounding line scenarios for the semidiurnal tidal constituent. The changes during this period can be divided into four distinct phases over the time period under investigation:

3.2.1.1. 21–16 kyr BP

Between 21 and 18 kyr BP both amplitudes and dissipation rates largely reflect the LGM state and remain fairly constant throughout the period. Dissipation mainly occurs in waters deeper than 500 m, as most of the shelf seas were emergent during this period. Large tides can be observed in the Labrador Sea, along the European coast, and along the ice margins in the Weddell Sea. For both scenarios, the initial flooding of the shelf seas between 18 and 16 kyr BP leads to a slight drop in Labrador Sea amplitudes accompanied by an increase of the amplitudes on the European shelf. The dissipation rates remain constant over this period.

3.2.1.2. 16–10 kyr BP

As the shelf seas continue to flood pronounced drops in amplitudes and dissipation can be seen for both grounding line scenarios with dissipation shifting from the deep ocean to the shelf seas. The changes in

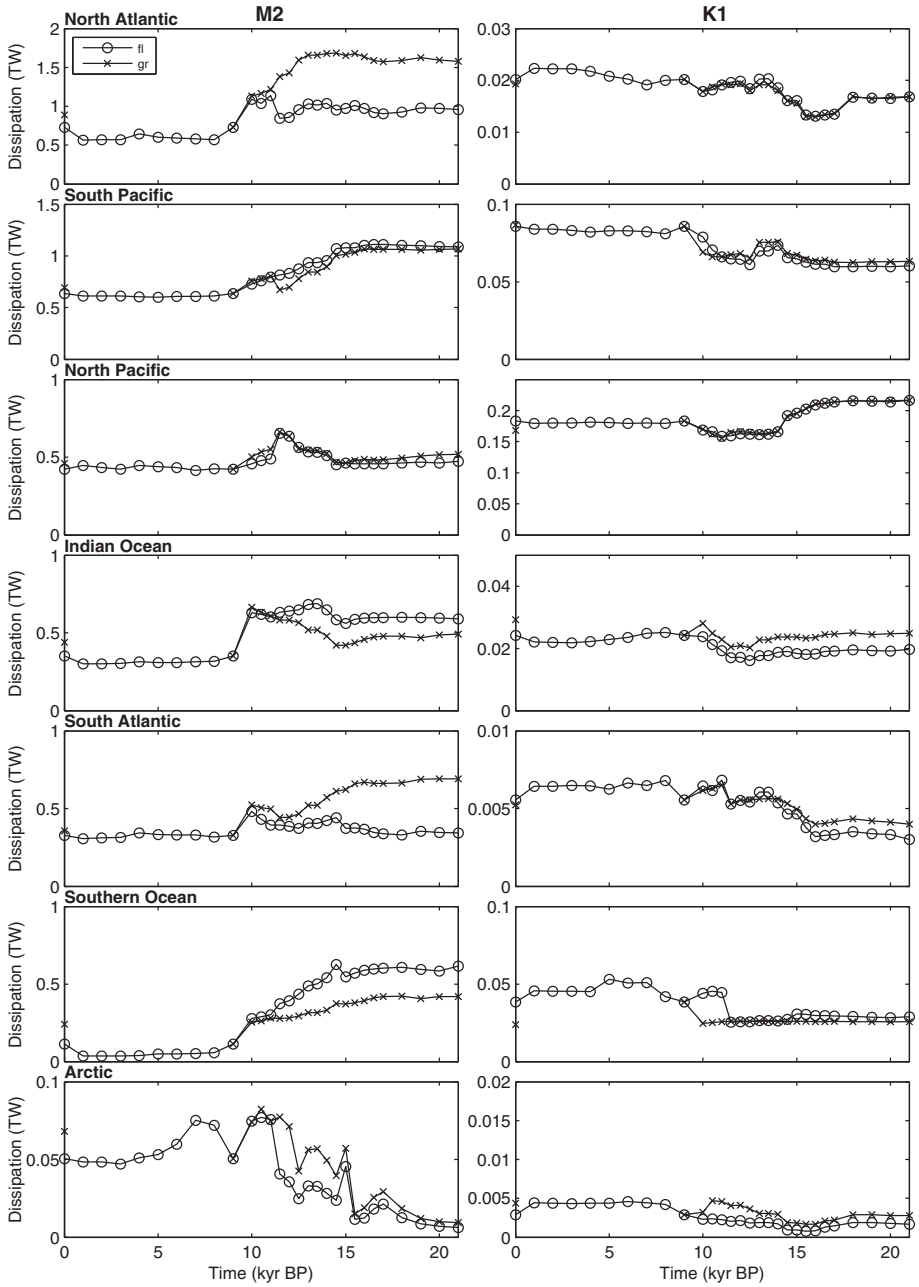

Figure 6. Regional total dissipation for M_2 and K_1 from 21 kyr BP to present for both GR and FL scenarios.

dissipation take place gradually and are more pronounced for the GR case with total dissipation decreasing by 0.8 TW, and deep dissipation by 1.8 TW. For the FL case, the drops amount to 0.4 and 1.3 TW, respectively (Figure 7). These figures correspond to the results presented by *Uehara et al.* [2006] who report decreases in dissipation of a very similar magnitude from simulations with a coarse resolution global tidal model for this time period. For the FL scenario, initially, the total dissipation remains fairly constant. A gradual decrease in amplitudes in the Labrador Sea can be seen commencing around 14 kyr BP corresponding to increased flooding of shelf seas which acts to reduce the deep dissipation rates. At this point, the dissipation in the Southern Ocean and South Atlantic also begin to drop whereas dissipation in the North Pacific and the

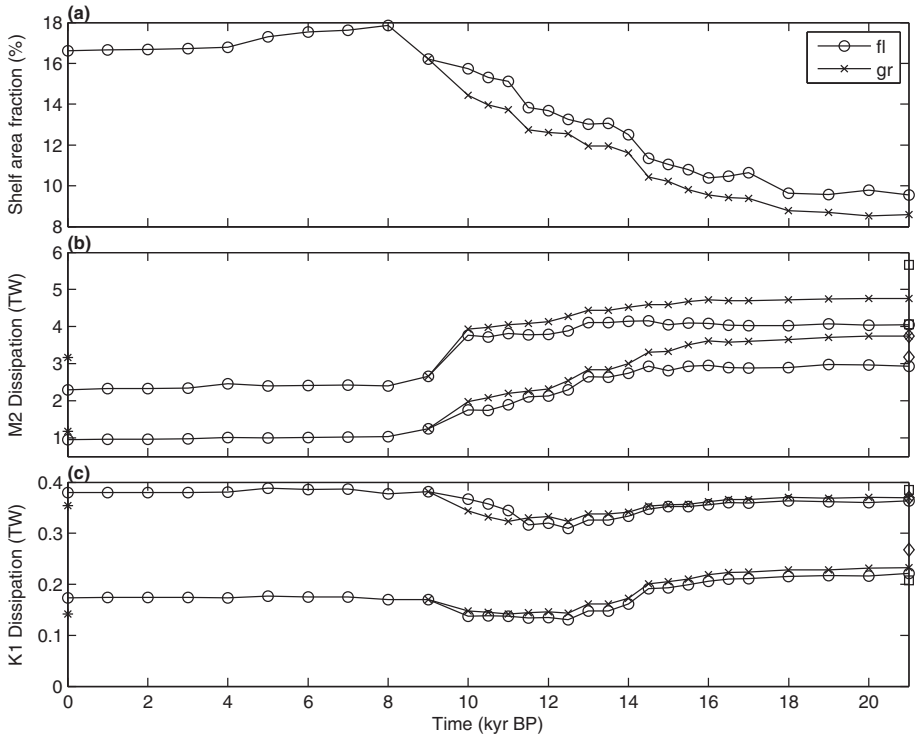

Figure 7. (a) Proportion of bathymetry that is shallower than 500 m; total (black) and deep (>500 m water depth, gray) dissipation for (b) M_2 and (c) K_1 for each of the for grounding line scenarios. Squares and diamonds mark the dissipation values for IT drag multiplied by a factor of 0.5 and 2, respectively. The stars at 0 kyr BP give the dissipation values for the grounded PD ice sheet case.

Indian Ocean increases due to the formation of new shallow seas. An especially pronounced drop in tidal amplitudes in the North Atlantic occurs between 12 and 11 kyr BP when the shelf area fraction increases by nearly 2% and parts of the Weddell and Ross Seas and the Patagonian Shelf flood. The flooding of these areas, which are all highly efficient dampers, consequently reduces the Atlantic tides and decreases dissipation. A large drop in dissipation can also be found in the North Pacific due to the flooding of the Yellow Sea. For the GR scenario both amplitudes and dissipation remain fairly constant in the North Atlantic region between 16 and 14 kyr BP, despite the large topographical changes. Decreases in dissipation can be seen in the Southern Ocean, South Atlantic and South Pacific. From 14 to 10 kyr BP pronounced changes in global tidal dynamics take place: tidal amplitudes in the Labrador Sea strongly decrease whereas large amplitudes can now be seen on the European Shelf. With the flooding of the shelf seas North Pacific and Indian Ocean dissipation initially increases, but for the Pacific the trend is reversed around 11.5 kyr when sea level rises abruptly.

3.2.1.3. 10–8 kyr BP

The most pronounced drop in global dissipation takes place between 10 and 9 kyr BP for both grounding line cases—a result very similar to those in *Uehara et al*. [2006]. For the FL scenario large drops in amplitude occur throughout the Atlantic and Indian Oceans, as well as in the Weddell and Ross Sea where amplitudes decrease locally with over 1 m. These drops coincide with the partial opening of the Nares Strait and changes in water depth of over 50 m in both the Weddell and Ross Sea due to the melting of the ice occupying these embayments (as given by changes in ICE-5G ice thicknesses). For the GR case we assume that the ice sheets in the Weddell and Ross Sea unground between 10 and 9 kyr BP. Consequently, the amplitude and dissipation rates follow the FL case from that point onward. The ungrounding event may have taken place at an earlier or later stage, but the effects are very similar regardless the timing. The ungrounding of the ice sheet in the Weddell and Ross Seas leads to a large decrease of the global total dissipation. For the GR case, these drops take a very similar pattern as for the FL case in this time step, i.e., the

dissipation decreases throughout the Atlantic, Indian Ocean, and Southern Ocean, but it is strongly enhanced around Antarctica and slightly increased throughout the remaining ocean basins. These changes in dissipation are driven by large tidal amplitudes in the Weddell and Ross Seas, and pronounced drops in amplitudes in all of the large ocean basins. The largest changes in amplitude for the FL scenario take place between 9 and 8 kyr and coincide with the retreat of large parts of the Laurentide Ice Sheet [e.g., *Dyke and Prest*, 1987]. The resulting extensive flooding led to an increase of the global shelf sea area by 2%, the largest increase over the simulation period. With the flooding of the Hudson Strait and Hudson Bay, amplitudes in the Labrador and Weddell Sea drop drastically by up to 1.5 m for both cases whereas an increase in amplitudes can be seen on the Patagonian Shelf. Large tidal amplitudes also appear in the newly formed Hudson and Nares Straits in the Canadian Arctic (Figures 8g and 8h).

3.2.1.4. 8–0 kyr BP

The last 8000 years show only small variations of the M_2 tidal amplitudes, and, consequently, only minor changes in the dissipation rates. This is consistent with results presented by *Hill et al*. [2011] and *Hall et al*. [2013] who show that tides throughout the North Atlantic showed little change during this period. Therefore, this period is not discussed further.

3.2.2. K_1 Constituent

The K_1 amplitudes and dissipation stand in contrast to the response of the M_2 tide. The K_1 amplitudes at the LGM very much resemble the present-day tidal dynamics [see *Griffiths and Peltier*, 2009]. Changes in K_1 are on a local scale as opposed the large global shifts occurring for the M_2 tide. The most prominent shifts can be seen in the Pacific where the diurnal tidal constituent is dominant at present. Consequently, we see changes in the Sea of Okhosk (SoO), the South China Sea (SCS) and the Banda Sea (BS)—the changes in these regions have also been reported by *Uehara* [2005] and *Griffiths and Peltier* [2009]. The amplitudes in the SCS and BS reach up to 1 m, and in the SoO amplitudes range up to 3 m—a pattern in contrast with PD conditions [*Zu et al*., 2008; *Green and David*, 2013]. As opposed to M_2, there are no major global differences between the different ice sheet grounding line scenarios for the LGM. The alterations in tidal dynamics are purely regional in the proximity of the respective grounding lines and the differences in global tidal amplitudes are less than 5 cm. The SCS, SoO, and BS in the Pacific are also the locations in which the largest changes occur from the LGM to the Holocene. Again, in contrast to the semidiurnal tide, these shifts take place regionally, with no large changes in the global diurnal tidal dynamics during the past 21 kyr:

3.2.2.1. 21–16 kyr BP

During this period the results from both grounding line scenarios largely resemble those during the LGM. Amplitudes in the SoO, SCS, and BS remain high, and dissipation in the North and South Pacific stays at a constant level, not reacting to the initial small increase shelf area.

3.2.2.2. 16–11 kyr BP

During this time period the largest regional shifts can be seen as shelf areas flood, thus altering local tidal dynamics. Again, the changes are confined to those basins in which the K_1 tidal constituent is dominant at present. Between 16 and 14.5 kyr BP, a gradual decrease in dissipation can be seen in the North Pacific whereas for the South Pacific the dissipation rate increases slightly with the flooding of the shelf areas in the SCS and BS (Figure 6). The decrease in the North Pacific is linked to a drop in amplitudes in the SoO and a confinement of large amplitudes to the Shelikhov Gulf as sea level continues to increase. Between 14.5 and 14.0 kyr BP a stronger drop in amplitudes in the SoO, SCS, and BS can be seen corresponding to the largest increase in sea level (20 m in 500 years) during which the Gulf of Thailand and parts of the Australian shelf flood, and a strong decrease in dissipation takes place for the North Pacific (Figures 6, 9a, and 9b). The flooding of shelf areas results in a slight increase in dissipation in the South Pacific for both scenarios. The slight drop in dissipation in the South Pacific between 13 and 12 kyr BP coincides with further flooding of the shelf areas between Japan, China, and Northern Australia. As the sea level continues to rise both scenarios gradually move toward the present-day pattern (Figures 9c and 9d) [see *Green and David*, 2013]. Between 12 and 11 kyr BP for the FL scenario the ungrounding of the ice in the Weddell and Ross Sea results in an increase in dissipation in the Southern Ocean region, and considerable amplitudes of over 1 m can now be seen in the Weddell Sea.

3.2.2.3. 11–0 kyr BP

No major changes in dissipation or amplitudes occur over this period. The small changes that can be seen again occur locally as the ice sheets gradually further unground and shallow seas are formed. Between 11

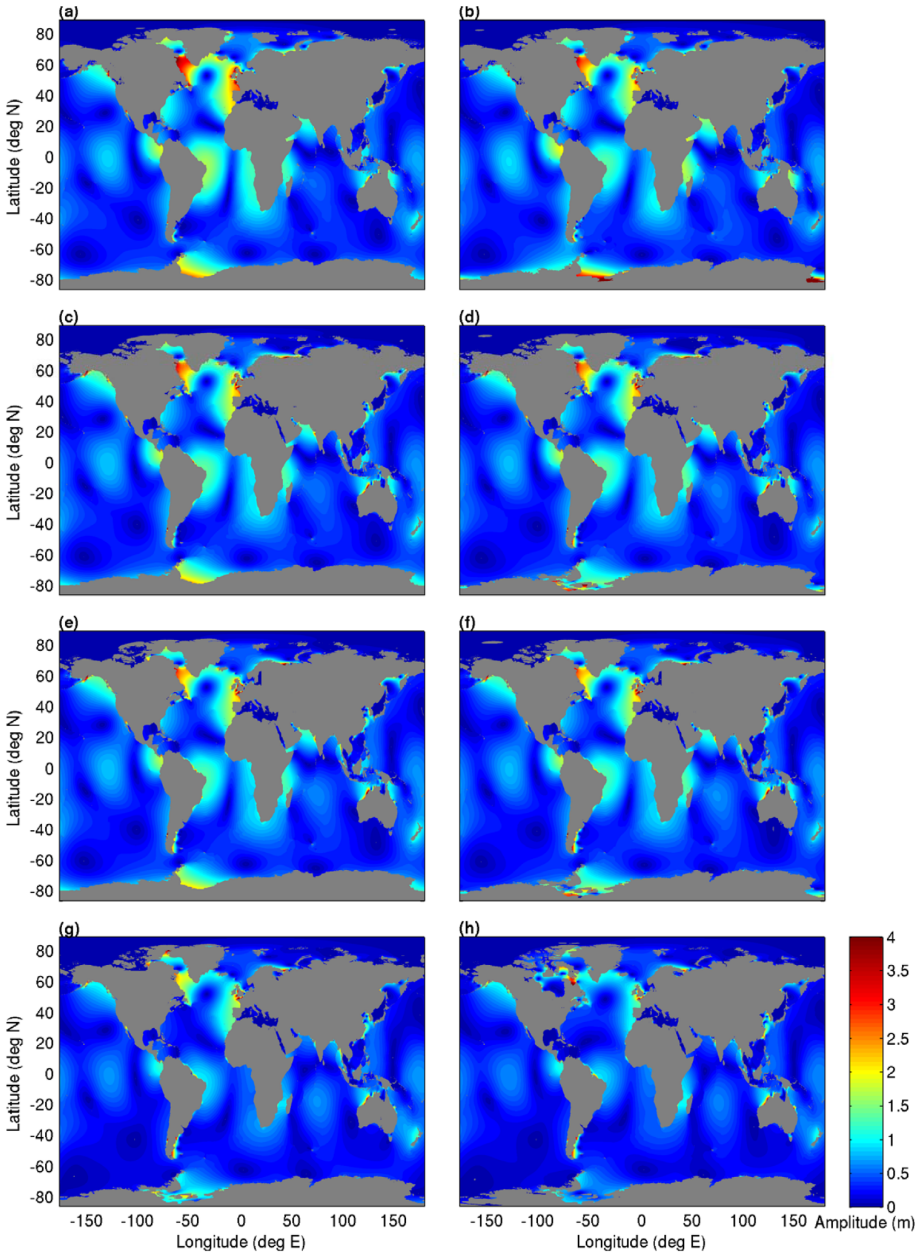

Figure 8. M_2 amplitudes at 14 kyr BP for (a) GR and (b) FL, at 11 kyr BP for (c) GR and (d) FL, at 10 kyr BP for (e) GR and (f) FL, and (g) 9 kyr BP and (h) 8 kyr BP for FL.

and 9 kyr BP, a small increase of the dissipation rates for both scenarios can be seen, which is linked to the ungrounding of the Antarctic ice sheets occupying the Weddell and Ross Sea. This is more pronounced for the GR scenario due to the larger drop in ice volume in these embayments. A small decrease in Weddell Sea amplitudes can be seen between 10 and 8 kyr BP. In contrast to the semidiurnal constituent the diurnal tides seem to have been unaffected by the large increase in sea level between 9 and 8 kyr BP (Figures 9g and 9h).

3.3. Wider Implications

The grounding line locations in the Weddell and Ross Sea appear to have a significant impact on the M_2 tidal dynamics both regionally and globally (see *Rosier et al.* [2014] for possible future effects). The situation

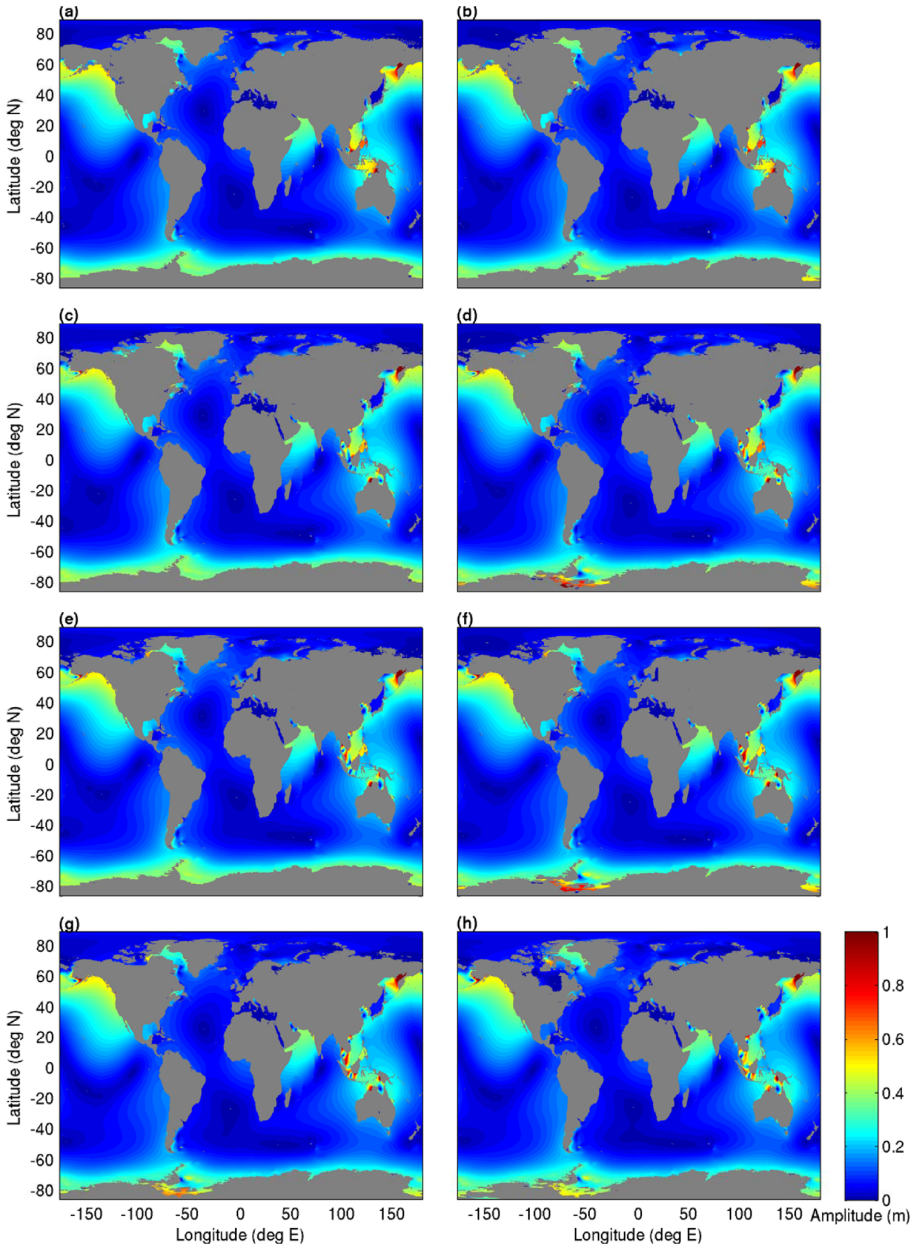

Figure 9. Same as Figure 8 but for K_1 amplitudes.

with grounded ice during the LGM gives a 1.5 times higher dissipation rate than the floating ice scenario, and was arguably the most likely configuration for the LGM. The enhanced LGM dissipation rates in the North Atlantic are thus not only due to regional resonance but also caused by feedback effects from Antarctica. This also holds for the PD simulation: if the ice shelves ground at the PD ice front, tidal dissipation rates are enhanced by a factor of 1.4 in the Northern Hemisphere, but the impact is slightly suppressed compared to the glaciation. It must be noted that this latter case is the actual bathymetry in the first version of GEBCO and highlights the importance of using accurate bathymetric databases in tidal models.

Why do K_1 and M_2 differ so strongly in their evolution from the LGM to present? In contrast to K_1, M_2 tides appear to be controlled by sea level—today a large proportion of the tidal energy dissipates in shelf seas

which were not present during the LGM. During the LGM, the North Atlantic region, the Coral Sea, the Gulf of Aden, the area north of the Mozambique Channel, and the Gulf of Panama are closer to resonance because the removal of the shelf seas acts to decrease the effective damping of the tide [*Egbert et al*., 2004; *Green*, 2010]. For the North Atlantic, continuing to lower sea level (experiments not shown here) does not increase dissipation further, suggesting that the North Atlantic is as close to resonance as it can be at the LGM. However, resonance may not be the entire story: Antarctic grounding line location appears to play a significant role in controlling global amplitudes and dissipation rates, and thus, global semidiurnal tidal dynamics. In contrast, for K_1, the areas in which large amounts of dissipation occur today—the SoO and SCS—were present during the LGM and none of the large ocean basins are close to resonance at present and during the LGM [*Platzman et al*., 1981]. This therefore leads to little change between the LGM and the present, and the responses seen are mechanistically not the same as for the M_2 constituent.

4. Discussion

With this work we present a detailed picture of the evolution of tides from the LGM to the present. Large alterations can be seen for the M_2 tidal constituent over this time period as previously suggested by a number of studies [*Egbert et al*., 2004; *Arbic et al*., 2004; *Uehara et al*., 2006; *Griffiths and Peltier*, 2009; *Green*, 2010], whereas for K_1 only small changes in the global tidal dynamics occur consistent with *Egbert et al*. [2004], *Uehara* [2005], and *Griffiths and Peltier* [2009].

In contrast to *Egbert et al*. [2004], who present time slices every 5000 years between LGM and present for M_2, we provide a much more detailed picture in 500–1000 year time intervals and we run at a much higher spatial resolution than *Uehara et al*. [2006] who present 1000 year time slices for the same period. Our simulations differ somewhat from those by *Egbert et al*. [2004] and *Uehara et al*. [2006] in that their results suggest little change in global total dissipation between 15 and 10 kyr BP. In contrast, we find that, depending on the grounding line scenario, nearly half the decrease in dissipation occurs during the transition from the LGM to the Holocene due to the large bathymetric changes resulting from the deglaciation. Furthermore, the results by *Egbert et al*. [2004] provide no indication of the exact timing of the decrease in dissipation takes place between 10 and 5 kyr BP, whereas our simulations indicate that the largest changes in dissipation take place when the ice sheets occupying the Weddell and Ross Sea unground which coincides both in timing and magnitude with the largest decreases in dissipation that *Uehara et al*. [2006] find. The largest shifts in global amplitudes take place between 9 and 8 kyr BP, when large parts of the Laurentide ice sheet disintegrated and the Hudson Bay and Straits flooded, and a large increase in sea level occurred [e.g., *Clarke et al*., 2003]. *Hill et al*. [2011] also report large changes in tidal amplitudes along the east coast of middle and Central America for this time period. Thereafter, only small changes in dissipation take place. These results highlight that the large changes in semidiurnal tides from the LGM to present did not occur linearly but are intricately tied to the ice dynamics of the major ice sheets, and their link to global sea levels.

In contrast to *Griffiths and Peltier* [2008, 2009] we do not find "megatides" in the Arctic basin during the LGM in our normal setup. Arctic tides in our simulations are enhanced by up to a factor of 5 along the north coast of Greenland and in the Canadian Basin to values only slightly smaller than reported by *Thomas and Sündermann* [1999] who find amplitudes of up to 70 cm. Increasing the TPXO7.2 elevation boundary conditions at 89°N by a factor 8 to match the amplitudes found at the same latitude by *Griffiths and Peltier* [2008, 2009], but not altering the grounding line location of the ice sheet covering the Queen Elisabeth Islands, enables us to reproduce the several metre amplitudes they find along the Arctic coastline. As *Griffiths and Peltier* [2008, 2009] use a truly global model we conclude that the Arctic megatides reported by *Griffiths and Peltier* [2008, 2009] are a likely feature. *Egbert et al*. [2004] carried out experiments with the same model we use and remark that neither changing the boundary conditions in the Arctic, placing a "vertical wall" in the center of the Arctic nor running the model in a truly global setup with the North Pole shifted into Greenland alters the global tides outside the Arctic basin which is supported by our boundary condition experiments.

Griffiths and Peltier [2008, 2009] use the ICE-5G v 1.3 paleotopography reconstruction (based on the 2min ETOPO2 present-day bathymetry) interpolated to a grid spacing that ranges from 50 km at the equator to 5 km at the poles, whereas we run with a bathymetry with a horizontal resolution of 12 km by 13.5 km at the equator to 2 km by 13.5 km horizontal resolution in the center of the Arctic Basin and superimpose the

change in topography between present day and the past time slice onto a present-day bathymetry at 1/8° resolution to retain present-day topographical features.

Our results are consistent with the damped harmonic oscillator hypothesis presented by *Egbert et al*. [2004], and further explored by *Green* [2010]. The removal of shelf seas during the LGM due to the 120 m sea-level drop reduces the damping and pushes the ocean closer to resonance, which is an effect that is especially prominent in the North Atlantic. It can be seen that notable reductions in deep dissipation occur synchronously with shelf seas flooding (e.g., at around 14 kyr BP when parts of both the Patagonian and the European Shelf flood, or between 9 and 8 kyr BP when Hudson Bay and Strait flood), meaning that the Atlantic is moved away from resonance. This agrees with work by *Arbic et al*. [2009] who show that blocking each of these three shelves in a present-day bathymetry acts to increase North Atlantic and especially Labrador Sea tides. We also show that altering the grounding line of the ice sheets in Antarctica not only has an effect on the regional tides [*Griffiths and Peltier*, 2009], but that the grounding line location also has a significant effect on the global tides, and that a change in the former can lead to notable changes in global dissipation. Our simulations therefore highlight the importance of improving the reconstructions for ice sheet extent and dynamics during the LGM and deglaciation. This is especially important as it has been hypothesized that the large tides in the Labrador Sea may have influenced the breakup of the Laurentide ice sheet during the deglaciation, and may have been one of the mechanisms of rapid ice sheet discharge of the Heinrich events during the last glacial [e.g., *Arbic et al*., 2004, 2008; *Griffiths and Peltier*, 2008, 2009]. Similarly, we suggest that the large tides found in the Weddell Sea during the LGM, for the scenarios with floating ice, could have aided in breaking up and retreating the ice from the continental shelf as also put forward by *Griffiths and Peltier* [2009] who hypothesize that the Antarctic Ice Sheet may have experienced similar instability events as the Northern Hemisphere Ice Sheets. Recent work from cores around Antarctica [*Weber et al*., 2011] indicates that the retreat of the Antarctic Ice Shelf from the shelf may have begun as early as 19.3 kyr BP in the south-eastern Weddell Sea, in an area which corresponds to the locations in which our simulations suggest large tidal amplitudes during this period.

With this work we have extended the knowledge about the K_1 tidal dynamics between the LGM and the present, the only time slices that had been explored previously [e.g., *Griffiths and Peltier*, 2008, 2009; *Green*, 2010]. In contrast to the semidiurnal tides the K_1 constituent experiences much less change between the LGM and present and between the individual time steps. Changes do not take place on a global scale but are confined to the regions in which K_1 tides are important at present, i.e., the North Pacific and especially the SoO, the SCS, and the seas around Indonesia and were also reported by *Uehara* [2005] and *Griffiths and Peltier* [2009]. Therefore, none of the dramatic shifts in dissipation that can be seen for M_2 appear for K_1. Nevertheless, considerable alterations in the tidal dynamics in these small basins can be seen. Some of these changes can be explained by shelf-blocking experiments [*Skiba et al*., 2013]. For example, blocking of the Sahul shelf enhances the tidal amplitudes in the SCS and the BS. Between 14 and 12 kyr BP when the Sahul shelf begins to flood it can be seen in our simulations that amplitudes in the Banda Sea strongly decrease. A very similar effect which is also explored by *Skiba et al*. [2013] is evident between 15 and 14 kyr BP when the Gulf of Tonkin begins to flood, and amplitudes in the South China Sea strongly decrease.

It has recently been suggested that the present tidal conversion parameterization may not be the best for this type of tidal model and that the one presented by *Nycander* [2005] gives the highest accuracy of the tidal simulation [*Green and Nycander*, 2013]. There are, however, two issues with *Nycander*'s [2005] scheme. First, it requires a 3-D stratification field for the entire ocean. For the present this is straightforward, and one could possibly use results from a paleomodel for the LGM field, but we still lack relevant data for the other time slices between the LGM and PD. Furthermore, *Egbert et al*. [2004] showed that increasing the global conversion coefficient with factors between 0.5 and 4 had relatively small effects on the global dissipation rates during the LGM. This is to some extent supported by *Green and Huber* [2013], who show that during the early Eocene (50 Ma) the abyssal M_2 dissipation rates were twice as large as at present even though the vertical stratification was 3–4 times stronger than today. One could of course argue that we could use Nycander's scheme but with a slightly modified PD stratification all the way through, but the second problem with using Nycander's parameterization is that of resolution. The conversion coefficient C_w in equation (1) must be computed at at least 1/30° resolution for Nycander's parameterization to be accurate, which is far too detailed for the paleo-slices, and consequently we have to rely on other parameterizations at the moment. To obtain a likely range of the LGM dissipation rates and highlight the insensitivity, we repeated

the sensitivity analysis by *Egbert et al*. [2004] and multiplied the conversion coefficient by a factor 0.5 or 2. There is an associated change in the abyssal dissipation—in both our results and those by *Egbert et al*. [2004]—but only with some 10–15% either way (see the diamonds and squares in Figures 7b and 7c) and the changes in global average amplitudes lie in the order of 20% either way. This is because of the coupling in the model: when the IT drag is reduced, the velocity field may increase which leads to an increased dissipation and decreased amplitudes (and vice versa for an increased drag). These results show that the abyssal tidal dissipation rates are relatively insensitive to changes in hydrography, and the modified IT-drag runs presented give a quite probable range of paleo-dissipation rates and amplitudes in the ocean.

Predictions of sea-level rise over the present century range significantly, but most lie between 0.75 and 1.9 m for the period 1990–2100 [*Bindoff et al*., 2007; *Pfeffer et al*., 2008; *Vermeer and Rahmstorf*, 2009], although there are large uncertainties. A 2 m future sea-level rise would flood some 1.5% of the present-day dry land—a number roughly corresponding to the peak in shelf area 4 kyr BP. There is therefore a potential for even moderate future sea-level rise to have far-reaching effects, not only on regional tides [e.g., *Ward et al*., 2012; *Pelling et al*., 2013] but also on the global tides. These regional studies imply that the tides are sensitive to the way future sea-level rise is implemented, and they stress the need for high-resolution simulations of global tides.

Acknowledgments
J.A.M.G. acknowledges funding from the Natural Environmental Research Council through grant NE/F014821/1 and from the Climate Change Consortium for Wales. S.B.W. received a PhD studentship from Fujitsu through HPC Wales, who also provided computer facilities. Discussions with John Simpson, James Scourse, and Adam Wainwright improved the manuscript and Ade Fewings at HPC Wales provided invaluable technical support.

References

Amante, C., and B. W. Eakins (2009), ETOPO1 1 Arc-Minute Global Relief Model: Procedures, data sources and analysis, *NOAA Tech. Memo. NESDIS NGDC 24*, 19 pp., National Geophysical Data Center, NOAA, doi:10.7289/V5C8276M.

Anderson, J. B., S. S. Shipp, A. L. Lowe, J. S. Wellner, and A. B. Mosola (2002), The Antarctic ice sheet during the Last Glacial Maximum and its subsequent retreat history: A review, *Quat. Sci. Rev.*, *21*, 49–70, doi:10.1016/S0277-3791(01)00083-X.

Arbic, B. K., D. R. Macayeal, J. X. Mitrovica, and G. A. Milne (2004), Paleoclimate: Ocean tides and Heinrich events, *Nature*, *432*, 460.

Arbic, B. K., P. St-Laurent, G. Sutherland, and C. Garrett (2007), On the resonance and influence of the tides in Ungawa Bay and Hudson Strait, *Geophys. Res. Lett.*, *34*, L17606, doi:10.1029/2007GL030845.

Arbic, B. K., J. X. Mitrovica, D. R. MacAyeal, and G. A. Milne (2008), On the factors behind large Labrador Sea tides during the last glacial cycle and the potential implications for Heinrich events, *Paleoceanography*, *23*, PA3211, doi:10.1029/2007PA001573.

Arbic, B. K., R. H. Karsten, and C. Garrett (2009), On tidal resonance in the global ocean and the back-effect of coastal tides upon open-ocean tides, *Atmos. Ocean*, *47*, 239–266, doi:10.3137/OC311.2009.

Bindoff, N. L., et al. (2007), Observations: Oceanic climate change and sea level, in *Climate Change 2007: The Physical Science Basis. Contribution of Working Group I to the Fourth Assessment Report of the Intergovernmental Panel on Climate Change*, edited by S. Solomon et al., pp. 387–432, Cambridge Univ. Press, Cambridge, U. K.

Broecker, W. S., and G. H. Denton (1990), What drives glacial cycles, *Sci. Am.*, *262*(1), 48–56.

Clarke, G., D. Leverington, J. Teller, and A. Dyke (2003), Paleoclimate. Superlakes, megafloods, and abrupt climate change, *Science*, *301*(5635), 922–923, doi:10.1126/science.1085921.

Domack, E. W., E. A. Jacobson, S. Shipp, and J. B. Anderson (1999), Late Pleistocene - Holocene retreat of the West Antarctic Ice-Sheet system in the Ross Sea: Part 2—Sedimentologic and stratigraphic signature, *Geological Society of America Bulletin*, *111*(10), 1517–1536, doi: 10.1130/0016–7606(1999)111.1517.

Dyke, A. S., and V. K. Prest (1987), Late Wisconsinan and Holocene history of the Laurentide ice sheet, *Geogr. Phys. Quaternaire*, *41.2*, 237–263.

Egbert, G. D., and S. Y. Erofeeva (2002), Efficient inverse modeling of barotropic ocean tides, *J. Atmos. Oceanic Technol.*, *19*, 183–204.

Egbert, G. D., and R. D. Ray (2001), Estimates of M2 tidal energy dissipation from Topex/Poseidon altimeter data, *J. Geophys. Res.*, *106*, 22,475–22,502.

Egbert, G. D., B. G. Bills, and R. D. Ray (2004), Numerical modeling of the global semidiurnal tide in the present day and in the Last Glacial Maximum, *J. Geophys. Res.*, *109*, C03003, doi:10.1029/2003JC001973.

Green, J. A. M. (2010), Ocean tides and resonance, *Ocean Dyn.*, *60*(5), 1243–1253, doi:10.1007/s10236-010-0331-1.

Green, J. A. M., and G. R. Bigg (2011), Impacts on the global ocean circulation from vertical mixing and a collapsing Ice Sheet, *J. Mar. Res.*, *69*, 1–24.

Green, J. A. M., and M. Huber (2013), Tidal dissipation in the early Eocene and implications for ocean mixing, *Geophys. Res. Lett.*, *40*, 2707–2713, doi:10.1002/grl.50510.

Green, J. A. M., and J. Nycander (2013), A comparison of tidal conversion parameterizations for tidal models, *J. Phys. Oceanogr.*, *43*(1), 104–119, doi:10.1175/JPO-D-12–023.1.

Green, J. A. M., C. L. Green, G. R. Bigg, T. P. Rippeth, J. D. Scourse, and K. Uehara (2009), Tidal mixing and the meridional overturning circulation from the Last Glacial Maximum, *Geophys. Res. Lett.*, *36*, L15603, doi:10.1029/2009GL039309.

Green, J. M., and T. W. David (2013), Non-assimilated tidal modeling of the South China Sea, *Deep Sea Res., Part I*, *78*, 42–48, doi:10.1016/j.dsr.2013.04.006.

Griffiths, S. D., and W. R. Peltier (2008), Megatides in the Arctic Ocean under glacial conditions, *Geophys. Res. Lett.*, *35*, L08605, doi:10.1029/2008GL033263.

Griffiths, S. D., and W. R. Peltier (2009), Modeling of polar ocean tides at the Last Glacial Maximum: Amplification, sensitivity, and climatological implications, *J. Clim.*, *22*, 2905–2924, doi:10.1175/2008JCLI2540.1.

Hall, B. L., and G. H. Denton (2000), Extent and chronology of the Ross sea ice sheet and the Wilson Piedmont Glacier along the Scott Coast at and since the Last Glacial Maximum, *Geogr. Ann., Ser. A*, *82A*, 337–363, doi:10.1111/1468-0459.00128.

Hall, G. F., D. F. Hill, B. P. Horton, S. E. Engelhart, and W. R. Peltier (2013), High-resolution study of tides in Delaware Bay: Past conditions and future scenarios, *Geophys. Res. Lett.*, *40*, 338–342, doi:10.1029/2012GL054675.

Hein, A. S., C. J. Fogwill, D. E. Sugden, and S. Xu (2011), Glacial/interglacial ice-stream stability in the Weddell Sea embayment, Antarctica, *Earth Planet. Sci. Lett.*, *307*(1–2), 211–221, doi:10.1016/j.epsl.2011.04.037.
Hill, D. F., S. D. Griffiths, W. R. Peltier, B. P. Horton, and T. E. Törnqvist (2011), High-resolution numerical modelling of tides in the western Atlantic, Gulf of Mexico, and Caribbean Sea during the Holocene, *J. Geophys. Res.*, *116*, C10014, doi:10.1029/2010JC006896.
Hillenbrand, C.-D., M. Melles, G. Kuhn, and R. D. Larter (2012), Marine geological constraints for the grounding-line position of the Antarctic Ice Sheet on the southern Weddell Sea shelf at the Last Glacial Maximum, *Quat. Sci. Rev.*, *32*, 25–47, doi:10.1016/j.quascirev.2011.11.017.
Huang, R. X. (1999), Mixing and energetics of the oceanic thermohaline circulation, *J. Phys. Oceanogr.*, *29*, 727–746.
Jakobsson, M., R. Macnab, L. Mayer, R. Anderson, M. Edwards, J. Hatzky, H. W. Schenke, and P. Johnson (2008), An improved bathymetric portrayal of the Arctic Ocean: Implications for ocean modeling and geological, geophysical and oceanographic analyses, *Geophys. Res. Lett.*, *35*, L07602, doi:10.1029/2008GL033520.
Johnson, G. C., S. G. Purkey, and J. M. Toole (2008), Reduced Antarctic meridional overturning circulation reaches the North Atlantic Ocean, *Geophys. Res. Lett.*, *35*, L22601, doi:10.1029/2008GL035619.
Larter, R. D., A. G. Graham, C.-D. Hillenbrand, J. A. Smith, and J. A. Gales (2012), Late Quaternary grounded ice extent in the Filchner Trough, Weddell Sea, Antarctica: New marine geophysical evidence, *Quat. Sci. Rev.*, *53*, 111–122, doi:10.1016/j.quascirev.2012.08.006.
Lenderink, G., and R. J. Haarsma (1994), Variability and multiple equilibria of the thermohaline circulation, associated with deep water formation, *J. Phys. Oceanogr.*, *24*, 1480–1493.
Livingstone, S. J., C. Ó. Cofaigh, C. R. Stokes, C.-D. Hillenbrand, A. Vieli, and S. S. Jamieson (2012), Antarctic palaeo-ice streams, *Earth Sci. Rev.*, *111*(1–2), 90–128, doi:10.1016/j.earscirev.2011.10.003.
McKay, R., G. Dunbar, T. Naish, P. Barrett, L. Carter, and M. Harper (2008), Retreat history of the Ross Ice Sheet (Shelf) since the Last Glacial Maximum from deep-basin sediment cores around Ross Island, *Palaeogeogr. Palaeoclimatol. Palaeoecol.*, *260*(1–2), 245–261, doi:10.1016/j.palaeo.2007.08.015.
Mosola, A. B., and J. B. Anderson (2006), Expansion and rapid retreat of the West Antarctic Ice Sheet in eastern Ross Sea: Possible consequence of over-extended ice streams?, *Quat. Sci. Rev.*, *25*(17–18), 2177–2196, doi:10.1016/j.quascirev.2005.12.013.
Müller, M. (2008), Synthesis of forced oscillations, Part I: Tidal dynamics and the influence of the loading and self-attraction effect, *Ocean Modell.*, *20*, 207–222.
Nycander, J. (2005), Generation of internal waves in the deep ocean by tides, *J. Geophys. Res.*, *110*, C10028, doi:10.1029/2004JC002487.
Pelling, H. E., and J. A. M. Green (2013), Sea level rise and tidal power plants in the Gulf of Maine, *J. Geophys. Res. Oceans*, *118*, 2863–2873, doi:10.1002/jgrc.20221.
Pelling, H. E., J. A. M. Green, and S. L. Ward (2013), Modelling tides and sea-level rise: To flood or not to flood, *Ocean Modell.*, *63*, 21–29, doi:10.1016/j.ocemod.2012.12.004.
Peltier, W. (2004), Global glacial isostasy and the surface if the ice-age earth: The ICE-5G (VM2) model and Grace, *Annu. Rev. Earth Planet. Sci.*, *32*, 111–149.
Pfeffer, W. T., J. T. Harper, and S. O'Neel (2008), Kinematic constraints on glacier contributions to 21st-century sea-level rise, *Science*, *321*, 1340–1342, doi:10.1126/science.1159,099.
Platzman, G. W. (1975), Normal modes of the Atlantic and Indian Oceans, *J. Phys. Oceanogr.*, *5*, 201–221.
Platzman, G. W., G. A. Curtis, K. S. Hansen, and R. D. Slater (1981), Normal modes of the world ocean 2. Description of modes in the periods range 8 to 80 hours, *J. Phys. Oceanogr.*, *11*, 579–603.
Rahmstorf, S. (2002), Ocean circulation and climate during the past 120,000 years, *Nature*, *419*, 207–214.
Rosier, S. H. R., J. A. M. Green, J. D. Scourse, R. Winkelmann (2014), Modeling Antarctic tides in response to ice shelf thinning and retreat, *J. Geophys. Res. Oceans*, *119*, 87–97, doi:10.1002/2013JC009240.
Shipp, S., J. B. Anderson, and E. W. Domack (1999), Late Pleistocene-Holocene retreat of the west Antarctic ice-sheet system in the ross sea: Part 1—Geophysical results, *Geol. Soc. Am. Bull.*, *111*, 1486–1516, doi:10.1130/0016-7606(1999)111-1486.
Skiba, A. W., L. Zeng, B. K. Arbic, M. Müller, and W. J. Godwin (2013), On the resonance and shelf/open-ocean coupling of the global diurnal tides, *J. Phys. Oceanogr.*, *43*(7), 1301–1324, doi:10.1175/JPO-D-12-054.1.
Smith, W. H., and D. T. Sandwell (1997), Global sea floor topography from satellite altimetry and ship depth soundings, *Science*, *277*(5334), 1956–1962, doi:10.1126/science.277.5334.1956.
Stolldorf, T., H.-W. Schenke, and J. B. Anderson (2012), LGM ice sheet extent in the Weddell Sea: Evidence for diachronous behavior of Antarctic Ice Sheets, *Quat. Sci. Rev.*, *48*, 20–31, doi:10.1016/j.quascirev.2012.05.017.
Stommel, H. M. (1961), Thermohaline convection with two stable regimes, *Tellus*, *13*, 224–230.
Thomas, M., and J. Sündermann (1999), Tides and tidal torques of the world since the Last Glacial Maximum, *J. Geophys. Res.*, *104*, 3159–3183.
Uehara, K. (2005), Changes of ocean tides along Asian coasts caused by the post glacial sea-level change, in *Mega-Deltas of Asia: Geological Evolution and Human Impact*, edited by Z. Chen, Y. Saito, and S. L. Goodbred Jr., pp. 227–232, China Ocean Press, Beijing, China.
Uehara, K., J. D. Scourse, K. J. Horsburgh, K. Lambeck, and A. P. Purcell (2006), Tidal evolution of the northwest European shelf seas from the Last Glacial Maximum to the present, *J. Geophys. Res.*, *111*, C09025, doi:10.1029/2006JC003531.
Vermeer, M., and S. Rahmstorf (2009), Global sea level linked to global temperature, *Proc. Natl. Acad. Sci. U. S. A.*, *106*, 21,527–21,532.
Ward, S. L., J. A. M. Green, and H. E. Pelling (2012), Tides, sea-level rise and tidal power extraction on the European shelf, *Ocean Dyn.*, *62*, 1153–1167, doi:10.1007/s10236-012-0552-6.
Weber, M. E., W. Ricken, P. U. Clark, G. Kuhn, S. W. Hostetler, and J. X. Mitrovica (2011), Interhemispheric ice-sheet synchronicity during the Last Glacial Maximum, *Sciences*, *336*, 1265–1269, doi:10.1126/science.1209299.
Zaron, E. D., and G. D. Egbert (2006), Estimating open-ocean barotropic tidal dissipation: The Hawaiian Ridge, *J. Phys. Oceanogr.*, *36*, 1019–1035.
Zu, T., J. Gan, and S. Y. Erofeeva (2008), Numerical study of the tide and tidal dynamics in the South China Sea, *Deep Sea Res., Part I*, *55*(2), 137–154, doi:10.1016/j.dsr.2007.10.007.

AGU PUBLICATIONS

Geophysical Research Letters

RESEARCH LETTER
10.1002/2015GL063561

Key Points:
- Lower LGM sea level caused more deep ocean tidal energy dissipation
- As a result, deep ocean mixing increases strongly in a global climate model
- This accelerates the meridional overturning circulation by 21–46%

Supporting Information:
- Text S1, Figures S1–S3, and Tables S1–S3

Correspondence to:
A. Schmittner,
aschmitt@coas.oregonstate.edu

Citation:
Schmittner, A., J. A. M. Green, and S.-B. Wilmes (2015), Glacial ocean overturning intensified by tidal mixing in a global circulation model, *Geophys. Res. Lett.*, *42*, 4014–4022, doi:10.1002/2015GL063561.

Received 19 FEB 2015
Accepted 24 APR 2015
Accepted article online 29 APR 2015
Published online 22 MAY 2015

Glacial ocean overturning intensified by tidal mixing in a global circulation model

A. Schmittner[1], J. A. M. Green[2], and S.-B. Wilmes[2]

[1]College of Earth, Ocean, and Atmospheric Sciences, Oregon State University, Corvallis, Oregon, USA, [2]School of Ocean Sciences, Bangor University, Menai Bridge, UK

Abstract Due to lower sea levels during the Last Glacial Maximum (LGM), tidal energy dissipation was shifted from the shallow margins into the deep ocean. Here using a high-resolution tide model, we estimate that global energy fluxes below 200 m depth were almost quadrupled during the LGM. Applying the energy fluxes to a consistent tidal mixing parameterization of a global climate model results in a large intensification of mixing. Global mean vertical diffusivity increases by more than a factor of 3, and consequently, the simulated meridional overturning circulation accelerates by ~21–46%. In the model, these effects are at least as important as those from changes in surface boundary conditions. Our findings contrast with the prevailing view that the abyssal LGM circulation was more sluggish. We conclude that changes in tidal mixing are an important mechanism that may have strongly increased the glacial deep ocean circulation and should no longer be neglected in paleoclimate simulations.

1. Introduction

During the Last Glacial Maximum (LGM) (23,000–19,000 years before present), Earth's climate was colder [*Annan and Hargreaves*, 2013], ice sheets covered North America and northern Europe, and sea level was about 130 m lower than it is today [*Clark et al.*, 2009]. The LGM is one of the best studied time periods in Earth's history. Still, its ocean's meridional overturning circulation (MOC), although important for global heat, carbon, nutrient, and other fluxes, remains a topic of contention [*Lynch-Stieglitz et al.*, 2007]. The prevailing view of the recent literature is one of a sluggish abyssal circulation that is less ventilated and has accumulated more respired carbon [e.g., *DeVries and Primeau*, 2010; *Sigman et al.*, 2010; *Skinner et al.*, 2010]. Climate model simulations, such as those from the Paleoclimate Modeling Intercomparison Project, typically consider various changes in boundary conditions, but they do not account for differences in ocean mixing, despite its importance for the MOC [*Bryan*, 1987], and they produce conflicting results [*Green et al.*, 2009; *Otto-Bliesner et al.*, 2007]. A recent climate modeling study, assuming reduced deep ocean mixing during the LGM, concludes to have identified unambiguously the mechanism for observed large millennial time scale climate variability (Dansaard-Oeschger oscillations) [*Peltier and Vettoretti*, 2014]. Here we suggest that vertical mixing during the LGM was enhanced, and not reduced, thus questioning the conclusions of this study as well as the prevailing idea of a sluggish abyssal circulation during the LGM [*DeVries and Primeau*, 2010; *Sigman et al.*, 2010; *Skinner et al.*, 2010].

Mass fluxes across density layers in the upwelling part of the global MOC require an energy source to overcome gravity. In the contemporary, ocean tides are important [*Huang*, 1999; *Munk and Wunsch*, 1998], providing 3.5 TW (1 TW = 10^{12} W) globally, but most of this energy is lost to bottom friction on the shallow continental shelves (~0–200 m depth) with minor impacts on the MOC, which is controlled by mixing in the thermocline (~200–1000 m) and deep ocean (below 1 km). Only about 1–1.5 TW of tidal energy is dissipated below about 200 to 500 m depths [*Egbert and Ray*, 2000; *Schmittner and Egbert*, 2014], almost entirely through tidal flow over rough topography, which generates internal waves, the breaking of which leads to turbulence and mixing [*Jayne and St. Laurent*, 2001; *Ledwell et al.*, 2000; *St. Laurent et al.*, 2002]. During the LGM, much of the shallow tidal energy sink was removed because continental shelves were exposed due to the sea level drop. This must have generated larger tides and more dissipation in the deep ocean, which has triggered speculations that the LGM MOC must have been stronger than today [*Green et al.*, 2009; *Wunsch*, 2003].

Tide model simulations confirm larger LGM tides and suggest that energy dissipation of the major M_2 tide was globally about 50% larger during the LGM and tripled in the deep ocean [*Egbert et al.*, 2004; *Green*, 2010;

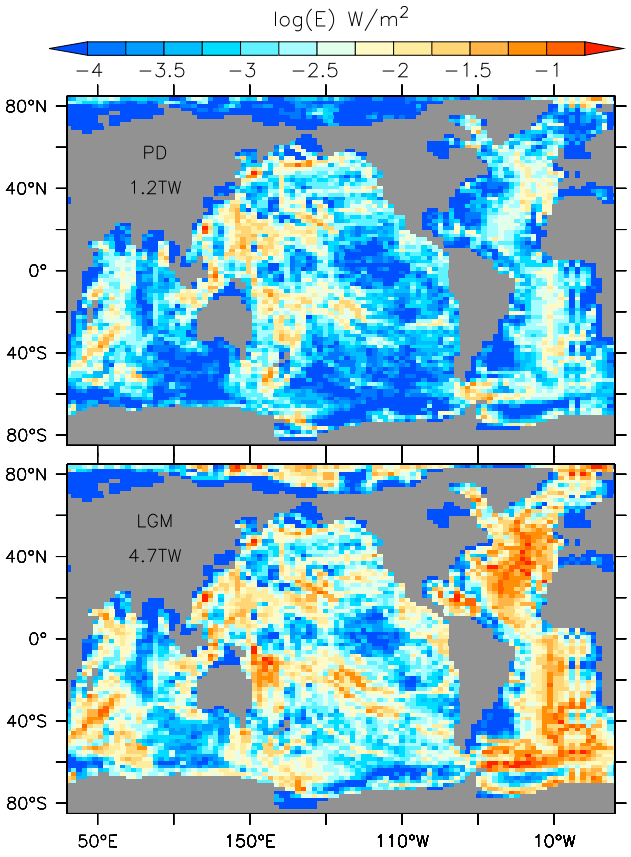

Figure 1. Maps of tidal energy dissipation due to internal wave drag E_w as a function of longitude (horizontal axis) and latitude (vertical axis). The sum of the dissipations of the four major tidal constituents (M_2, S_2, K_1, and O_1) calculated by the tide model for the (top) present day and the (bottom) LGM mapped onto the climate model grid is shown. The numbers over Asia denote the global integrals.

Wilmes and Green, 2014]. This implies much more vigorous deep ocean mixing and a stronger MOC. However, *Montenegro et al.* [2007] (M07), using a relatively coarse (0.5°) horizontal resolution tide model and the University of Victoria (UVic) climate model, report small changes in mixing and no consistent effects on the Atlantic MOC transport (M07 did not present other MOC aspects). Here we use a higher resolution tide model and an improved tidal mixing parameterization in a global climate-ocean circulation model to reassess this issue. We also consider additional MOC aspects not reported in M07.

2. Models and Experiments

A quasi-global tide model [*Wilmes and Green*, 2014] at 0.125° resolution (see Methods section for details) estimates energy fluxes $E_{TC} = E_{b,TC} + E_{w,TC}$ due to bottom drag E_b (important in the shallow ocean) and internal wave drag E_w (dominating at depths) from four major tidal constituents TC∈(M_2, S_2, K_1, and O_1). Together they account for more than 94% of today's dissipation [*Egbert and Ray*, 2003]. Various parameterizations for E_w have been proposed; see *Green and Nycander* [2013] for a recent review and comparison. Here we use a modified version of *Zaron and Egbert*'s [2006] scheme. For our first simulations, we applied a statistical fit to global present-day observations to obtain a globally averaged vertical stratification (described in terms of the buoyancy frequency $N = \sqrt{-g/\rho \partial \rho/\partial z}$, where g is the gravitational acceleration, ρ is the potential density, and z is the depth). In the second iteration runs presented in the supporting information, the parameterization was modified to use a spatially varying N computed from the climate model output. The main results from our study are likely insensitive to the specific internal wave drag parameterization used, because the spatial distributions of E_w are all similar for the different parameterizations [*Green and Nycander*, 2013]. The resulting horizontal distributions of E_w (Figure 1) are used as input to a tidal mixing parameterization in the global climate model [*Schmittner and Egbert*, 2014]. The UVic model (see Methods section for details) uses a three-dimensional ocean circulation model coupled to a simple one-layer energy-moisture balance model of the atmosphere. This setup allows multiple, 4500 yearlong sensitivity experiments, but it excludes wind or cloud interactions, that is, wind stress in the momentum forcing of the surface ocean and sea ice, advection velocities used in the horizontal transport of humidity, wind speed used in the air-sea gas and heat exchange, and atmospheric albedo are prescribed according to a mean annual cycle from reanalysis data.

Results from the last 500 years from three climate model experiments are presented: one present-day (preindustrial) control simulation (PD) and two LGM simulations. Both LGM runs use the same basic boundary conditions: prescribed ice sheets [*Peltier*, 2004], orbital parameters (which impact the seasonal and latitudinal distributions of solar irradiance), and atmospheric carbon dioxide concentrations (185 ppm, in

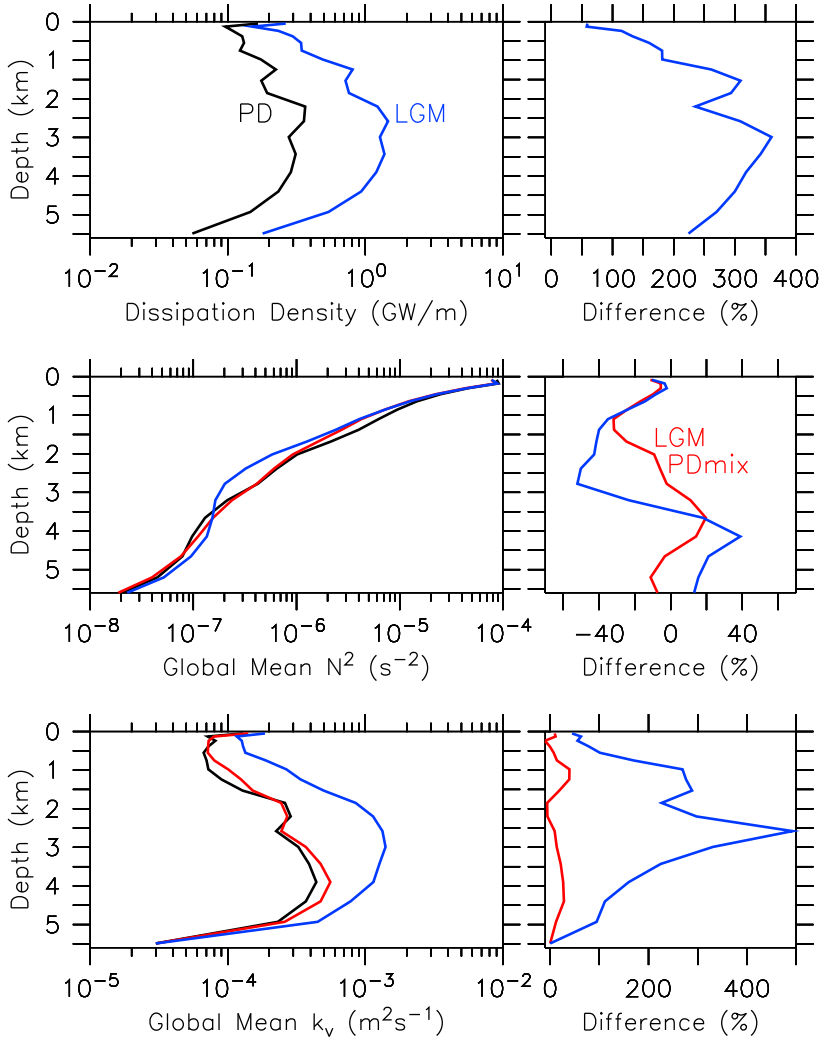

Figure 2. Vertical distributions of globally horizontally integrated (top) tidal energy dissipation density $E_w/\Delta z$ (per model layer thickness Δz) mapped on the climate model grid, (middle) averaged squared buoyancy frequency, and (bottom) averaged diapycnal diffusivity for the present day (black), LGM with PD mixing (red), and LGM (blue) experiments. (left) Absolute values and (right) percent differences with respect to PD (e.g., (LGM − PD)/PD × 100). N^2 was calculated using density referenced to 1 km depth (σ_1).

contrast to the 280 ppm concentrations of the PD; changes in minor greenhouse gases are neglected here). PD bathymetry is used in all climate model runs. The only difference between them is the tidal energy input E_w. Experiment "LGM PDmix" uses the present-day flux (Figure 1, top), whereas "LGM" (Figure 1, bottom) uses the flux from the tide model LGM simulation with lowered sea level but present-day stratification.

3. Results

The LGM tide model simulates a large intensification in tidal energy fluxes, with global total dissipation rates surging from 3.7 TW to 5.8 TW, consistent with previous studies [*Egbert et al.*, 2004; *Wilmes and Green*, 2014], whereas E_w almost quadruples from 1.3 TW to 4.7 TW (Table S1 in the supporting information and Figure 1). This implies that dissipation due to bottom drag decreased from 2.4 TW at PD to only 1.1 TW at the LGM, consistent with the reduced area covered by shallow oceans. Virtually all of the E_w enhancement occurs in the lower thermocline and deep ocean (below 200 m). Increases are particularly pronounced in the North Atlantic due to resonance effects [*Egbert et al.*, 2004; *Green*, 2010] (Figure 1).

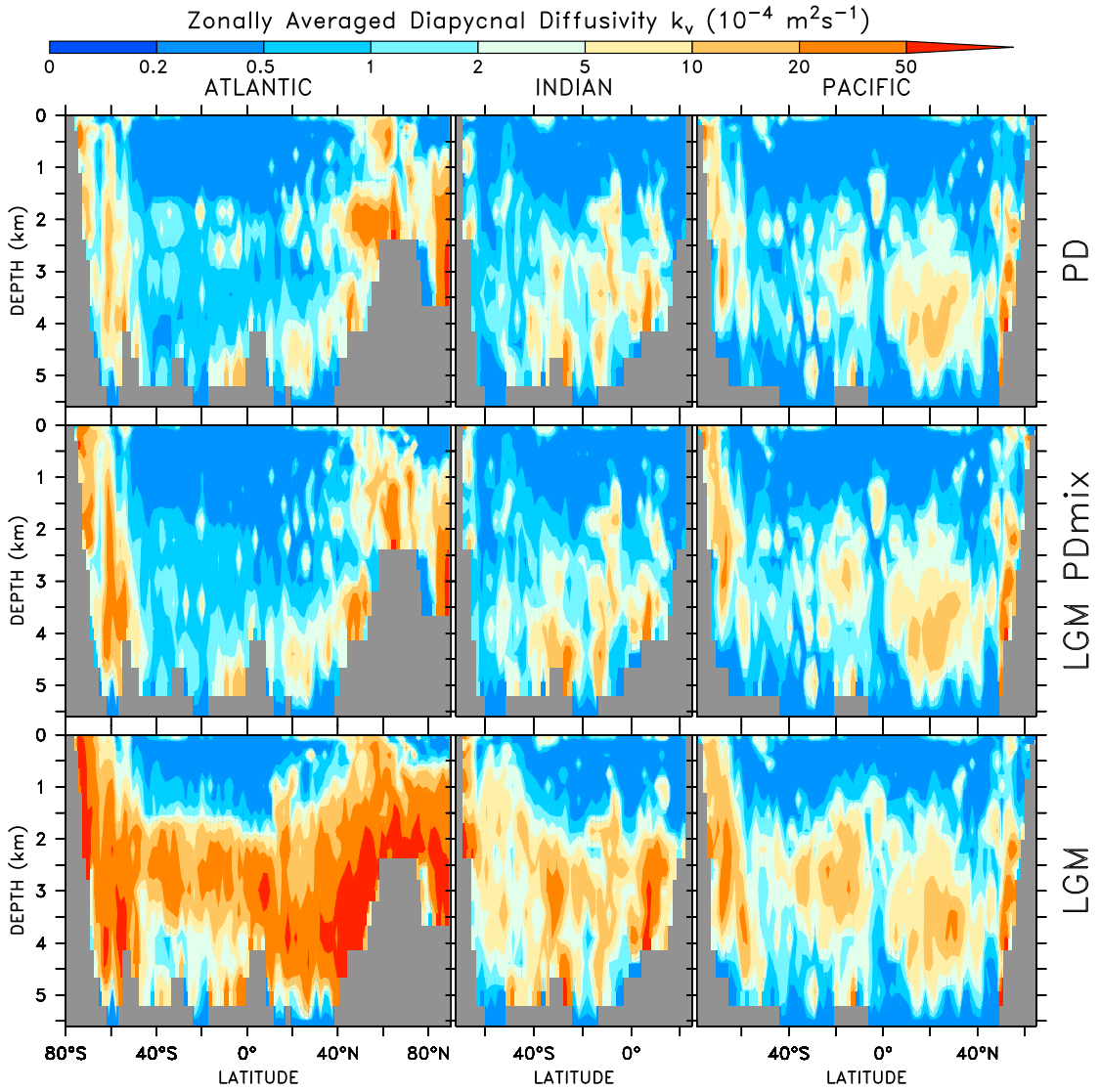

Figure 3. Zonally averaged diffusivities in the (left) Atlantic, (middle) Indian, and (right) Pacific at equilibrium in experiments (top) PD, (middle) LGM PDmix, and (bottom) LGM.

Horizontally integrated dissipation density increases at all depths but more so in the deep ocean than at the surface (Figure 2). At middepth, it is about 4 times larger in the LGM case compared with PD. Changes in stratification (N^2) are much smaller than those in dissipation. N^2 decreases slightly in both LGM simulations in the lower thermocline and middepths due to changes in surface boundary conditions. Increased mixing in the LGM simulation with respect to the LGM PDmix case causes a cooling of the upper ~2 km and a warming at depth (not shown), at least partially due to a deepening and increased flux of North Atlantic Deep Water (NADW), which decreases stratification between 2 and 3 km and increases it below 3.5 km.

Horizontally averaged diffusivities k_v increase substantially at all depths if LGM dissipation is used, whereas changes are much smaller for PD dissipation (Figure 2, bottom). Global mean k_v values are 2.1, 2.4, and 7.3 (all in $10^{-4}\,m^2\,s^{-1}$) for PD, LGM PDmix, and LGM, respectively. This indicates that changes in stratification have a much smaller impact on diffusivities than changes in dissipation. This conclusion is also supported by additional experiments exploring feedback between stratification, dissipation, and circulation (supporting information). The most dramatic increases in mixing occur in the Atlantic (by ~650% on average), whereas in the Indian (~320%) and Pacific (~190%), they are slightly more modest (Figure 3).

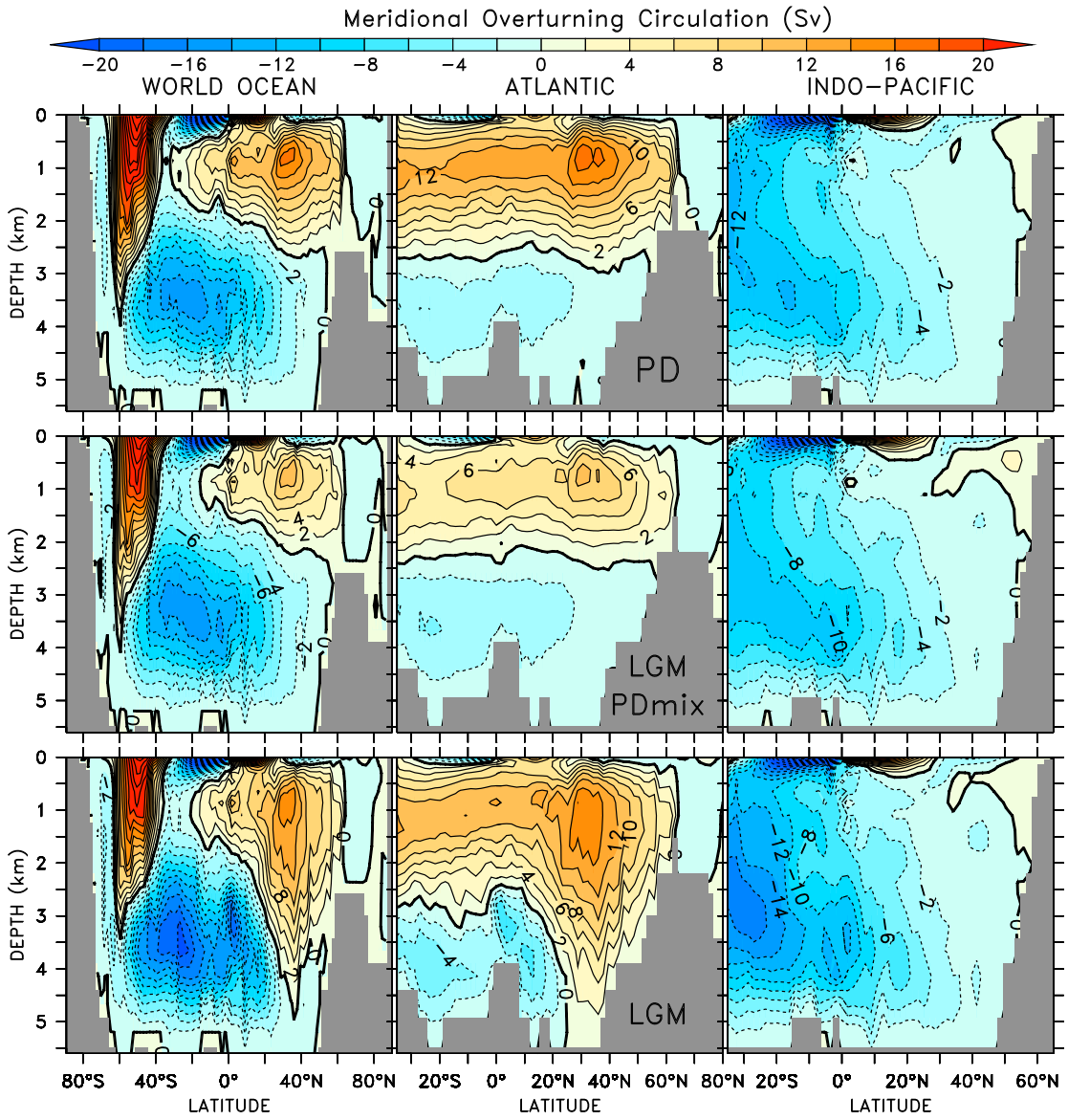

Figure 4. Meridional overturning circulation stream function of the (left) world ocean, (middle) Atlantic, and (right) Indian and Pacific in experiments (top) PD, (middle) LGM PDmix, and (bottom) LGM.

Changes in buoyancy forcing alone (LGM PDmix) lead to a large decrease (by 41–49%) of the middepth Atlantic MOC (AMOC) cell in our model (Figure 4 and Table S2 in the supporting information), consistent with previous results [*Weaver et al.*, 2001]. Circumpolar Deep Water (CPDW) inflow from the Southern Ocean into the Indian Ocean also decreases in LGM PDmix (by 30%), whereas the deep cells associated with Antarctic Bottom Water (AABW) flow into the Atlantic (0%) and CPDW flow into the Pacific (+6%) do not change much.

Including tidal mixing in the LGM simulations (experiment LGM versus LGM PDmix) leads to a large intensification of the MOC in the climate model. In the North and South Atlantic, the middepth overturning cell associated with NADW increases by 36% and 46%, respectively, almost entirely compensating for the decreases due to buoyancy forcing. (The reported percentage changes are with respect to the stronger MOC state in order to be comparable to the values reported for the buoyancy forcing; see also Table S2's caption in the supporting information.) AABW in the Atlantic accelerates by

21%, and CPDW fluxes into the Indian Ocean and Pacific increase by 32% and 24%, respectively. Thus, while for the AMOC, mixing effects are similar (albeit of opposite sign and slightly smaller) compared to buoyancy effects, for AABW and Pacific bottom water flow, mixing effects are much larger than buoyancy effects.

4. Discussion

The lower resolution tide model without Antarctic ice shelves and with a different internal wave drag parameterization used by M07 shows much smaller changes in dissipation (their Figure 1) than those simulated by our model (Figure S1 in the supporting information), particularly in the Atlantic. Changes there are likely sensitive to the resolved bathymetry owing to resonance effects [*Egbert et al*., 2004]. We infer that M07's small change in global E_w is the main reason for the differences with our results even though we cannot exclude other reasons. The results may also be sensitive to the choice of the internal wave drag parameterization. Differences in the k_v parameterization used in the climate model could also play a role. Quantification of these possibilities will be an important task for future research.

In their two simulations of glacial climate, *Peltier and Vettoretti* [2014] used values of k_v *smaller than or similar to* those used for their modern simulations: one globally constant value of $0.17 \times 10^{-4}\,m^2\,s^{-1}$ and one fixed vertical profile varying from $0.17 \times 10^{-4}\,m^2\,s^{-1}$ at the surface to $1 \times 10^{-4}\,m^2\,s^{-1}$ below ~1 km depth. These values are much smaller than the averaged values suggested by our LGM simulation (10^{-4}–$10^{-3}\,m^2\,s^{-1}$; Figure 2), and they are inconsistent with our results of *increased* LGM diffusivities compared to modern.

The parameterization of tidal mixing used here assumes that only a small constant fraction (1/3) of the energy dissipated into the internal wavefield contributes to local mixing. The remainder (2/3) propagates away and dissipates elsewhere, which is reflected in the constant background diffusivity $k_{bg} = 0.3 \times 10^{-4}\,m^2\,s^{-1}$. Given the large increase in tidal energy dissipation during the LGM, it is reasonable to assume that the energy dissipation in regions far from the internal wave generation sites would also increase. However, this was not considered in our simulations in which the background diffusivity was fixed. Thus, our estimate of changed tidal energy dissipation on k_v and the LGM MOC is conservative.

5. Conclusions

We conclude that large increases in tidal energy dissipation in the deep ocean during the LGM may have intensified the MOC's middepth and bottom flows. In our climate model, tidal mixing effects are more important than those from surface buoyancy fluxes, particularly for bottom flows. The effect of tidal mixing on the AMOC in our model (~+40%) is larger than the combined effects of bouyancy and momentum fluxes as simulated by most comprehensive models (~−20 to +40%) [*Otto-Bliesner et al*., 2007]. Assuming that reconstructions of a weakened LGM AMOC are true, one can infer that the combined effects of other forcings would need to lead to a weakening of the AMOC. Our simulated LGM circulation including LGM mixing is not realistic because it shows deeper NADW, whereas tracer distributions such as carbon isotopes indicate similar or shallower NADW flow [*Gebbie*, 2014]. This mismatch suggests that other forcings, and/or model responses to the forcings, are not correct and/or that transient effects played a role [*Green et al*., 2009; *Zhang et al*., 2013]. Closure of the Bering Strait due to sea level drop leads to less freshwater transport from the Pacific into the Arctic/Atlantic and hence a strengthening of the LGM AMOC [*Hu et al*., 2010]. In our model, this effect is not included because the Bering Strait is closed in both PD and LGM simulations. This raises the question which process(es) could counter the effects of enhanced mixing and the closed Bering Strait to produce the weaker and shallower AMOC implied by the reconstructions. Answering this question and reconciling paleoobservations with models will require more work.

Our model does not reproduce the high abyssal salinities inferred from South Atlantic sediments [*Adkins et al*., 2002], which may imply stronger stratification. The effects of realistic LGM stratification deserve careful assessment in future work, but here we note that effects on mixing and the MOC are not straightforward due to opposing effects of N on dissipation (equation (M2)) and k_v (equation (M5)). However, while our experiments show only small effects of changes in stratification (LGM PDmix versus PD; see also Table S3 and Figure S3 in the supporting information), the effects may be larger for more realistic LGM stratification.

Our findings are in contrast to the prevailing view that the abyssal circulation was more sluggish during the LGM [*DeVries and Primeau*, 2010; *Sigman et al*., 2010; *Skinner et al*., 2010], and they question far-reaching conclusions from a study in which LGM mixing was reduced [*Peltier and Vettoretti*, 2014].

6. Materials and Methods

We use tidal energy dissipation maps calculated from a tide model as input to a parameterization of tidal mixing used in the climate model.

6.1. Tide Model Description

The tidal simulations are based on those in *Wilmes and Green* [2014]—a further development of the model used by *Egbert et al*. [2004]. The model, OTIS, solves the linearized shallow water equations on a 0.125°×0.125° horizontal grid with an open boundary at 89°N. In the current simulations, data from TPXO7.2 are used to provide boundary conditions in the PD simulations, whereas the LGM simulations used a vertical wall at the northern boundary to eliminate uncertainties with the boundary forcing. The effects of this should be minimal as any modification of the conditions here will only have marginal effects on the large-scale tidal dynamics [*Wilmes and Green*, 2014]. The only other forcing is the astronomic tide-generating force. Momentum is dissipated through two processes: first, a quadratic (in velocity) bed friction term

$$\mathbf{F}_b = C_d \mathbf{U}|\mathbf{u}|/H, \tag{M1}$$

in which $C_d = 3\times10^{-3}$ is a drag coefficient, H is the depth of the seafloor, $\mathbf{U}=\mathbf{u}$H is the tidal transport vector, and $\mathbf{u}$ is the total tidal velocity from all constituents under consideration, and second, a linear transfer of energy to internal waves. The latter is based on the scheme given by *Zaron and Egbert* [2006] but with an allowance of a spatially varying stratification field $N(x,y,z)$ which comes from the climate model simulations:

$$\mathbf{F}_w = C|\nabla H|^2 \frac{N_H \overline{N}}{8\pi^2\omega}\mathbf{U}, \tag{M2}$$

where $C=2$ is a scaling factor, N_b is the buoyancy frequency at the bed, N is the depth-averaged buoyancy frequency, and ω is the tidal frequency. The corresponding energy dissipation for bottom drag is

$$E_b = \rho_0 C_d |\mathbf{u}|\mathbf{u}^2 \tag{M3}$$

and that for internal wave drag

$$E_w = \rho_0 C|\nabla H|^2 \frac{N_b \overline{N}}{8\pi^2\omega} H\mathbf{u}^2. \tag{M4}$$

Dissipation was computed by using modeled tidal velocity amplitudes in the respective parameterization, and the resulting (high-resolution) fields were averaged over 28×14 grid points before being adjusted to the UVic grid using linear interpolation.

6.2. Climate Model Description

The University of Victoria Earth System Climate Model [*Weaver et al*., 2001] is used in version 2.9 [*Eby et al*., 2009]. It consists of a coarse resolution (1.8×3.6°, 19 vertical layers) ocean general circulation model coupled to a one-layer atmospheric energy-moisture balance model and a dynamic thermodynamic sea ice model, both at the same horizontal resolution. The model is forced with seasonally varying solar irradiance at the top-of-the-atmosphere, cloud albedo, wind stress, and moisture advection velocities. This seasonal forcing does not change between different years. We use the tidal mixing parameterization developed by *Jayne and St. Laurent* [2001], *Simmons et al*. [2004], and *St. Laurent et al*. [2002] as improved by *Schmittner and Egbert* [2014], which includes the effect of subgrid-scale bathymetry on the depth of energy input and distinguishes between diurnal and semidiurnal tides. Briefly, the diapycnal diffusivity is

$$k_v = k_{bg} + \frac{\Gamma\varepsilon}{N^2}, \tag{M5}$$

where $k_{bg} = 0.3 \times 10^{-4}\ \mathrm{m^2\,s^{-1}}$ is the background diffusivitiy accounting for the effects of remotely dissipated tidal energy and other mixing processes, N is the buoyancy frequency, and $\Gamma = 0.2$ is the mixing efficiency. The energy dissipation rate is

$$\varepsilon = \frac{1}{\rho} \sum_{z'>z}^{H} \sum_{\mathrm{TC}} q_{\mathrm{TC}} E_{w,\mathrm{TC}}(x, y, z') F(z, z'), \tag{M6}$$

where $E_{w,\mathrm{TC}}(x,y,z')$ is the energy flux from the barotropic tide into the internal wavefield calculated from the tide model and mapped onto a climate model grid considering subgrid-scale bathymetry at high horizontal resolution (which introduced the z' dependence); F is the vertical decay function, which uses an e-folding depth of 500 m above the seafloor H; and

$$q_{\mathrm{TC}} = \begin{cases} 1, & \text{for } |y| > y_{c,\mathrm{TC}} \\ 0.33, & \text{else} \end{cases} \tag{M7}$$

is the local dissipation efficiency, which depends on the critical latitude y_c, which is 30° for diurnal tides (K_1 and O_1) and 70° for semidiurnal tides (M_2 and S_2).

Acknowledgments

A.S. has been supported by the National Science Foundation's Marine Geology and Geophysics program grant OCE-1131834 and Physical Oceanography program grant OCE-1260680. J.A.M.G. acknowledges funding from the Climate Change Consortium for Wales and from the Natural Environmental Research Council (Advanced Fellowship NE/F014821/1). S.B.W. has a PhD studentship from Fujitsu Europe through HPC Wales, who also provided computer access for the tidal model simulations. Data will be made freely available on the National Oceanographic and Atmospheric Administration's National Climatic Data Center.

The Editor thanks two anonymous reviewers for their assistance in evaluating this paper.

References

Adkins, J. F., K. McIntyre, and D. P. Schrag (2002), The salinity, temperature, and delta O-18 of the glacial deep ocean, *Science*, *298*(5599), 1769–1773.

Annan, J. D., and J. C. Hargreaves (2013), A new global reconstruction of temperature changes at the Last Glacial Maximum, *Clim. Past*, *9*(1), 367–376.

Bryan, F. (1987), Parameter sensitivity of primitive equation ocean general circulation models, *J. Phys. Oceanogr.*, *17*(7), 970–985.

Clark, P. U., A. S. Dyke, J. D. Shakun, A. E. Carlson, J. Clark, B. Wohlfarth, J. X. Mitrovica, S. W. Hostetler, and A. M. McCabe (2009), The Last Glacial Maximum, *Science*, *325*(5941), 710–714.

DeVries, T., and F. Primeau (2010), An improved method for estimating water-mass ventilation age from radiocarbon data, *Earth Planet. Sci. Lett.*, *295*(3–4), 367–378.

Eby, M., K. Zickfeld, A. Montenegro, D. Archer, K. J. Meissner, and A. J. Weaver (2009), Lifetime of anthropogenic climate change: Millennial time scales of potential CO_2 and surface temperature perturbations, *J. Clim.*, *22*(10), 2501–2511.

Egbert, G. D., and R. D. Ray (2000), Significant dissipation of tidal energy in the deep ocean inferred from satellite altimeter data, *Nature*, *405*(6788), 775–778.

Egbert, G. D., and R. D. Ray (2003), Semi-diurnal and diurnal tidal dissipation from TOPEX/Poseidon altimetry, *Geophys. Res. Lett.*, *30*(17), 1907, doi:10.1029/2003GL017676.

Egbert, G. D., R. D. Ray, and B. G. Bills (2004), Numerical modeling of the global semidiurnal tide in the present day and in the Last Glacial Maximum, *J. Geophys. Res.*, *109*, C03003, doi:10.1029/2003JC001973.

Gebbie, G. (2014), How much did Glacial North Atlantic Water shoal?, *Paleoceanography*, *29*, 190–209, doi:10.1002/2013PA002557.

Green, J. A. M. (2010), Ocean tides and resonance, *Ocean Dyn.*, *60*(5), 1243–1253.

Green, J. A. M., and J. Nycander (2013), A comparison of tidal conversion parameterizations for tidal models, *J. Phys. Oceanogr.*, *43*(1), 104–119.

Green, J. A. M., C. L. Green, G. R. Bigg, T. P. Rippeth, J. D. Scourse, and K. Uehara (2009), Tidal mixing and the meridional overturning circulation from the Last Glacial Maximum, *Geophys. Res. Lett.*, *36*, L15603, doi:10.1029/2009GL039309.

Hu, A., G. A. Meehl, B. L. Otto-Bliesner, C. Waelbroeck, W. Han, M.-F. Loutre, K. Lambeck, J. X. Mitrovica, and N. Rosenbloom (2010), Influence of Bering Strait flow and North Atlantic circulation on glacial sea-level changes, *Nat. Geosci.*, *3*(2), 118–121.

Huang, R. X. (1999), Mixing and energetics of the oceanic thermohaline circulation, *J. Phys. Oceanogr.*, *29*(4), 727–746.

Jayne, S. R., and L. C. St. Laurent (2001), Parameterizing tidal dissipation over rough topography, *Geophys. Res. Lett.*, *28*(5), 811–814, doi:10.1029/2000GL012044.

Ledwell, J. R., E. T. Montgomery, K. L. Polzin, L. C. St. Laurent, R. W. Schmitt, and J. M. Toole (2000), Evidence for enhanced mixing over rough topography in the abyssal ocean, *Nature*, *403*(6766), 179–182.

Lynch-Stieglitz, J., et al. (2007), Atlantic meridional overturning circulation during the Last Glacial Maximum, *Science*, *316*(5821), 66–69.

Montenegro, A., M. Eby, A. J. Weaver, and S. R. Jayne (2007), Response of a climate model to tidal mixing parameterization under present day and Last Glacial Maximum conditions, *Ocean Model.*, *19*(3–4), 125–137.

Munk, W., and C. Wunsch (1998), Abyssal recipes II: Energetics of tidal and wind mixing, *Deep Sea Res., Part I*, *45*(12), 1977–2010.

Otto-Bliesner, B. L., C. D. Hewitt, T. M. Marchitto, E. Brady, A. Abe-Ouchi, M. Crucifix, S. Murakami, and S. L. Weber (2007), Last Glacial Maximum ocean thermohaline circulation: PMIP2 model intercomparisons and data constraints, *Geophys. Res. Lett.*, *34*, L12706, doi:10.1029/2007GL029475.

Peltier, W. R. (2004), Global glacial isostasy and the surface of the ice-age Earth: The ICE-5G (VM2) model and GRACE, *Annu. Rev. Planet. Sci.*, *32*, 111–149.

Peltier, W. R., and G. Vettoretti (2014), Dansgaard-Oeschger oscillations predicted in a comprehensive model of glacial climate: A "kicked" salt oscillator in the Atlantic, *Geophys. Res. Lett.*, *41*, 7306–7313, doi:10.1002/2014GL061413.

Schmittner, A., and G. D. Egbert (2014), An improved parameterization of tidal mixing for ocean models, *Geosci. Model Dev.*, *7*(1), 211–224.

Sigman, D. M., M. P. Hain, and G. H. Haug (2010), The polar ocean and glacial cycles in atmospheric CO(2) concentration, *Nature*, *466*(7302), 47–55.

Simmons, H. L., S. R. Jayne, L. C. St. Laurent, and A. J. Weaver (2004), Tidally driven mixing in a numerical model of the ocean general circulation, *Ocean Model.*, *6*(3–4), 245–263.

Skinner, L. C., S. Fallon, C. Waelbroeck, E. Michel, and S. Barker (2010), Ventilation of the deep Southern Ocean and deglacial CO_2 rise, *Science*, *328*(5982), 1147–1151.

St. Laurent, L. C., H. L. Simmons, and S. R. Jayne (2002), Estimating tidally driven mixing in the deep ocean, *Geophys. Res. Lett.*, *29*(23), doi:10.1029/2002GL015633.

Weaver, A. J., et al. (2001), The UVic Earth System Climate Model: Model description, climatology, and applications to past, present and future climates, *Atmos. Ocean*, *39*(4), 361–428.

Wilmes, S.-B., and J. A. M. Green (2014), The evolution of tides and tidally driven mixing over 21,000 years, *J. Geophys. Res. Oceans*, *119*, 4083–4100, doi:10.1002/2013JC009605.

Wunsch, C. (2003), Determining paleoceanographic circulations, with emphasis on the Last Glacial Maximum, *Quat. Sci. Rev.*, *22*(2–4), 371–385.

Zaron, E. D., and G. D. Egbert (2006), Estimating open-ocean barotropic tidal dissipation: The Hawaiian Ridge, *J. Phys. Oceanogr.*, *36*(6), 1019–1035.

Zhang, X., G. Lohmann, G. Knorr, and X. Xu (2013), Different ocean states and transient characteristics in Last Glacial Maximum simulations and implications for deglaciation, *Clim. Past*, *9*(5), 2319–2333.